

Interplay between magnetic and dielectric phenomena  
at transition metal oxide interfaces

Der Fakultät für Mathematik, Informatik und Naturwissenschaften der RWTH Aachen University vorgelegte Dissertation zur Erlangung des akademischen Grades eines Doktors der Naturwissenschaften

von  
Diplom-Physiker  
Daniel Schumacher  
aus Düsseldorf

# Abstract

The present work is concerned with the preparation, characterization and analysis of thin film heterostructures of perovskite oxide materials. Two different systems have been analyzed in detail:  $\text{La}_{0.66}\text{Sr}_{0.33}\text{MnO}_3/\text{SrTiO}_3$  (LSMO/STO) heterostructures have been investigated in order to understand the unusual occurrence of an exchange bias effect in multilayers of these two oxides [1]. Monocrystalline LSMO single and LSMO/STO bilayers have been grown on STO by both High Oxygen Pressure Sputter Deposition (HSD) and Pulsed Laser Deposition. It was possible to reproduce the Exchange Bias effect in the samples grown by HSD by reducing the oxygen pressure during the layer growth. In fact, the size of the effect can be increased by further reduction of the oxygen pressure. The macroscopic sample analysis by X-ray Diffraction and Vibrating Sample Magnetometry suggests that the occurrence of the Exchange Bias effect is linked to oxygen deficiencies in the LSMO layer. By combining X-ray Reflectometry, Polarized Neutron Reflectometry and X-ray Resonant magnetic Scattering (XRMS), the magnetic depth profile of the samples has been determined. By this, a region in LSMO at the interface to STO has been detected, where the magnetic moment is strongly suppressed. By putting together the results of the macroscopic sample analysis and the scattering experiments, an explanation for the occurrence of the effect can be given: It is proposed, that a combination of strain and oxygen deficiencies shifts the LSMO at the interface in the antiferromagnetic phase of the LSMO strain vs. doping phase diagram. This interface region thus couples to the ferromagnetic part of the LSMO causing the Exchange Bias effect.

The second heterostructure system under investigation in this work are bilayers of  $\text{La}_{0.5}\text{Sr}_{0.5}\text{MnO}_3$  (LSMO) and  $\text{BaTiO}_3$  (BTO). A possible dependence of the interface near magnetic structure of  $\text{La}_{1-x}\text{Sr}_x\text{MnO}_3$  having a doping level  $x$  close to the ferromagnetic-antiferromagnetic phase diagram boundary on the orientation of the electric polarization in the BTO film was proposed theoretically [2]. Therefore, here it was the aim to analyze to what extent these predictions can be reproduced experimentally. Epitaxial  $\text{La}_{0.5}\text{Sr}_{0.5}\text{MnO}_3/\text{BaTiO}_3$  bilayers have been grown by Molecular Beam Epitaxy on conductive Nb doped STO substrates. It was found that the magnetic properties of the LSMO thin film highly depend on the stacking order of the bilayer: the sample with LSMO on top of BTO shows antiferromagnetic, the one with BTO on top of LSMO ferromagnetic behavior. This can be explained by the different strain states present in the two configurations and proves that the doping level  $x$  in the  $\text{La}_{1-x}\text{Sr}_x\text{MnO}$  layer is very close to the nominal value of 0.5. The magnetic depth profile in the samples has been determined by XRMS. The simulations reveal a continuous magnetization in the ferromagnetic sample and a small net magnetization in the antiferromagnetic sample probably is created by canted magnetic moments due to the applied magnetic field during the experiment. The experiment reveals that this small net moment is suppressed at the interface to air, which can be explained by the reduced dimensionality close to the surface. Therefore, this XRMS experiment reveals that it is possible with this technique to resolve magnetic profiles in samples with very small magnetic moments. So far, no dependence of the magnetic profile on the application of electric fields has been detected. Besides the possibility that the proposed effect cannot be reproduced experimentally in general, it is also possible that the electric polarization in BTO is not coherently switchable in the samples prepared in this work. The characterization and improvement of the ferroelectric properties needs to be the focus for future investigations on this system.

---

# Contents

<b>1</b>	<b>Introduction</b>	<b>1</b>
<b>2</b>	<b>Transition Metal Oxides</b>	<b>3</b>
2.1	Electronic Structure of Perovskites: Crystal Field Splitting . . . . .	4
2.2	Ferroelectricity in SrTiO <sub>3</sub> and BaTiO <sub>3</sub> . . . . .	6
2.3	Ordering Phenomena in La <sub>1-x</sub> Sr <sub>x</sub> MnO <sub>3</sub> . . . . .	7
2.3.1	Magnetic Ordering: Exchange Mechanisms . . . . .	8
2.3.2	Phase diagrams of La <sub>1-x</sub> Sr <sub>x</sub> MnO <sub>3</sub> . . . . .	10
<b>3</b>	<b>Motivation for the Analysed Oxidic Heterostructures</b>	<b>13</b>
3.1	La <sub>0.66</sub> Sr <sub>0.33</sub> MnO <sub>3</sub> /SrTiO <sub>3</sub> : Exchange Bias Effect . . . . .	13
3.2	La <sub>0.5</sub> Sr <sub>0.5</sub> MnO <sub>3</sub> /BaTiO <sub>3</sub> : Artificial Multiferroicity . . . . .	15
<b>4</b>	<b>Scattering theory</b>	<b>17</b>
4.1	Basic principles and Born approximation . . . . .	17
4.2	X-ray diffraction (XRD) . . . . .	19
4.3	Grazing incidence scattering . . . . .	21
4.3.1	Continuum description . . . . .	21
4.3.2	X-ray reflectometry (XRR) . . . . .	23
4.3.3	Polarized Neutron reflectometry (PNR) . . . . .	24
4.3.4	X-ray Resonant Magnetic Scattering (XRMS) . . . . .	25
<b>5</b>	<b>Thin Film Deposition Techniques with Oxygen</b>	<b>31</b>
5.1	Growth modes of epitaxial thin film . . . . .	31
5.2	High Oxygen Pressure Sputter Deposition (HSD) . . . . .	33
5.3	Pulsed Laser Deposition (PLD) . . . . .	34
5.4	Oxide Molecular Beam Epitaxy . . . . .	34
<b>6</b>	<b>Experimental Methods</b>	<b>37</b>
6.1	Sample Characterization . . . . .	37
6.1.1	Rutherford Backscattering (RBS) . . . . .	37
6.1.2	Reflection High Energy Electron Diffraction (RHEED) . . . . .	38
6.1.3	Atomic Force Microscopy (AFM) . . . . .	38
6.2	Macroscopic Magnetic and Ferroelectric Analysis . . . . .	39
6.2.1	Vibrating Sample Magnetometry . . . . .	39
6.2.2	Electrical Hysteresis Measurements . . . . .	40
6.3	Mesoscopic Structural and Magnetic Analysis . . . . .	40
6.3.1	X-ray Reflectometry (XRR) and X-ray Diffraction (XRD) . . . . .	41
6.3.2	Polarized Neutron Reflectometry . . . . .	41
6.3.3	X-ray Resonant Magnetic Scattering (XRMS) in reflectometry geometry . . . . .	42
<b>7</b>	<b>Results and Discussion I: La<sub>0.66</sub>Sr<sub>0.33</sub>MnO<sub>3-δ</sub>/SrTiO<sub>3</sub></b>	<b>45</b>
7.1	Preparation of stoichiometric LSMO single and LSMO/STO bilayers . . . . .	45

7.2	Sizeable Exchange Bias induced by oxygen deficiencies . . . . .	51
7.3	Drastically reduced magnetization at LSMO/STO interfaces in EB samples . . . . .	58
7.4	Possible explanation of EB effect in the LSMO/STO thin film system . . . . .	77
<b>8</b>	<b>Results and Discussion II: <math>\text{La}_{0.5}\text{Sr}_{0.5}\text{MnO}_3/\text{BaTiO}_3</math></b>	<b>79</b>
8.1	Preparation of stoichiometric and epitaxial LSMO/BTO bilayers by OMBE . . . . .	79
8.2	Macroscopic magnetic and ferroelectric characterization . . . . .	86
8.3	Analysis of the magnetic depth profile . . . . .	89
<b>9</b>	<b>Summary, Conclusion and Outlook</b>	<b>97</b>
<b>A.</b>	<b>Fit results of the XRR and PNR data evaluation</b>	<b>101</b>
<b>B.</b>	<b>List of Figures</b>	<b>113</b>
<b>C.</b>	<b>Abbreviations</b>	<b>115</b>
<b>D.</b>	<b>Physical Constants</b>	<b>117</b>
	<b>Bibliography</b>	<b>119</b>
	<b>Acknowledgments</b>	<b>127</b>

# 1 Introduction

One of the big scientific interests in ongoing condensed matter research is the preparation, analysis and understanding of strong correlated electron systems in complex oxides [3]. The equilibrium of these fascinating materials is determined by the interplay of lattice, charge, spin and orbital degrees of freedom. Therefore, a huge variety of extraordinary properties have already been discovered in oxide materials such as superconductivity [4], the colossal magnetoresistance (CMR) effect [5] or the multiferroic effect [6]. Due to the improvements over the last decades in thin film deposition techniques like High Oxygen Pressure Sputter Deposition (HSD) [7, 8], Pulsed Laser Deposition (PLD) [9] and Oxide Molecular Beam Epitaxy [10], heterostructures of two or more of these materials with almost atomically flat interfaces can be designed. The arrangement in a thin film system can lead to even more interesting and novel effects due to the coupling of the different properties via the common interface or the additional lattice strain present at the interface - or a combination of both. To only name a few, superconductivity between insulating layers [11], magnetism between non-magnetic materials [12] or ferromagnetism between antiferromagnetic oxides [13] have been realized.

One of the most prominent combinations - not only in thin films - is the preparation of an interface between an antiferromagnet and a ferromagnet which in a lot of cases causes an Exchange bias (EB) effect in the system, i.e. a shift of the hysteresis curve along the field axis. Even though the EB effect is known for more than 50 years [14], there is still no comprehensive understanding of all the different occurring variations [15, 16]. But in general there is one requirement for the presence of the EB: the sample needs to contain an antiferromagnetic region which is in contact to a region having a net magnetic moment (ferro- or ferrimagnet). It is therefore very surprising that an EB effect has been reported by Zhu et al [1, 17, 18] in multilayers of ferromagnetic  $\text{La}_{0.66}\text{Sr}_{0.33}\text{MnO}_3$  and non-magnetic  $\text{SrTiO}_3$ . One of the major goals of this work is the analysis of the magnetic structure in  $\text{La}_{0.66}\text{Sr}_{0.33}\text{MnO}_3$  arranged in a epitaxial thin film in contact with  $\text{SrTiO}_3$  in order to understand the origin of the EB effect in this system. This is not only of importance from the scientific point of view to reveal another unusual facet of the EB effect. In addition to the numerous realizations in metallic systems, the usage in oxide systems also opens up a lot more possibilities of combining the EB effect with other oxide properties. As an example, switching between the two distinct EB states by reversing the electric polarization of  $\text{BiFeO}_3$  has already been realized in  $\text{BiFeO}_3/\text{La}_{0.66}\text{Sr}_{0.33}\text{MnO}_3$  thin films [19], showing the importance of the EB effect for possible device applications and the necessity of a better understanding of the effect.

The just mentioned coupling effect in  $\text{BiFeO}_3/\text{La}_{0.66}\text{Sr}_{0.33}\text{MnO}_3$  belongs to another “hot topic” in oxide heterostructures: the possibility of influencing one macroscopic order parameter in the system by another one. Of particular interest for future applications would be the possibility of controlling the magnetic structure of the sample by switching an electric polarization in one of the materials: such a device - if reliably working - could for example ultimately lead to faster and more energy efficient Random Access Memories (RAM), where the information is electrically written and read via the TMR effect. It thus would combine the advantages of ferroelectric and ferromagnetic RAMs. Unfortunately, there are only very rare examples of materials (multiferroics), which exhibit both ferroelectric and (ferro-)magnetic properties due the fact that the first in general requires empty and the second non-empty  $d$ -orbitals [20]. In addition, the coupling

between the two order parameters in these rare bulk multiferroic materials is very weak. A possible way to circumvent this problem, is to combine a pure ferroelectric with a magnetic material in order to create an artificially multiferroic system with a strong coupling via the common interface. Recently, different possibilities to achieve such coupling have been proposed theoretically. In one of these works, the possibility of influencing the magnetic structure of  $\text{La}_{0.5}\text{Sr}_{0.5}\text{MnO}_3$  at the interface to  $\text{BaTiO}_3$  was predicted by switching the electric polarization in  $\text{BaTiO}_3$ . Therefore, the second thin film system analyzed in this work is  $\text{La}_{0.5}\text{Sr}_{0.5}\text{MnO}_3/\text{BaTiO}_3$  heterostructures in order to investigate, whether and to what extent the theoretical predictions can be reproduced experimentally.

## Outline of the present work

In order to address the above mentioned scientific questions, the scope of the present work covers the investigation of  $\text{La}_{0.66}\text{Sr}_{0.33}\text{MnO}_3/\text{SrTiO}_3$  and  $\text{La}_{0.5}\text{Sr}_{0.5}\text{MnO}_3/\text{BaTiO}_3$  thin film heterostructures. The work on both systems can be divided in two major parts: first the preparation and characterization of the heterostructures. The samples have been grown by three different methods, namely High Oxygen Pressure Sputter Deposition, Pulsed Laser Deposition and Oxide Molecular Beam Epitaxy. The preparation parameters has been optimized by characterizing the structural quality of the samples during and after the growth. The second major part is the detailed analysis of the magnetic and structural properties of the prepared samples. Besides the determination of the macroscopic magnetic behavior of the samples by Vibrating Sample Magnetometry, special emphasis is placed on the investigation of the mesoscopic structure of the samples. X-ray-Diffraction, X-ray Reflectometry, Polarized Neutron Reflectometry and X-ray Resonant Magnetic Scattering have been combined to gain a detailed picture of the structural and magnetic depth profile of the analyzed heterostructure systems.

A short introduction on transition metal oxides in general and the bulk properties of the materials used in this work in particular is given in chapter 2. Afterwards, the motivation for the analyzed heterostructures is stressed in more detail in chapter 3. Since the determination and analysis of the microscopic and mesoscopic properties of the oxide heterostructures is done by means of scattering methods, the basic principles of the scattering theory for the methods applied in this work are summarized in chapter 4. As mentioned before, one of the main parts of the present work is the sample characterization. All three preparation methods, their differences and advantages are introduced in chapter 5. After and during the preparation, the samples have been characterized and analyzed by several experimental techniques. The methods and the instruments used in this work are presented in chapter 6. In the two following chapters, the experimental results are presented and discussed. Chapter 7 deals with the preparation, characterization and analysis of the  $\text{La}_{0.66}\text{Sr}_{0.33}\text{MnO}_3/\text{SrTiO}_3$  heterostructures. Based on the data evaluation of the experimental results, an explanation for the occurrence of the Exchange Bias effect in this system is given in section 7.4. In analogy, the results for the  $\text{La}_{0.5}\text{Sr}_{0.5}\text{MnO}_3/\text{BaTiO}_3$  thin film system are discussed in chapter 8. In addition to a summary of the present work and the resulting conclusions, the final chapter will give an outlook for future experiments.

## 2 Transition Metal Oxides

The group of Transition Metal Oxides (TMO) is far too big and diverse to be introduced here completely (for a broader overview see for example [21]). The same is true for the huge variety of interesting phenomena that occur in TMO. Therefore, in this chapter only the basic concepts and characteristics of TMO relevant for this work will be summarized, followed by an overview of the general properties of the TMO, which are used in the oxidic heterostructures investigated in this work.

TMO can crystallize in many different crystal structures. The TMO under investigation in this work have the chemical composition  $ABO_3$ , where A is either an alkaline earth metal (Sr or Ba) or the rare earth metal La and B a TMO (Ti or Mn). A very common crystal structure for this type of TMO is the perovskite structure, named after the compound  $CaTiO_3$  [22]. As we will see in the following sections, one of the most important parameters, which defines the electronic and thereby metallic properties of any TMO, is the oxygen coordination of the transition metal atom. In perovskites the TMO atom is surrounded by six nearest oxygen atoms forming an octahedron. In the highest symmetric case this  $BO_3$  octahedron is regular with the oxygen atoms located at the centers of the six faces of a cube created by eight A atoms (figure 2.1). As the A site cation in this structure needs to be larger than the B site cation, the A site cation usually has the same or a lower oxydation state. With oxygen always being  $O^{2-}$  in all TMO this still leaves a broad range of possible valencies for the transition metal ion: not only can the combinations  $A^{3+}B^{3+}(O^{2-})_3$ ,  $A^{2+}B^{4+}(O^{2-})_3$  and  $A^{5+}B^{3+}(O^{2-})_3$  be realized, by doping the A site cation with a different metal also mixed valencies for the transition metal ion are possible (e.g.  $La_{1-x}Sr_xMnO_3$  with x ranging between 0 and 1)

A rough estimate whether or not a  $ABO_3$  TMO crystallizes in the perovskite structure can be obtained by looking at the empirical found tolerance factor  $t$  introduced by Goldschmidt [23]

$$t = \frac{R_A + R_O}{\sqrt{2}(R_B + R_O)} \quad (2.1)$$

where  $R_A, R_B$  and  $R_O$  are the ionic radii of atoms A, B and O, respectively. The perovskite structure is stable for tolerance factors between 0.78 and 1.05, but only for values between 0.81 and 1 the cubic unit cell with space group  $Pm3m$  is formed. For bigger values the transition metal atom is too small for the octahedra resulting in possible shifts of the atom away from the center of the octahedron. By this an electric polarization might be created, leading to distortions of the cubic unit cell (figure 2.1b). In case of having a macroscopic spontaneous polarization, which can be switched by an electric field, the material is called a ferroelectric. Examples are  $BaTiO_3$  or strained  $SrTiO_3$  (see section 2.2). For  $t < 0.81$  the A atoms are too small to fill the space between the oxygen octahedra. As a result the octahedra can tilt in various ways to minimize the spacings to the A atoms, which often results in the creation of more complicated unit cells (figure 2.1c). A detailed overview of the possible structures formed by the buckling of the octahedra is given in [24].



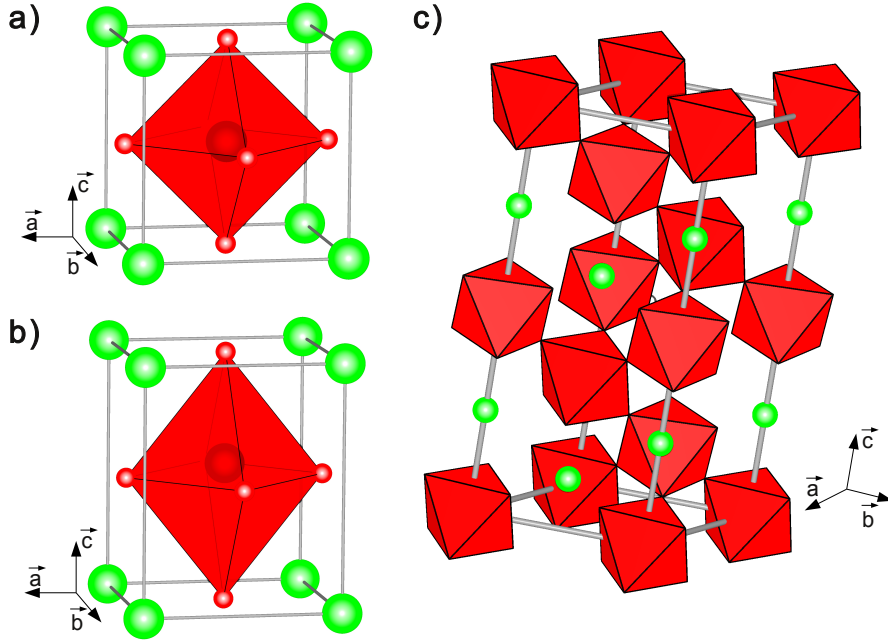


**Figure 2.1:** Different unit cells for the perovskite structure. a) cubic, b) tetragonal: the unit cell is elongated along  $\vec{c}$ . In addition the central atom is shifted along the same direction, c) rhombohedral unit cell due to tilting of the oxygen octahedra

## 2.1 Electronic Structure of Perovskites: Crystal Field Splitting

The physical properties of TMO are determined to a big extent by the  $d$  electrons of the transition metal ion. In the octahedral oxygen surrounding, these energy levels split in two groups in order to minimize the Coulomb repulsion (Crystal Field Splitting (CFS), figure 2.2): two of five  $d$  orbitals are pointing towards oxygen ions ( $d_{x^2-y^2}$  and  $d_{3z^2-r^2}$ ) and thus shift to a higher energy than the other three, which are pointing in between the negatively charged ligands ( $d_{xy}$ ,  $d_{zx}$  and  $d_{yz}$ ). These two energy levels are called  $t_{2g}$  and  $e_g$  orbitals, respectively, and are separated by an energy gap  $10D^1$ . Since the total energy needs to be the same compared to an imaginary equally distributed oxygen surrounding, the  $e_g$  orbitals are shifted upwards by  $\frac{3}{5}10D$  and the  $t_{2g}$  levels downwards by  $\frac{2}{5}10D$ . The size of the energy gap  $10D$  is dependent on the distance between the TMO ion and the oxygen ligands. The smaller the distance is, the bigger gets the overlap of the  $e_g$  orbitals with the oxygens  $p$  orbitals, and hence the bigger  $10D$  becomes. The value of  $10D$  is important, if the TMO ion possesses more than three  $d$  electrons. In this case it depends on the comparison of the crystal field splitting with the internal exchange energy  $J_H$ , which favors the configuration with maximal spin (Hund's first rule), whether the fourth electron is filled in the  $t_{2g}$  ( $10D > J_H$ , "low-spin" state) or  $e_g$  orbital ( $10D < J_H$ , "high-spin" state).

Besides the splitting of the energy levels, the crystal field has another important impact on the total magnetic moment of the transition metal ion: it can be shown that the orbital moment  $L$  of the transition metal ion vanishes in a crystal field of low enough symmetry (quenching of the

<sup>1</sup>It should be pointed out, that the CFS is highly dependent on the geometry of the TMO environment. E.g. in a tetrahedral oxygen surrounding one finds exactly the opposite situation: Here the  $e_g$  orbitals are energetically more favourable than the  $t_{2g}$  levels.

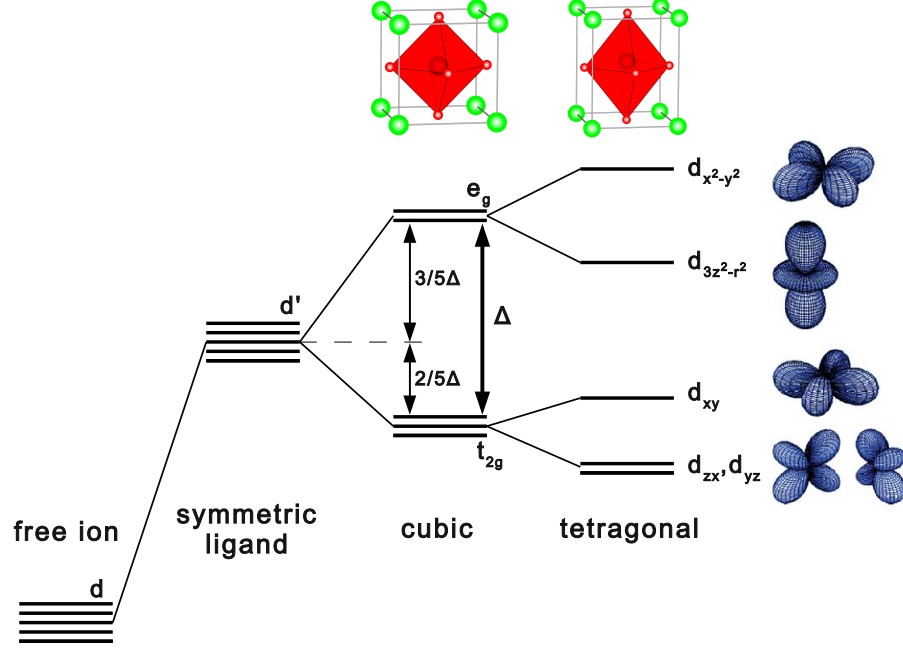


**Figure 2.2:** Influence of the octahedral coordination of the transition metal ion on the electronic energy levels in a local picture

orbital moment) and that the total effective moment  $\mu_{eff}$  is determined in most cases simply by the spin moment  $S$ :

$$\mu_{eff} = 2\mu_B \sqrt{S(S+1)} \quad (2.2)$$

This becomes clear by looking at one of the components of the angular momentum operator, e.g.  $L_z$ :

$$L_z = \frac{\hbar}{i} \left( x \frac{\partial}{\partial y} - y \frac{\partial}{\partial x} \right) \quad (2.3)$$

For a real wave function follows, that  $\langle \Psi | L_z | \Psi \rangle$  will be purely imaginary. This is in contradiction to the fact, that  $L_z$  is a hermitian operator, i.e. the diagonal elements are real. Hence the only possible solution for all the components is

$$\langle \Psi | L_z | \Psi \rangle = \langle \Psi | L_x | \Psi \rangle = \langle \Psi | L_y | \Psi \rangle = 0 \quad (2.4)$$

It can be shown by group theory [25] that for a lot of electronic configurations of the  $d$  orbitals including  $\text{Mn}^{3+}$   $\Psi$  is real resulting in a quenched orbital moment  $L$ .

As far as we have discussed the crystal field splitting in perovskites it would not be clear, which of the two still degenerate orbitals of the  $e_g$  level the fourth electron in  $\text{Mn}^{3+}$  would occupy. But it has already been found in the 1930s by Jahn and Teller, that “the nuclear configuration of any nonlinear polyatomic system in a degenerate electronic state is unstable with respect to nuclear displacements that lower the symmetry and remove the degeneracy” (Jahn-teller-Theorem [26]). Why this leads to an energetically favourable situation can be understood exemplarily in the case of the  $\text{Mn}^{3+}$  ion located in an oxygen octahedron: assuming, that the electron occupies the  $d_{3z^2-r^2}$  orbital, one would expect that it pushes away the two oxygen anions closest to the  $d_{3z^2-r^2}$  orbital due to Coulomb repulsion. By doing this, a tetragonal distorted unit cell is obtained. But in this situation the two  $e_g$  orbitals are no longer degenerate. Due to the now bigger distance

to the oxygen anions in the  $d_{3z^2-r^2}$  orbital, the  $d_{x^2-y^2}$  is lifted in energy (figure 2.2). Since every oxygen atom is part of two neighboring octahedra, these distortions are not independent for every single unit cell. In fact, this often leads to regular patterns in the crystal resulting e.g. in “ferro-orbital” (in all unit cells the  $e_g$  electron occupies the same orbital) or “antiferro-orbital” structures. These re-arrangements can be fluctuating (dynamic Jahn-Teller-Effect). In this case the unit cell might be undistorted on average. Usually the dynamic distortions are a local phenomenon at higher temperatures, whereas below a certain ordering temperature  $T_{JT}$  long range cooperative distortions might be established (cooperative Jahn-Teller-Effect).

Even though it will not be outlined here in detail, one should mention that the phenomena discussed in this section related to the electronic structure in crystal fields can be very well described in the framework of Crystal Field Theory (CFT). The CFT describes the system as a central atom surrounded by (pointlike) ligands by means of quantum mechanical electrostatic interactions. It is a quite simple model of the system, but a powerful tool in describing the crystal field effects discussed in this section. More details about a group theoretical analysis of the crystal field splitting can be found for example in [27].

## 2.2 Ferroelectricity in $\text{SrTiO}_3$ and $\text{BaTiO}_3$

Shifting the transition metal atom away from the center of the octahedra creates a net electric polarization. If such a shifting occurs cooperatively to the same direction in neighbouring unit cells, the TMO exhibits a spontaneous macroscopic electric polarization (Ferroelectricity). It is already known for a long time that ferroelectricity is favoured in TMO with empty  $d$  orbitals (“ $d^0$ -ness”) [20]. The reason is that shifting the transition metal ion in general costs energy due to the electrostatic Coulomb repulsion. Hence a shifting can only be favourable, if this energy cost is compensated by the hybridization energy gained due to stronger overlap between the oxygen  $2p$  and TMO  $d$  orbitals. It can be shown that the gain in hybridization energy is maximal for empty  $d$  states [28–30]. Even though fulfilling the “ $d^0$ -ness” condition,  $\text{SrTiO}_3$  (STO) is one of the few examples for a TMO that exhibits the undistorted cubic structure at room temperature with a lattice constant of  $3.905 \text{ \AA}$ . Due to the empty  $d$  orbitals, STO is an insulating non-magnetic TMO. In the unstrained bulk state it does not show ferroelectric behaviour at any temperature, even though large dielectric constants at low temperatures reveal a polar instability [31,32]. STO undergoes two structural phase transitions at lower temperatures due to tilting of the oxygen octahedra: below 105 K a tetragonal  $I4/mcm$  is formed by an alternating tilt of the oxygen octahedra around the tetragonal axis (“antiferrodistortive transition” (AFD)) [33,34]. There is theoretical evidence that the formation of this tetragonal phase prevents a ferroelectric transition [35–37], which without the tetragonal phase is theoretically predicted to occur around 30 K [38]. In addition it is suggested, that quantum fluctuations suppress the ferroelectric transition even stronger than the AFD transition [32,38,39]. The calculations also show, that the AFD transition temperatures would be higher without the quantum fluctuations.

Due to the strong instability with respect to polar distortions, STO can be quite easily forced to become ferroelectric by growing it as a strained thin film and a very rich strain-temperature phase diagram with several different ferroelectric phases has been established [37,40]. Since the transition temperature was found to increase with strain, STO can even be made ferroelectric at room temperature when grown on the appropriate substrate [40]. Another proof for the strong polar instability of STO was the discovery of ferroelectricity in STO below 23 K, when  $^{16}\text{O}$  is exchanged by  $^{18}\text{O}$  [41].

Even though the ferroelectricity of STO still is of big scientific interest, it is not part of this work. Here STO is used as a substrate for both heterostructures, which have been prepared and anal-

ysed. In addition, it has been deposited as a cap layer on some of the  $\text{La}_{0.66}\text{Sr}_{0.33}\text{MnO}_3$  single layers to form a  $\text{La}_{0.66}\text{Sr}_{0.33}\text{MnO}_3/\text{SrTiO}_3$  bilayer. For the second system ( $\text{La}_{0.5}\text{Sr}_{0.5}\text{MnO}_3/\text{BaTiO}_3$ ), conductive Nb doped STO substrates have been used to have the possibility to use it as a bottom electrode for applying electric fields to the  $\text{BaTiO}_3$  layer.

$\text{BaTiO}_3$  (BTO) in many ways behaves very similar to STO, but there are some important differences. At high temperatures, above 400 K, BTO also features the undistorted cubic unit cell. However, compared to STO it has a bigger lattice constant of 4.01 Å. Although the theoretical models in the same way like for STO predict quantum fluctuations, for BTO they are not strong enough to suppress the ferroelectricity: bulk BTO becomes tetragonal below 400 K, but in contrary to STO not by rotation of the oxygen octahedra. Here a displacive structural phase transition takes place, where Ba and Ti ions are shifted in one lattice direction with respect to the oxygen positions (figure 2.1). By this the unit cell becomes elongated along the direction of the shift of the atoms and a ferroelectric polarization is created in the same direction. At lower temperatures there are two further transitions, first to an orthorhombic, then to a rhombohedral structure. In those two phases the Ti ions are shifted along a (011) and (111) direction, respectively, causing the polarization to point in the same directions. A theoretical model to describe the BTO bulk behaviour with temperature was already proposed more than fifty years ago (displacive model [42]). However, it turned out that the simple picture of shifting the cations first along one (cubic to tetragonal), then along two (tetragonal to orthorhombic) and then along all three lattice directions (orthorhombic to rhombohedral) could not be the whole story, e.g. x-ray measurements revealed that the Ti atoms are shifted along all directions already in all the phases [43]. More recently a model, which can explain the experimental results, where the displacive model fails, has been established [43–45]: rather than being in the center of the octahedra in the cubic phase in this model the Ti atoms are shifted in all three lattice directions but the displacements are aligned in an antiferroelectric pattern. Then at each phase transition the Ti antiferroelectric order is abandoned for one of the lattice directions until a ferroelectric order is obtained in all three directions in the rhombohedral phase.

Under epitaxial strain BTO shows the same tendencies like STO. The ferroelectric transition temperatures increases by around 300 K per % strain [46]. Whereas BTO takes on orthorhombic phases under tensile strain, compressive strain stabilizes the tetragonal phase described above for bulk BTO. In this work BTO was deposited on STO substrates giving an in-plane compressive strain of about 2.5%. In this case the tetragonal ferroelectric phase is stable from far above room temperature down to lowest temperatures. More details about epitaxial strained BTO thin films including temperature-strain phase diagrams can be seen for example in [47–49].

## 2.3 Ordering Phenomena in $\text{La}_{1-x}\text{Sr}_x\text{MnO}_3$

Out of the large group of strong correlated oxides  $\text{La}_{1-x}\text{Sr}_x\text{MnO}_3$  (LSMO) is one of the most studied materials due to the Colossal-Magneto-Resistance (CMR) [5, 50, 51] effect and the huge variety of spin, charge and orbital orders that can be established by changing the doping level [52, 53]. All of these phenomena are strongly connected with the  $d$  electrons of manganese, which is the major difference of LSMO compared to STO and BTO. Due to the valency difference between  $\text{La}^{3+}$  and  $\text{Sr}^{2+}$ , the doping level  $x$  determines the ratio of  $\text{Mn}^{3+}$  (pure  $\text{LaMnO}_3$ ) and  $\text{Mn}^{4+}$  (pure  $\text{SrMnO}_3$ ). Due to the small crystal field splitting in  $\text{La}_{0.66}\text{Sr}_{0.33}\text{MnO}_3$ , the fourth  $d$  electron in  $\text{Mn}^{3+}$  occupies one of the  $e_g$  orbitals (“high-spin” state). In section 2.1 it has been discussed, how the crystal field in a TMO influences the electronic structure and the effective magnetic moment - both spin and orbital - of the transition metal ion. In the following the most important factors on the magnetic coupling between neighbouring transition metal ions will be

introduced. After that the resulting complex and diverse properties of  $\text{La}_{1-x}\text{Sr}_x\text{MnO}_3$  will be summarized.

### 2.3.1 Magnetic Ordering: Exchange Mechanisms

Exchange interactions are well known from the quantum mechanical description of simple molecules (Heitler-London): due to the fermionic character of electrons and the Pauli exclusion principle, is in a  $\text{H}_2$  molecule an asymmetric spin part of the total wavefunction energetically favorable. Therefore, the spins will be aligned antiparallel in the ground state. Very similar exchange interactions can be found in TMO for the interplay of the magnetic moments of the transition metal ions. However, the big difference in TMO is the fact, that the orbitals of different transition metal ions do not overlap directly. The exchange interactions take place via the  $p$  orbitals of the oxygen atoms between the transition metal atoms. There is a huge variety of different exchange interactions present in TMO. The competition between these determines, whether and what magnetic order is established in the respective compound. The general rule for all these interactions is, that a spin configuration for neighboring transition metal ions is favored, that allows hopping (virtual) processes of electrons between the different atoms via the oxygen connection. The reason for this is, that such hopping processes minimize kinetic and thus total energy. A lot of these exchange mechanisms, can be described by a Heisenberg-Spin-Hamiltonian  $\mathcal{H}_{spin}$  [54]:

$$\mathcal{H}_{spin} = \sum_{i,j} J_{i,j} \mathbf{S}_i \cdot \mathbf{S}_j \quad (2.5)$$

where  $\mathbf{S}_i$  and  $\mathbf{S}_j$  are considered as classical spin vectors. The strength of the interaction between two spins in the system is described by the pair interaction  $J_{i,j}$ . A ferromagnetic alignment is favored for  $J_{i,j} < 0$ , an antiferromagnetic one for  $J_{i,j} > 0$ . In a lot of cases the nearest neighbor interaction is the dominant contribution, which further simplifies the expression.

For  $\text{La}_{1-x}\text{Sr}_x\text{MnO}_3$  the two most important are the Superexchange (SE) and the Double Exchange (DE). Both phenomena can be understood by looking at the electronic configuration of two neighboring Mn atoms linked by an oxygen atom (figure 2.3): in  $\text{La}_{1-x}\text{Sr}_x\text{MnO}_3$  depending on the doping level  $x$   $\text{Mn}^{3+}$  and  $\text{Mn}^{4+}$  ions are present. The SE interaction usually takes place between electrons in the  $t_{2g}$  levels of neighboring Mn atoms. In the most simple case, the  $e_g$  orbitals are unoccupied (SMO). Even though the  $t_{2g}$  are pointing in between two oxygen atoms, there is still enough overlap with the  $p$  orbital of an oxygen anion to enable hopping processes. Since the binding  $p$  orbital of the connecting oxygen atom is fully occupied, each hopping process takes place in two steps (virtual hopping processes in a perturbation calculation approach): first an electron from the  $p$  orbital transfers to one of the Mn ions. No matter whether this Mn valency is 3+ or 4+, the  $t_{2g}$  orbitals of this Mn ion is occupied by three electrons with parallel oriented spins. Therefore, only the electron with anti-parallel oriented spin from the  $p$  orbital can hop to the Mn site. The second step is the refill of the free electron orbital of the oxygen atom by an electron from the second Mn ion participating in this process. But this second step is only possible, if the spins in the second Mn ion are aligned anti-parallel to the first Mn atom. Hence, complete hopping processes can only be done, if the spins of neighboring Mn atoms are aligned anti-parallel, which is, why the SE interaction favors an antiferromagnetic order of Mn. The situation gets more complicated for filled or partially filled  $e_g$  orbitals. Since the  $e_g$  orbitals are pointing towards the oxygen atoms, the SE interactions involving the  $e_g$  orbitals are much stronger than the SE between  $t_{2g}$  orbitals and hence determine the magnetic properties of the TMO. Whether a ferromagnetic or antiferromagnetic alignment is favored by the SE via the  $e_g$  orbitals, can be deduced from the semi-empirical Goodenough-Kanamori rules, which have been

proven to predict very reliably the correct resulting magnetic interactions [55–57] depending on the  $e_g$  orbital occupancy and the bonding angle Mn-O-Mn:

1. The  $180^\circ$  exchange between empty or filled  $e_g$  orbitals is strong and antiferromagnetic<sup>2</sup>
2. The  $180^\circ$  exchange between one empty and one filled orbital is weak and ferromagnetic
3. The  $180^\circ$  exchange between filled orbitals is weak and ferromagnetic

Applied to LMO this leads to the following situation (figure 2.4): due to the cooperative Jahn-Teller effect, the electron in the oxygen octahedra are distorted alternatively in the x,y-plane with the  $e_g$  electrons occupying the  $d_{3z^2-r^2}$  orbital pointing along the distortion. Therefore, in the x,y-plane all exchange paths via the connecting oxygen combine a filled  $d_{3z^2-r^2}$  and an empty  $d_{x^2-y^2}$  orbital (not shown in figure 2.4). Note that the overlap between neighboring  $d_{3z^2-r^2}$  orbitals oriented perpendicular to each other is so small that it does not play a significant role here. Hence, a ferromagnetic order is established in the x,y-plane. All exchange paths in z direction combine two empty  $d_{x^2-y^2}$  orbitals resulting in antiferromagnetic order. In total, LMO exhibits ferromagnetically ordered planes, which are stacked antiferromagnetically (a-type antiferromagnet).

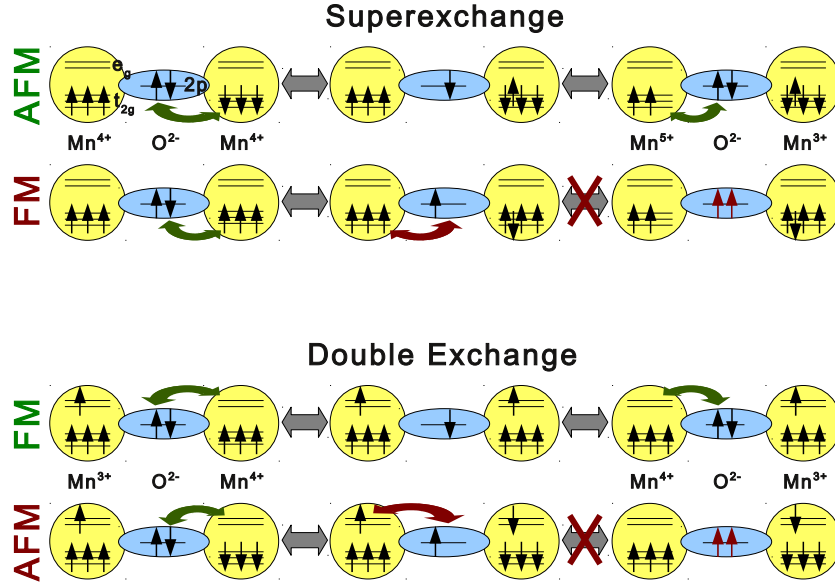


**Figure 2.3:** Figurative explanation of exchange interactions in LSMO. A superexchange interaction between the  $t_{2g}$  orbitals and the double exchange between Mn ions of different valencies is shown. The illustrated  $t_{2g}$  SE between Mn ions of the same valence state results in a preferred antiferromagnetic orientation (strictly speaking, this only holds for a  $180^\circ$  Mn-O-Mn bonding angle). The DE between Mn ions of different valence state results in a preferred ferromagnetic ordering of the magnetic moments. In addition, further SE interactions can occur also between Mn ions of the same valency via the  $e_g$  orbitals. Depending on the occupation of the  $d$  orbitals, the semi-empirical Goodenough-Kanamori rules can be applied to predict the magnetic SE mechanisms in LSMO [55–57].

For LSMO the same rules apply for the SE interactions, but in addition DE is possible. The DE is an exchange interaction, which takes place between the  $e_g$  orbitals of neighboring transition metal ions with different valencies, i.e. in case of  $\text{La}_{1-x}\text{Sr}_x\text{MnO}_3$  between one  $\text{Mn}^{3+}$  and one  $\text{Mn}^{4+}$  atom connected by an oxygen atom [58]. The hopping process can again be visualized

<sup>2</sup>the exchange between empty  $e_g$  orbitals corresponds to the case of SMO discussed before

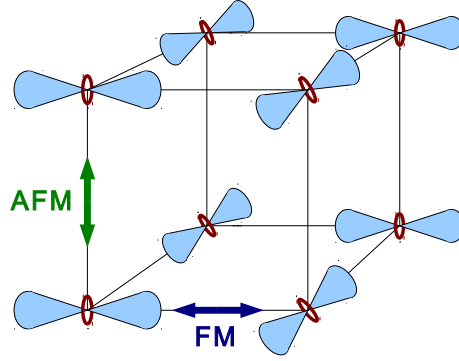


**Figure 2.4:** Orbital order in LMO due to Jahn-Teller distortions. By applying the Goodenough-Kanamori rules one obtains ferromagnetic order in the x-y-plane and antiferromagnetic order along z, resulting in total in an a-type antiferromagnetic order. The empty  $d_{x^2-y^2}$  orbitals are not depicted.

in two steps (figure 2.3). First an electron transfers from the oxygen to the empty  $e_g$  orbital of the  $\text{Mn}^{4+}$  atom. In contrary to the SE interaction between the  $t_{2g}$  this now needs to be the electron with the spin aligned parallel to the three  $t_{2g}$  electrons according to Hund's rule. Thus, the free level in the oxygen orbital can only be refilled by an electron from the  $\text{Mn}^{3+}$  atom, if the spins of both Mn ions are aligned parallel. Therefore, the DE interaction favors a ferromagnetic order of Mn atoms. In addition, the DE unlike the SE describes not only a virtual hopping process and thus also leads to electric conductivity. Thus, this mechanism can also explain qualitatively the extensively studied Colossal Magneto Resistance (CMR) effect in ferromagnetic  $\text{La}_{0.66}\text{Sr}_{0.33}\text{MnO}_3$ : close to the Curie temperature the conductivity is suppressed, since the Mn moments are not perfectly aligned. However, they can easily be forced to order ferromagnetically by a magnetic field. Thereby the DE hopping processes will be enabled resulting in a drastic drop of the resistivity.

### 2.3.2 Phase diagrams of $\text{La}_{1-x}\text{Sr}_x\text{MnO}_3$

The most important effects, which determine the properties of LSMO have been discussed. It will be pointed out now, how they influence the physical properties of LSMO. Due to the additional parameter of the doping level  $x$ , there already is a very rich temperature versus Sr concentration  $x$  phase diagram (figure 2.5(a)) [52]. As presented before, the DE interaction is only possible between Mn ions of different valencies. As discussed in the previous section, LMO exhibits an a-type antiferromagnetic (AFM) order due to the SE interaction and the cooperative Jahn Teller effect. It also is insulating, because the  $e_g$  close to the Fermi energy are unfilled. For concentration  $0 < x < 0.2$  a huge amount of papers exist with partly contradicting results. One reason for this is that LSMO, especially in the low concentration region, is even more sensitive to other stoichiometry deviations than to the doping level  $x$ . E.g. a slightly different oxidation level similarly to changing the La/Sr ratio, also changes the doping level, hence leading to completely different properties [59]. Therefore, nominally identical LSMO samples might show different behavior, when those small deviations in stoichiometry are not detected. Only the main aspects of the complex phase diagram will be discussed here to understand the results presented in this work. At low Sr concentrations ( $x < 0.1$ ) the AFM phase remains stable. However, a ferromagnetic component evolves, which can be explained either by phase separation [13] or a canted AFM structure [60]. Between  $x=0.1$  and  $x=0.17$  a ferromagnetic insulating phase is established. In addition, for the whole range  $0 < x < 0.17$  the long range cooperative Jahn-Teller effect and the resulting orbital order remains stable. At Sr concentrations  $x > 0.17$  there is a sufficient number

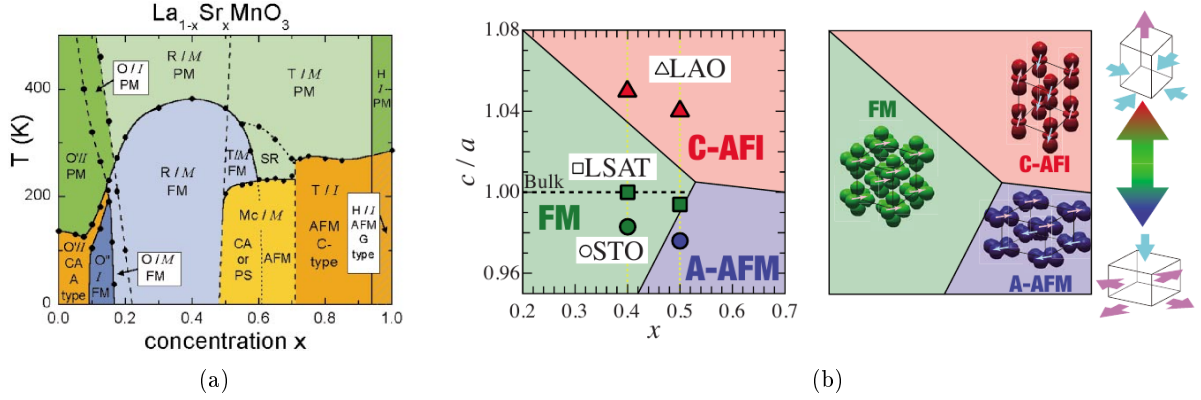


**Figure 2.5:** Magnetic phase diagrams of  $\text{La}_{1-x}\text{Sr}_x\text{MnO}_3$ . a) Temperature versus doping level phase diagram taken from [52]. b) Strain versus doping level phase diagram taken from [62] (Original data by [63]). The magnetic structures of the different phases are shown in the right diagram. The notation follows the definitions by [64].

of  $\text{Mn}^{4+}$  ions to enable the DE interaction to become more dominating than the SE. Hence a large ferromagnetic (FM) regime is found ranging up to Sr concentrations  $x=0.5$ . The Curie temperature peaks around the  $x=0.33$  composition at around 360 K. Due to the partly occupied  $e_g$  orbitals, the phase transition around  $x=0.17$  is accompanied by a metal-insulator transition and LSMO becomes metallic in the ferromagnetic region [51]. Above  $x=0.5$  the SE interaction again gets stronger and causes LSMO to order antiferromagnetically. Up to concentrations of  $x=0.7$  LSMO still is metallic. Between  $x=0.7$  and 1.0 an insulating c-type AFM is formed. The exact temperature dependent structure of the phase diagram in the region between  $x=0.5$  and  $x=0.7$  is still under discussion for single crystals of LSMO. However, in epitaxial  $\text{La}_{0.5}\text{Sr}_{0.5}\text{MnO}_3$  thin films deposited on STO substrates an a-type AFM order has been found [61].

In epitaxial thin films, the strain gives additional possibilities to tune the properties of LSMO. In figure 2.5(b) the strain versus Sr concentration is shown schematically [63]. It can be seen, that the AFM region, which starts for bulk LSMO at  $x=0.5$ , extends to lower Sr concentrations with increasing strain: LSMO films exhibit a c-type AFM order for compressive and an a-type AFM order for tensile strain. In addition to changing the magnetic order, Konishi et al [63] also found that, depending on the strain, orbital order or disorder can be induced. Finally, there are extended studies on the influence of cation ordering on the properties of LSMO, which can be realized in thin films by growing digital superlattices of  $(\text{LaMnO}_3)_n(\text{SrMnO}_3)_m$ . For example superlattices corresponding to ferromagnetic metallic LSMO ( $m=2, n=1$ ) [65], antiferromagnetic metallic LSMO ( $m=1, n=1$ ) [61] or antiferromagnetic LSMO ( $m=1, n=2$ ) [66] have been investigated, where the ordered stacking of  $\text{Mn}^{3+}$  and  $\text{Mn}^{4+}$  again can result in new phenomena, e.g. enhanced transition temperatures compared to the randomly mixed LSMO.





# 3 Motivation for the Analysed Oxidic Heterostructures

As seen in the previous chapter, TMO offer a huge variety of fascinating phenomena due to the complex interplay of lattice, spin, charge and orbital degrees of freedom. An even larger playground is accessible by arranging several of these materials in thin film systems, where the different properties can interact via the common interfaces. In addition, in epitaxially grown heterostructures, the strain mediated by the substrate can change the picture completely, as already mentioned before. In this chapter the oxide heterostructures under investigation in this work will be introduced and it will be outlined, why the two chosen systems are of big scientific interest.

## 3.1 $\text{La}_{0.66}\text{Sr}_{0.33}\text{MnO}_3/\text{SrTiO}_3$ : Exchange Bias Effect

The Exchange Bias Effect (EB) has already been discovered more than fifty years ago by Meiklejohn and Bean [14]. In their original paper, they reported that “a new type of magnetic anisotropy has been discovered which is best described as an exchange anisotropy”. The EB “manifests itself in the form of a displaced hysteresis curve”. Meiklejohn and Bean found the effect in a system consisting of ferromagnetic Co nanoparticles embedded in antiferromagnetic CoO. Its origin is the exchange coupling between the antiferromagnetic and the ferromagnetic material at the common interface, which - as we will see later - results in an unidirectional anisotropy and thus in shifting of the hysteresis curve along the magnetic field axis. Over the years the EB has been reproduced not only in an immense number of different, mostly thin film, systems, but also in a numerous different ways. This diversity also gave rise to several theoretical approaches to try to cover all the different aspects of the EB effect. Since it is impossible here to present even a fraction of these, only a phenomenological model will be presented here, which helps to understand the origin and basic concept of the EB. For a more detailed summary of the most important material systems and theoretical models of EB, chapter 3 of [67] can be recommended.

In figure 3.1 it is shown how an EB can be established in a system, where a ferromagnet is in direct contact with an antiferromagnet. First it is necessary to cool the system in a magnetic field below the Curie temperature  $T_C$  of the ferromagnetic material to align the spins along an easy axis. After that the system is cooled further down below the Neel temperature  $T_N$ , where it orders in a way, that the exchange energy to the ferromagnet at the interface is minimized. Here we assume a layered antiferromagnetic structure, hence the first atomic layer of the antiferromagnet will order either completely parallel or completely anti-parallel to the ferromagnet depending on the exchange energy. Due to this coupling to the antiferromagnet, the magnetization of the ferromagnet becomes harder to turn to the opposite direction, when the magnetic field is switched. Therefore the coercive field  $H_C$  will be higher compared to an isolated ferromagnetic layer of the same material. Similarly, when the hysteresis curve is completed back to the cooling field, the magnetization will return at a lower field to the energetically favored direction resulting in a hysteresis curve shifted by the EB field  $E_B$ . Caused by the coupling to the antiferromagnet, the uniaxial anisotropy of the ferromagnetic material alone is changed

to an unidirectional anisotropy in the bilayer system. It should be mentioned that there are nowadays elaborated theoretical models, which can not only describe this idealized case of an layered antiferromagnetic/ferromagnet interface, but also other antiferromagnetic and ferrimagnetic structures, interface roughnesses, domains, and so on. Also we assumed in this simple phenomenological model that the antiferromagnet remains unchanged, when the magnetic field is changed. That this is not the case in real systems becomes visible in the “training effect”, i.e. a subsequent reduction of the hysteresis curve shift, when the field is cycled several times until finally a symmetric hysteresis curve is obtained. This shows that the biased state of the antiferromagnet is not stable. What mechanisms are causing this instability is still not well established.

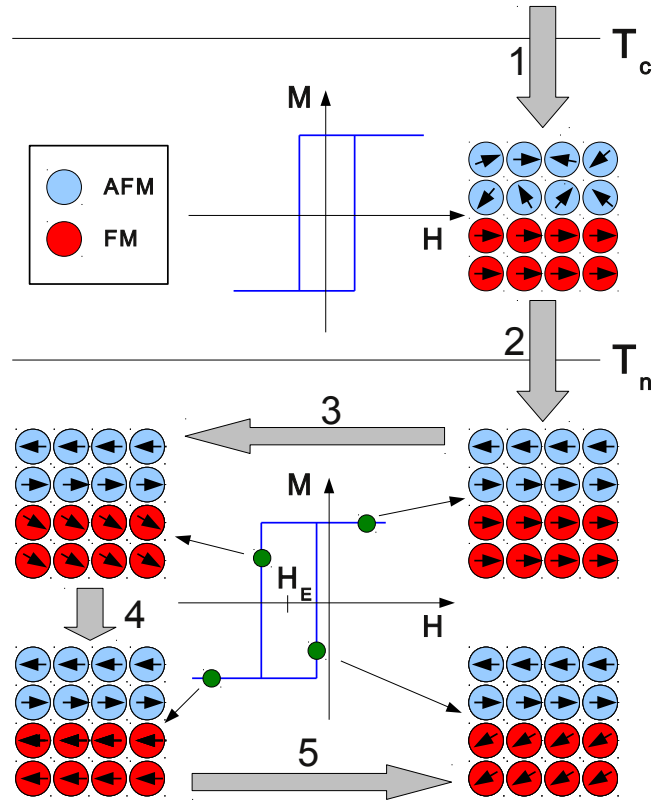


**Figure 3.1:** Schematic explanation of the Exchange Bias effect: When cooled in field, the ferromagnet orders at the Curie temperature  $T_C$  (1). Further cooling results in ordering of the antiferromagnetic material at  $T_N$  (2). In this simple example of a layered antiferromagnetic material, the direction of spins at the interface is determined by the exchange energy between the ferromagnet and antiferromagnet. Due to this pinning by the uncompensated spins of the antiferromagnet, the magnetization of the ferromagnet resists to being turned to the opposite direction by switching the magnetic field (3). Hence the coercive field becomes bigger compared to the case, when the ferromagnet is not coupled to the antiferromagnet (4). On the other hand, when the field is switched back to the original cooling field direction, the magnetization of the ferromagnet already reverses at a lower field in order to return to the energetically favored orientation (5). As a result the hysteresis curve is shifted along the magnetic field axis.

A better understanding of the complexity of the EB effect is of great interest not only from the scientific point of view. A comprehensive understanding of the EB also might open up

completely new possibilities for modern spintronic applications. The EB effect already is applied especially in spin valves of storage media, readout sensors or Magnetic Random Access Memories (MRAM). New device application might arise from using the EB in oxide heterostructures. One recent example is the switching between two distinct exchange bias states in bilayers of ferromagnetic  $\text{La}_{0.66}\text{Sr}_{0.33}\text{MnO}_3$  and ferroelectric/antiferromagnetic  $\text{BiFeO}_3$  by switching the electric polarization in  $\text{BiFeO}_3$  [19].

Some years ago, the EB effect was found in LSMO/STO multilayers by Zhu et al [1,17,18]. Since there is no nominal antiferromagnet present in the system it was proposed that an disordered spin state at the interface creates the EB probably most likely caused by the strain mediated by the STO. A vertical shift of the hysteresis loops along the magnetization axis was a hint for this assumption. It is important to notice that in case the EB effect is purely due to the LSMO layer and the STO substrate is only needed to mediate the strain, one would not be limited to having to chose an antiferromagnet on the one side and a ferromagnet on the other side of the chemical interface to create an EB effect. This opens up the opportunity of choosing the second material independently as long as it sets the right strain to the magnetic layer. Like in our case, it would not need to be magnetic at all, but could have other properties, which possibly create completely new and more versatile effects. Therefore,  $\text{La}_{0.66}\text{Sr}_{0.33}\text{MnO}_3/\text{SrTiO}_3$  thin film systems have been analysed with two major objectives: first to investigate whether the occurrence and strength of the effect can be tuned by the growth conditions; the second main aspect was the determination of the magnetic depth profile of the samples by means of polarized neutron reflectometry and resonant x-ray magnetic reflectometry in order to understand, where the antiferromagnetic layer is created, which is necessary to cause the observed EB.

### 3.2 $\text{La}_{0.5}\text{Sr}_{0.5}\text{MnO}_3/\text{BaTiO}_3$ : Artificial Multiferroicity

Multiferroics are materials that exhibit more than one “ferroic” properties, which are in most cases ferroelectricity and some kind of magnetic order (ferromagnetism or antiferromagnetism) in the same phase. The search for materials, where the different ordering parameters control each other in a sufficiently strong way, has stimulated strong research activities during the last years due to their technological relevance [6,68]. E.g. controlling the ferromagnetism by an electric field via the ferroelectric properties could be a breakthrough in reducing the power consumption of magnetic data storage devices. Used in Random Access Memories (RAM), multiferroics could combine the advantages of both ferroelectric and ferromagnetic RAM in a device, where the information is electrically written and read via the Tunnel Magnetoresistance (TMR) effect. However as presented in 2.2, ferroelectricity and ferromagnetism are in general mutually exclusive: they require empty and partially filled  $d$  orbitals, respectively. Therefore, single-phase multiferroicity can only be found under exceptional circumstances [28–30]. In addition, the polarization and hence the coupling between the order parameters in these materials is very weak, which hampers their way to technological applications.

Oxide heterostructures offer several promising routes to circumvent the problems of establishing multiferroicity in bulk materials. First of all as already addressed in chapter 2, strain can change the situation completely. As an example  $\text{EuTiO}_3$ , a paraelectric antiferromagnetic bulk material, becomes ferroelectric and ferromagnetic under biaxial strain [69]. Another possible way is the separation of the two ordering parameters: by combination of a strong ferroelectric and a strong ferromagnet, a much stronger coupling via the common interface can be expected [70–72] compared to single-phase bulk multiferroics. One example for a successful realization of such a system is the electrical control of the exchange bias state in the above mentioned  $\text{La}_{0.66}\text{Sr}_{0.33}\text{MnO}_3/\text{BiFeO}_3$  bilayers [19]. Recently, different possibilities to achieve such coupling

have been proposed theoretically [2,73]. In [2] it was predicted that the magnetic order in LSMO near 50% doping can be changed by switching the polarization in BTO. The electron density varies depending whether the polarization in BTO points towards or away from the interface. The different electron densities influence the equilibrium between super- and double-exchange favoring a ferromagnetic or an antiferromagnetic order at the interface for the two different orientations of the polarization.

The aim of this work is to prepare high quality LSMO/BTO thin film samples and to look for the theoretical predicted interface effect. To force the electric polarization of BTO to point out-of-plane, a compressive strain needs to be set by the substrate. For this purpose, Nb doped STO substrates are chosen, which not only have the suitable lattice parameters, but also can be used as a bottom electrode. In addition, the BTO should be strained as much as possible at the LSMO interface, to maximize a possible effect. Due to relaxation this limits the BTO thickness to about 15 unit cells [74]. Since the interface has been analyzed by polarized neutron reflectometry and resonant x-ray magnetic reflectometry, a coherent polarization needs to be switchable over a large area. Both, the small thickness and the large area, are in conflict to the well known leakage problem in BTO thin films [75], which cause shortage effects as soon as the film gets too thin or the area too large and thus result in a not ferroelectric behavior of the BTO especially at higher temperatures. In order to avoid the leakage currents, an additional insulating STO layer is deposited first to act as a spacer layer and to increase the distance between bottom and top electrode.

## 4 Scattering theory

Scattering methods provide a unique non-destructive insight to the chemical, magnetic and electronic structure of matter on an atomic length scale. The most detailed information about the oxide heterostructures under investigation in this work are obtained by several different scattering techniques. In this section the basic theoretical concepts of the applied methods are introduced. The concepts in the following chapter are taken from [76], where also more details about this subject can be found.

### 4.1 Basic principles and Born approximation

The general geometry of a scattering event is depicted in figure 4.1. A beam of the particles used for the experiment is pointing on the sample under investigation. The distance between source and sample usually is large enough to describe the incoming particles as a plane wave with wave vector  $\vec{k}_i$  ("Fraunhofer approximation"). In a scattering event, an incoming particle gets scattered by interaction with the sample into a different direction described by the angles  $2\theta$  and  $\phi$  with respect to the incoming direction. It gets detected at a distance from the sample, where it again is justified to approximate the particle by a plane wave with wave vector  $\vec{k}_f$ . Due to momentum conservation, the momentum

$$\hbar\vec{Q} = \hbar(\vec{k}_f - \vec{k}_i) \quad (4.1)$$

has been transferred to the sample. In the following  $\vec{Q}$  will be denoted as "scattering vector". In this work only elastic scattering is performed, i.e. no energy is transferred to or from the sample and  $|\vec{k}_i| = |\vec{k}_f|$ . In a scattering experiment the  $n'$  particles of the incoming flux  $j$  are detected, which are scattered in the solid angle  $d\Omega$ , that is covered by the detector. The angular dependent scattering probability is defined as differential cross section  $d\sigma/d\Omega$ :

$$\frac{d\sigma}{d\Omega} = \frac{n'}{jd\Omega} \quad (4.2)$$

The challenge of a scattering experiment is to extract the desired information on the properties of the sample from the differential cross section.

In order to derive an expression for  $d\sigma/d\Omega$  for the case of an incoming neutron beam, the Schrödinger equation

$$(\Delta + k^2)\Psi = \frac{2m_n}{\hbar^2}V(\vec{r})\Psi \quad (4.3)$$

needs to be solved for the neutron probability density amplitude  $\Psi^1$ . For an incident plane wave  $\Psi^0 = e^{i\vec{k}\vec{r}}$  the differential equation (4.3) can be converted to the following integral equation:

$$\Psi(\vec{r}) = \Psi^0(\vec{r}) + \frac{2m_n}{\hbar^2} \int G(\vec{r}, \vec{r}')V(\vec{r}')\Psi(\vec{r}')d^3r' \quad (4.4)$$

---

<sup>1</sup>for x-rays instead the Maxwell equations are the starting point, if a macroscopic approximation can be used (e.g. reflectometry). Since this leads to a similar wave equation for the electromagnetic field amplitude, the theory is very similar from that point. Hence, the following results are formally true for x-rays as well even though the underlying principles are different.

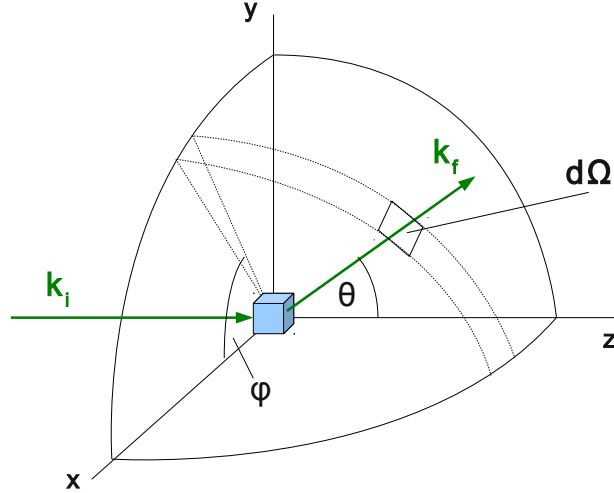


**Figure 4.1:** Scattering geometry for a general scattering event of a particle with incoming wavevector  $k_i$  and outgoing wavevector  $k_f$

where  $G(\vec{r}, \vec{r}')$  is the Green function satisfying the condition

$$(\Delta + k^2)G(\vec{r}, \vec{r}') = \delta(\vec{r} - \vec{r}') \quad (4.5)$$

The implicit integral equation (4.4) ("Lippmann-Schwinger" equation) can be solved iteratively by substituting this solution for  $\Psi(\vec{r})$  in the right hand side for  $\Psi(\vec{r}')$ . This subsequently results in terms of higher order of the interaction potential  $V$  ("Born-series"). For weak interaction potentials the first order already is a very good approximation. With  $G(\vec{r}, \vec{r}') = \frac{e^{i\vec{k}|\vec{r}-\vec{r}'|}}{4\pi|\vec{r}-\vec{r}'|}$  as a solution of (4.5) one obtains:

$$\Psi^1(\vec{r}) = e^{i\vec{k}\vec{r}} + \frac{2m_n}{\hbar^2} \int \frac{e^{i\vec{k}|\vec{r}-\vec{r}'|}}{4\pi|\vec{r}-\vec{r}'|} V(\vec{r}') e^{i\vec{k}\vec{r}'} d^3r' \quad (4.6)$$

This describes a superposition of the incident plane wave (first term) with the scattered wave (second term). Only one scattering event is described by 4.6. As expected for stronger interaction potentials  $V$  multiple scattering events and hence higher order terms of the Born series need to be taken into account. Subsequently, the second order term accounts for particles being scattered twice, the third term for particle being scattered three times and so on.

For large distance  $\vec{R}$  from the sample, e.g. at the position of the detector, (4.6) becomes:

$$\Psi^1(\vec{r}) = e^{i\vec{k}\vec{R}} + \frac{2m_n}{\hbar^2} \frac{e^{i\vec{k}\vec{R}}}{4\pi R} \int V(\vec{r}') e^{i\vec{Q}\vec{r}'} d^3r' \quad (4.7)$$

which is a sum of the incident plane wave plus a spherical wave emitted from the sample. Since  $\frac{d\sigma}{d\Omega}$  was defined as the angular dependent scattering probability, the differential cross section is equal to the absolute square of the amplitude  $A(\vec{Q})$  of the scattered wave:

$$\left( \frac{d\sigma}{d\Omega} \right)_{neutrons} = |A(\vec{Q})|^2 = \left| \frac{m_n}{2\pi\hbar^2} \int V(\vec{r}') e^{i\vec{Q}\vec{r}'} d^3r' \right|^2 \quad (4.8)$$

Therefore, in first Born approximation the measured intensity  $I$  is proportional to the absolute square of the Fourier transform of the interaction potential. As mentioned before, a similar

expression can be derived for x-ray scattering. Since photons are predominantly interacting with the electrons of the sample, for x-ray scattering the amplitude of the scattered wave is proportional to the Fourier transform of the electron density  $\rho_e$ :

$$\left(\frac{d\sigma}{d\Omega}\right)_{xray} = |A(\vec{Q})|^2 \propto \left| \int \rho_e e^{i\vec{Q}\vec{r}} d^3r \right|^2 \quad (4.9)$$

These formula reveal the so called "phase problem" for scattering experiments: One can not simply derive the scattering density from the angular dependent measurement of the intensity, because the information of the phase of the scattering amplitude gets lost by taking the absolute square. Therefore, the usual way to analyze scattering data is to set up a model of the sample, calculate the expected intensity and refine it until it matches the experimental data.

## 4.2 X-ray diffraction (XRD)

In this work XRD is used to determine the lattice parameters of the epitaxially grown thin films. To model the scattered intensity for a single monocrystalline layer, one needs to know the electron density  $\rho_e$  for the thin film. For the samples in this work, the out-of-plane direction of the thin films is parallel to one of the crystallographic axis. Hence, the layer consists of  $N$ ,  $M$  and  $P$  unit cells along the  $x$ ,  $y$  and  $z$  direction, respectively, where  $z$  should be the out-of-plane direction in the following. The lattice constants of the thin film are  $\vec{a}$ ,  $\vec{b}$  and  $\vec{c}$  in the respective directions. In analogy to single crystal diffraction, the overall structure of the thin film can be described mathematically as a convolution of a lattice having  $N \cdot M \cdot P$  lattice points and of the unit cell structure. Thus, the Fourier transform of  $\rho_e$  can be simplified to the product of the Fourier transform of the lattice function  $\rho_L$  times the Fourier transform of the unit cell function  $\rho_S$  (convolution theorem).  $\rho_L$  is proportional to:

$$\rho_L \propto \sum_{n=0}^{N-1} \sum_{m=0}^{M-1} \sum_{p=0}^{P-1} \delta(\vec{r} - (n\vec{a} + m\vec{b} + l\vec{c})) \quad (4.10)$$

Hence, the Fourier transform of  $\rho_L$  becomes a geometrical series

$$A_L(\vec{Q}) \propto \sum_{n=0}^{N-1} e^{in\vec{Q}\vec{a}} \sum_{m=0}^{M-1} e^{im\vec{Q}\vec{b}} \sum_{p=0}^{P-1} e^{ip\vec{Q}\vec{c}} \quad (4.11)$$

which would result in the so called "Laue-function" for the scattered intensity, if the unit cell only consists of one pointlike scatterer:

$$I(\vec{Q}) \propto \frac{\sin^2 \frac{1}{2} N \vec{Q} \vec{a}}{\sin^2 \frac{1}{2} \vec{Q} \vec{a}} \cdot \frac{\sin^2 \frac{1}{2} M \vec{Q} \vec{b}}{\sin^2 \frac{1}{2} \vec{Q} \vec{b}} \cdot \frac{\sin^2 \frac{1}{2} P \vec{Q} \vec{c}}{\sin^2 \frac{1}{2} \vec{Q} \vec{c}} \quad (4.12)$$

The function is plotted in figure 4.2 for the case that  $\vec{Q}$  is parallel to  $\vec{a}$ . There are main maxima for  $Q = p \cdot 2\pi/|\vec{c}|$  (analogous for the other directions). These main maxima are the well known Bragg reflections. The intensity of the Bragg reflections scale with  $N^2$ , the width with  $2\pi/P$ . I.e. for our model layer with growth direction along  $\vec{c}$  one can in principle deduce the layer thickness  $d = P \cdot |\vec{c}|$  from the width of the reflection. More precisely, the width indicates the coherently scattering planes in the particular direction. Due to e.g. lattice imperfections, mosaicity or strain, this does not necessarily equal to the size of the layer (or crystal) in this direction. In addition especially for sharp Bragg reflections, the instrumental resolution also might influence the width of the Bragg reflections.



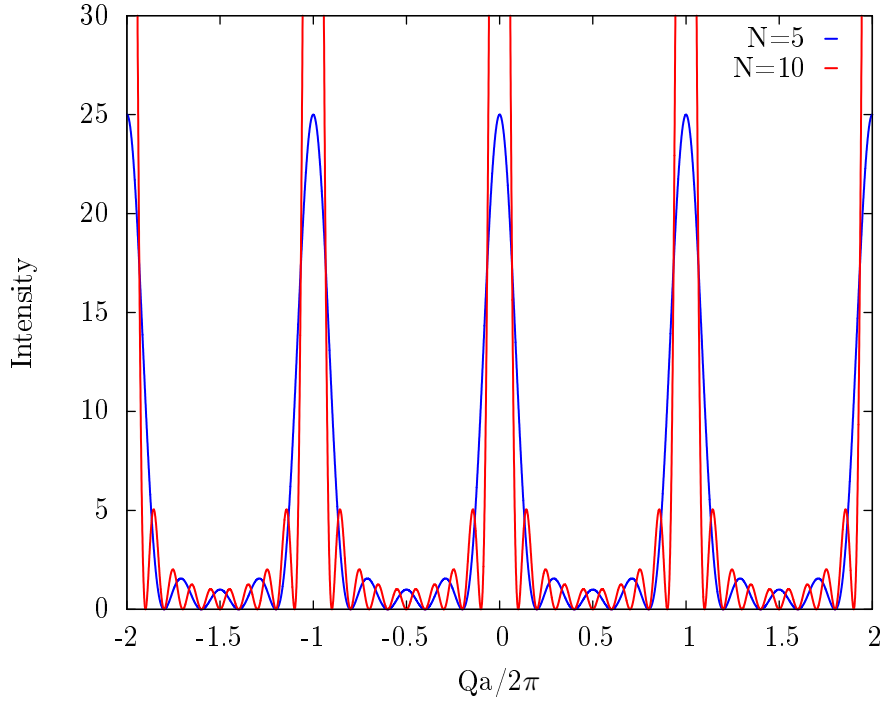


**Figure 4.2:** Plot of the Laue function for  $N=5$  and  $N=10$

The intensity of the Bragg-reflections is modulated by the second factor, namely the Fourier-transform of  $\rho_S$ . For a unit cell of volume  $V_S = (\vec{a} \times \vec{b}) \cdot \vec{c}$  with  $L$  atoms at positions  $\vec{r}_j$  one obtains with  $\vec{r} = \vec{r}_j + \vec{r}'$  for the so called structure factor  $A_S$  of the unit cell:

$$A_S \propto \int_{V_S} d^3r \rho_S(\vec{r}) e^{i\vec{Q}\vec{r}} = \sum_{j=1}^L \int_{V_j} d^3r \rho_S(\vec{r}) e^{i\vec{Q}\vec{r}} = \sum_{j=1}^L e^{i\vec{Q}\vec{r}_j} \underbrace{\int_{V_j} d^3r' \rho_S(\vec{r}') e^{i\vec{Q}\vec{r}'}}_{F_j^0(\vec{Q})} \quad (4.13)$$

Here  $V_j$  is the “volume” of atom  $j$ . The integral in the last step now is independent from the unit cell structure and corresponds to the scattering potential of the atom  $j$ . It is called atomic form factor  $F_j^0(\vec{Q})$ . Thus, the total scattered intensity from a single layer consists of Bragg reflections at  $\vec{Q}$  positions determined by the unit cell parameters. The intensity is modulated by the structure factor of the unit cell. Due to the structure factor, Bragg reflections can even be forbidden. From the intensity pattern one can deduce the unit cell structure.

The same considerations are also true for the substrate, where the thin films are deposited on. Since  $P$  tends to infinity for a standard substrate with macroscopic thickness, one would expect infinitely sharp (for a perfect instrumental resolution) and infinitely intense (limited by the incident beam intensity) Bragg reflections. The reason for this unphysical result is that absorption has been neglected so far. This is a valid approximation for scattering from thin films. For the scattering from the substrate an exponential damping factor  $e^{-2l/\tau}$  needs to be taken into account, where  $\tau$  is the penetration depth of the x-rays and  $l$  the distance traveled by the x-rays through the material of the sample. The Fourier transform of this exponential function results in a Lorentzian function proportional to  $\frac{\mu}{\mu^2 + Q^2}$ , where the width  $\mu$  is antiproportional to the penetration depth  $\tau$ .

In summary, for XRD at monocrystalline single or bilayers deposited on a monocrystalline substrate, Bragg reflections for each layer and the substrate can be expected. For a substrate of good

structural quality the Bragg reflections will have a Lorentzian-curve shape. For the thin films they follow the Laue-function. The intensity of the reflections is modulated by the corresponding structure factor.

## 4.3 Grazing incidence scattering

### 4.3.1 Continuum description

Grazing incidence scattering is a very powerful technique to determine depth resolved mesoscopic properties of thin films. The standard scattering geometry from a single surface is shown in figure 4.3. This section focuses on the special case of small angles  $\theta$  between incident beam and sample surface. Only the case of specular reflectivity, e.g. the incident angle is equal to the outgoing angle, will be discussed here.

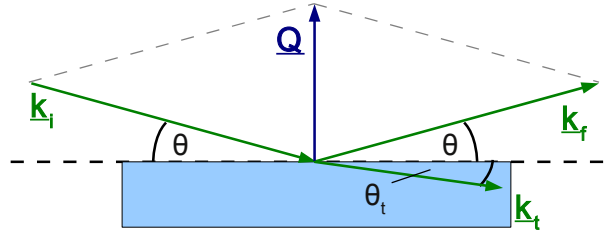


**Figure 4.3:** Definitions of symbols for the general case of a reflectometry experiment

For small angles  $\theta$  also the scattering vector  $\vec{Q}$  is small. It can be seen from formula (4.9) that the Born approximation does not hold for small  $\vec{Q}$ , as it predicts an infinite intensity. The approximation breaks down, since multiple scattering events can not be neglected any more in this kind of very surface sensitive scattering experiments [77]. Therefore a different approach to solve formula (4.3) needs to be taken. A quite graphic argumentation makes clear that grazing incidence experiments are not sensitive to structures on an atomic length scale (figure 4.4): The structure of a thin film can be described mathematically by an undisturbed microscopic periodic lattice multiplied by the mesoscopic variations of the sample. Similar to the discussion in the previous section, the Fourier transform of this product (which is proportional to the measured intensity in the reflectometry experiment) gives the convolution of both functions in  $Q$  space. For small  $\vec{Q}$  only a delta function at  $Q = 0$  needs to be considered for the reflectometry experiment. Back-transformation to real space reveals that the microscopic information has been lost.

Hence, each material in the thin film system can be described by a complex index of refraction  $n_t = k_f/k$ , where the real part describes the refraction and the imaginary part the absorption of the material. Solving the wave equation leads to the same well known result that the incoming wave is partly reflected and partly transmitted at the surface of the sample. The ratio between reflected and transmitted beam is given by the reflection and transmission coefficients  $R$  and  $T$  ("Fresnel formulas"):

$$R = \left| \frac{\theta - n\theta_t}{\theta + n\theta_t} \right|^2 \quad (4.14)$$

$$T = \left| \frac{2\theta}{\theta + n\theta_t} \right|^2 \quad (4.15)$$

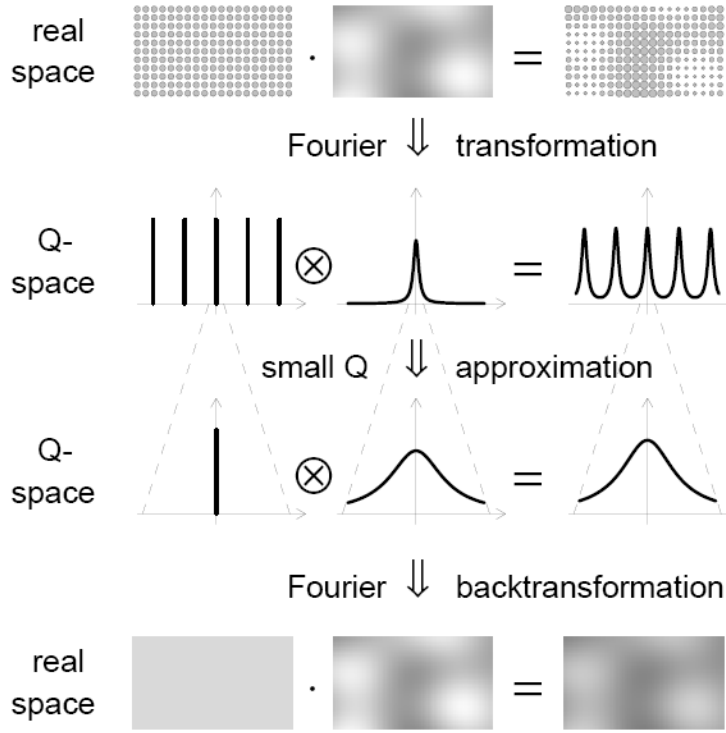


**Figure 4.4:** Graphical explanation for the non-sensitivity to microscopic length scales in a reflectometry experiment (taken from [76]).

where the angle of the transmitted beam is given by  $n = \cos\theta / \cos\theta_t$  (Snell's law). In the next two sections it will be shown that the indices of refraction for both x-ray and neutron reflectivity in general are smaller than 1, which causes the transmitted beam to be refracted towards the interface. Therefore, for incident angles smaller than a critical angle  $\theta_c$  there is no beam transmitted into the medium, i.e. the entire beam is reflected (region of total reflection). It can be shown that for larger angles than the critical angle, the reflected intensity for a perfectly smooth surface decreases proportional to  $Q_z^{-4}$  [78]. Additionally, roughness can be taken account by a Debye-Waller factor, which then results in an intensity drop  $I(Q_z) \propto Q_z^{-4} \exp(-Q_z^2 \sigma^2)$ . Here  $\sigma$  is the root mean square (rms) roughness of the surface, i.e. the average deviation of the real surface from the nominal ideal surface. It therefore has the dimension of a length and is usually given in nm or Å.

So far, only a single surface has been discussed. For the case of a single layer the incoming beam is partly reflected and transmitted also at the interface to the substrate according to the Fresnel formulas, which now depend on the indices of refraction of the layer and the substrate. The resulting total reflected intensity then is a superposition of the reflected beams of the surface and the interface. Like in optics, at certain angles the path difference between both reflected beams leads to constructive or destructive interference (figure 4.5). By simple geometric considerations one finds for  $\theta_t \approx \theta$  that for a layer of thickness  $d$  the condition that needs to be fulfilled is (Bragg condition):

$$\lambda = 2d \cdot \sin\theta \quad (4.16)$$

These interference effects result in oscillations of the reflectometry curve at angles higher than the critical angle. The higher the difference between the indices of refraction of layer and substrate material (also called contrast), the stronger are the oscillations. The description of several layers can be generalized in an analogous way. The reflectometry pattern might look more irregular,

since complicated interference effects caused by the additional reflected beams at the additional interfaces occur. Each of the layers then is represented by a complex index of refraction, a layer thickness and a layer roughness. A formalism to describe complex layered structures mathematically was introduced by Parratt [79]. The presented phenomena can be applied to both x-ray and neutron reflectometry. The differences will be addressed in the next two sections.

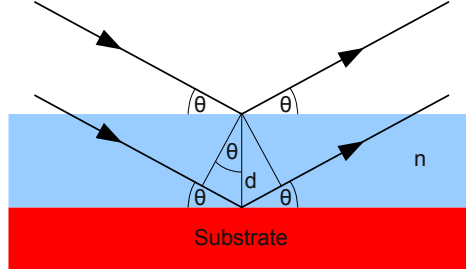


**Figure 4.5:** Reflectometry from a single layer: The path difference between the beam reflected at the surface and at the interface leads to the Bragg condition for constructive interference

### 4.3.2 X-ray reflectometry (XRR)

The main difference between x-ray and neutron reflectometry is the way of interaction for both methods: Photons are interacting with the electron density in the material. The interaction potential can be deduced from electrodynamics and gives

$$V = \frac{e^2}{2mc^2} A^2 - \frac{e}{mc} \vec{p} \vec{A} \quad (4.17)$$

where  $\vec{A}$  is the vector potential and  $\vec{p}$  the electron momentum. In addition the photons might also interact with the spin moments of the electrons, yet this interactions is much weaker than the charge scattering and needs not to be taken into account for the non-resonant case of XRR. By solving the Maxwell equations it can be shown that the complex index of refraction for XRR is given by

$$n = 1 - \frac{N_A}{2\pi} r_0 \lambda^2 \sum_j \rho_j F_j = 1 - \delta - i\beta \quad (4.18)$$

where  $r_0 = e^2/4\pi\epsilon_0 m_e c^2 = 2.818 \times 10^{-15}$  m is the classical electron radius,  $\lambda$  the wavelength,  $\rho_j$  the material density of material  $j$ .  $F_j$  is the complex atomic scattering factor, which is in general written as:

$$F(\vec{Q}, \omega) = F^0(\vec{Q}) + F'(\omega) - iF''(\omega) =: f_1(\omega) - if_2(\omega) \quad (4.19)$$

Here  $F^0(\vec{Q})$  is the atomic form factor, which has already been introduced in (4.13).  $F'(\omega)$  and  $F''(\omega)$  are the anomalous scattering factors, which take into account refraction and absorption processes, respectively. They become particularly important for resonant x-ray scattering (section 4.3.4). The tabulated values, which can be taken for XRR simulations, usually are the Henke-Gullikson factors  $f_1$  and  $f_2$  [80].  $f_2$  can be determined quite easily in an absorption measurement. Since it can be derived that  $f_1$  and  $f_2$  are not independent,  $f_1$  can be calculated, if  $f_2$  is known (Kramers-Kronig relation [81,82]). Similarly to neutrons (see next section) a real and imaginary

part of a scattering length density can be defined by setting:

$$\delta = \frac{\lambda^2}{2\pi} \cdot N b'_r \quad (4.20)$$

$$\beta = \frac{\lambda^2}{2\pi} \cdot N b''_r \quad (4.21)$$

where  $N$  is the number of scattering sites per volume and  $b'_r$  and  $b''_r$  are the real and imaginary parts of the complex scattering length.

### 4.3.3 Polarized Neutron reflectometry (PNR)

Similarly to XRR, one can derive an expression for the complex index of refraction by solving equation (4.3):

$$n = k_n/k = \sqrt{1 - \frac{\lambda^2}{\pi} \sum_i b_i \rho_i} \approx 1 - \frac{\lambda^2}{2\pi} \sum_i b_i \rho_i \quad (4.22)$$

where  $b_i$  now is the complex scattering length for atoms of type  $i$ . The approximation is valid, as for neutrons  $n$  is very close to 1. The big difference to XRR is the interaction process of neutrons with the sample: Neutrons interact with the nuclei of the atoms in the material via the strong interaction. In addition, they also interact via dipol-dipol interaction with the magnetic moments of the unpaired electrons. For neutrons both interaction processes need to be taken into account, since they are of similar order of magnitude. The total interaction potential operator for neutrons thus becomes:

$$\hat{V} = \frac{2\pi\hbar^2}{m_n} (\rho_N \hat{1} + \rho_M \hat{\sigma} \cdot \mathbf{b}) \quad (4.23)$$

where  $\hat{\sigma}$  is the vector of Pauli-matrices and  $\mathbf{b}$  the unity vector in the direction of the sample magnetization.  $\rho_N$  and  $\rho_M$  are the nuclear and magnetic scattering length densities, respectively. The dependence on the magnetic structure can be used to obtain information not only on the chemical (like in XRR), but also on the magnetic depth profile. Figure 4.6 shows the geometry of a typical PNR experiment. An in-plane magnetic field  $\vec{H}$  is applied to the sample which causes a sample induction  $\vec{B}$  with two in-plane components parallel ( $B_{\parallel}$ ) and perpendicular ( $B_{\perp}$ ) to  $\vec{H}$ .  $\vec{H}$  also sets a quantization axis for neutron beam that is reflected from the samples surface: The incoming neutron beam is polarized with the neutron spins oriented either parallel (Up) or anti-parallel (Down) to the magnetic field. For each of the two incoming beams the intensity of the reflected beam again can be detected polarization dependent resulting in four possible channels that can be measured (Up-Up, Down-Down, Up-Down, Down-Up).

Assuming that the incoming neutrons can be described by plane waves with wave vector  $\vec{k}_0$  and energy  $\hbar^2 k_0^2 / (2m)$ , the interaction potential operator in equation (4.23) leads to a set of coupled one dimensional equations for the two possible spinor components  $\Psi_+$  (Up) and  $\Psi_-$  (Down) of the neutrons:

$$\Psi''_+(z) + [k_z^2 - 4\pi(\rho_N - \rho_M b_{\parallel})] \Psi_+(z) = 4\pi\rho_M b_{\perp} \Psi_-(z) \quad (4.24)$$

$$\Psi''_-(z) + [k_z^2 - 4\pi(\rho_N + \rho_M b_{\parallel})] \Psi_-(z) = 4\pi\rho_M b_{\perp} \Psi_+(z) \quad (4.25)$$

The solutions of these equations enable calculations of the reflectivity for the four above mentioned polarization channels. From the simulation of the PNR data  $\rho_N$  can be determined depth resolved perpendicular to the samples surface.

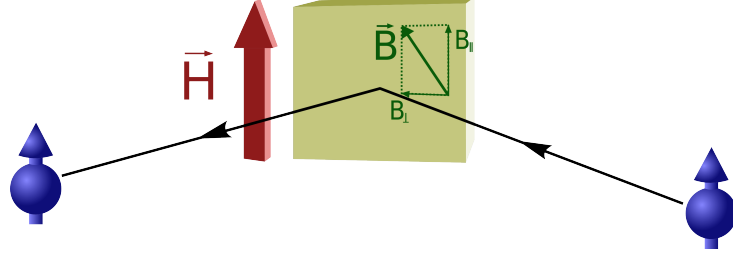


**Figure 4.6:** Scattering geometry of the PNR experiment: The Up-Up channel is shown, i.e. the spins of both the incoming and reflected neutrons are oriented parallel to the applied magnetic field  $\vec{H}$ .  $\vec{H}$  causes a magnetization  $\vec{M}$ , leading to a magnetic induction  $\vec{B} = \mu_0(\vec{H} + \vec{M})$  in the sample with two in plane components  $B_{\parallel}$  and  $B_{\perp}$ .

#### 4.3.4 X-ray Resonant Magnetic Scattering (XRMS)

It was already mentioned before that x-rays not only interact with the charge density of a material (Thomson scattering), but also with the spins of the electrons. However, for photon energies below 10 keV typical scattering cross sections for magnetic scattering are several orders of magnitude smaller compared to charge scattering. Therefore the magnetic contributions can be neglected for the laboratory reflectometers and diffractometers used in this work, as they use Cu  $K_{\alpha}$  radiation (8048 eV). The situation changes drastically, if a photon energy is used close to an absorption edge between atomic energy levels of the analyzed material. In this case resonant absorption and scattering events can become an important, maybe dominant contribution of the interaction processes. As will be shown in this section, this also enables the investigation of magnetic properties. After summarizing the basic concepts of x-ray resonant scattering in general and introducing the phenomenon of X-ray Magnetic Circular Dichroism (XMCD) (more details about these two paragraphs can be found for example in [83]), the particular X-ray Resonant Magnetic Scattering (XRMS) method used in this work will be explained.

##### X-ray resonant scattering

In a classical picture the resonant interaction of a photon (electromagnetic field  $\vec{E}_0 e^{-i\omega t}$ ) and a core electron  $n$  with binding energy  $E_n = \hbar\omega_n$  and coordinates  $\vec{x}$  can be described by the following equation of motion for a forced harmonic oscillator:

$$\frac{d^2\vec{x}}{dt^2} + \Gamma_n \frac{d\vec{x}}{dt} + \omega_n^2 \vec{x} = -\frac{e\vec{E}_0}{m_e} e^{-i\omega t} \quad (4.26)$$

Here, dissipation of energy of the applied field is taken into account by the damping constant  $\Gamma_n$ . From the solution of this equation one can deduce for the frequency dependent part of the scattering factor (4.19):

$$F_n(\omega) = \frac{\omega^2}{\omega^2 - \omega_n^2 + i\omega\Gamma_n} \quad (4.27)$$

Even though the classical approach does not describe the system correctly, this result already clarifies the enhanced scattering probability for photons with energies close to  $E_n$ . The quantum mechanical description of resonant x-ray absorption and scattering was derived by Kramers and Heisenberg [84] and Dirac [85]. In this framework the interactions are expressed by the transition probability per unit time  $T_{if}$  from an initial state  $|i\rangle$  to a final state  $|f\rangle$  (second

order perturbation theory):

$$T_{if} = \frac{2\pi}{\hbar} \left| \underbrace{\langle f | \mathcal{H}_{int} | i \rangle}_{\text{first order}} + \underbrace{\sum_n \frac{\langle f | \mathcal{H}_{int} | n \rangle \langle n | \mathcal{H}_{int} | i \rangle}{\epsilon_i - \epsilon_n}}_{\text{second order}} \right|^2 \delta(\epsilon_i - \epsilon_n) \rho(\epsilon_f) \quad (4.28)$$

$\rho(\epsilon_f)$  is the density of final states per unit energy and

$$\mathcal{H}_{int} = \frac{e^2}{2m} \vec{A}^2 - \frac{i\hbar e}{m} \vec{A} \cdot \vec{\nabla} \quad (4.29)$$

is the interaction Hamiltonian corresponding to the classical potential introduced in formula (4.17). By inserting formula (4.29) in formula (4.28) one obtains terms that are proportional to  $\vec{A}$  or to  $\vec{A}^2$ . In the quantum mechanical theoretical description, the vector potential  $\vec{A}$  is proportional to the operators that describe the annihilation and the creation of photons [86]. Therefore, the terms linear in  $\vec{A}$  correspond to processes, where a photon is created or annihilated, and the terms, which are quadratic in  $\vec{A}$ , describe processes, where a photon can be destroyed and created. This leads to the following possible interaction processes (figure 4.7): The first order term in equation (4.28) linear in  $\vec{A}$  describes absorption and stimulated emission of a photon. The first order quadratic term describes charge scattering as described before (Thomson-scattering). In this case the initial and final state  $i$  and  $f$  are identical. The second order term becomes particularly important for incident photon energies, that match the difference between electronic energy levels of the scattering material. Therefore, this term describes in general resonant absorption processes, which can be followed by several different events, e.g. the emission of a photoelectron. In particular, elastic resonant scattering processes are possible, when the initial and final states are identical. In this case the excitation of the electron and the re-emission of the photon are only virtual processes.

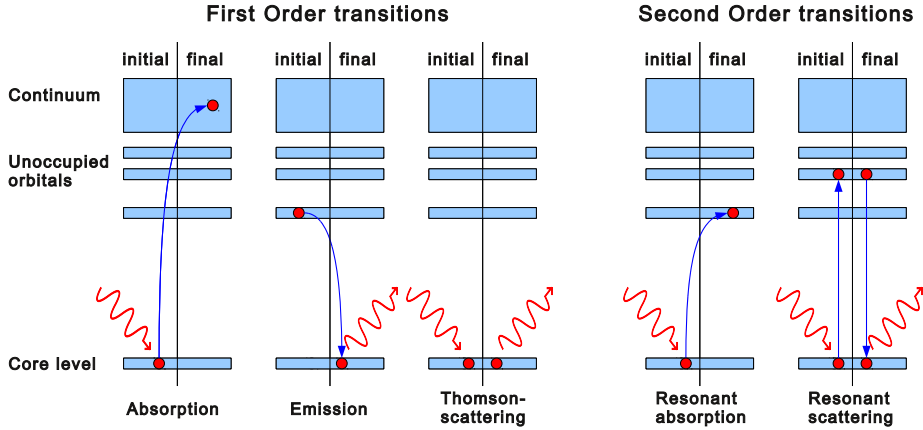


**Figure 4.7:** Figurative explanation of the first order and second order processes described by formula (4.28).

### X-ray Magnetic Circular Dichroism

It now needs to be clarified, how the basic processes introduced before depend on the x-ray polarization and the electronic (hence magnetic) configuration of the sample. Since  $\vec{E} = \frac{\partial \vec{A}}{\partial t}$ , it can be expected that the interaction Hamiltonian  $\mathcal{H}$  in general depends on the polarization

of the photon. It is also clear that the absorption depends on the electronic configuration of the final energy level in two ways: First of all there need to be free states where the absorbing electron can be excited in. Secondly, the transition has to obey the dipole selection rules for the quantum numbers of the electron (orbital angular momentum  $l$ , magnetic quantum number  $m_l$  and spin quantum number  $m_s$ ):

1.  $\Delta l = \pm 1$
2.  $\Delta m_l = q = 0, \pm 1$
3.  $\Delta m_s = 0$

$\hbar q$  is the angular momentum of the photon, which is 0 for linear polarization, +1 for right circular and -1 for left circular polarization (RCP and LCP, respectively). For transitions from the  $2p$  core levels to the  $3d$  valence band (L-edge) in 3d metals this results in the following situation 4.8: Due to spin orbit coupling there are two energetically different transitions, one from the  $2p_{3/2}$  and one from the  $2p_{1/2}$  states. They are called  $L_3$  and  $L_2$  edges, respectively, and result in two peaks in an energy dependent absorption measurement. It can be shown that the sum of the integrated intensities of both edges  $I_{L_3} + I_{L_2}$  for a x-ray beam of average polarization - e.g. the sum of a RCP and a LCP spectra - is proportional to the number of holes  $N_h$  in the valence band (first sum rule) [83]:

$$N_h = (I_{L_3} + I_{L_2})/C \quad (4.30)$$

with  $C$  being the proportionality factor. It is necessary to take an average polarization, since it turns out due to the selection rules that at one of the two edges the absorption probability for RCP x-rays is higher than for LCP x-rays and vice versa for the other edge (Fano-effect). Therefore, the difference between an absorption measurement with LCP x-rays and RCP x-rays is negative at one and positive at the other edge. Furthermore, it is possible to calculate not only the total, but also the spin  $m_s$  and orbital moments  $m_o$  separately from the integrated intensities  $A$  and  $B$  of the positive and negative difference signals by applying the second and third sum rule:

$$m_s = \frac{\mu_B(-A + 2B)}{C} \quad m_o = \frac{\mu_B(A + B)}{3C} \quad (4.31)$$

$C$  again is the same proportionality constant as in the first sum rule. The dependence of the absorption spectrum on the polarization of the incident photon beam is called X-ray Magnetic Circular Dichroism (XMCD). It should be emphasized that it not only is a powerful technique to determine the spin and orbital fraction of the total moment. Due to the resonant absorption, it also is an element specific determination of the magnetic moments, which becomes important, if different magnetic atoms are present in the analyzed material.

### X-ray Resonant Magnetic Reflectometry

It was shown in the last paragraph, how the XMCD can help to gain information on the magnetic configuration of magnetic atoms in the samples under investigation. However, the determined values are only averaged over the area exposed to the x-ray beam. In order to become sensitive to the magnetic depth profile in the thin film system, the resonant scattering is performed in reflectometry geometry. Like for PNR and XRR, the sample can be described as a continuum and only variations on a meso- or macroscopic length scale can be detected. As seen before, in this case the propagation of x-rays through the medium is simply determined by the complex index of refraction  $n$ . The interaction of the x-rays with electric field  $\vec{E}$  and energy  $E$  and the sample material can also be described by the dielectric tensor  $\epsilon(E)$  defined by

$$\vec{D} = \epsilon\epsilon_0\vec{E} \quad (4.32)$$



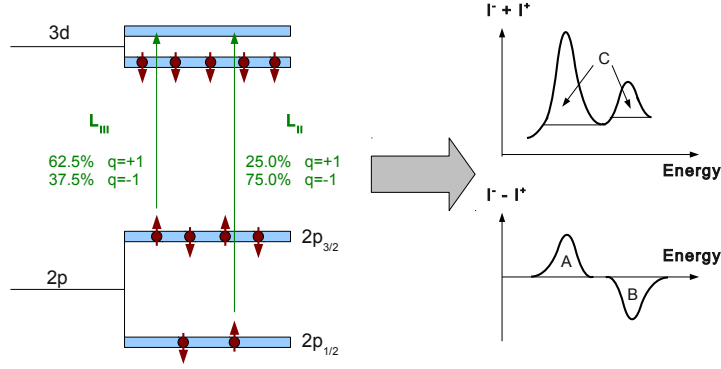


**Figure 4.8:** Illustration of the origin of XMCD. Depicted is the band structure and atomic electronic configuration for a  $3d$  metal with half filled d-orbital. The calculated absorption probabilities depending on the angular momentum  $q$  for the photon ( $+1$  corresponds to RCP,  $-1$  to LCP) for the  $L_3$  and  $L_2$  edges. On the left hand side, the resulting sum and difference signal of the two possible circular polarizations is shown. A, B and C indicated intensities needed to apply the sum rules (formula (4.30) and (4.31)).

where  $\vec{D}$  is the electric displacement field induced in the material by  $\vec{E}$ . For an isotropic non-magnetic medium,  $\epsilon$  becomes a scalar and is equal to the square of  $n$ . This is also true for magnetic materials as long as the x-ray energies are not close to an absorption edge. For resonant x-ray scattering the processes discussed in the previous sections on a quantum mechanical basis need to be taken into account. It can be shown that for a reflectivity experiment, where the continuum description is valid, all these resonant effects can be summarized in one additional energy dependent complex parameter  $Q(E)$  (magneto-optical coefficient) [87]. Like  $n$ ,  $Q(E)$  is strongly energy dependent around an absorption edge [88,89]. For a fixed energy,  $Q$  is proportional to the mesoscopic magnetization of the sample. Therefore similar to PNR, anti-ferromagnetic order can not be detected. Here, only the situation relevant for the experimental setup in this work will be discussed, i.e. the magnetization of the sample is assumed to lie in the plane of the film and in the scattering plane defined by  $\vec{k}_i$  and  $\vec{k}_f$  (figure 4.9). In this case, some of the off-diagonal elements of  $\epsilon(E)$  vanish and it becomes:

$$\epsilon(E) = n(E)^2 \begin{pmatrix} 1 & 0 & -iQ(E) \\ 0 & 1 & 0 \\ iQ(E) & 0 & 1 \end{pmatrix} \quad (4.33)$$

In analogy to the imaginary part of  $n(E)$  being proportional to the (non-resonant) absorption, the imaginary part of  $Q(E)$  is proportional to the XMCD. The corresponding real part again can be calculated by using a Kramers-Kronig relation.

The theoretical calculation of the reflected intensity of an incoming x-ray beam can be done in the framework of magneto-optics: by using  $\epsilon(E)$  the Maxwell equations with the correct boundary conditions at the surface of the sample need to be solved. By doing this the entries of the Fresnel reflection matrix

$$R(\theta, E) = \begin{pmatrix} r_{ss}(\theta, E) & r_{sp}(\theta, E) \\ r_{ps}(\theta, E) & r_{pp}(\theta, E) \end{pmatrix} \quad (4.34)$$

can be calculated dependent on the incident angle  $\theta$  and energy  $E$ .  $r_{ij}$  is the ratio of incident  $j$  polarized x-ray radiation and the reflected  $i$  polarized x-ray beam.  $s$  and  $p$  polarization correspond to the polarization being perpendicular to or lying in the scattering plane, respectively.

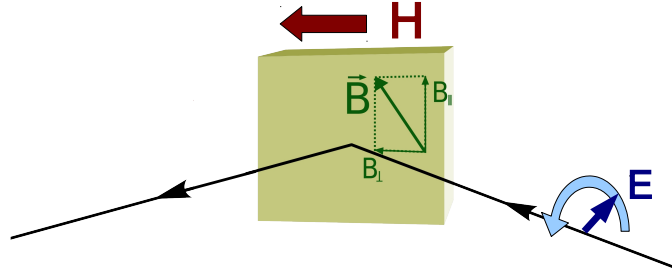


**Figure 4.9:** Scattering geometry of the XRMS experiment: the incoming circular polarized beam is reflected from the surface of the sample. In contrast to the PNR scattering geometry, the magnetic field is applied in the scattering plane. This also results in a magnetic induction in the sample in the scattering plane, i.e.  $B_{\parallel} = 0$ . In this case the dielectric tensor  $\epsilon$  is given by (4.33).

The ratios that mix  $s$  and  $p$  polarization  $r_{sp}$  and  $r_{ps}$  correspond to magnetic scattering processes. With  $R$ , the reflected intensity  $I$  is determined by

$$I = |R(\theta, E) \cdot E_{In}|^2 \quad (4.35)$$

with  $E_{In}$  being the incident polarization in Jones vector notation [90,91]. Of particular interest in this work is the use of RCP (-) and LCP (+) x-rays. In this case  $E_{in}$  becomes

$$E_{In}^{\pm} = A \begin{pmatrix} 1 \\ \mp i \end{pmatrix} \quad (4.36)$$

Hence, for the sum and difference of both measurements one obtains

$$I^+ + I^- = A^2 [ |r_{ss}|^2 + |r_{pp}|^2 + \dots ] \quad (4.37)$$

$$I^+ - I^- = -4A^2 [ r_{ss}^* r_{sp} + r_{pp} r_{ps}^* ] \quad (4.38)$$

$I^+ + I^-$  then is a purely chemical signal, whereas  $I^+ - I^-$  contains both chemical ( $r_{ss}$  and  $r_{ss}^*$ ) and magnetic ( $r_{sp}$  and  $r_{ps}^*$ ) contributions.

The difficult task in this process is the calculation of the Fresnel reflection matrix. Analytical calculations already become complicated for just a single surface [92,93]. Therefore, for the case of several interfaces<sup>2</sup>, a matrix formalism is used, that initially was derived for the analysis of the magneto-optical Kerr effect (MOKE) [94,95]. Similar to PNR a model of the chemical and magnetic structure of the sample is used to simulate  $I^+$  and  $I^-$  intensities and compare it with the experimental data.

Experimentally, the depth resolved information of the magnetic structure in the sample can be obtained similarly to PNR by performing a reflectivity scan, i.e. a  $\theta/2\theta$  scan, with an x-ray beam having a constant energy at the absorption edge of the magnetic element. Since the reflection matrix is a function not only of  $\theta$ , but also of the x-ray energy  $E$ , at a synchrotron another experimental technique is often applied in order to gain the same information: At a fixed incident angle  $\theta$  the x-ray energy is scanned across the resonant edge of the magnetic element. In principle, both type of scans contain the same information.

<sup>2</sup>This can also be the case for a single layer, which does not have a homogeneous magnetization and hence needs to be split in layers to model the depth profile



# 5 Thin Film Deposition Techniques with Oxygen

The oxide heterostructures have been prepared by three different methods:  $\text{La}_{0.66}\text{Sr}_{0.33}\text{MnO}_3$  single and  $\text{La}_{0.66}\text{Sr}_{0.33}\text{MnO}_3/\text{SrTiO}_3$  bilayers have been grown by both, High Oxygen Pressure Sputtering (HSD) and Pulsed Laser Deposition (PLD).  $\text{La}_{0.5}\text{Sr}_{0.5}\text{MnO}_3/\text{BaTiO}_3$  samples have been prepared by Oxide Molecular Beam Epitaxy (OMBE). The methods differ in the way, how the material, which should be deposited on the substrate, is transferred from the target to the substrate. All three methods will be introduced in this chapter. It will be addressed how the differences between the methods might influence the quality of the samples. Detailed process parameters will be given in the sample preparation section of chapter 7.

## 5.1 Growth modes of epitaxial thin film

In this section the different possible growth modes and the parameters, which determine the growth mode of a thin film will be presented. A more detailed overview of this subject can be found for example in [96]. The samples in this work are grown epitaxially on single crystalline substrates, i.e. the layers adapt the lattice structure and the orientation of the substrates. Epitaxial growth is only possible, if the bulk lattice parameters of film and substrate match approximately. Usually a mismatch of some percent is acceptable for epitaxial growth. As will be shown in chapter 7, the surfaces of the substrates used in this work have atomically flat terraces, which are separated by atomic steps. The thermodynamic processes during deposition on a terrace like surface can be summarized in the following way: since a higher coordination number (i.e. the number of surrounding atoms) is energetically favorable, atoms which are adsorbed on the surface from the gas phase will more likely settle down at one of the steps than in the middle of a terrace. A second possibility to increase the number of nearest neighbors is the formation of clusters with other adsorbed atoms, which have not diffused to the next step yet. Which of the two processes is dominant, is in principle determined by three parameters: the mobility of the adatoms, the deposition rate, and the terrace size. For homoepitaxy, i.e. the growth on a single crystalline substrate of the same material (figure 5.1), these parameters determine the growth mode of the layer: for high mobilities, low deposition rates and small terraces, almost all adatoms will diffuse to the next surface step before they can agglomerate in clusters and step flow mode is established. For low mobility, large terraces and high deposition rates, the atoms will agglomerate with other arriving atoms before reaching the next step. In this case, islands are formed on the surface of the sample. As long as atoms are able to jump down from islands, the layer grows in the 2D-island mode, which in fact still is a layer-by-layer growth, since the lowest incomplete layer gets completed before the growth of the next layer begins. If the jumping is kinetically hindered, the film grows in 3D-island mode, which no longer is layer-by-layer growth. Since an atom during the jumping process is almost completely desorbed from the surface, it is not surprising that the jumping process can be energetically unfavored. For a growth of a well defined layer with smooth surfaces like in this work, the 3D-island growth should be avoided. Usually this can be done by choosing a high enough substrate temperature

to increase the mobility of the atoms, which are then able to overcome the energy barrier for the jumping processes.

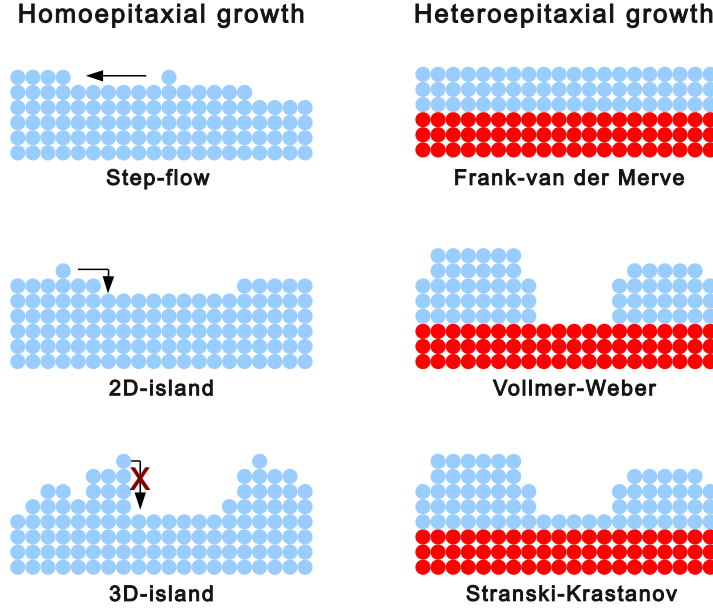


**Figure 5.1:** The different possible growth modes for homoepitaxial (left) and heteroepitaxial growth (right).

For the heteroepitaxial growth, i.e. the growth of a layer on a substrate of a different material, the same aspects as for the homoepitaxy apply, but the picture becomes a bit more complicated. Additionally, the surface energy of the layer  $\gamma_{layer}$ , the interface energy between the layer and the substrate  $\gamma_{layer,substrate}$  and the free energy of the substrate  $\gamma_{surface}$  determine the growth mode. Similar to the condition, whether a liquid spreads over a surface or forms droplets, for  $\gamma_{layer} + \gamma_{layer,substrate} < \gamma_{substrate}$  layer-by-layer growth is favored (Frank-van der Merve growth mode, figure 5.1). For  $\gamma_{layer} + \gamma_{layer,substrate} > \gamma_{substrate}$  island growth takes place (Vollmer-Weber growth mode). The second major difference to homoepitaxy is the strain mediated by the substrate due to the lattice mismatch, which can lead to further growth modes different from the two described before. Since a strained layer-by-layer growth costs energy, an island growth mode, where the layer material has space to relax, might be energetically favored, even though it requires a higher surface energy. This can result for example in a layer-by-layer growth for the first few monolayers, which then changes to island growth, when the energy needed to sustain the strain in a larger volume would become too high (Stranski-Krastanov). The relaxation of the lattice strain in the grown film in general is a very complicated process, which can occur in many different ways. The main important way to degrade the strain are misfit dislocations, i.e. additional atoms are inserted in tensile strained layers or taken away in compressive strained ones. The length scales on which a layer relaxes strongly depends on the materials of the layer and the substrate. It is important to mention that a strained layer usually can relax in the out of plane direction to keep the material density constant. Hence, a strained layer can not be distinguished from an unstrained layer by means of reflectometry measurements.

In order to obtain the desired growth mode, one needs to determine and adjust the correct parameters for the growth process accordingly. The most important parameters are temperature and deposition rate. In this work the aim is to prepare epitaxially thin films with well defined smooth interfaces. Therefore, the substrate temperature needs to be high enough to enable

epitaxial growth and high mobility of the adsorbed atoms. On the other hand, too high temperatures lead to high desorption rates possibly resulting in a zero net deposition. The deposition rate depends on very different parameters for the different techniques, which will be introduced in the following. It has to be adjusted to provide sufficient time of the deposited material to smoothen the surface.

## 5.2 High Oxygen Pressure Sputter Deposition (HSD)

Sputtering in general is the process of removing material from a target by ion bombardment. It is called “sputter deposition”, if the material is removed to be deposited on a substrate to grow a thin film. In this case the target consists of the material that should be deposited. For sputter deposition a process gas is ionized by applying either a DC or AC voltage to it. The plasma ions then are accelerated by the same voltage onto the target, where they sputter the material. After that the evaporated target atoms can settle down on the substrate placed opposite to the target. In contrary to the other two techniques, the target material is not pointing on the substrate in a directional beam. The evaporated material gets scattered in the gas atmosphere several times and then arrives at the target from a random direction.

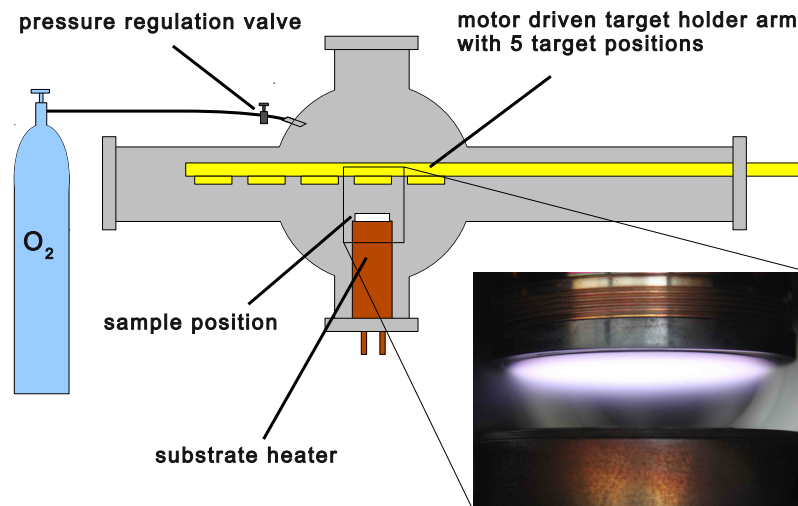


**Figure 5.2:** Sketch of the HSD chamber used in this work. The picture shows the oxygen plasma burning at the target during deposition. In the lower part the shielding of the substrate heater is visible. The substrate is deposited on top of it facing the target.

As a part of this work, a new sputter tool for the preparation of oxidic heterostructures has been taken into operation. Figure 5.2 shows a sketch of this sputter chamber. Even though the design has been optimized over the last years at the Institut für Festkörperforschung (IFF) in Jülich [7], still a lot of effort is put in increasing the quality of the samples. The most promising approach is to optimize the homogeneity of the oxygen plasma over a larger area, to minimize layer thickness inhomogeneities. Therefore, for each material the process of attaching the sputter target to the target holder and the design of the holder itself is of crucial importance. Targets with diameter of 2 in for both, AC and DC sputtering, have been soldered onto a Cu target holder with a coherent connection over the entire backside of the target. By this, a constant electric

and thermal contact is achieved for the complete target. This not only ensures a homogeneous plasma during deposition, it also is crucial for avoiding temperature gradients in the target. The thermal stress would cause the targets to crack, which inhibits a homogeneous plasma or even makes the target completely useless. In the inset of figure 5.2 the homogeneous burning plasma on the entire target surface is visible achieved by the soldering process.

Before deposition, the chamber is evacuated down to about  $1 \cdot 10^{-6}$  mbar. It then gets filled by the process gas, which in our case is oxygen. The big advantage of this sputter tool is the ability of growing the samples at comparable high pressures of several mbar. By this much better oxidation of the films is obtained [7] as compared to sputter deposition at lower oxygen pressures. The growth at lower oxygen pressures often results in oxygen deficient thin films, which then requires additional annealing steps. This not only takes time, the heat needed for the annealing might also harm the quality of the layers, e.g. by interdiffusion. The pressure in the chamber is controlled through a regulation valve. Up to five different targets can be loaded on an automatically operating motor driven target holder arm. The substrate is placed on a oven, which can be heated up to almost 1000 °C to give the required temperature for epitaxial and homogeneous growth. The distance between sample and target can be adjusted and typically is in the range of a few centimeters. This distance besides the applied voltage and the oxygen pressure determines the sputter rate, which typically is in the range of a few nanometers per hour.

### 5.3 Pulsed Laser Deposition (PLD)

In a PLD chamber the target material is ablated by a pulsed laser beam from a rotating cylindrical target (figure 5.3). The big difference to HSD is that by the laser ablation a high energetic plasma beam of the target material is created pointing on the substrate, where the material is deposited. The substrate again is placed on a heater to reach temperatures at which monocrystalline growth is possible. During deposition a constant oxygen flow at the sample position ensures sufficient oxidation of the layers. Typical oxygen pressures of  $5 \times 10^{-3}$  up to 0.5 mbar can be realized at the sample position. The advantages of this method are much higher deposition rates of typically 0.6 nm/s. On the other hand, since only a few pulses already grow a thin film of the order of one unit cell, it is very difficult to obtain the required layer thickness, if an accuracy of the order of unit cells is needed. In addition, the high deposition energies might influence the surface quality of the films and the directional material beam also tends to create larger thickness gradients on the samples surface compared to sputtered thin films. The deposition rate is determined by the laser power and pulse rate. Typical values to obtain the above mentioned deposition rates around 0.6 nm/s are laser powers of some J/cm<sup>2</sup> and pulse rates of some Hz. The exact growth parameters used in this work are given in chapters 7 and 8.

### 5.4 Oxide Molecular Beam Epitaxy

The  $\text{La}_{0.5}\text{Sr}_{0.5}\text{MnO}_3/\text{BaTiO}_3$  have been grown in a customized DCA OMBE chamber at the Center for Nanoscale Materials (CNM) at Argonne National Laboratory (ANL), Argonne, IL. The growth by OMBE probably is the most complex method of the three used in this work. Figure 5.4 gives an overview of the chamber design. The substrates are first inserted to a preparation chamber via a loadlock, where they can be outgassed before they are transferred to the main chamber, where the deposition takes place. In the main chamber of the OMBE system the target material is heated in a crucible to temperatures, where an sufficient fraction of the

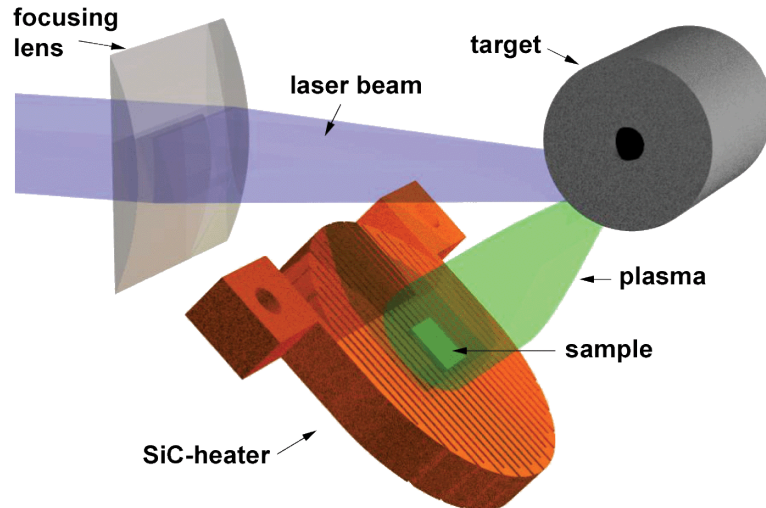


**Figure 5.3:** Sketch of the PLD chamber used in this work. The picture shows the oxygen plasma burning at the target during deposition. In the lower part the shielding of the substrate heater is visible. The substrate is deposited on top of it facing the target. Figure is taken from [97].

material evaporates (effusion cells). In the CNM chamber, 10 cells are arranged in a circular way around the cylindrical main chamber of the OMBE tool. All of them are pointing on the sample position under the same angle. In addition, 3 electron guns are available, where evaporation is caused by pointing an electron beam directly on the target material. The electron guns are not used for the preparation of the samples in this work. In contrast to the other two methods, the material needed for the thin film is not evaporated from a stoichiometric sample. The different elements are evaporated from different effusion cells. To calibrate their rates an oscillating quartz crystal (Quartz Crystal Monitor, QCM) is placed at the samples position. Then one source after another deposits material for a distinct amount of time (usually 20 minutes) on the QCM. The deposited mass slows down the oscillation of the QCM and enables one to calculate the deposition rate by monitoring the frequency. The determined rates are used to adjust the shutter opening times for each effusion cell in order to obtain the desired stoichiometry at the substrate position. To avoid oxidation of the target materials, the chamber is operated at pressures as low as possible. Ultra High Vacuum (UHV) conditions can be reached before the deposition by the use of a set of turbomolecular pumps. On the other hand oxygen needs to be offered to the sample during deposition to obtain fully oxidized stoichiometric films. The CNM system is an ozone assisted OMBE, i.e. a steady flow of pure, distilled ozone is pointing at the sample from a water cooled nozzle during rate calibration and film deposition. By this an optimal oxidization of the films is ensured. As a compromise to minimize the oxidation problem for the sources, the lower part of the chamber, where the sources are located, is differentially pumped to one to two orders of magnitude lower pressures. Of course there is also the possibility to heat the substrate. The temperature can be controlled by a pyrometer. In addition, the growth can be in-situ analyzed by RHEED (see next chapter). Even though the effusion cells create a directional beam similar to PLD, much higher thickness homogeneities are obtained due to the larger source-to-substrate distance. The deposition rate can be adjusted by the temperature of the effusion cells and usually is of the order of some Ångstrom per minute. In combination with the RHEED, the low deposition rate enables one to control the layer thickness on an atomic length scale.



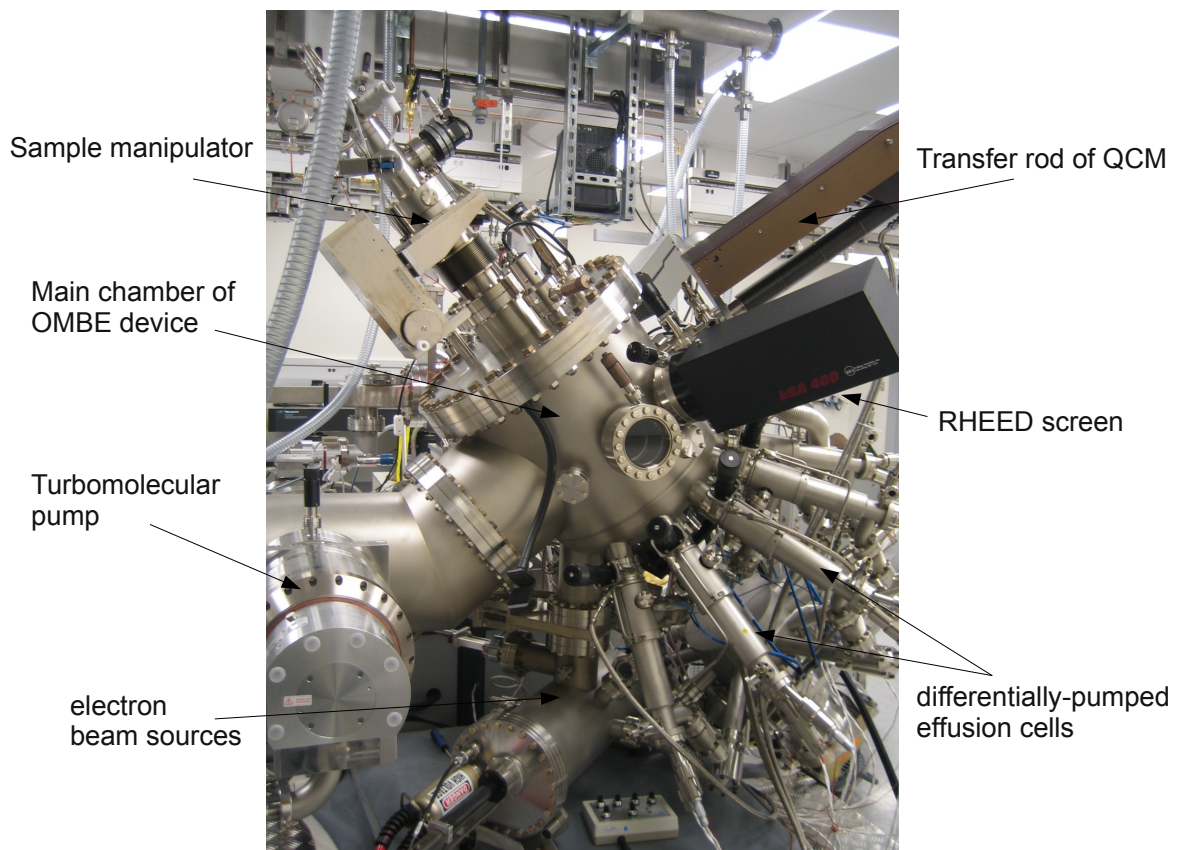


**Figure 5.4:** Picture of the OMBE system used in this work.

# 6 Experimental Methods

## 6.1 Sample Characterization

### 6.1.1 Rutherford Backscattering (RBS)

RBS is a versatile technique, that can determine not only the chemical composition and film thicknesses of a layered system, but can also test, whether a film is grown epitaxially. The instrument employed in this work uses a Tandetron tandem accelerator, which produces  $\text{He}^+$  ion flow of 1.4 MeV. The beam is pointed on the sample. In a scattering event a  $\text{He}^+$  ion loses a fraction of its initial energy  $E_0$ , which is determined by the scattering angle  $\theta$  and the mass of the atom  $m_{At}$  it scattered from. The resulting energy  $E_1$  is described by the kinematical factor  $k$  [98]:

$$E_1 = k \cdot E_0 \quad (6.1)$$

$$k = \left( \frac{\cos(\theta) + \sqrt{\left(\frac{m_{At}}{m_{He}}\right)^2 - \sin^2(\theta)}}{1 + \frac{m_{At}}{m_{He}}} \right)^2 \quad (6.2)$$

where  $m_{At}$  is the mass of the  $\text{He}^+$  ion. In order to maximize the mass resolution, an angle close to  $180^\circ$  is chosen. In addition the ions lose energy, when travelling through the sample. The energy loss  $dE/dz$  is given by the Bethe-Bloch formula [98]. Thus the final energy  $E_2$  of a  $\text{He}^+$ , after traveling the distance  $d_1$  through the sample, the scattering event, and travelling the distance  $d_2$  before exiting the sample can be calculated by

$$E_2(z) = k \left( E_0 - \int_0^{d_1} \left( \frac{dE}{dz} \right) dz \right) - \int_0^{d_2} \left( \frac{dE}{dz} \right) dz \quad (6.3)$$

The probability for a scattering event is given by the differential cross section [98]

$$\frac{d\omega}{d\Omega} = \left( \frac{Z_{He} Z_{At} e^2}{4E_0} \right)^2 \frac{1}{(\sin(\theta/2))^4} \quad (6.4)$$

where  $Z_{He}$  and  $Z_{At}$  are the atomic numbers of the  $\text{He}^+$  ion and the scattering atom, respectively. From equations (6.3) and (6.4) the chemical composition can be determined depth resolved by measuring the backscattered intensity of the incident  $\text{He}^+$  energy resolved. In addition, by turning the sample one might find directions where the  $\text{He}^+$  atoms point in the direction of a crystal axis of the sample. Since the scattering objects are aligned behind each other the scattering probability decreases drastically for such a direction. If this behaviour is observed (channeling), it is a proof for the monocrystallinity of the sample.

### 6.1.2 Reflection High Energy Electron Diffraction (RHEED)

The growth of the thin films deposited by OMBE has been in-situ characterized by RHEED. In this technique, high energetic electrons are reflected elastically under a small angle from the surface, where the thin film is deposited. Since the targets usually are mounted almost perpendicular to the substrate, the RHEED instrumentation (unlike a Low Energy Electron Diffraction (LEED) device) does not shield the material beam of the incoming particles. Therefore, it nowadays is the most prominent in-situ characterization method of thin film growth, as it can be used during the deposition. In this technique, high energetic electrons are reflected elastically under a small angle from the surface, where the thin film is deposited. Due to the strong interactions of the electrons with the sample, the penetration depth is only one or very few monolayers. Therefore, RHEED is an extremely surface sensitive experiment. If the film grows epitaxially a regular pattern can be observed on a two dimensional fluorescence screen. Besides the specular reflected beam, the spots on the screen correspond to the allowed reflections from the epitaxial surface. A detailed theoretical description of the RHEED scattering process can be found e.g. in [99]. From the RHEED pattern several conclusions can be drawn: first of all the sharpness of the spots is an indication for the crystal quality of the growing layer. A more disoriented growth results in a broadening of the peaks. Furthermore, the intensity of the spots is oscillating, if the thin film is growing in layer-by-layer mode (figure 6.1): For an incomplete layer the surface roughness is higher and the off-specular scattering is enhanced. Therefore, the spot intensity of the specular reflection is maximized every time a layer gets completed. The oscillations not only are a proof of layer-by-layer growth. They also can be used to count the number of unit cells grown and thus help to accurately determine the layer thickness.

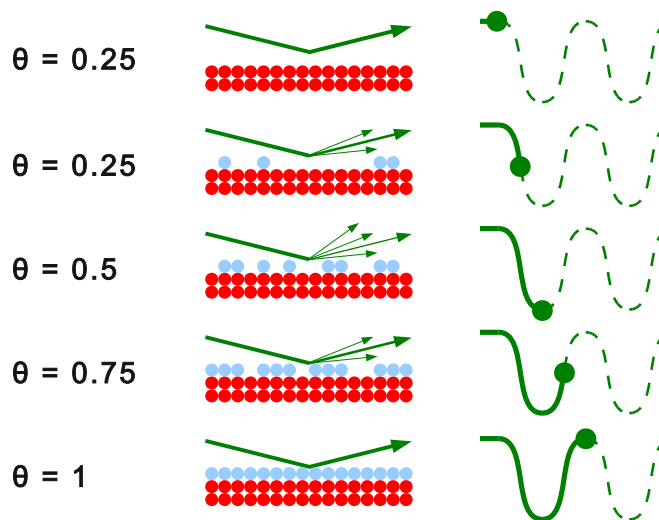


**Figure 6.1:** Schematic explanation of the RHEED intensity oscillations of the specular intensity during layer by layer growth. Depending on the coverage rate  $\theta$ , the roughness of the surface and hence off-specular scattering increases resulting in a reduction of the specular intensity. After arriving at a minimum for  $\theta = 0.5$ , the specular intensity increases again until it returns to a maximum, when the layer is completed.

### 6.1.3 Atomic Force Microscopy (AFM)

By AFM information on the surface morphology of a sample can be obtained on an atomic length scale. A tiny sharp tip (usually only some few atoms broad) is placed close to the surface

under investigation. The tip is attached to a cantilever. In “tapping mode” a piezo crystal exerts oscillations of the cantilever. The amplitude of the oscillations depends on the distance to the surface. Whereas the sample is moved in lateral direction, the instrument adjusts the  $z$  coordinate in order to keep the amplitude constant, i.e. to keep the distance constant. These adjustments are monitored and give a laterally resolved picture of the surface. Besides analysing possible surface structures, also the rms-roughness can be calculated from the measurement by averaging the height distribution of the surface. In addition, the phase difference between the voltage, that is applied to the piezo crystal, and the cantilever oscillation is monitored. The phase difference depends on the material underneath the tip and thus can give information on chemically different domains or terminations on the surface. The AFM pictures in this work were taken with a Agilent 5400 instrument (figure 6.2). To monitor the oscillations of the tip, a laser beam is pointed on the back side of the cantilever and gets reflected to a two dimensional detector. To minimize any external disturb signals, the AFM is located on a heavy slab, which is hang-up with shock damping elastic ropes inside a sound absorbing box.

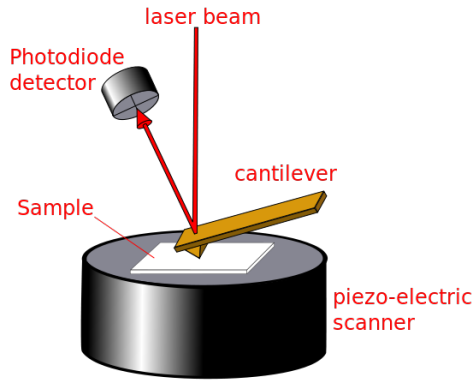


**Figure 6.2:** Schematic drawing of the AFM instrument used in this work taken from [97].

## 6.2 Macroscopic Magnetic and Ferroelectric Analysis

### 6.2.1 Vibrating Sample Magnetometry

The analysis of the macroscopic properties of the samples was done in a Quantum Design Physical Properties Measurement System (PPMS) using the Vibrating Sample Magnetometry (VSM) option. In a VSM the magnetic sample is placed between two so called “pick-up coils” (figure 6.3). When the magnetic sample is moved with respect to the pick-up coils, the magnetic flux  $\Phi$  through the pick-up coils temporarily changes. Thereby, a time dependent voltage  $V_{coil}$  is induced in the pick-up coils:

$$V_{coil} = \frac{d\Phi}{dt} = \left( \frac{d\Phi}{dz} \right) \left( \frac{dz}{dt} \right) \quad (6.5)$$

In the PPMS a piezo crystal is used to oscillate the sample in a sinusoidal vibrating motion. In this case, the induced voltage in the pick-up coils is proportional to the magnetization  $m$  in the sample:

$$V_{coil} = 2\pi f C m A \sin(2\pi f t) \quad (6.6)$$

Here  $C$  is a coupling constant,  $A$  is the amplitude of the oscillation and  $f$  is the frequency of the oscillation.  $V_{coil}$  is read out by a lock-in amplifier. In addition, it is possible to change the

temperature in the PPMS to 2 K and apply magnetic fields up to 9 T. These options allow one to measure hysteresis curves and temperature dependent magnetization scans.

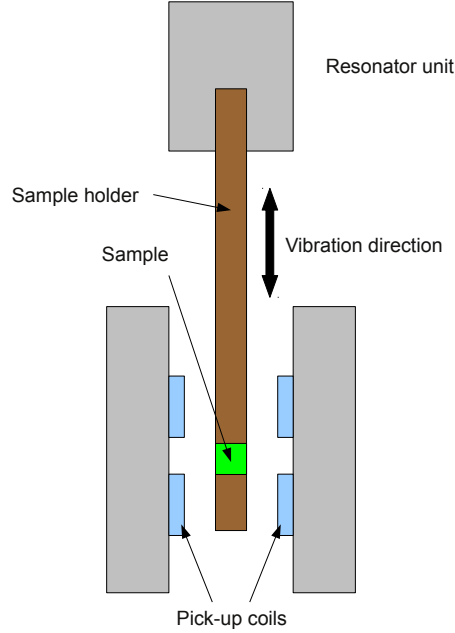


**Figure 6.3:** Sketch of a VSM like it is used in this work inside the Quantum Design PPMS.

### 6.2.2 Electrical Hysteresis Measurements

In order to analyze the ferroelectric properties of the BTO layers, electrical hysteresis measurements have been performed using a commercial Radiant Precision LC apparatus. Via electrical contacts the charge  $Q$ , which gets transferred through the sample, is measured during switching the applied voltage  $V$ . The polarization  $P$  of the sample can be calculated from the switched charge. By calculating the corresponding electric field  $E_a$  from the applied voltage  $V$ , one obtains for a ferroelectric material the characteristic hysteresis loop  $P(E)$ . The remanent polarization  $P_r$  of the sample can be calculated for a parallel-plate capacitor by

$$Q = 2P_r A + \sigma E_a t \quad (6.7)$$

where  $A$  is the area of the capacitor,  $\sigma$  the electrical conductivity and  $t$  the measuring time. The second term is zero for an ideal ferroelectric. It takes into account dielectric loss currents caused by the non zero electrical conductivity.

## 6.3 Mesoscopic Structural and Magnetic Analysis

The theory for this chapter was already presented in chapter 4. In this section the instruments used in this work will be introduced.

### 6.3.1 X-ray Reflectometry (XRR) and X-ray Diffraction (XRD)

The XRR and XRD data has been taken with three different instruments. The first one is a Bruker D8 reflectometer. A sketch of the instrument is shown in figure 6.4. The x-ray radiation is emitted from a Cu anode, which mostly provides x-rays with wavelength  $1.54 \text{ \AA}$  ( $\text{Cu K}\alpha$ ). The radiation is parallelized by a first Göbel mirror, after which two slits reduce the background and define the beam width. The parallelized beam is reflected from the sample and enters the detector arm through an absorber and a third slit, which again only reduces the background. A second Göbel mirror focuses the reflected beam to a fourth slit which defines the resolution of the measurement. The detector is placed immediately behind this last slit. Both the source and detector arm can be moved independently in the scattering plane.

The second instrument is a Huber four circle diffractometer allowing additional rotations of the sample around two further angles. The angles are defined in figure 6.5. This allows for measuring reflections by XRD that also have an in-plane component, which is not possible on the other instrument. Finally, a Bruker four circle diffractometer located at the CNM has been used. In contrary to the first two instruments, the one at CNM has a double monochromator to filter out all additional wavelengths created by the x-ray tube. By this a monochromatic x-ray beam is created with wavelength of  $\text{Cu K}\alpha_1$  radiation.

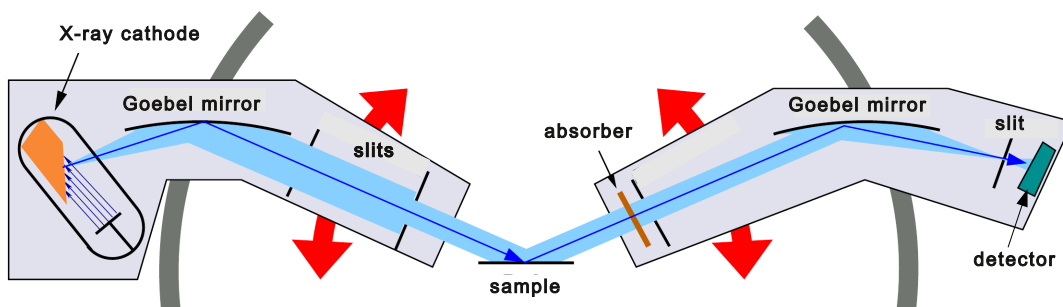
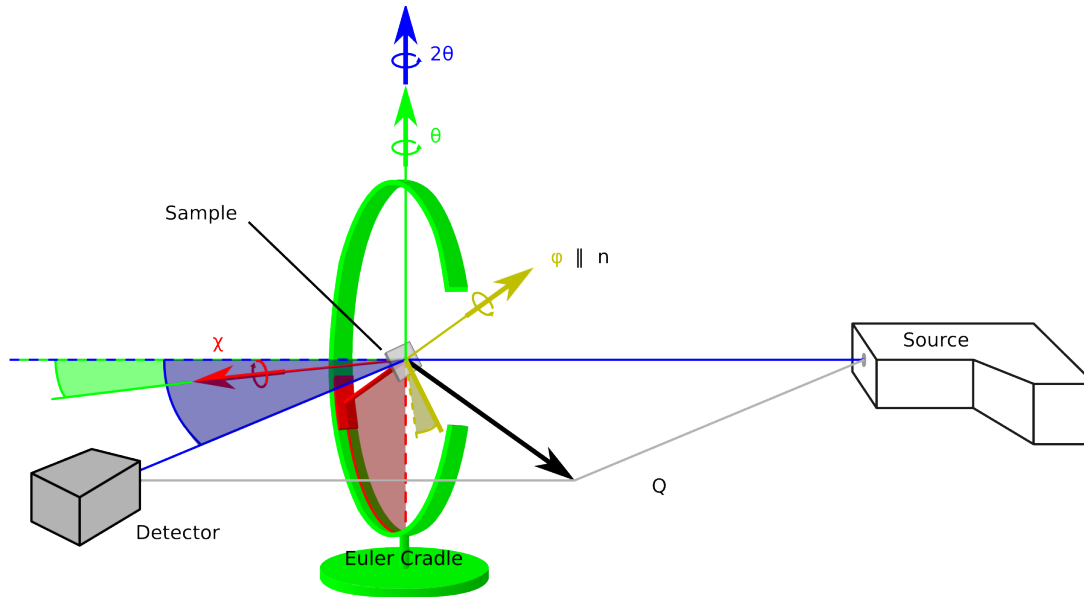


Figure 6.4: Drawing of the reflectometer geometry taken from [97].

### 6.3.2 Polarized Neutron Reflectometry

Polarized Neutron Reflectometry was performed on the Magnetic Advanced Grazing Incidence Spectrometer (MAGICS) at beamline 4A of the Spallation Neutron Source (SNS) at Oak Ridge National Laboratory (ORNL). A schematic drawing of the instrument is shown in figure 6.6. In the spallation source proton bunches are accelerated onto a liquid mercury target inducing the spallation process. The SNS usually operates at a frequency of 60 Hz. The generated neutrons are slowed down by a moderator and guided to the experiments through an array of neutron optics. MAGICS operates in time-of-flight (TOF) mode (figure 6.7): all neutrons created by a certain proton pulse of the SNS leave the moderator within a narrow time window. Depending on the wavelength they arrive at different times at the detector after being reflected from the sample. By this, in contrast to a monochromatic reflectometer, a broad  $Q$  range can be covered at one incident angle  $\theta$  simultaneously. Due to the limited time resolution of the detector, the flight path needs to be long enough in order to obtain a sufficient  $Q$  resolution. At MAGICS the distance between moderator and detector is about 19 m. To avoid overlap between slow neutrons of one bunch with fast neutrons of the next bunches, the wavelength range needs to be limited (figure 6.7). For a 18 m flight path and a pulse frequency of 60 Hz the maximum wavelength range



**Figure 6.5:** Drawing of the 4-circle geometry taken from [97].

is approximately  $3 \text{ \AA}$ . The selection is done by a set of wavelength choppers. Three choppers are needed at MAGICS to avoid that slow neutrons can pass the choppers with a subsequent bunch. Behind the choppers the neutron beam is collimated by slits before it gets polarized by a supermirror. The following spin flipper allows for setting the incidence beam polarization to "Up" or "Down". The beam then gets reflected from the sample placed in a closed cycle cryomagnet attached on a goniometer table. The polarization of the reflected beam is analyzed in analogous way to the polarization process by a spinflipper and a supermirror. Finally the reflected neutron beam is detected by a two-dimensional position sensitive  $^3\text{He}$  detector.

### 6.3.3 X-ray Resonant Magnetic Scattering (XRMS) in reflectometry geometry

The XRMS experiments have been carried out on beamline 4-ID-C of the Advanced Photon Source (APS) at Argonne National Laboratory (ANL). In the standard operation mode 7 GeV electrons are inserted in the 1104 m circumference storage ring of the APS, which usually results in a 100 mA current. The insertion device of sector 4 is an electromagnetic circular polarizing undulator (CPU), which can deliver both a circular or linear polarized x-ray beam in the soft x-ray energy range between 500 and 2800 eV (700 to 2800 eV for linear polarization). The optics of beamline 4-ID-C are shown in figure 6.8. The polarized beam is reflected by a first mirror on a spherical grating monochromator, where the desired energy is selected (resolution  $\frac{\Delta E}{E} = 2 \cdot 10^{-4}$ ). After that a second mirror reflects the beam to the sample position and can focus the beam to a spot size of  $300 \mu\text{m}$  times  $100 \mu\text{m}$ . In this work, the XRMS station of beamline 4-ID-C has been used, where the reflected x-ray beam can be measured up to  $2\theta \approx 45^\circ$  (figure 6.9). The detector is an x-ray photodiode from International Radiation Detectors. In addition, two techniques are used to measure the absorption of the sample simultaneously: electrons that refill the holes created in the core orbitals by the x-ray absorption can lose their excess energy in two ways. The first is emission of fluorescence photons. The number of fluorescence photons is proportional to the absorption of the sample. The fluorescence signal is measured by a SII-Vortex detector (Total Fluorescence Yield (TFY)). By TFY up to 20 nm of the sample at the surface can be probed, which is more than the layer thicknesses of the samples used in this work. The disadvantage

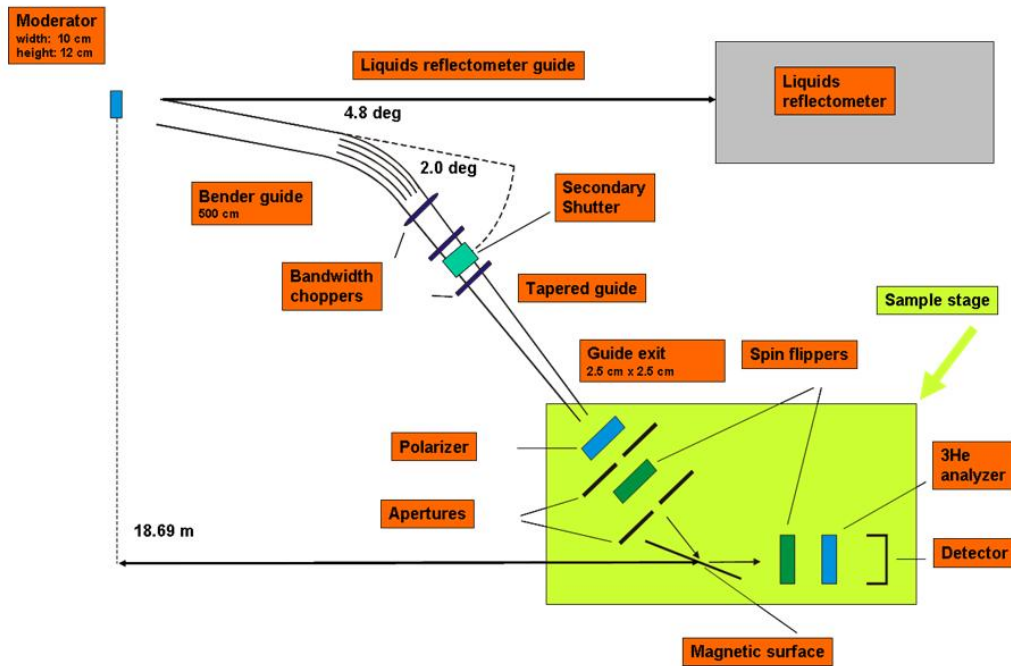


Figure 6.6: Beamline layout of the polarized neutron reflectometer MAGICS at the SNS taken from [100]

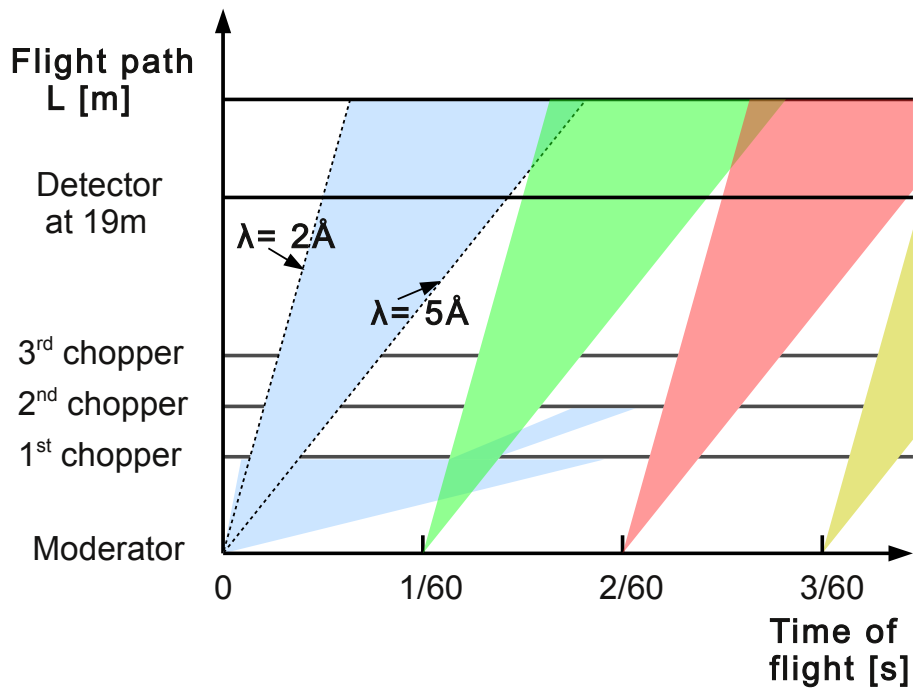
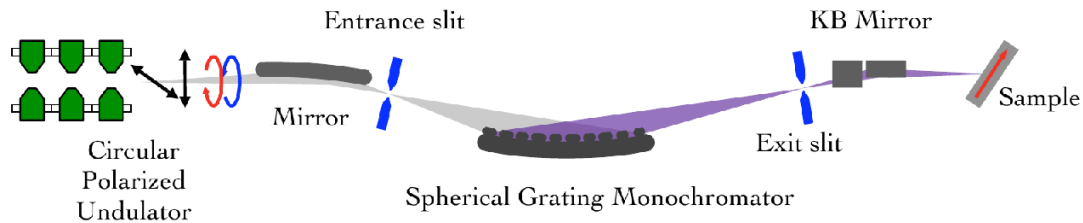


Figure 6.7: Schematic drawing of the TOF principle for the parameters used at MAGICS



of this method is a usually weak signal, since Auger processes are much more likely to happen in the soft x-ray regime than photon emission. In an Auger process the electron that fills the core level transfers the excess energy to another electron (Auger electron). The Auger electrons distribute the additional energy by inelastic scattering processes to other electrons in the sample. The resulting current can be measured. Again it is proportional to the absorption of the sample (Total Electron Yield (TEY)). Even though the intensity is larger than for TFY, the depth probed by TEY is much smaller due to the small free mean path of the electrons. Therefore, only the absorption of the top 1-2 nm of the samples can be measured by TEY.



**Figure 6.8:** Scattering geometry of beamline 4-ID-C at Sector 4 of the APS taken from [101]

At the sample position, magnetic field up to 500 Oe can be applied in the film plane and in the scattering plane by an electromagnet. In addition, the sample can be cooled by a continuous flow cryostat to about 15 K.

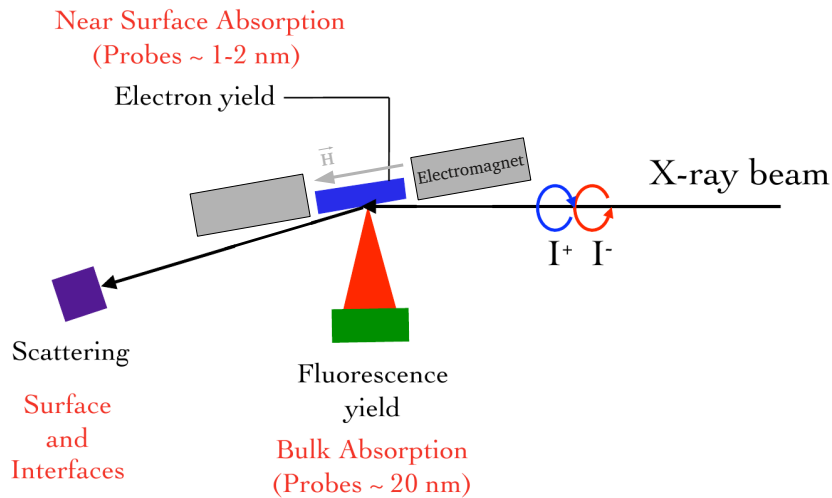


**Figure 6.9:** Experimental configuration at the XRMS station of beamline 4-ID-C (taken from [102]).

# 7 Results and Discussion I:

## $\text{La}_{0.66}\text{Sr}_{0.33}\text{MnO}_{3-\delta}/\text{SrTiO}_3$

### 7.1 Preparation of stoichiometric LSMO single and LSMO/STO bilayers

$\text{La}_{0.66}\text{Sr}_{0.33}\text{MnO}_3/\text{SrTiO}_3$  bilayers and  $\text{La}_{0.66}\text{Sr}_{0.33}\text{MnO}_3$  single layers have been prepared by both HSD and PLD on single crystalline (001) oriented  $\text{SrTiO}_3$  substrates. Before deposition, the substrates have been annealed in an oven for one hour at  $900^\circ\text{C}$ . The heating and cooling rates have been  $100^\circ\text{C}/\text{h}$  to avoid cracking of the substrates. By this procedure organic residues are removed from the substrate. In addition the surface gets as smooth as possible, i.e. the only remaining roughness is the steps of unit cell height from one atomically flat terrace to the next one. Since there always is some mis-cut of the surface with respect to the lattice planes, these terraces are unavoidable and become smaller with increasing mis-cut. An AFM picture of the surface of the substrate can be seen in figure 7.1. In the phase picture, the clearly distinct regions probably correspond to the two possible different terminated surface area, namely  $\text{SrO}$  and  $\text{TiO}_2$ .

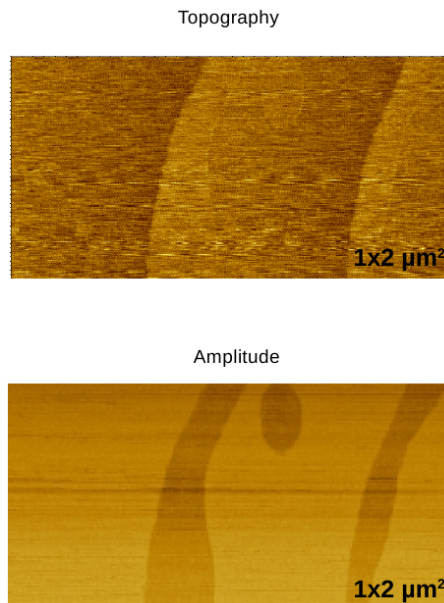


**Figure 7.1:** AFM picture of a substrate after the annealing procedure. Atomically flat surfaces can be seen in the topography picture. In the phase picture different colored areas correspond to different terminated surface regions ( $\text{SrO}$  or  $\text{TiO}_2$ )

For the HSD sample preparation commercial Lesker  $\text{La}_{0.66}\text{Sr}_{0.33}\text{MnO}_3$  and  $\text{SrTiO}_3$  targets with diameter 2 inch have been used. LSMO has been deposited by DC sputtering at a voltage of

370 V, STO by AC sputtering with a power of 80 W. Both materials have been deposited at a temperature of  $T_s=750^\circ\text{C}$ . The oxygen pressure during sputtering has been varied for different samples between 2.0 and 0.6 mbar. Thereby also the deposition rates varied between  $1.0 \text{ \AA}/\text{min}$  at 2.0 mbar and  $1.7 \text{ \AA}/\text{min}$  at 0.6 mbar

For the PLD growth an excimer laser (LAMBDA LPX305) with wavelength 248 nm, a repetition rate of 10 Hz and an energy density of  $3.5 \text{ J}/\text{cm}^2$  was used. The cylindrical target consists of sintered powder with the nominal stoichiometry  $\text{La}_{0.66}\text{Sr}_{0.33}\text{MnO}_3$  for the LSMO and a single crystal target for the  $\text{SrTiO}_3$ . A typical deposition rate of  $0.6 \text{ nm}/\text{s}$  was achieved for both materials. Substrates were placed on a resistive SiC heater. Deposition temperatures in the range of  $T_s=750^\circ\text{C}$  were applied during the growth.

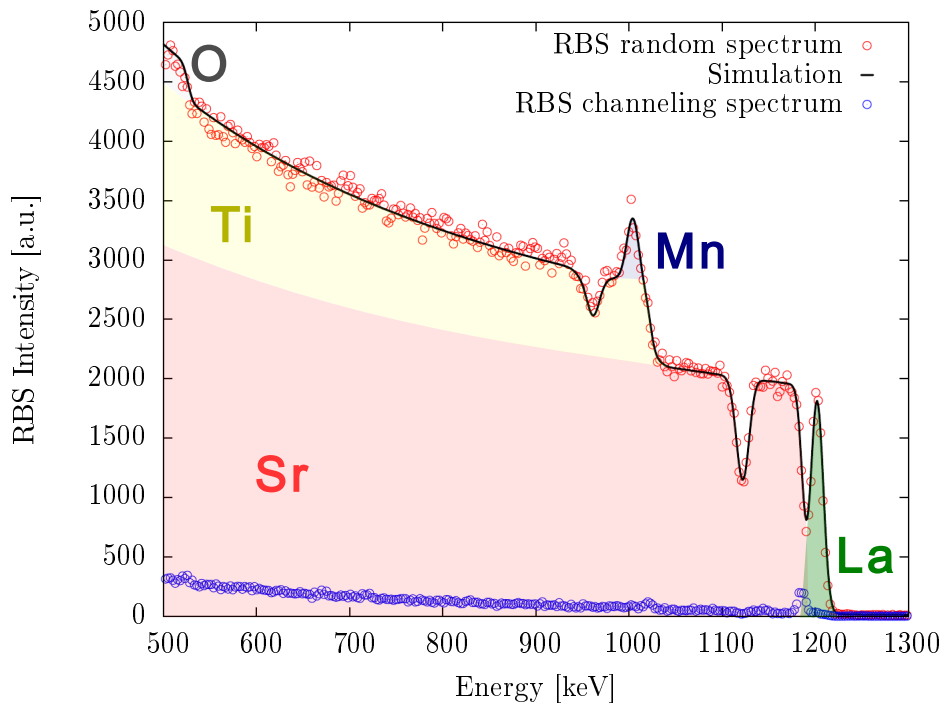


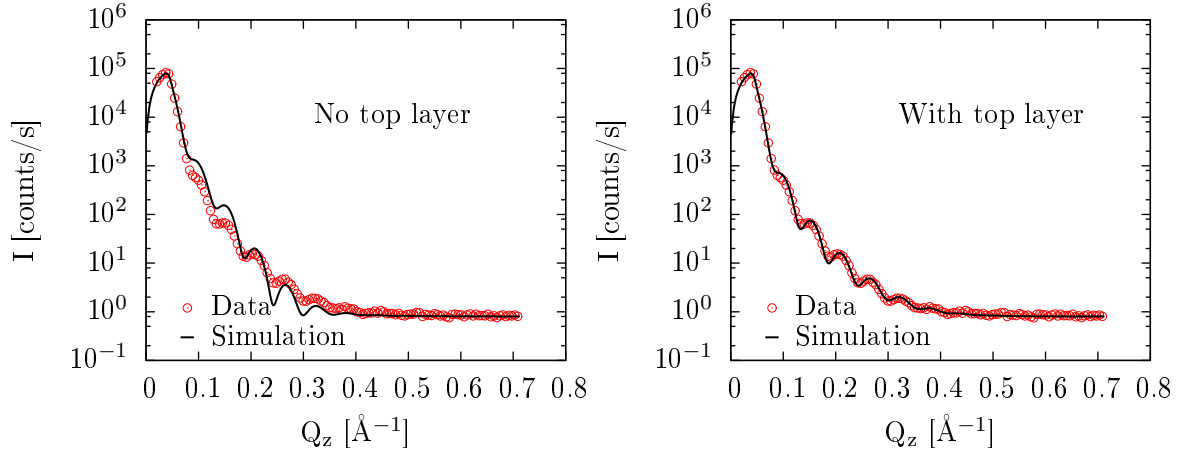
**Figure 7.2:** RBS measurement of a LSMO/STO bilayer grown by PLD. The colored areas correspond approximately to the contributions of the different elements to the RBS spectrum for incidence along a random direction (but almost perpendicular to the sample surface). The simulation is the expected spectrum for a  $\text{La}_{0.66}\text{Sr}_{0.33}\text{MnO}_3/\text{SrTiO}_3$  bilayer grown on a  $\text{SrTiO}_3$  substrate with layer thicknesses of 95 and 580  $\text{ \AA}$ , respectively, confirming the desired stoichiometry. The channeling spectrum is shown as well (blue data points).

Samples grown by both methods have been analyzed first by RBS (figure 7.2). The stoichiometry of the samples grown by PLD as well as by HSD have been determined to be  $\text{La}_{0.66}\text{Sr}_{0.33}\text{MnO}_{3-\delta}$  within the uncertainty of the method (about 5%). However, by this method only the ratio between the metal elements can be checked. Due to the small atomic mass of oxygen, the error bar on the oxygen value is much larger indicated by the  $\delta$  in the chemical formula. Thus oxygen deficiencies (or excess) can not be detected by this method. By rotating the sample an incident direction was found for which the RBS signal is drastically suppressed (blue data points in figure 7.2). This “channeling“ can only occur for single crystalline samples, if the incident direction is along one of the crystal axis. A suppression down to about 5% of the signal along a random direction confirms the good crystal quality of the sample (see also XRD characterization below).

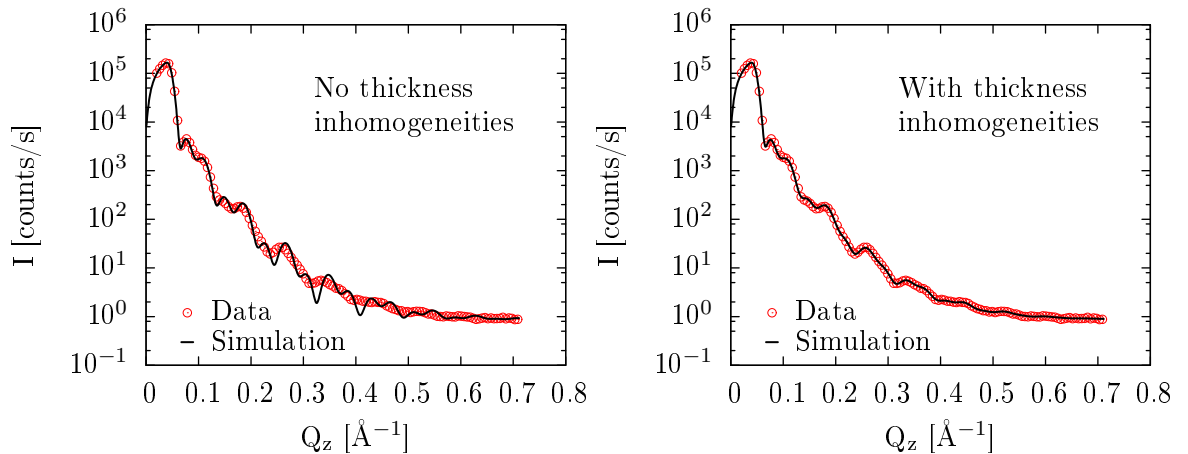
Even though layer thicknesses can in principle be extracted from the RBS data as well, XRR was applied to determine layer thicknesses and roughnesses of the samples more accurately. The data has been modeled using Parratts formalism discussed in chapter 4 [79, 103]. In order to find a good agreement with the experimental data, the fitting procedure tries to minimize the following expression (Figure of Merit (FOM))

$$FOM = \frac{1}{N} \sum_i^N (\log(D_i) - \log(S_i))^2 \quad (7.1)$$

where  $D_i$  are the  $N$  experimental intensity data points.  $S_i$  are the corresponding simulated intensity values. This particular FOM is suitable, if the data points span over several orders of magnitude. The differences of the logarithms ensures that small values are not underrated. This FOM will also be used in the following to estimate the quality of the fits.



(a) Influence of the introduction of a thin surface layer. The plot shows XRR data and simulation of a LSMO single layer grown by HSD. Introduction of a surface layer is necessary to reproduce the experimental measurement.



(b) Influence of thickness inhomogeneities. Displayed are the data and simulation of a LSMO/STO bilayer grown by PLD. Good agreement can only be obtained by introducing thickness inhomogeneities

**Figure 7.3:** Motivation for the two additional aspects introduced to fit the XRR data

Since the stoichiometry of the layers already is confirmed by RBS, the scattering length densities are not fitted, but kept fixed at the bulk values of LSMO and STO. Therefore, the only free parameters are the layer thicknesses and the roughnesses of the layers and the substrate. For all samples this simple model was not sufficient to represent the data by the simulations. The two adjustments needed to obtain satisfying results will be discussed in the following. Their influences on the simulations can be seen in figure 7.3.

The first adjustment needs to be done on the surface of the sample (figure 7.3a). Due to the large difference in the scattering length densities of air and sample material, the XRR data is extremely sensitive to the structure of the surface of the sample. Therefore, it often is not sufficient to model the surface by just the rms-roughness parameter of the top layer. To overcome this problem a thin surface layer (around 1 nm) with an additional roughness parameter is introduced for all samples. Figure 7.4 illustrates, how different density profiles, i.e. differences in the structure of the surface roughness, can be obtained depending on the choice of the two rms-roughness parameters at the surface. For all samples, the scattering length density of the surface layer was significantly smaller than the one for the material of the top layer. This is in accordance with the interpretation of this layer being a region that is only partially filled by top layer material to model the surface roughness. The thickness of this region is added to the thickness of the underlying layer scaled by the density of the surface region: e.g. if the fit for a LSMO single layer gives a 8 Å surface region with 50 % of the density of LSMO, 4 Å are added to the fitted value of the LSMO layer to obtain the total LSMO layer thickness of the sample (figure 7.4).

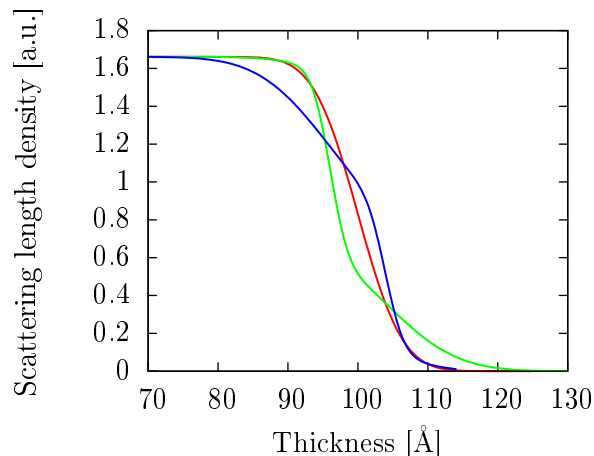


**Figure 7.4:** Three different profiles for the surface of a LSMO layer of a total thickness of 100 Å. Red: 100 Å LSMO with rms-roughness 5 Å and no additional surface layer. For the simulations of the XRR measurement this simple model of the surface is not sufficient to represent the data. Green: 96 Å LSMO layer with rms-roughness 3 Å and a 8 Å surface layer with rms-roughness 7 Å. The density of the surface layer is 50 % resulting in a total LSMO layer thickness of 100 Å. Blue: 96 Å LSMO layer with rms-roughness 8 Å and a 8 Å surface layer with rms-roughness 3 Å.

The second aspect, which is taken into account, are thickness inhomogeneities (figure 7.3b). As discussed in chapter 5, especially samples prepared by PLD usually reveal some thickness distribution: due to the inhomogeneous plasma particle beam coming from the target, the deposition rate is highest in the center of the substrate. As a result the thickness oscillations in a XRR experiment smear out. The assumption of thickness inhomogeneities is supported by the comparison of a PLD and a HSD LSMO/STO bilayer of similar layer thicknesses: from the data in figure 7.5a and b it can be seen, that the oscillations in the HSD sample are more pronounced suggesting more homogeneous layer thicknesses as expected. Detailed information on how the layer inhomogeneities are modeled can be found in [97]. For the samples in this

work it turned out that it is a sufficient assumption that the amount of thinner thicknesses than the maximum layer thickness - which is expected to be reached in the center of the sample - are distributed Gaussian like. In this way, the width of the Gaussian  $\sigma_{inhom}$  is a measure for the thickness inhomogeneities. As expected, the simulations reveal a larger  $\sigma_{inhom}$  and hence thickness inhomogeneity for the PLD sample than for the HSD samples (table 7.1).

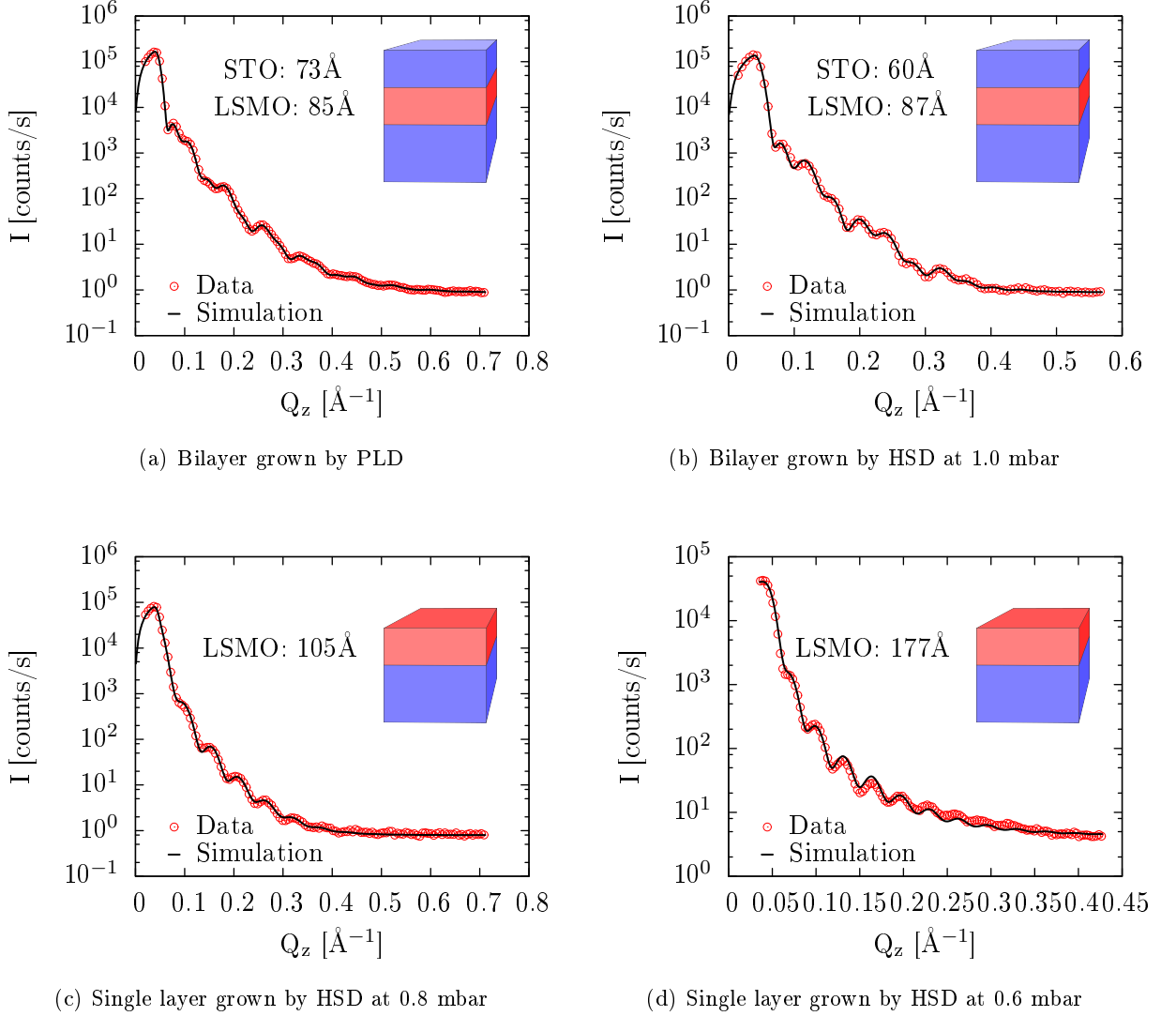


**Figure 7.5:** XRR data of the four samples under detailed investigation in this work. The thicknesses indicated are determined by the simulation of the reflectivity data. Detailed results can be found in table 7.1

In this work, the data of four samples will be discussed in detail: One sample grown by PLD and three samples grown by HSD at different oxygen pressures. The PLD sample and the HSD sample grown at 1.0 mbar are LSMO/STO bilayers, whereas the two HSD samples grown at 0.8 and 0.6 mbar are LSMO single layers. The corresponding XRR data and the fits are shown in figure 7.5. With the two adjustments discussed before a very good agreement between the experimental data and the simulations was obtained. The results of the fits can be seen in table 7.1. The layer roughnesses for both bilayers are very small ranging between 2 and 5 Å. The roughness of the LSMO layers in the HSD samples increase up to 19 Å with decreasing

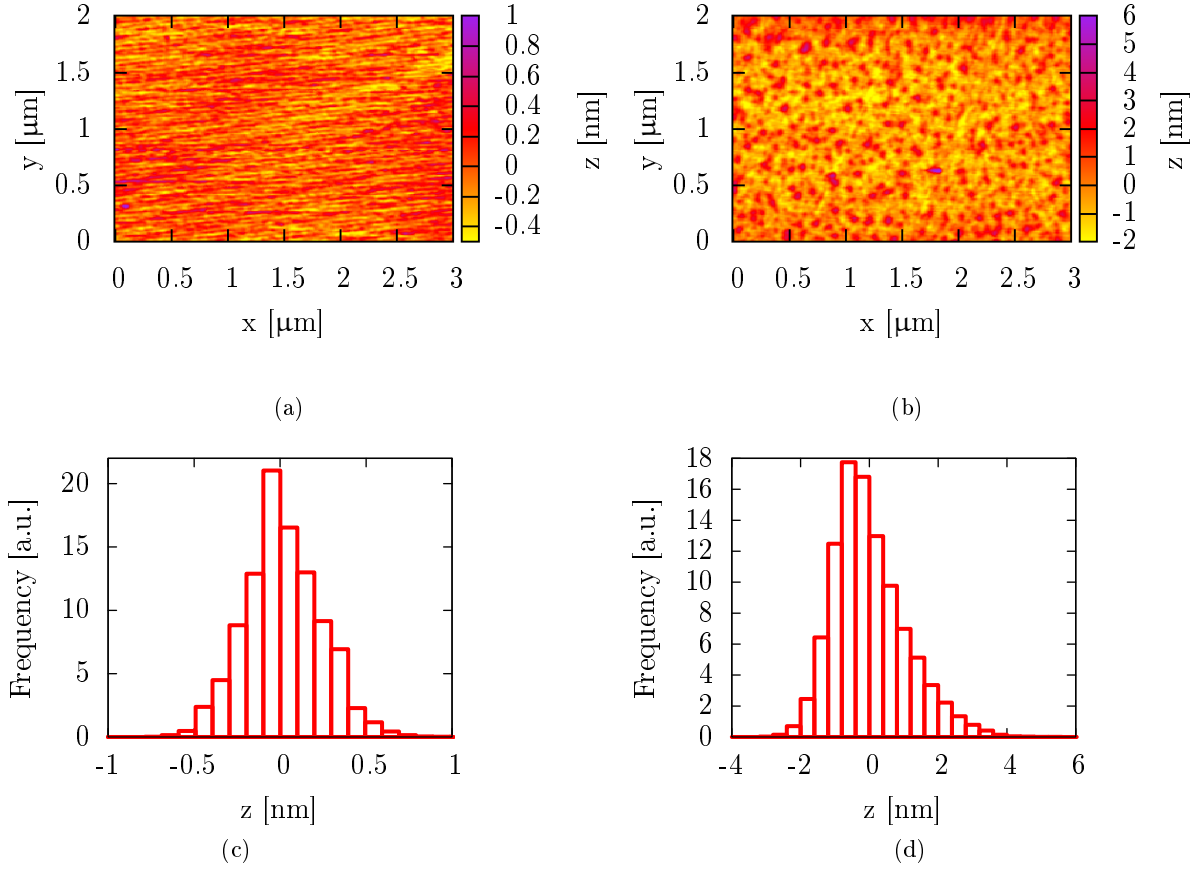


**Figure 7.6:** AFM measurements of the surfaces of (a) the bilayer grown by PLD and (b) the LSMO single layer grown by HSD at 0.8 mbar. The histograms of the height distribution for both samples are shown in (c) and (d), respectively. Higher roughnesses and asymmetric height distribution is visible for the HSD sample, which probably is the reason for the necessity of introducing a surface layer in the XRR experiments: the surface roughness cannot be simulated by a single rms roughness parameter.

oxygen pressure during deposition, which could have several reasons: first of all the LSMO layer thicknesses also increase from about 90 Å to almost 180 Å. And the thicker a epitaxial thin film gets the higher normally the surface roughnesses become. Secondly, as mentioned before, the deposition rates have been oxygen pressure dependent. Even though they have been very small for all samples, the higher rates at lower oxygen pressures might result in a higher fraction of island growth mode.

For all samples the surface roughnesses determined by XRR show the same dependence like the roughnesses determined by AFM (figure 7.6): the lower the oxygen pressure during HSD growth, the higher the surface roughness becomes (table 7.1). The AFM measurements also give some indication, why the introduction of the surface layer for simulating the XRR data is especially important for the HSD samples: compared with the PLD bilayer (figure 7.6c) the surface height distribution of the HSD samples (figure 7.6d) are asymmetric and deviate from a Gaussian distribution. Similar parallels have also been found for other thin film systems [97]. Therefore, it is not possible to model the surface roughness by a single rms roughness parameter.

The errors on the fitted parameters given in table 7.1 are estimated by determining their influence

on the simulation by varying the parameters. This becomes difficult for parameters that are coupled to each other like some of the roughness parameters. Since the layer thicknesses are almost independent of all other parameters and due to the very good agreement between data and simulations, the thicknesses can be determined very accurately. This is important for the analysis of the PNR data (section 7.3).

Summarizing, single crystalline  $\text{La}_{0.66}\text{Sr}_{0.33}\text{MnO}_{3-\delta}$  single and  $\text{La}_{0.66}\text{Sr}_{0.33}\text{MnO}_{3-\delta}/\text{SrTiO}_3$  bilayers have been prepared by both, PLD and HSD. The stoichiometric ratios between La, Sr and Mn have been proved to agree with the nominal values within the experimental error of the RBS measurements. The structural properties (layer thicknesses, roughnesses, inhomogeneities) have been determined XRR and AFM.

**Table 7.1:** Summary of the XRR measurements

Listed are the rms-roughnesses  $\sigma$  and layer thicknesses  $d$  of the substrate (*sub*), the LSMO layer, the STO layer and of the surface layer (*surf*). In addition, the surface roughnesses determined by AFM and the width of the Gaussian to model the thickness inhomogeneity are listed.  $\sigma_{inhom}$  is given in percent of the total layer thickness. The FOM has been calculated from formula (7.1). For all additional parameters see Appendix, section A.

	PLD	HSD		
		1.0 mbar	0.8 mbar	0.6 mbar
$\sigma_{sub}$ [Å]	2.4 (5)	3.0 (5)	4.4 (5)	2.0 (5)
$d_{LSMO}$ [Å]	85 (2)	87 (2)	105 (1)	177 (2)
$\sigma_{LSMO}$ [Å]	2.0 (5)	4.5 (5)	16 (2)	21 (3)
$d_{STO}$ [Å]	72 (2)	60 (2)	-	-
$\sigma_{STO}$ [Å]	2.5 (5)	4.4 (5)	-	-
$\sigma_{surf}$ [Å]	4.2 (5)	12 (1)	3.3 (5)	2.0 (5)
$\sigma_{AFM}$ [Å]	2.2 (1)	10.1 (4)	22 (1)	25 (1)
$\sigma_{inhom}$ [%]	6.8 (4)	5.0 (3)	5.6 (4)	3.9 (3)
$FOM$ [ $10^{-3}$ ]	0.66	1.95	2.69	2.93

## 7.2 Sizeable Exchange Bias induced by oxygen deficiencies

Since it is very hard to determine the oxygen stoichiometry of samples accurately - especially by a non-destructive method - information on the oxygen content can only be obtained indirectly. One possible way is to analyze the crystal structure and compare it with stoichiometric samples. For LSMO thin films it is well known, that oxygen deficiency leads to a shift of the pseudo-cubic out-of-plane lattice constant<sup>1</sup> to larger values [104], which can in principle be determined by  $\theta/2\theta$  scans. However, there are some obstacles in determining the out-of-plane lattice constant of a single LSMO thin film deposited on STO. Due to the very similar lattice structure and lattice parameters (bulk STO: 3.905 Å, pseudo cubic lattice constant of bulk LSMO: 3.875 Å), the thin film Bragg reflections always are close to a substrate reflection. Since the Bruker reflectometer offers the highest incident x-ray intensity of the three instruments used in this work, it would in general be the first choice to measure the weak out-of-plane reflections of the single LSMO thin films. But the proximity of the layer reflections to the substrate peaks makes the analysis

<sup>1</sup>In what follows, all notations and discussions of the LSMO thin films refer to the pseudo-cubic unit cell structure.



impossible on a instrument without monochromator: the out-of-plane layer reflection vanishes in the huge background created by Bremsstrahlung (figure 7.7). Therefore, the out-of-plane parameters have been measured on the Bruker four-circle-diffractometer located at CNM. The measurements with the monochromatic Cu  $K_\alpha$  radiation uncover the layer reflections, which first of all gives the important information that the layers have been grown epitaxially. However, it comes for the prize of a drastically reduced incident intensity (almost three orders of magnitude) compared to the reflectometer. In addition, to separate the substrate and layer peak as much as possible, reflections at high  $Q$  values should be investigated, which further diminishes the intensity. Hence the signal-to-noise-ratio of the layer reflection is reduced to values as small as 2 for some samples (figure 7.7 blue curve), which increases the measurement time significantly. Furthermore, any additional thickness oscillations can not be revealed, as they vanish in the background. Using formula (4.2) it still is possible to simulate the  $\theta/2\theta$  scans taken on the CNM diffractometer and determine the out-of-plane lattice constant of the single layers. Due to the superposition with the additional reflection from the STO cap layers, the simulation is more difficult for the PLD and HSD bilayers, which so far hinders the determination of the lattice constants.

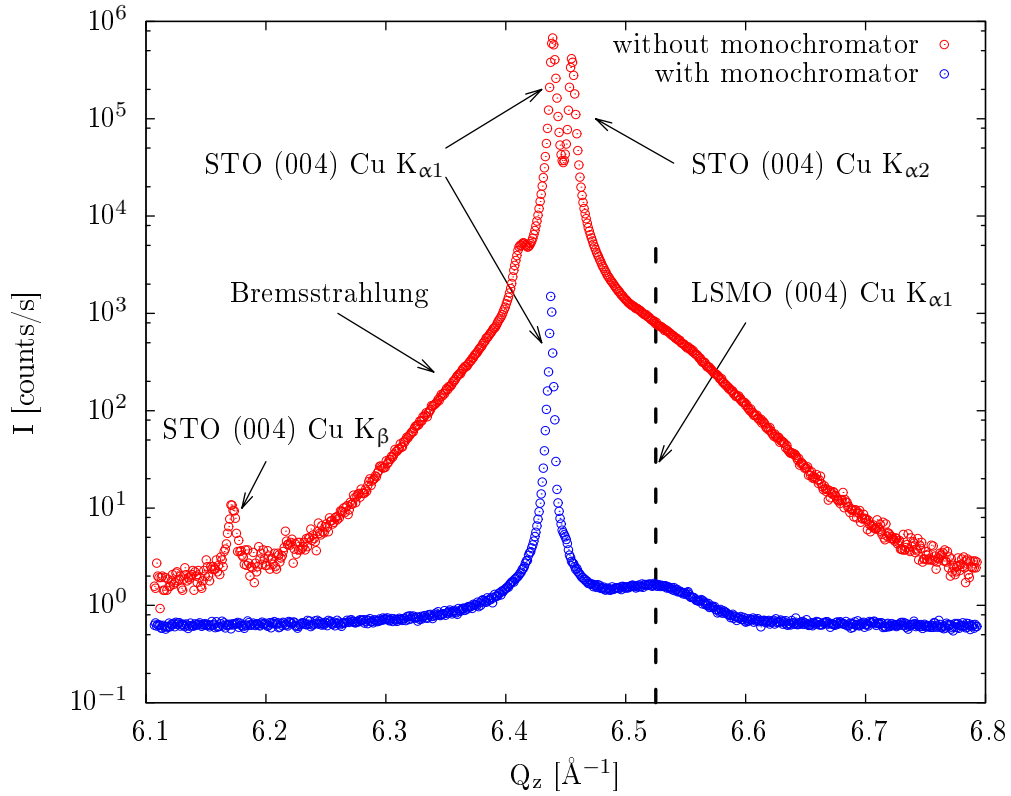


**Figure 7.7:**  $\theta/2\theta$ -scan around the (004) reflections of STO and LSMO. Red: data taken on Bruker reflectometer without monochromator. Blue: data taken on Bruker diffractometer with monochromator

Figure 7.8 shows the results of the fits for the two single layers grown by HSD at 0.8 and 0.6 mbar of the STO and LSMO (004) reflections (solid lines). The LSMO layer peak is clearly shifted to smaller  $Q_z$  values for the sample grown at 0.6 mbar and strongly merges with the substrate reflection. The increase of the out-of-plane lattice constant has been reported numerous times for

oxygen deficient manganite films [104–107]. It is generally attributed to the change of the  $\text{Mn}^{3+}$  to  $\text{Mn}^{4+}$  ratio: in oxygen deficient films  $\text{Mn}^{4+}$  is substituted by  $\text{Mn}^{3+}$ . Thus, the larger  $\text{Mn}^{3+}$  ions cause the lattice to expand resulting in the larger out-of plane lattice constant [105]. Therefore, the XRD measurements indicate that the oxygen content in the LSMO layers can be controlled by the oxygen pressure during the HSD growth. The fits give out of plane lattice parameters of  $3.876(4) \text{ \AA}$  and  $3.841(4) \text{ \AA}$  for the samples grown at 0.6 and 0.8 mbar, respectively. In addition, the width of the reflection is determined by the layer thickness of LSMO. It gives  $72(2) \text{ \AA}$  and  $136(5) \text{ \AA}$  for the two samples. Both values are significantly smaller than the thicknesses determined by XRR ( $105 \text{ \AA}$  and  $177 \text{ \AA}$ , respectively). A possible explanation for the discrepancy might be that only a part of the layers is scattering coherently. This can occur due to lattice imperfections or also a different strain and hence lattice parameter in the region of the layers, that do not contribute to the main Bragg reflection. Therefore, a possible scenario for the diffraction from the single layers is that the peaks are caused by the major part of the layer, which is at least partially relaxed. In the data of the sample grown at 0.6 mbar one finds another hint supporting this explanation: there is additional intensity at higher  $Q_z$  values that cannot be represented by the simulation of the  $136 \text{ \AA}$  LSMO layer. The simulation of a roughly  $40 \text{ \AA}$  LSMO thin film - which is the missing thickness to the total measured LSMO layer thickness by XRR - with a smaller lattice constant of  $3.84 \text{ \AA}$  fits quite well to this additional signal. Hence the observed data might be explained by a  $177 \text{ \AA}$  LSMO layer grown on STO, where the first  $40 \text{ \AA}$  are under larger compressive strain and the remaining  $136 \text{ \AA}$  exhibit a larger out-of-plane lattice constant due to relaxation. Of course, the relaxation in the sample probably does not occur in this step like manner. It can be expected though, that even a more gradual transition might lead to similar observations. For the sample grown at 0.8 mbar such additional intensity at higher  $Q_z$  values is not visible. However, the main reflection already is much weaker than for the 0.6 mbar sample and also “missing” thickness compared with XRR is smaller, which probably causes the signal to vanish in the background even if it is present like in the other sample.

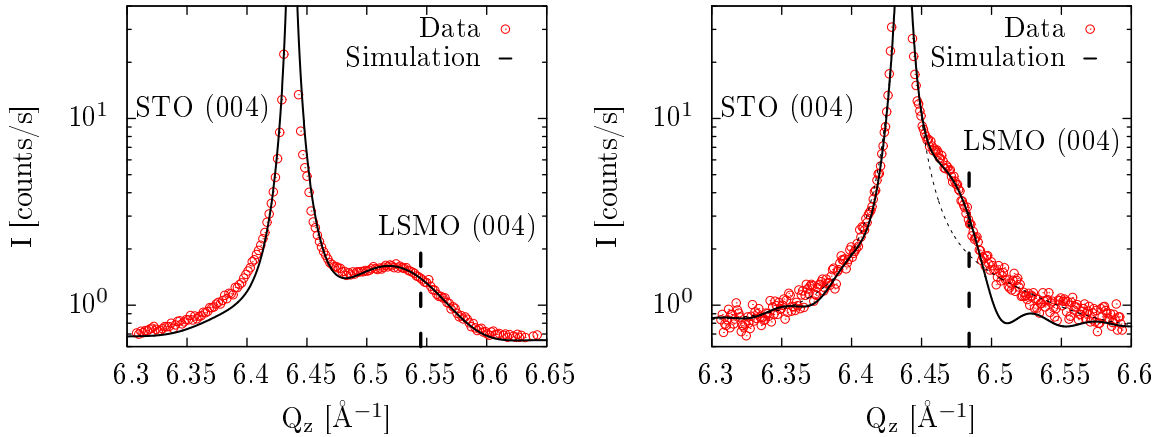


**Figure 7.8:**  $\theta/2\theta$ -scans around the (004) reflections of STO and LSMO. Fits are obtained by using the *plot.py* data evaluation software [108]. Left: LSMO single layer grown at 0.8 mbar. The fit yields an out-of-plane lattice constant of  $3.840 \text{ \AA}$ . Right: LSMO single layer grown at 0.6 mbar. The fit yields an out-of-plane lattice constant of  $3.876 \text{ \AA}$  (solid line). The corresponding positions of the LSMO (004) reflections are indicated, which seem to be shifted to higher  $Q_z$  values due to the merging with the substrate reflection. A possible explanation for the additional intensity at higher  $Q_z$  is a strained LSMO region at the STO interface (dashed line).

To analyze the in-plane lattice parameters, (HKL) reflections with non zero H or K need to be

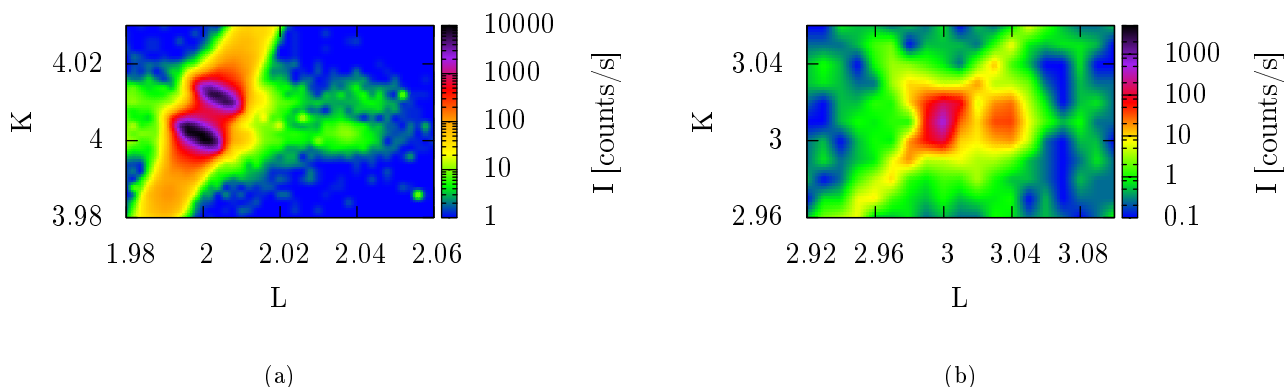


**Figure 7.9:** (0KL)-maps of a (a) LSMO/STO multilayer with 5 periods grown by PLD under the same conditions like the PLD bilayer discussed in this work and (b) a thick ( $\sim 1500$  Å) LSMO single layer grown by HSD. The K and L indices refer to the lattice parameter. In (a) the substrate reflection is splitted in a  $Cu-K_{\alpha 1}$  and  $Cu-K_{\alpha 2}$  reflection. The strong background in  $K = L$  direction is due to Bremsstrahlung. In (b) the splitting between  $Cu-K_{\alpha 1}$  and  $Cu-K_{\alpha 2}$  is not resolved, but the Bremsstrahlung background is visible as well. For both samples, the thin film reflection reveals the same K value - and hence the same in-plane lattice parameter - like the STO substrate indicating epitaxial growth. The L values are about 2.04 and 3.04 in (a) and (b), respectively. Data was taken on the Huber diffractometer without monochromator.

investigated. Since these reflections usually are weaker than the out-of-plane peaks - especially at the large  $Q$  values needed to separate the layer reflection from the substrate peak - quantitative analysis of the single and bilayers discussed in this work was not possible. However, measurements on two other samples lead to the conclusion, that the LSMO layers take on the in-plane lattice components of STO (figure 7.9): the (024) reflection of a multilayer prepared by PLD at the exact same conditions like the bilayer under investigation in this work, only with 5 periods of LSMO/STO, exhibits the same in-plane lattice parameter as the STO substrate. The same is true for a thick (about 1500 Å) LSMO single layer prepared by HSD. Both measurements suggest that also the samples under investigation are grown epitaxially by adopting the in-plane lattice constants of the STO substrate. The data shown in figure 7.9 has been taken on the Huber diffractometer, which is possible, since the LSMO reflections with in-plane component no longer are superimposed by the Bremsstrahlung. However, for the analysis of the single layers the intensity still is not sufficient, as it is some orders of magnitude smaller than the intensity of the Bruker reflectometer without monochromator.

Additionally to the determination of the lattice constants, the crystal quality of the LSMO single layers grown at 0.8 and 0.6 mbar can be estimated from the width of the rocking curves measured at the (004) reflection of the LSMO layers (figure 7.10). Good agreement to the measured curves was obtained by fitting Gaussian functions to the peaks. The obtained full-width-half-maxima (FWHM) for the samples grown at 0.8 and 0.6 mbar are  $0.0160(1)^\circ$  and  $0.0187(3)^\circ$ , respectively. These values are only about three times larger than the width of the substrate reflections, indicating a high crystal quality for both samples. It is also evident that the oxygen stoichiometry does not influence the structural quality of the samples drastically. It should be mentioned that even though a Gaussian function fits the peaks of the measurements very well, a broad low intense Lorentzian needs to be added to the Gaussian to model the broad background of the peaks. This additional contribution most probably is caused by the nearby substrate reflection.

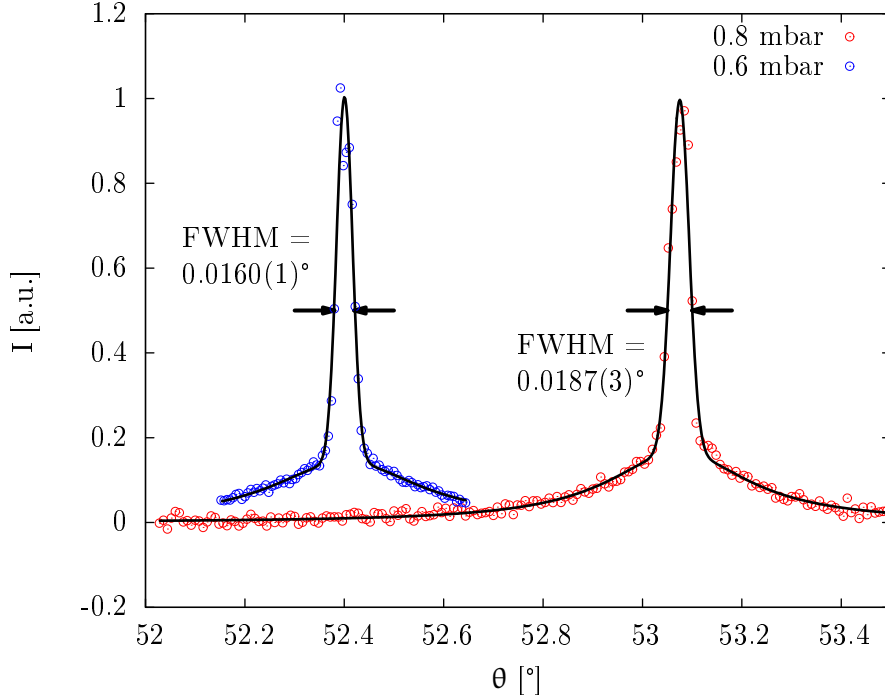


**Figure 7.10:** Rocking curves ( $\theta$ -scans) around the (004) reflections of the LSMO single layers grown at 0.8 and 0.6 mbar. Small FWHM indicate high crystalline quality for both samples. The broad Lorentzian-shaped background is probably caused by the nearby substrate reflection.

Besides the influence of the crystal structure, it is also well known, that oxygen deficient ferromagnetic manganites exhibit lower Curie-temperatures  $T_C$  than stoichiometric samples [59, 109, 110]. Ju and Sohn [109] interpret this effect on the basis of magnetic inhomogeneities in the LSMO layer. Instead of having a continuous ferromagnetic magnetization below the Curie temperature, they propose that different ferromagnetic regimes (spin clusters) are not aligned perfectly parallel and are maybe even separated by nonmagnetic regions, where  $\text{Mn}^{3+}$  ions accumulate. This inhomogeneous structure then gives rise to a smaller magnetic coupling and hence a lower Curie temperature. Since these inhomogeneities only occur in oxygen deficient LSMO layers, the determination of  $T_C$  is another reliable method to detect deficiencies indirectly. Therefore, temperature scans from 5 to 340 K in 0.5 mT during heating after cooling in a magnetic field of 1 T have been performed in the Quantum Design PPMS device. The temperature scans reveal a strong dependence of the Curie-Temperature  $T_C$  on the oxygen pressure during preparation: For the PLD grown samples and the sputtered samples grown at high oxygen pressure  $T_C$  is approximately 320 K. With decreasing oxygen pressure during sample preparation  $T_C$  decreases continuously down to 57 K for the sample grown at 0.6 mbar (figure 7.11). The values for  $T_C$  have been estimated by linear extrapolation to the x-axis. In addition to the decreasing Curie-temperature the temperature dependent behavior below  $T_C$  for the samples grown at 0.8 and 0.6 mbar differ from typical ferromagnetic materials. Similar effects have been observed for oxygen deficient  $\text{LaCaMnO}_3$  films, which according to the authors showed spin-glassy behavior and again can be interpreted on the basis of the inhomogeneity model [109, 110].

Even though the temperature dependent behavior seems to differ from standard ferromagnetic behavior for the samples grown at low oxygen pressures, all samples are clearly ferromagnetic below  $T_C$ : All samples show ferromagnetic hysteresis loops at low temperatures. Figure 7.12(b) compares the hysteresis curves at 5 K for the different samples. Two important results can be

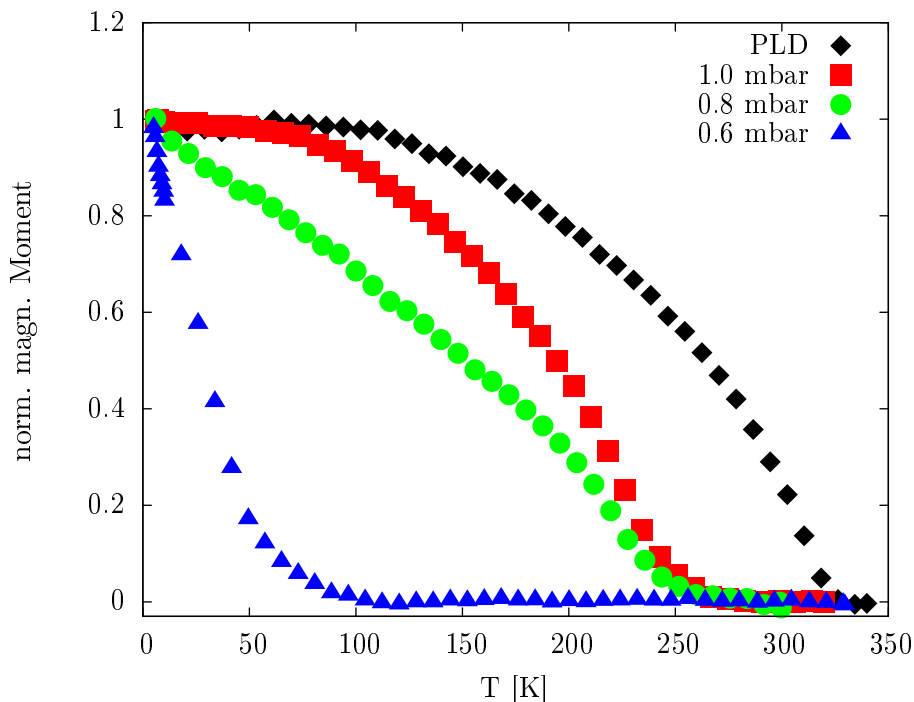


**Figure 7.11:** Temperature scans at 0.5 mT. The magnetic moment has been normalized to the moment at 5 K.  $T_C$  drops significantly with decreasing oxygen pressure during growth.

extracted from the hysteresis measurements: First of all we observe an increase of the coercive field with decreasing oxygen pressure during sample growth from 5 mT for a sample grown by PLD to 120 mT for the sample grown by sputtering at a oxygen pressure of 0.6 mbar. The increase in coercivity is a further well known effect not only in oxide systems, but in general inhomogeneous ferromagnets [111, 112]. The second result is the presence of an exchange bias effect in the samples grown at oxygen pressures of 1 mbar or smaller. Samples grown at higher pressures and the PLD samples do not exhibit an EB effect. Similar to the coercive fields, the exchange field  $H_E$  - i.e. the shift of the hysteresis curves - becomes bigger with decreasing oxygen pressure: It increases from 6 mT for the sample grown at 1 mbar to 29 mT for 0.6 mbar. Table 7.2 gives an overview of the results of the obtained values for the coercive and EB fields. The errors on the coercive and EB field values correspond to the accuracy of the instrument given by Quantum Design. Compared to these values the statistical errors of the measurement are much smaller.

Similar to the trm scans, there are also indications in the hysteresis measurements for deviations from purely ferromagnetic behaviour. the hysteresis curves suggest that the samples consist of different regions with different magnetic hardness: even though the coercive fields are smaller than 150 mT for all samples, it takes much higher fields (between 500 and 1000 mT) to saturate the samples. Even the not exchanged biased sample grown by PLD reveals such anomalous behaviour: at low fields soft and weak ferromagnetism can be seen, but at higher fields the hysteresis curves opens. These observances might also be explained by inhomogeneities in the magnetic structure of the LSMO layers. In different regions the ferromagnetic coupling might be weaker or stronger. It is also possible that regions, which order antiferromagnetically at low fields, are forced to order ferromagnetically at higher fields.

The temperature dependence of the coercive and EB field has been analyzed by taking hysteresis curves at different temperatures. Before each hysteresis measurement, the sample has been cooled

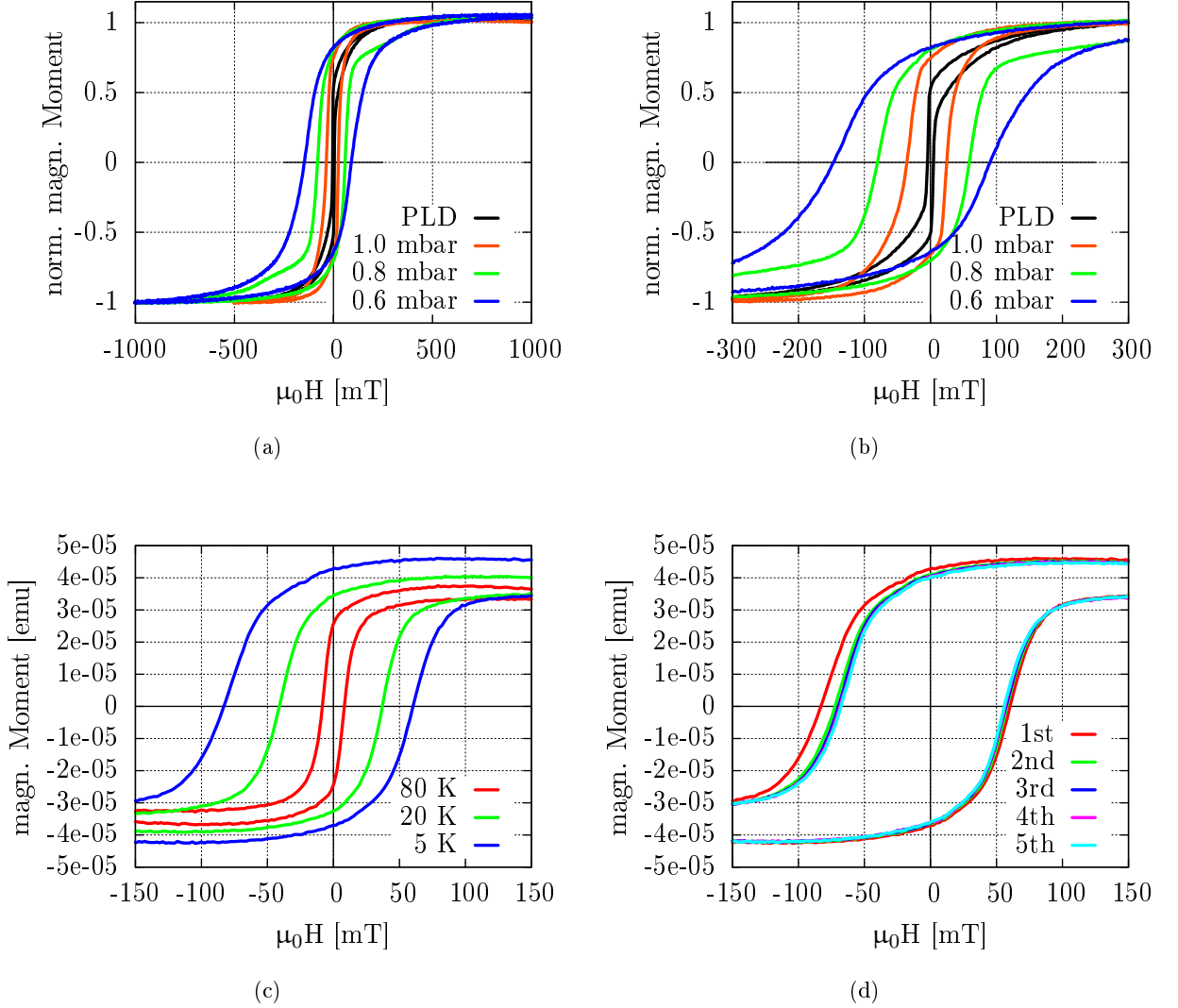


**Figure 7.12:** Hysteresis curve measurements. (a) Comparison of the hysteresis curves taken at 5K of the samples grown at different oxygen pressure measured after field cooling in 1 T. (b) The same data shown with a smaller field range to highlight the shift of the hysteresis curves.  $H_C$  and  $H_E$  values can be seen in table 7.2. (c) Temperature dependence of the coercive and EB field of the sample grown by HSD at 0.8 mbar. Before each hysteresis curve the sample has been cooled down in from room temperature in a field of 1 T.  $H_C$  and  $H_E$  values are listed in table 7.3.  $H_E$  vanishes around 50K comparable to the results of Zhu et al [1]. (d) Hysteresis curve measured several times at 5K for the sample grown by HSD at 0.8 mbar after field cooling in 1 T. A subsequent decay of the  $H_E$  is visible (training effect).

**Table 7.2:** Results of the VSM characterization.

Pressure [mbar]	$\mu_0 H_E$ [mT]	$\mu_0 H_C$ [mT]	$T_C$ [K]
PLD	0(1)	5(1)	320(2)
1.0	6(1)	31(1)	252(3)
0.8	7(1)	65(1)	249(3)
0.6	29(1)	119(1)	57(5)

down from room temperature in a field of 1 T with a rate of 2 K/min (figure 7.12(c)). The data are in agreement with the results reported by Zhu et al. The EB field occurs at temperatures below 50 K and increases with decreasing temperature (table 7.3). The samples also shown the well known training effect as can be seen in figure 7.12(d), where the hysteresis curve is measured several times at 5 K. The EB field decreases subsequently, but is still not vanished completely after 5 measured cycles.

**Table 7.3:** Temperature dependence of the exchange bias and coercive fields of the sample grown by HSD at 0.8 mbar. The corresponding hysteresis curves are shown in figure 7.12(c).

Temperature [K]	$\mu_0 H_E$ [mT]	$\mu_0 H_C$ [mT]
80	1(1)	84(1)
40	8(1)	209(1)
20	20(1)	391(1)
10	53(1)	420(1)
5	114(1)	716(1)

In summary, XRD and PPMS data both reveal typical results for oxygen deficient LSMO layers. The size of the oxygen deficiencies can be controlled by the oxygen pressure during HSD. However, changing the oxygen content does not influence the structural quality of the layers. Furthermore, it was possible to reproduce the results reported by Zhu et al and link them to the oxygen deficiencies present in the samples. Several hints similar to the results by Ju and Sohn have been observed which possibly are due to an inhomogeneous ferromagnetic structure in the LSMO layers. However, the question still remains, how the EB effect can be present in a system with no nominal antiferromagnetic material especially since it has not been observed in oxygen deficient bulk LSMO.

### 7.3 Drastically reduced magnetization at LSMO/STO interfaces in EB samples

In order to obtain an EB effect an antiferromagnetic region needs to be present somewhere in the samples. Therefore, the magnetic depth profile has been analyzed depth dependent by the two complementary experimental techniques PNR and XRMS (for the theoretical description see chapter 4.3, the instruments are introduced in chapter 6.3).

PNR data has been taken at two different temperatures: at 340 K, i.e. above the Curie temperature, and at 5 K after field cooling in 1 T. During the measurements a field of 1 T was applied

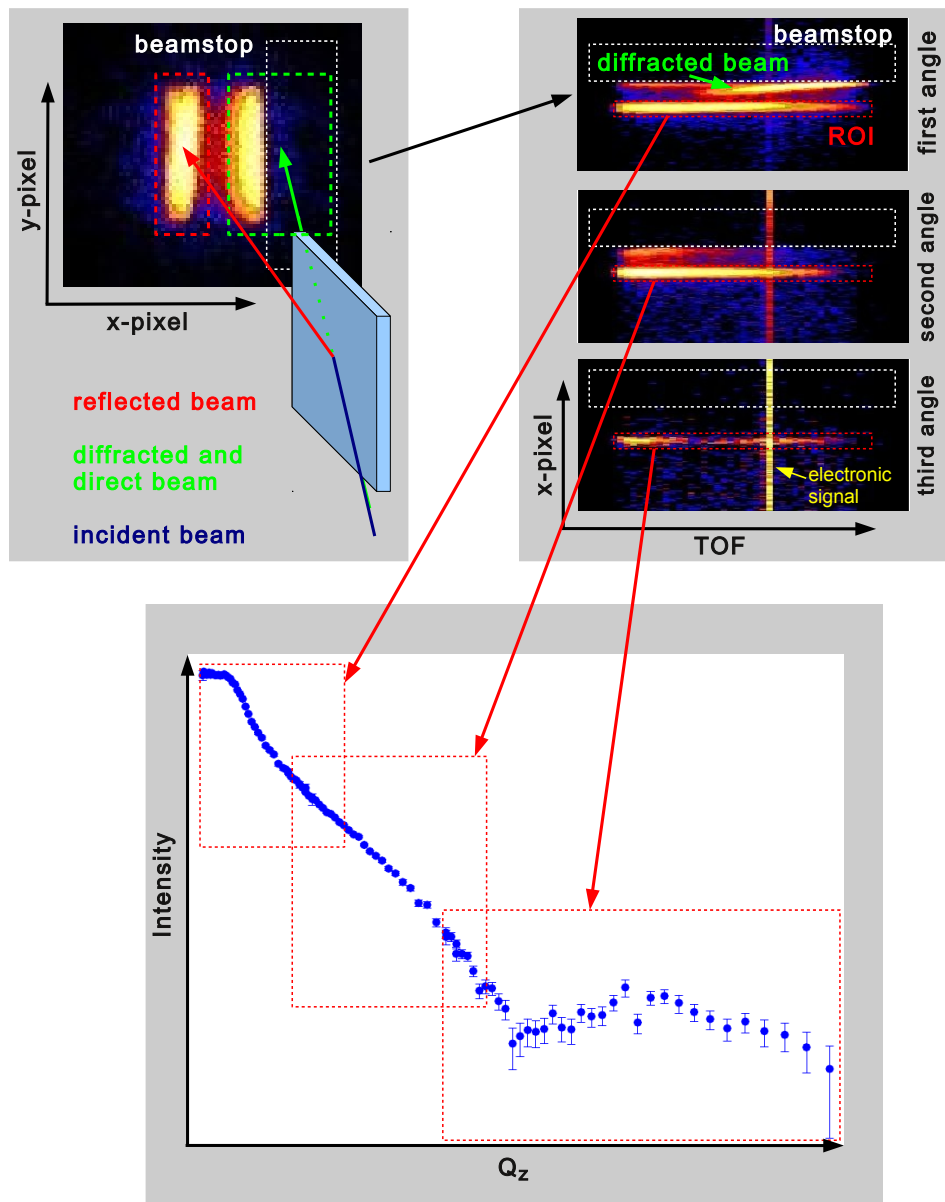


**Figure 7.13:** Overview of the SNS data reduction procedure. Top left: raw data picture on the 2-dimensional position sensitive detector. The angle of reflection can be calculated from the x-pixel position (the farther to the left, the larger the angle of reflection). The red rectangle indicates the reflected signal, the green one the direct (the part of the primary beam which passes the sample) and diffracted beam. The direct beam is mostly shaded by the beamstop (white rectangle). Top right: the same raw data set, but shown in x-pixel versus TOF (first angle,  $\theta = 0.2^\circ$ ). Also shown are the measurements at the two other angles  $\theta = 0.4^\circ$  and  $\theta = 0.8^\circ$ . In the first angle picture the diffracted beam can clearly be seen. In the third angle measurement thickness oscillations already are visible in the reflected signal. An error signal is caused by the instruments electronics and is related to the chopper rotation speed (therefore, it always is at the same TOF pixel). This error signal is eliminated by subtraction of the data to the background. The region of interest (ROI) is shown for all three angles. Bottom: the raw data within the ROI for every angle is reduced and transferred to the corresponding  $Q_z$  values. The measurements at different angles can be combined by matching them in the overlap regions to obtain a single reflectivity curve.



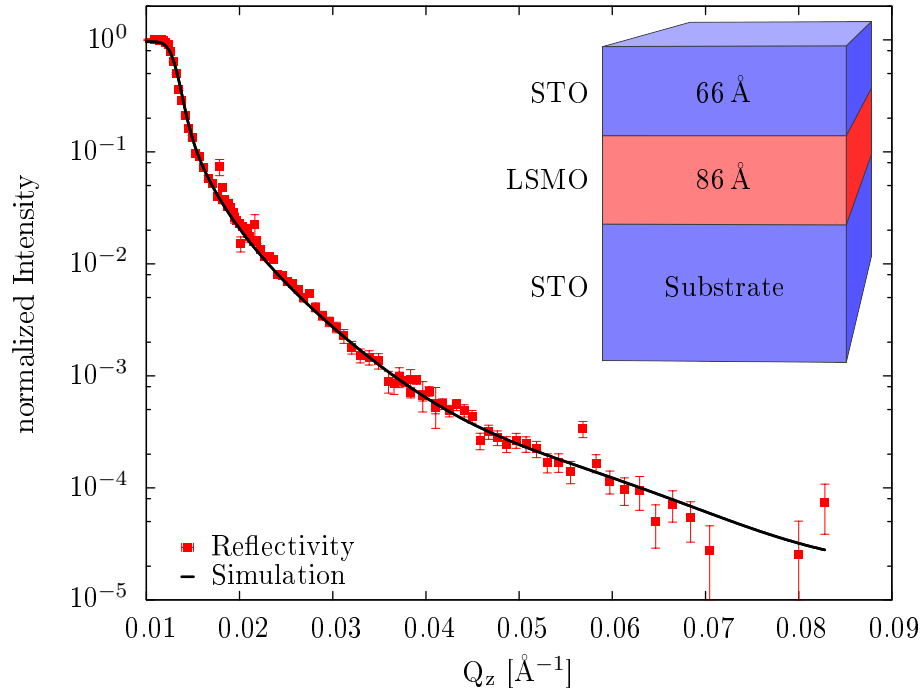
to saturate the magnetization of the sample. As discussed in the experimental chapter, the desired  $Q_z$  range can not be covered at one incident angle due to the limitation of the neutron wavelength distribution of 3 Å. Therefore, at each temperature the reflected intensity has been measured time resolved at three different incident angles ( $\theta = 0.2, 0.4$  and  $0.8^\circ$ ). Figure 7.13 gives an overview of the data reduction procedure. The neutrons are detected spatially resolved in x-direction (which is related to the reflection angle) and y-direction as well as time resolved as a function of the time-of-flight from the moderator to the detector. A region of interest (ROI) is chosen in x-direction that covers the reflected signal. The angle of reflection is calculated from the center position of the reflection in x-direction. For every single time point the intensities within the ROI are summed up along the x-direction (data reduction). The corresponding  $Q_z$  value is calculated from the TOF and the angle of reflection (which is equal to the incident angle). The three incident angles are chosen in a way that the data overlaps a little bit in  $Q_z$ . By combining the data sets taken at different incident angles with the correct scaling factors given by the overlap regions, one obtains a single reflectivity curve covering the  $Q_z$  range from the plateau of total reflection (smallest  $Q_z$  values of the first angle) up to the largest  $Q_z$  values of the measurement at the third incident angle.

Figure 7.14 shows the PNR data for both temperatures 340 and 5 K of the LSMO/STO bilayer prepared by PLD which did not show an EB effect in the macroscopic data analysis. Since the measurement at 340 K was performed above the Curie temperature of the sample, no difference between different spin channels was expected. Hence, to increase the incident neutron beam intensity in order to save time, the measurements at 340 K have been performed with an unpolarized beam. There are hardly any thickness oscillations visible in both, the experimental data and the simulation. This is not surprising, since above the Curie-temperature the contrast between the materials simply is the difference in nuclear scattering length densities. For bulk LSMO and STO these values are  $3.68 \text{ \AA}^{-2}$  and  $3.53 \text{ \AA}^{-2}$ , respectively, hence the contrast is very small. Even though this fact makes it impossible to determine the chemical layer thicknesses in the sample from the high temperature measurements, the big advantage is that at low temperatures all thickness oscillations are caused by the magnetic profile in the sample. The high temperature data can be used to some extent to determine the nuclear scattering length densities in the sample: the critical edge for total reflection in the samples under investigation in this work is mostly determined by the nuclear scattering length density of the substrate. This is different to XRR, where the density of the top layer of the sample determines the position of the critical edge. The reason for the difference is the much smaller interaction potential for PNR in addition to the very thin layers in the samples used in this work<sup>2</sup>. Therefore, the nuclear scattering length density of the STO substrate is determined by the critical angle. This value then also determines the NSD for the layer materials, as they need to be close enough to the substrate value to avoid thickness oscillations to become visible. Hence, the high temperature measurement can only be used to check, whether the substrate NSD and subsequently all other NSD are in agreement with the bulk values. Since the layer thicknesses also cannot be determined by the high temperature data, in fact the low temperature data has been analyzed first. Then by setting the magnetic scattering length densities to zero, it has been checked, whether the structural results (chemical layer thicknesses and roughnesses) are in agreement with the data at 340 K as well.

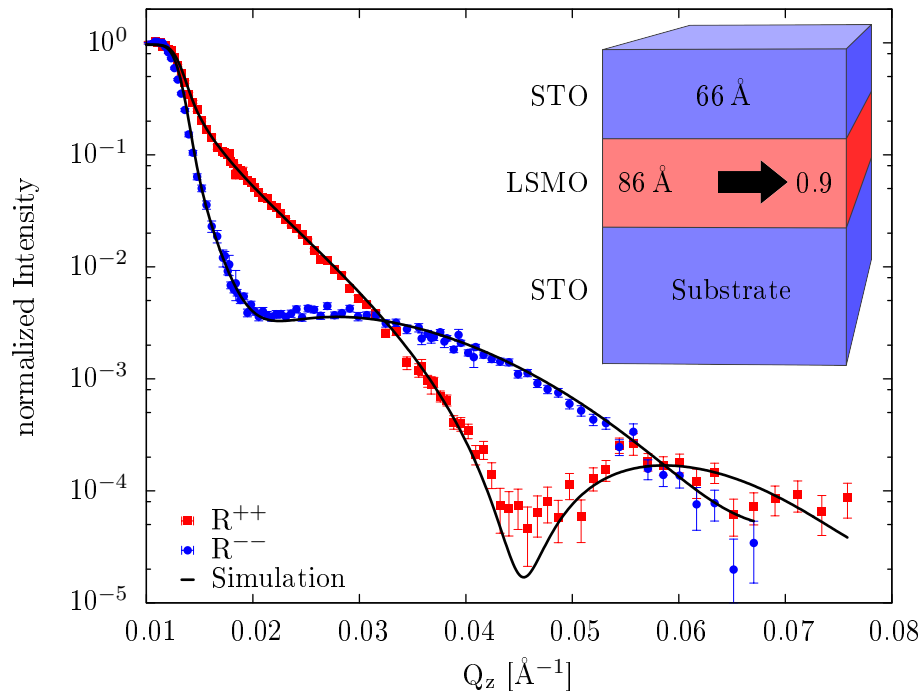
The experimental data at 5 K and the corresponding simulations for the bilayer grown by PLD are shown in figure 7.14(b). There is a strong difference between the  $R^{++}$  and  $R^{--}$  channel at this temperature caused by the magnetic profile of the sample. Oscillations are visible from which the FM layer thickness can be deduced. The best fit to the data is obtained for a  $86 \text{ \AA}$

---

<sup>2</sup>Note that the situation might be different for thick layers and especially for multilayer systems. In these cases there might be so much material on top of the substrate that the critical edge for total reflection is influenced significantly by the scattering length densities of the layer materials.



(a)



(b)

**Figure 7.14:** PNR data of the PLD sample. Top: 340 K data measured with an unpolarized beam at 1 T. Bottom: 6 K data taken at 1 T. The thicknesses indicated are determined by the simulation of the low temperature reflectivity data. The arrow indicates a layer with non zero magnetic scattering length density, where the number to the right gives the fraction of the maximum theoretical value. Detailed results can be found in table 7.4.

thick FM layer having a magnetic scattering length density close to the bulk value of LSMO (90 %) and a 66 Å thick (macroscopically) nonmagnetic layer on top. Even though we can not clearly identify the chemical interfaces between LSMO and STO by PNR, the ferromagnetic layer thickness matches perfectly the LSMO layer thickness determined by XRR. From that we can conclude that the complete LSMO layer is ordered ferromagnetically at 5 K and 1 T. In addition, the thickness of the nonmagnetic layer on top of the FM layer is slightly smaller, but very close to the STO thickness resulting from the XRR experiment. The roughnesses determined by PNR are slightly higher than for XRR, but still ranging around 1 nm. It also needs to be mentioned that the error on the roughnesses is much higher than for the XRR data, since the PNR data are much less sensitive on these parameters. The nuclear scattering length densities are not kept fixed at the bulk values as it was done for the XRR analysis. They seem to be slightly smaller in general - a fact which is true for all further samples as well: For all fits the values range between  $3.1 \text{ \AA}^{-2}$  and  $3.5 \text{ \AA}^{-2}$  which looks like a rather large discrepancy to the bulk values. However similarly to the roughnesses, the error on these values is rather large: The angle of reflection is calculated from the x-pixel where the center of the ROI for the data reduction is located. If for example the center of the ROI is shifted by just one channel for the smallest angle measurement, the nuclear scattering length density of the substrate already changes more than  $0.3 \text{ \AA}^{-2}$ . In order to keep the contrast constant, the NSD for the layers will shift accordingly. The setting of the center of the ROI is not the only possible source for a systematic error on the NSD: The incident angle (or angle of reflection) is calculated from the center of the ROI and the position of the primary beam. The channel number of the center of the primary beam is determined before the beamtime and underlies the same reading error as the center of the ROI. Even though it has been checked from time to time during the beamtime the primary beam position might also slightly shift - even a change of only half a channel would add something around  $0.16 \text{ \AA}^{-2}$  to the systematic error on the NSD. Taking these considerations into account, the determined differences of the NSD to the bulk values are within the errorbars of the experimental data.

Summarizing, in the LSMO/STO bilayer grown by PLD which does not exhibit an EB effect, a completely ferromagnetically ordered LSMO has been found at 5 K by PNR. All other parameters are in good agreement with the XRR results and show the expected behavior. The data taken above the Curie-temperature can be simulated with exactly the same parameters by just setting the magnetic scattering length density of the ferromagnetic layer to zero (figure 7.14(a)).

The PNR data taken at 5 K of the single layer grown by HSD at 0.8 mbar is shown in figure 7.15. In contrast to the results for the bilayer grown by PLD the best fit for this sample results in a ferromagnetic layer thickness which is about 10 Å smaller than the LSMO thickness determined by x-ray-reflectometry (95 and 105 Å, respectively). Due to the almost equal NSD of LSMO and STO, again we can only conclude by comparison with the XRR result that about 10 Å of LSMO at the interface to the STO substrate are not ordered ferromagnetically, but are macroscopically nonmagnetic - which does not rule out an antiferromagnetic order. In order to emphasize that this effect is significant and detectable by PNR, figure 7.15(b) shows the best possible fit for the case of a 105 Å ferromagnetic LSMO layer. The data also reveals that the ferromagnetic layer is on top of the LSMO layer and the nonmagnetic layer at the interface to the STO substrate. The other way around - i.e. a non magnetic layer on top of a 95 Å ferromagnetic layer of LSMO - also leads to a clearly different situation. This can also be shown by comparison of the *FOM* parameters for the different models. Like for XRR, the same expression for the *FOM* has been used to fit the data (formula (7.1)). A value of 6.64 is obtained for the best fit. In contrast, the smallest *FOM* for a completely ferromagnetic LSMO layer is 13.7. For a non magnetic layer on top of the LSMO layer the best fit yields a *FOM* of 16.0, which means that for both alternativ models the *FOM* is more than two times larger than for the best fit. The *FOM* values obtained for the ONR data are in general larger than the ones determined by XRR due to the larger

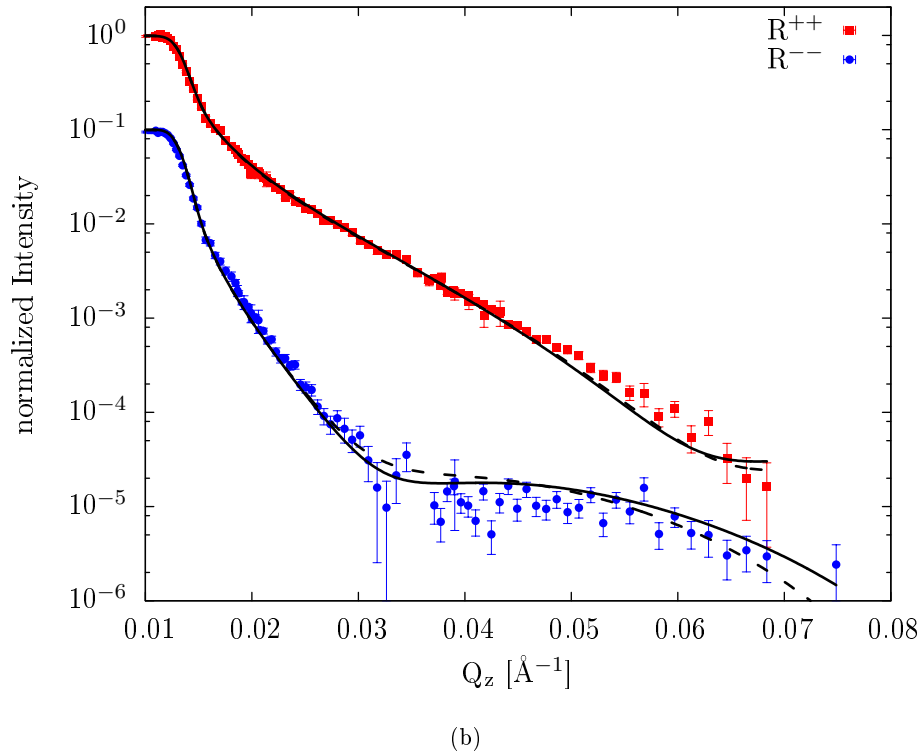
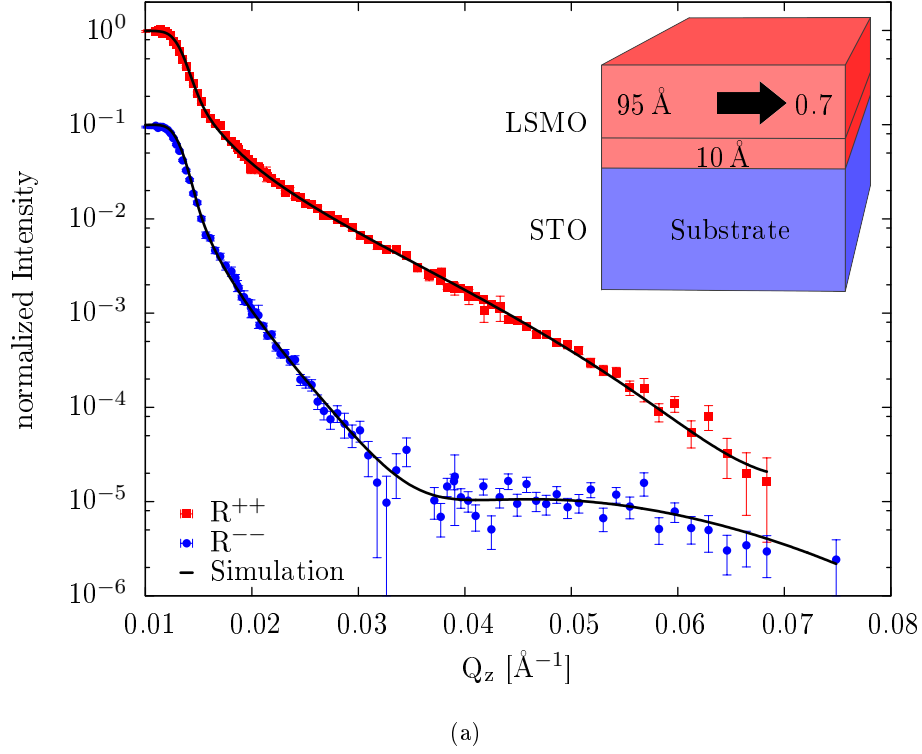


**Figure 7.15:** PNR data of the HSD sample grown at 0.8 mbar. The  $R^{--}$  data are divided by 10 for better visibility. Top: 6 K data taken at 1 T. The thicknesses indicated are determined by the simulation of the PNR data. The arrow indicates a layer with non zero magnetic scattering length density, where the number to the right gives the fraction of the maximum theoretical value. Detailed results can be found in table 7.4. Bottom: Two alternative simulations are shown to emphasize the significant difference to the best fit profile: one for a completely ferromagnetic LSMO layer (solid line) and one for a nonmagnetic LSMO layer on the top of the LSMO layer at the interface to air (dashed line).

statistical error bars on the experimental data.

Like for all other samples the NSD of LSMO and STO are slightly smaller than the bulk values, but within the errorbars as discussed before. The roughnesses again are slightly higher than the XRR results. The magnetization of the ferromagnetic part of the LSMO layer is significantly smaller than for the PLD sample. It is reduced to about 70 % of the bulk magnetic scattering length density. Besides the effects caused by oxygen deficiencies that have been discussed in the macroscopic sample analysis section, the reduction of the average magnetization is a further result known for oxygen deficient LSMO layers. It can also be explained in the framework of the cluster model for a magnetically non homogeneous LSMO layer [109].

The analysis of the other two HSD samples, the bilayer grown at 1.0 mbar and the single layer grown at 0.6 mbar, is much harder due to the smaller sample size of only  $5 \times 5 \text{ mm}^2$  compared to the size of the two other samples of  $10 \times 10 \text{ mm}^2$ . This automatically reduces the signal-to-noise-ratio of the PNR experiment by a factor of 4. Therefore, from the data taken on the bilayer grown at 1.0 mbar it is not possible to deduce, whether the entire LSMO layer is ordered ferromagnetically or not (figure 7.16). The *FOM* for the two cases are almost the same (12.3 and 11.9, respectively). The reason is that the significant points of the reflectivity curve, where both models could be distinguished, already are too close to the background level. A small difference between both simulation can only be seen around  $0.05 \text{ \AA}^{-1}$  in the  $R^{++}$  channel, which is just about the  $Q_z$  range, where the data drops to the background level. For a four times bigger sample this region still might be well above the background enabling to distinguish between both cases.

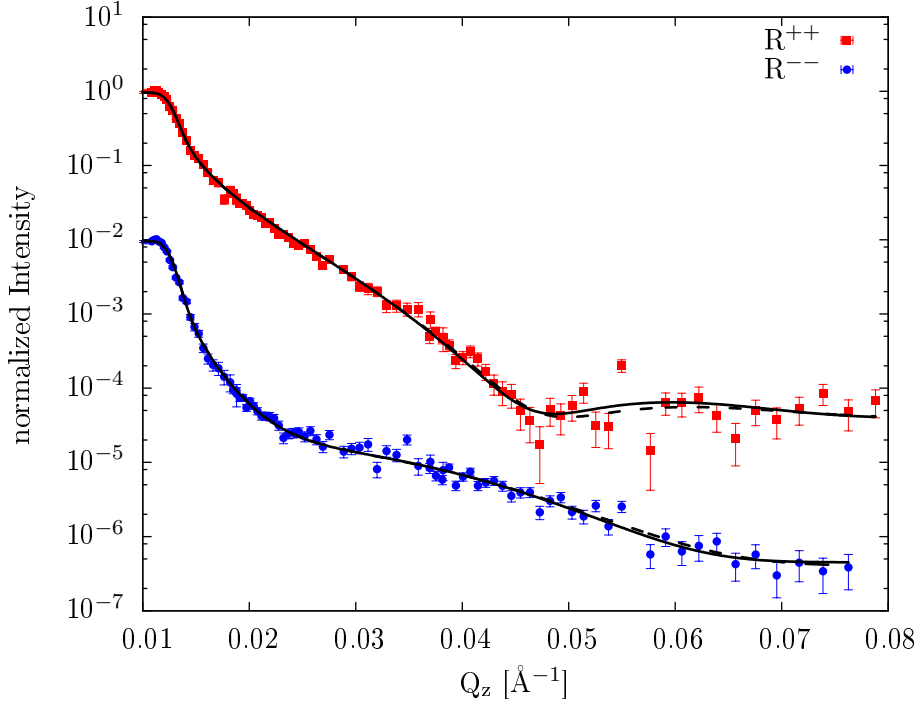


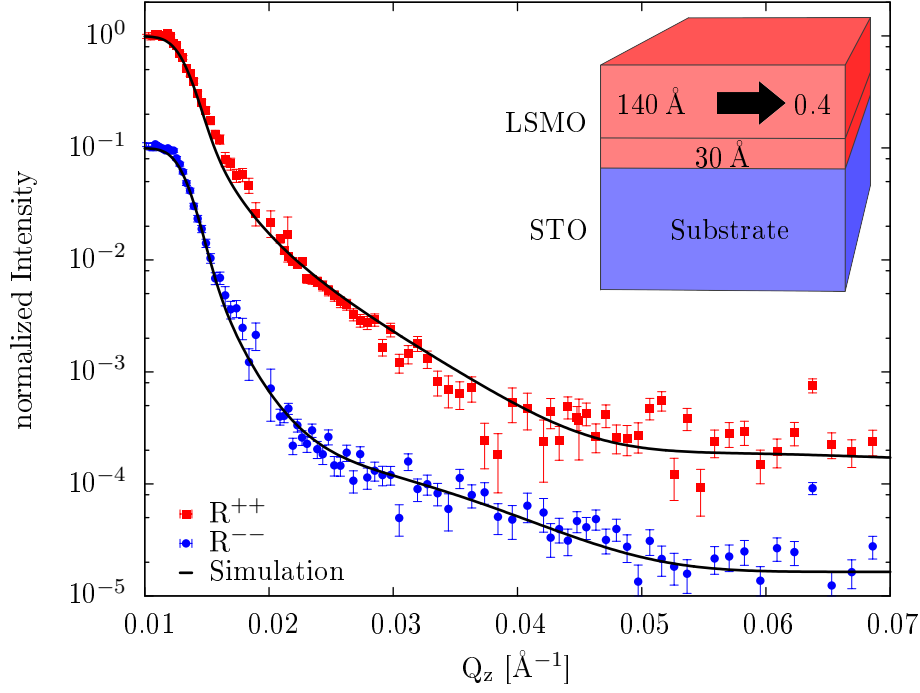
**Figure 7.16:** PNR data of the HSD sample grown at 1.0 mbar taken at 6 K and 1 T. The  $R^{--}$  data are divided by 10 for better visibility. The simulation of a completely ferromagnetic LSMO layer (solid line) and a non-magnetic LSMO layer at the interface to STO (dashed line) are shown. Due to the smaller signal-to-noise-ratio both cases can not be distinguished.

Even though the intensity problem also holds for the LSMO single layer grown at 0.6 mbar, there are some indications in the PNR data for a interface layer similar to the sample grown at

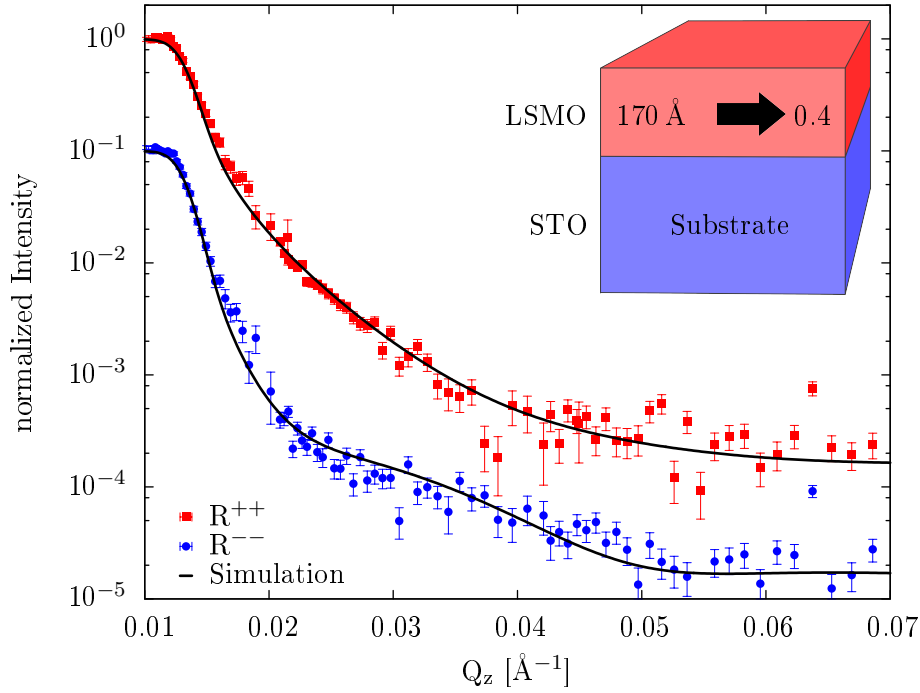
0.8 mbar (figure 7.17): The data - especially the  $R^{--}$  channel - is best resembled by a 140 Å thick ferromagnetic layer (figure 7.17(a)), i.e. the difference to the chemical thickness of the LSMO layer determined by XRR (170 Å) is even larger in this sample. In comparison to the single layer grown at 0.8 mbar the magnetic scattering length density of the ferromagnetic layer is further reduced to 35 % of the bulk value of LSMO. In addition to the intensity problem due to the sample size, the weak magnetic scattering and hence less pronounced oscillations further increases the problem of a weaker sensitivity to the magnetic depth profile. But even if the situation is not as clear as for the sample grown at 0.8 mbar, the simulation for a completely ferromagnetic LSMO layer does not reproduce the shape of the reflectivity curve as accurate as the fit with a thinner ferromagnetic layer. For the NSD and the layer roughnesses the same tendencies are found as for the previous samples. Since the macroscopic analysis already suggests that the oxygen deficiency of this sample is bigger than for the sample grown at 0.8 mbar, it is no surprise that the magnetic scattering length density of LSMO is further decreased down to only 35 % of the bulk value of LSMO. Some fraction of this reduction might also be due to the fact that this sample is not yet fully saturated at 6 K (figure 7.11). Even though the  $R^{--}$  channel indicates the presence of a non-magnetic interface region, it needs to be mentioned that the  $R^{++}$  channel is better reproduced by a completely ferromagnetic LSMO layer. This results in an almost identical  $FOM$  for the two cases (82.0 for the non-magnetic interface region, 81.7 for the completely ferromagnetic layer). It is therefore hard to tell from the PNR, how the situation exactly looks like in this sample. The much larger  $FOM$  compared to the other samples are mostly due to the larger statistical errors on the data points caused by the lower intensities.

Although a significant difference between the magnetic profiles in the samples without EB compared to the sample with EB grown at 0.8 mbar has been detected by PNR, XRMS measurements have been conducted as a complimentary method in order to confirm the small interface effects for the PLD sample and the HSD samples grown at 0.8 and 0.6 mbar. Data has been taken at about 20, 30 and 150 K to check the temperature dependence of the magnetic depth profile. At each temperature the reflected intensity of both, right and left circular polarized light, has been measured for three different angles of reflection, namely  $\theta = 5, 10$  and  $15^\circ$ . At each angle the incident energy has been scanned from 630 to 660 eV. This energy range covers both, the  $L_{II}$  and  $L_{III}$  edges of Mn. Since there always is a small difference between the initial intensities of the incident LCP and RCP x-ray beam, each measurement is performed at two opposing fields, i.e. at + and  $-50$  mT. By subtracting the XMCD signals of both measurements, the difference between the initial intensities is eliminated (see section 8.3). As presented in chapter 4.3.4, the sum of the reflected intensities of an incident LCP and RCP x-ray beam has been used to model the chemical structure of the samples (similar to non-resonant XRR). Thereafter, simulations including the magnetic structure of the samples have been done to reproduce the difference of both intensities, i.e. the reflected XMCD signal, according to formula (4.35). For the simulation indices of refraction  $n(E)$  and magneto-optical constants  $Q(E)$  have been used which have been determined from a LSMO "standard sample", a 60 nm thick LSMO film (the data can be seen in [102]). It was seen before, that no information on the chemical structure of the samples can be extracted from the PNR data due to the small contrast in nuclear scattering length densities. The huge advantage of the XRMS data is that it is very sensitive to both, the chemical and magnetic sample profile, at the same time.

In figure 7.18 the temperature dependence of the XMCD signal is shown for the measurements at  $\theta = 10$  deg of the sample grown by HSD at 0.8 mbar. It can be seen, that the strength of the signal decreases with increasing temperature. This corresponds to the drop of the total magnetic moment of the sample with increasing temperature (figure 7.11). A quantitative comparison of the VSM and XRMS data dependence is difficult due to the fact that the temperature in the XRMS chamber is not measured at the sample position. Especially at low temperatures, this



(a)



(b)

**Figure 7.17:** PNR data of the HSD sample grown at 0.6 mbar and 1 T. Top: best fit to the 6 K data. The  $R^{--}$  data are divided by 10 for better visibility. The thicknesses indicated are determined by the simulation of the reflectivity data. The arrow indicates a layer with non zero magnetic scattering length density, where the number to the right gives the fraction of the maximum theoretical value. Detailed results can be found in table 7.4. Bottom: Alternative simulation for the case of a completely FM layer.

Especially the thickness oscillation visible in the  $R^{--}$  channel is shifted to too small  $Q_z$  values.

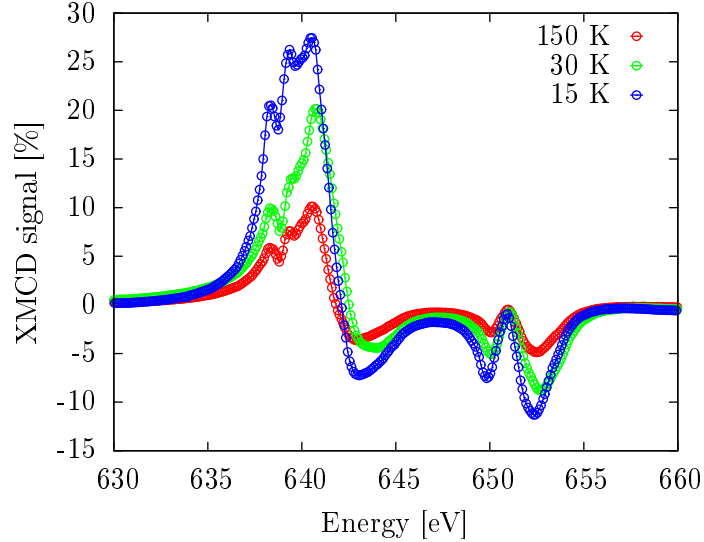


**Figure 7.18:** Temperature dependence of the XRMS signal at  $\theta = 10^\circ$  of the LSMO single layer grown by HSD at 0.8 mbar and 0.05 T. Like for all other XMCD plots, the reflected XMCD signal (difference of reflected intensities for an incident LCP and RCP x-ray beam) is given in percent of the average signal (sum of reflected intensities for an incident LCP and RCP x-ray beam)

results in quite a large errors on the temperature values up to  $\pm 10$  K given in this work. This hinders an accurate comparison of the temperature dependences determined by both methods. However, what can be said, is that the shape of the XMCD signal only changes marginally indicating that the magnetic depth profile apart from the scaling of the average moment remains the same<sup>3</sup>. The same results have been found for all other samples at all incident angles. Therefore, in the following only the data taken at 30 K will be discussed for the determination of the magnetic profile.

For the simulations a slab structure of the sample is defined representing the different layers. In addition to LSMO and STO layers, interface roughnesses and surface roughnesses can be modeled by introducing layers with a mixed index of refraction  $n(E)$  (and possibly magneto optical constant  $Q(E)$ ). For example an interface roughness between an LSMO and an STO layer can be represented by a layer having an averaged index of refraction  $n(E) = (n_{lsmo}(E) + n_{sto}(E))/2$ . This is possible due to the fact that XRMS similar to XRR and PNR is not sensitive to the microscopic structure of the sample. In analogy, a surface roughness is introduced by averaging the index of the refraction of the top layer material with the value for air, i.e.  $n_{air}(E) = 1$ . In principle such surface and interface layers can be subdivided in several slabs in order to model concentration or roughness gradients, but for all samples under investigation in this work it turned out that this does not influence the simulated intensities significantly. Hence, a single surface layer was sufficient to model the experimental data. All results presented in this section have been determined by simulating the experimental data for all three incident angles simultaneously with the same chemical and magnetic structure for the respective sample. An overview and summary of the fit results for the LSMO layers obtained by XRR, PNR and XRMS for all samples is given in table 7.4.

As an example for the simulations of the average reflectivity - i.e. the sum of the reflected intensities for incident LCP and RCP x-rays - experimental data and simulations for the LSMO single layer grown by HSD at 0.8 mbar are shown in figure 7.19. The simulations yield an LSMO layer thickness of 91 Å. The layer thickness is composed of a 85 Å continuous LSMO layer plus

<sup>3</sup>the sensitivity of the XMCD scans to changes in the magnetic depth can be seen in figure 7.23



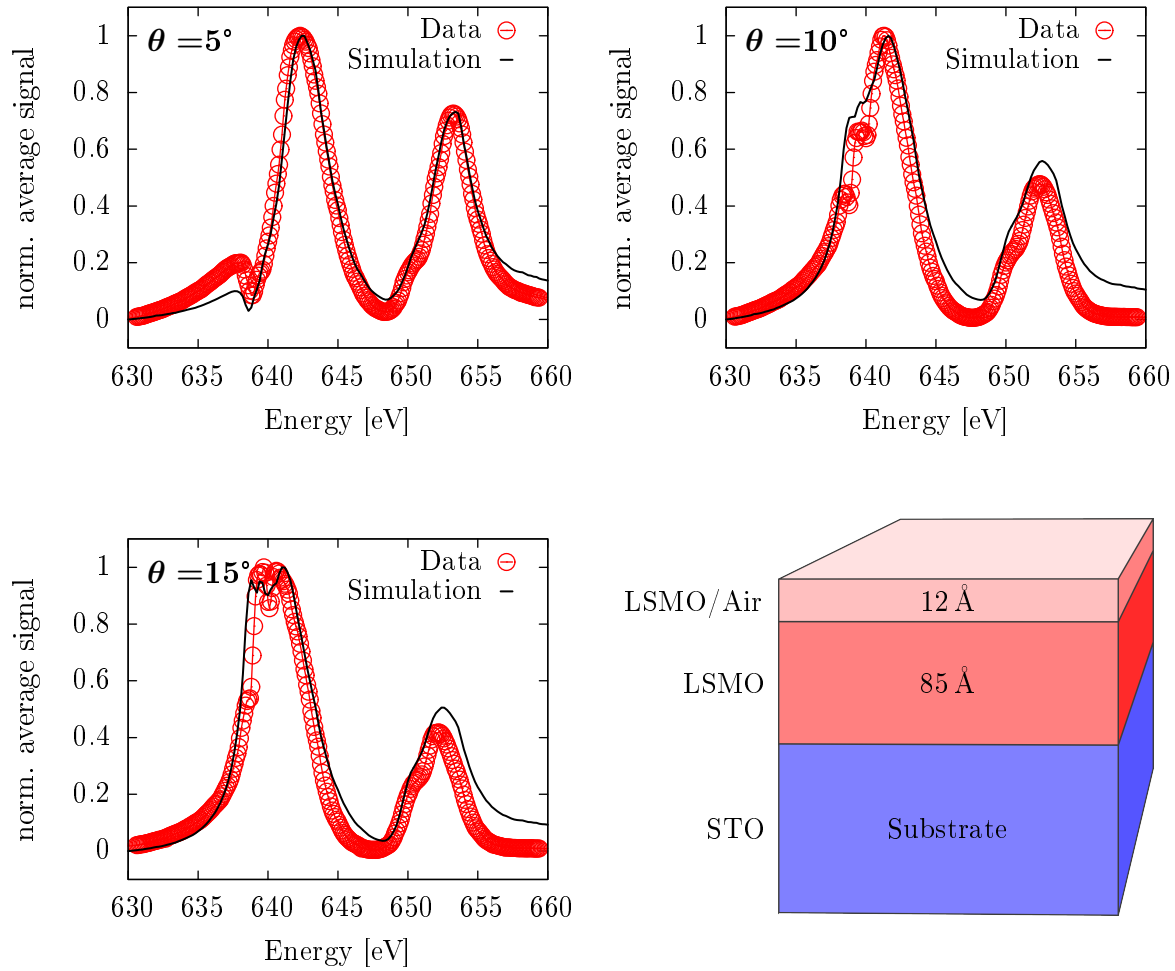


**Figure 7.19:** Average signal - i.e. sum of reflected RCP and LCP incident x-rays - of the LSMO single layer grown by HSD at 0.8 mbar for all three incident angles. The maxima at around 641 and 652 eV correspond to the  $L_{III}$  and  $L_{III}$  absorption edges, respectively. The slab structure of the sample for the simulations is shown in the bottom right.

half of the thickness of the surface layer consisting half LSMO and half air. This calculation of the total layer thickness is done in analogy to the case of XRR and PNR, where the thickness of the interface region defined by the interface roughness is added partly to the bottom and partly to the top layer at both sides of the interface. The simulations show a strong sensitivity to the total layer thickness. The introduction of the surface layer is necessary as well to obtain the quality of the fit shown in figure 7.19. However, the simulations are hardly sensitive to the interface structure at the LSMO/STO interface, i.e. introducing an interface roughness does not change the simulations compared to a perfectly smooth interface as long as the total layer thickness remains constant. This result holds for all other samples as well. Therefore, no roughness is introduced at the interface between the STO substrates to the LSMO layers. Compared to the XRR results the chemical LSMO layer thickness determined by XRMS is about  $14 \text{ \AA}$  smaller. Even though the discrepancy is biggest for this sample, this is a common result for all following simulations and it is not fully understood, where the difference originates from. A possible source for deviations in the layer thicknesses might be the different sample areas where the data is taken: whereas the entire sample is illuminated by the x-ray beam during an XRR laboratory experiment and also by the neutron beam in a PNR experiment, the beamsize of the beam at the Sector 4 during the synchrotron experiment is something about  $1 \times 1 \text{ mm}^2$ . If the beam does not hit the sample in the exact center, the thickness inhomogeneities might result in different layer thicknesses obtained by both methods. The difference especially for the sample grown at 0.8 mbar seems to be a bit to high, though, to be explained just by the thickness inhomogeneities.

After finding the best agreement between the experimental and simulated data of the average signal, the XMCD signal is fitted by including the magnetic structure of the sample. The results for the PLD sample without EB effect are shown in figure 7.20. Except some differences in the energy scan at  $\theta = 5^\circ$ , a very good agreement between experimental data and simulations is obtained. Apart from the slightly smaller layer thicknesses, the same results on the magnetic profile is found like in the PNR experiment: the entire LSMO layer is ordered ferromagnetically. Compared to PNR, where the average magnetic moment per Mn atom was slightly smaller than the maximum theoretical value of  $3.66 \mu_B$ , the magnetic moment extracted from the XRMS data matches the theoretical value. Only a thin interface and surface layer needs to be introduced in agreement with the small interface and surface roughnesses determined by the other reflectivity methods.

In a very similar way, the XRMS experiments also reproduce the magnetic profile determined by PNR for the LSMO single layer grown by HSD at an oxygen pressure of 0.8 mbar (figure 7.21): at the LSMO/STO interface a  $10 \text{ \AA}$  layer with reduced net magnetic moment is detected. At first sight, this seems to be in contrast to the PNR results presented above, where the interface layer has a zero net magnetization. However, the case of a reduced magnetic moment can not be excluded by the PNR data either. In figure 7.22 a simulation of the PNR data is shown with a magnetic profile similar to the one obtained by XRMS. By slightly adjusting the roughnesses and NSD, this yields a similar good agreement with the experimental data (*FOM* for non magnetic interface layer (figure 7.15(a)): 6.64; *FOM* for slightly magnetic interface layer (figure 7.22): 7.26). However, the value for the magnetization of the interface layer is limited to some value smaller than a third of the magnetization of the rest of the LSMO layer. Otherwise the simulation approaches the case for a layer with a homogeneous magnetization shown and discussed before (figure 7.15(b)). On the other hand, it is not possible to obtain a good simulation for the XRMS data with a macroscopically non magnetic layer at the interface. In fact, the XRMS simulation prove to be very sensitive to even small changes in the magnetic and also the chemical profile of the sample. To get an impression on these effects, some alternative simulations for the data taken at the incident angle  $\theta = 15^\circ$  with slightly different sample configurations are shown in figure 7.23. Therefore, the magnetic depth profile resembling both experimental data sets, PNR

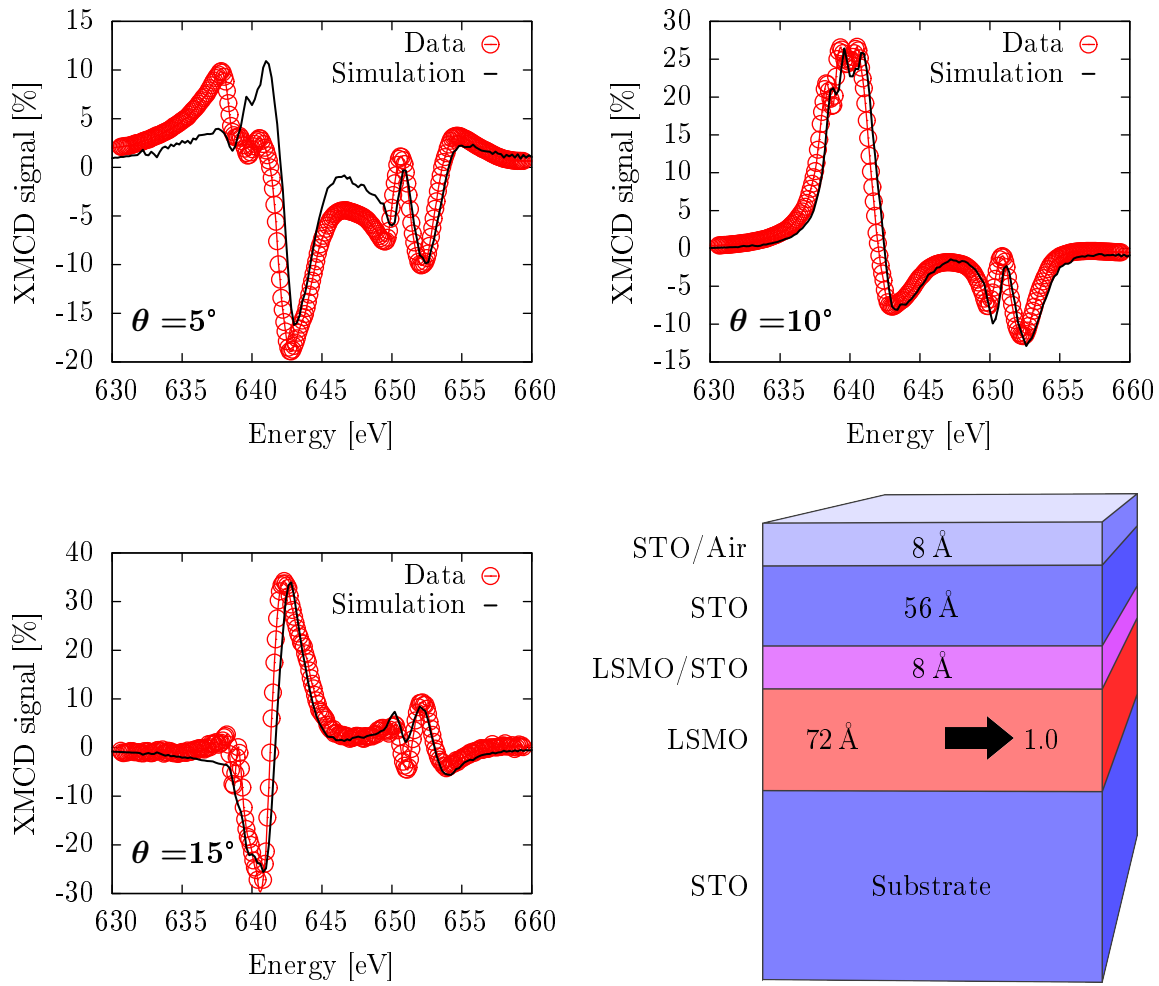


**Figure 7.20:** XMCD signal of the LSMO/STO bilayer grown by PLD for all three incident angles taken at 30 K in a field of 0.05 T. The slab structure of the sample for the simulations is shown in the bottom right. The thicknesses indicated are determined by the simulation of the reflectivity data. The arrow indicates a layer with non zero magnetic scattering length density, where the number to the right gives the fraction of the maximum theoretical value. Detailed results can be found in table 7.4.

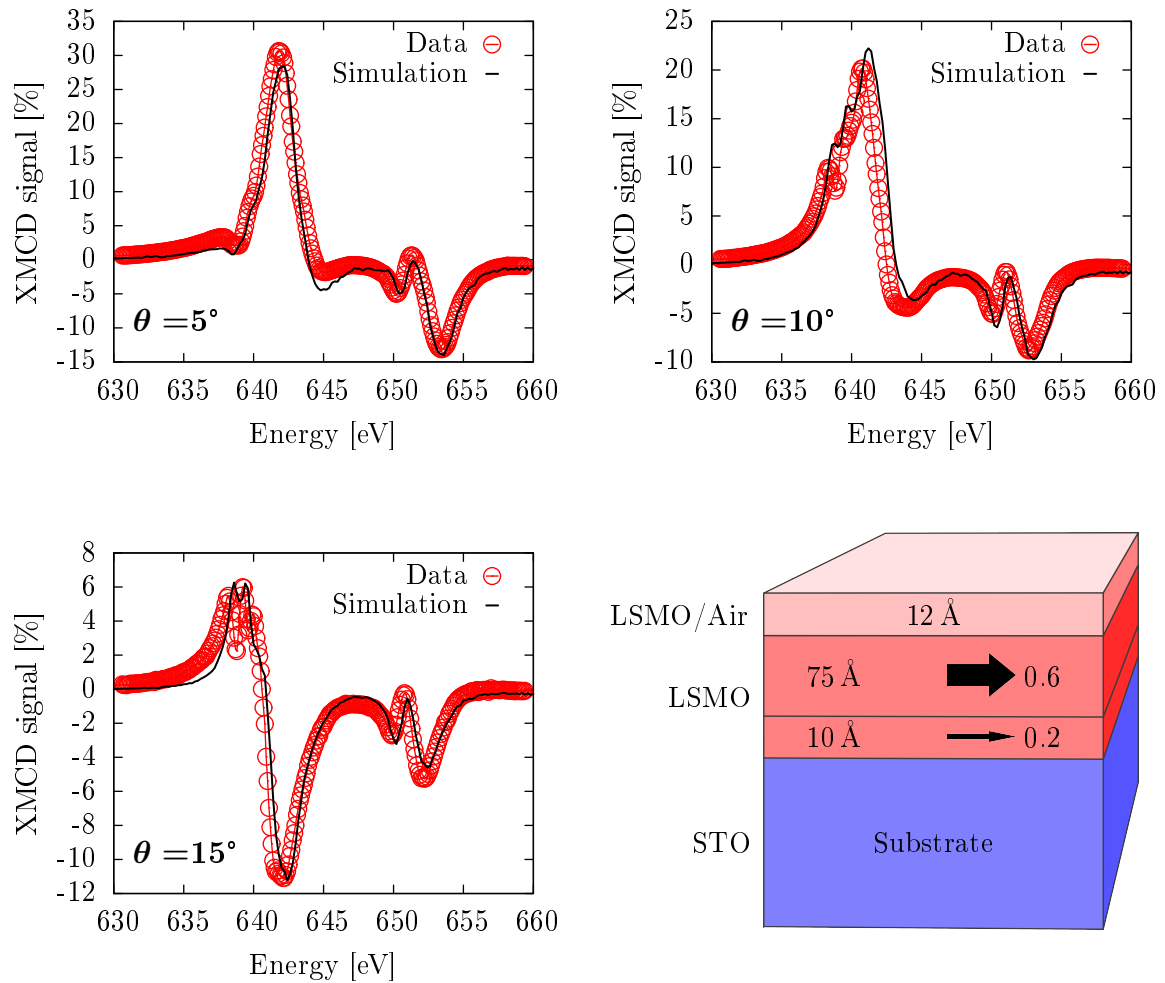


**Figure 7.21:** XMCD signal of the LSMO single layer grown by HSD at 0.8 mbar for all three incident angles taken at 30 K in a field of 0.05 T. The slab structure of the sample for the simulations is shown in the bottom right. The thicknesses indicated are determined by the simulation of the reflectivity data. The arrow indicates a layer with non zero magnetic scattering length density, where the number to the right gives the fraction of the maximum theoretical value. Detailed results can be found in table 7.4.

and XRMS, is an interface with a drastically reduced, but non zero average magnetic moment. The average magnetization of LSMO at the interface to STO is reduced to at least one third of the magnetization of the rest of the LSMO layer. The magnetization of the main part of the LSMO layer is found to be slightly smaller with XRMS compared to the PNR result (60 % and 70 %, respectively). The difference can be explained by the different temperatures at which both experiments have been conducted: whereas the PNR data was taken at 6 K, the XRMS scan was performed at about 30 K. The temperature dependent macroscopic PPMS measurements already revealed that the total magnetization of the sample grown at 0.8 mbar is slightly reduced at 30 K (figure 7.11). Another possible origin for different results in the magnetic profiles is the different treatment of roughnesses in both experiments: in PNR the rms roughnesses parameter models a gaussian-like transition from one to the next layer in the scattering length densities. In the XRMS models, the interface and surface layers only represent a step like transition. However, as mentioned before, a more differentiated interface region modelled by more than one interface layer did not change the XRMS simulations significantly. Therefore, one interface layer seems to be sufficient for the XRMS data simulations to take layer roughnesses into account.

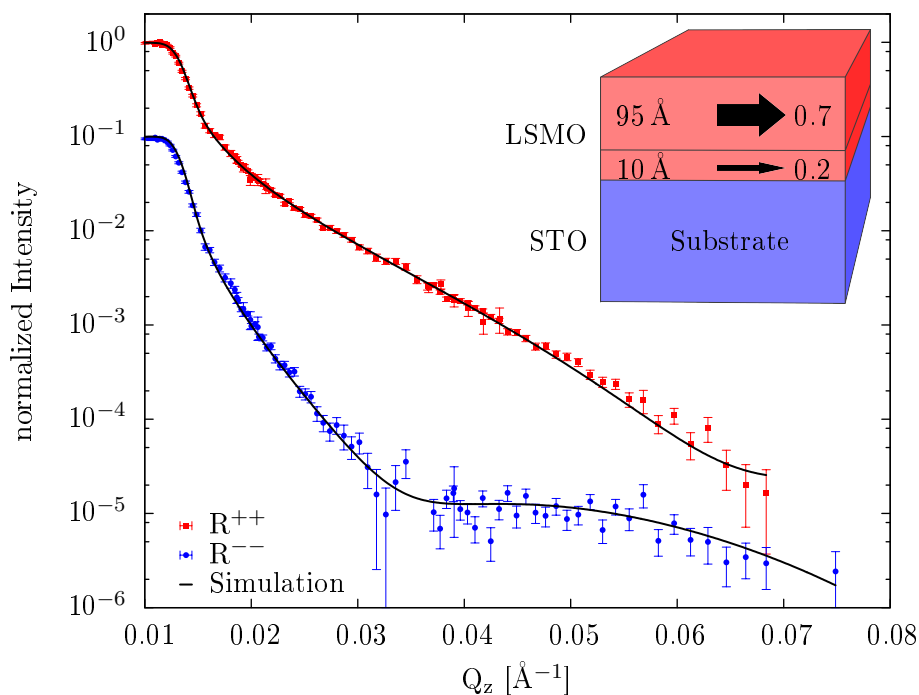


**Figure 7.22:** Alternate simulation for the PNR data at 6 K of the LSMO single layer grown by HSD at 0.8 mbar. A similar good agreement compared to the fit presented in figure 7.15(a) can be found with a small net magnetization at the LSMO/STO interface. This alternate magnetic profile is identical to the one found by XRMS.

Since the PNR results for the HSD sample grown at 0.6 mbar are afflicted with quite big uncertainties, the XRMS data is needed most for this sample in order to get a more trustful picture of the magnetic depth profile. The resulting simulations and simulation parameters are shown in figure 7.24. The resulting LSMO layer thickness adds up to 163 Å which again is slightly thinner than the XRR thickness. The magnetic profile is very similar to the one found for the sample grown at 0.8 mbar: At the interface to the STO substrate a region of strongly reduced - i.e. 25 % of the rest of the LSMO layer - magnetic moment is present. However, the thickness of this interface near layer of 30 Å is much larger than the one obtained for the previous sample. The average magnetic moment in the main part of the layer is only 20 % of the value determined by

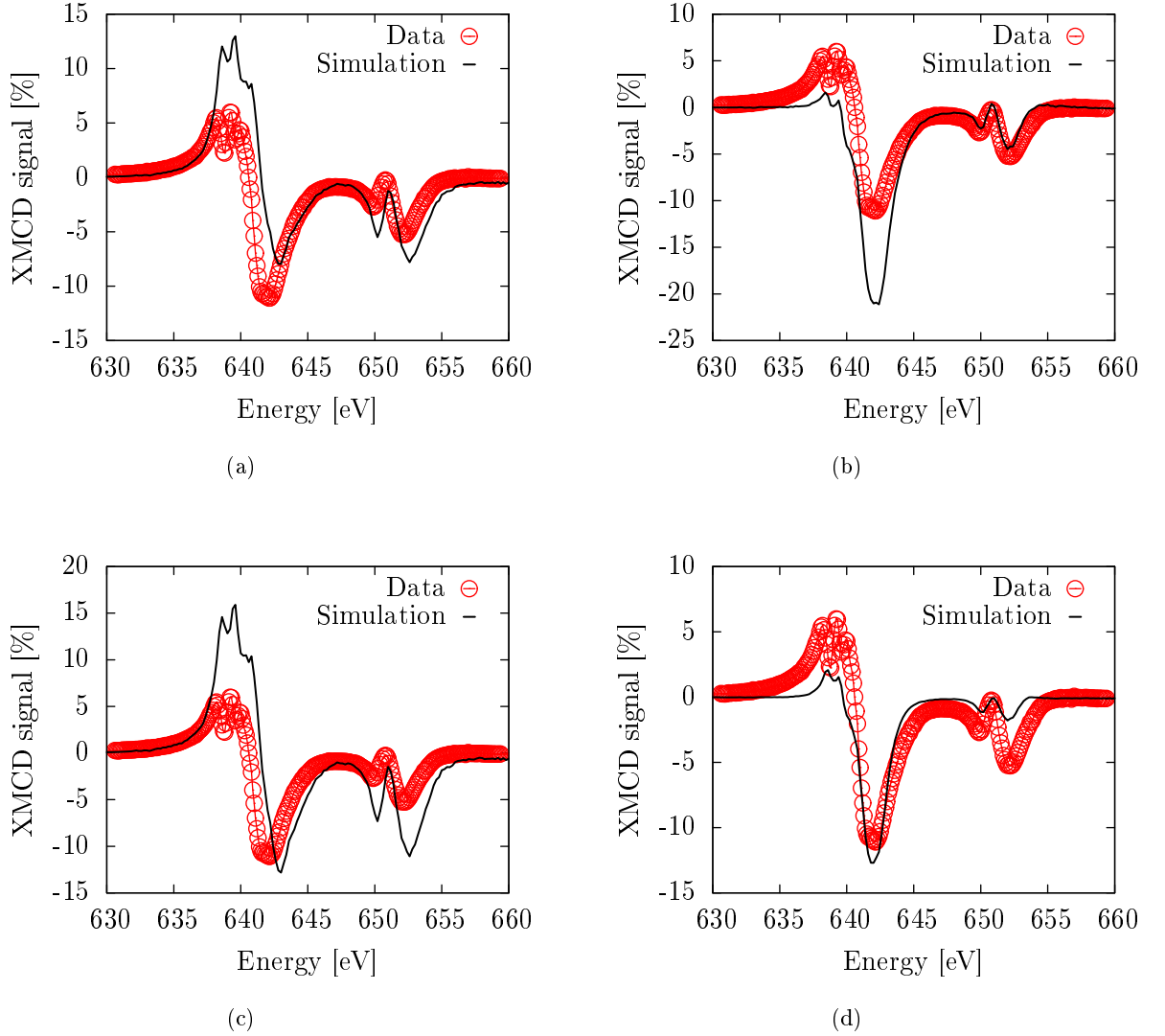


**Figure 7.23:** Alternate simulations to the XMCD data taken at  $\theta = 15^\circ$  of the LSMO single layer grown by HSD at 0.8 mbar in order to emphasize the sensitivity of the XMCD signal to small changes in the magnetic and/or chemical profile of the sample. All parameters are kept identical to the parameters obtained by the best fit shown in figure 7.21 except for the following changes. a) Simulation for a 5 Å thick interface layer and 80 Å rest layer (instead of 10 Å and 75 Å, respectively). b) Simulation for a 15 Å thick interface layer and 70 Å rest layer (instead of 10 Å and 75 Å, respectively). c) Simulation for an LSMO layer having a homogeneous magnetization of 60% of the theoretical bulk value. d) Simulation for a 10 Å interface layer with no net magnetic moment.

PNR. This again can be explained by the different temperatures during the experiments. For this sample (Curie temperature of 57 K) the reduction is much more drastic due to the sharp drop of the total magnetic moment from 6 to 30 K (figure 7.11).

## Summary of the PNR and XRMS results

The results for the LSMO layers of the PNR and XRMS simulations of the different samples are summarized in table 7.4. For the PLD bilayer, PNR at 6 K yields a ferromagnetic layer thickness, which is identical (within the errorbars) with the chemical LSMO layer thickness determined by XRR. The chemical layer thickness can not be extracted from the PNR data, but from the combination of both measurements it can be concluded that the complete LSMO layer is ordered ferromagnetically. By the same argumentation, a region with a drastically reduced magnetization was detected for the two samples grown by HSD at 0.8 and 0.6 mbar at the interface to the STO substrate. It can not be clarified by PNR, whether this interface region is macroscopically non magnetic or exhibits a small net magnetic moment. The XRMS data evaluation however yields a non zero magnetization for the interface region somewhere around 20 to 30 % of the magnetization of the rest of the LSMO layer. The thickness of the interface increases with increasing oxygen deficiency from 0 Å for the PLD sample to about 10 Å for the single layer grown at 0.8 mbar and finally up to 30 Å for the sample grown at 0.6 mbar. All parameters, i.e. scattering length densities (or indices of refraction), roughnesses and magnetic profiles, are in agreement for the results obtained from the three experimental techniques, XRR, PNR and XRMS. The only discrepancy is the slightly smaller layer thicknesses determined by XRMS. As discussed before, the layer inhomogeneities are a possible reason for the differences.

**Table 7.4:** Summary of all reflectivity measurements for the fit parameters of the LSMO layers. The PNR results correspond to the measurement at 5 K.  $\sigma_{lsmo}$  gives the rms-roughnesses obtained by XRR and PNR. For XRMS instead the thickness of the surface or interface layer is listed.  $d_{lsmo}$  is the chemical layer thickness of the LSMO layer, The index *fm* refers to parameters of the ferromagnetic part of the LSMO layers, *nm* to the region of strongly reduced magnetic moment. *d* are the corresponding layer thicknesses and *m* the average magnetic moment per Mn atom. The latter ones are normalized to the maximum expected theoretical value  $m_{th} = 3.66 \mu_B$  per Mn atom. Like for XRR, the FOM of the PNR fits is given by formula (7.1). Since the XRMS data has only been simulated, but not fitted, a FOM is not determined. For all additional parameters see Appendix, section A.

	PLD			0.8 mbar			0.6 mbar		
	XRR	PNR	XRMS	XRR	PNR	XRMS	XRR	PNR	XRMS
$\sigma_{lsmo}[\text{Å}]$	2(5)	6(6)	8(4)	16(2)	15(2)	12(3)	21(3)	17(3)	14(3)
$d_{lsmo}[\text{Å}]$	85(2)	-	76(2)	105(1)	-	91(2)	177(2)	-	163(3)
$d_{fm}[\text{Å}]$	-	86(3)	76(2)	-	95(4)	75(2)	-	140(10)	126(5)
$m_{fm}/m_{th}$	-	0.91(6)	1.0(4)	-	0.71(5)	0.60(4)	-	0.23(3)	0.08(3)
$d_{nm}[\text{Å}]$	-	-1(4)	0(2)	-	10(5)	10(2)	-	37(12)	30(5)
$m_{nm}/m_{th}$	-	-	-	-	0.15(2)	0.20(3)	-	0.04(5)	0.02(2)
$FOM$ [ $10^{-3}$ ]	0.66	11.3	-	2.69	6.64	-	2.93	82.1	-

On behalf of the XRMS data evaluation, one additional fact needs to be reminded: As mentioned before, for the simulation indices of refraction  $n(E)$  and magneto-optical constants  $Q(E)$  have been used which have been determined from a LSMO "standard sample", a 60 nm thick LSMO

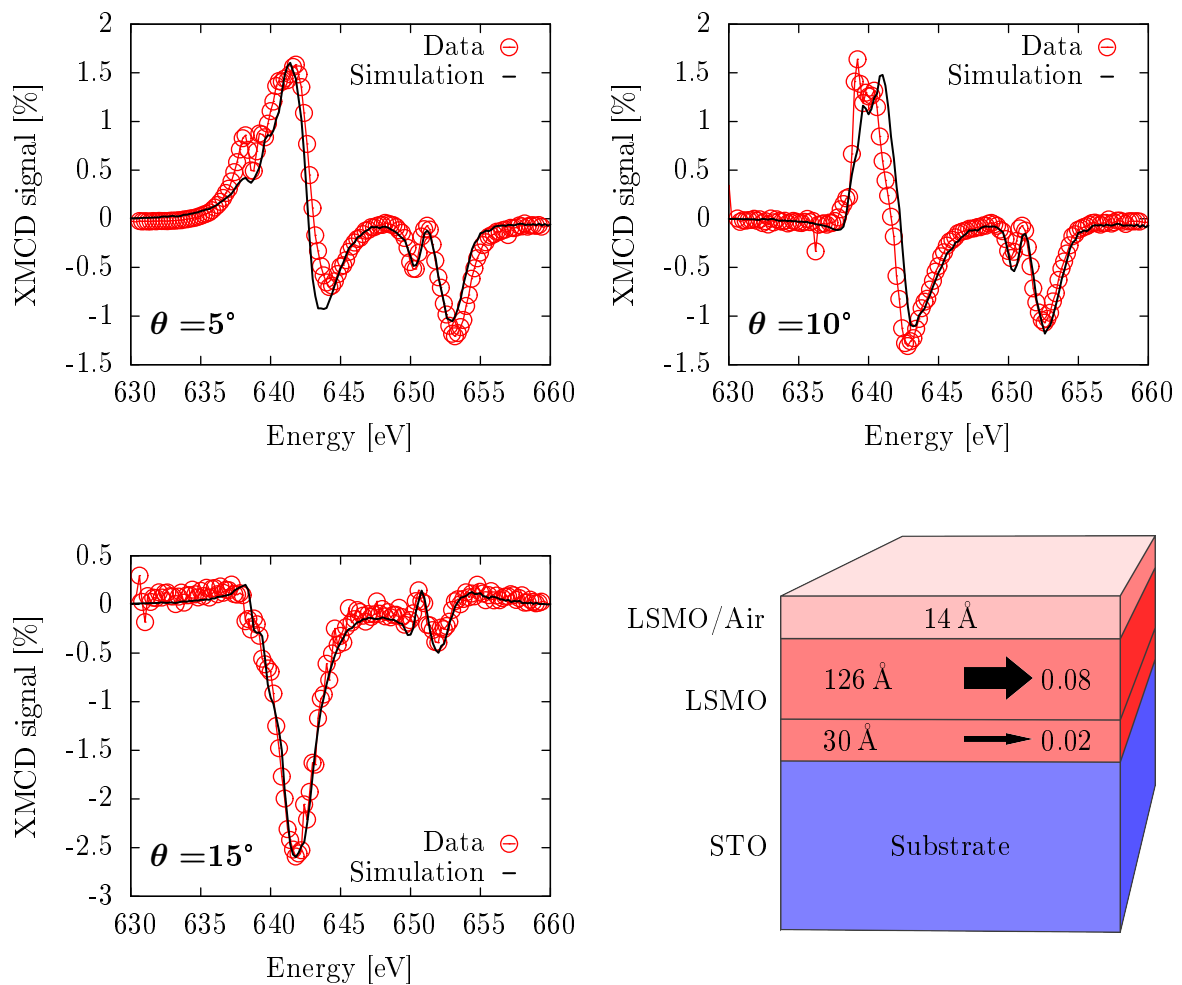
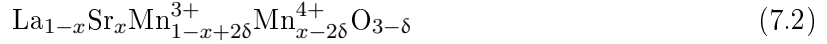


**Figure 7.24:** XMCD signal of the LSMO single layer grown by HSD at 0.6 mbar for all three incident angles taken at 30 K in a field of 0.05 T. The slab structure of the sample for the simulations is shown in the bottom right. The thicknesses indicated are determined by the simulation of the reflectivity data. The arrow indicates a layer with non zero magnetic scattering length density, where the number to the right gives the fraction of the maximum theoretical value. Detailed results can be found in table 7.4.



film. Since there is no detailed study on how the values for  $n(E)$  and  $Q(E)$  change with the oxygen level in a LSMO film, it is not clear to what extent it is valid to use the values of the standard sample for the simulations of the oxygen deficient layers. However, extracting oxygen from a LSMO layer basically has the same effect like changing the La/Sr ratio to the La rich direction: The  $\text{Mn}^{4+}/\text{Mn}^{3+}$  ratio gets smaller. This means oxygen deficient  $\text{La}_{0.66}\text{Sr}_{0.33}\text{MnO}_{3-\delta}$  can be assumed to have the same  $\text{Mn}^{4+}/\text{Mn}^{3+}$  ratio - and hence the same XMCD signal - like a fully oxidized  $\text{La}_{1-x}\text{Sr}_x\text{MnO}_3$  with a La/Sr ratio larger than 2. The influence of the Sr doping  $x$  and the oxygen deficiency  $\delta$  on the  $\text{Mn}^{4+}/\text{Mn}^{3+}$  ratio is described quantitatively by the following chemical formula (oxygen vacancy model [113,114]):



Since the dependence on the Sr doping of the index of refraction around the  $L_{II}$  and  $L_{III}$  has been shown to be very small [115], the used  $n(E)$  and  $Q(E)$  values can be assumed to be a very good approximation for the true values of the different samples analyzed in this work. In addition, the fact that the XRMS data yield results in agreement with the PNR data can be taken as an indication that the  $n(E)$  and  $Q(E)$  values of the standard sample are close to the true values. Furthermore, one can expect that simultaneous fitting of data for three different angles is not possible with "wrong"  $n(E)$  and  $Q(E)$  values. So in total there is strong evidence that it is justified to use the indices of refraction and magneto optical constants determined from the standard LSMO sample for the samples investigated in this work.

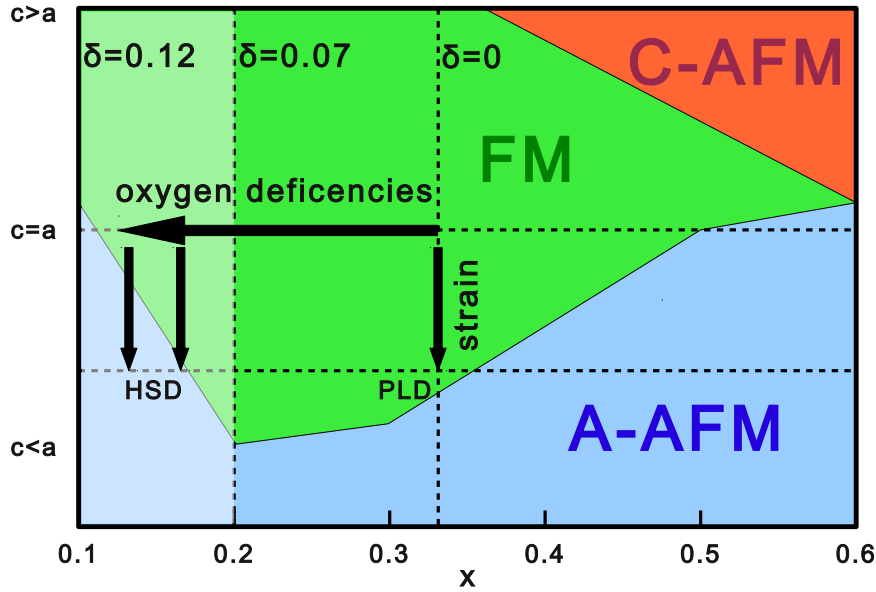


**Figure 7.25:** Strain vs. doping phase diagram of LSMO. The information for the doping range between  $x = 0.2$  and  $x = 0.6$  is taken from [116] and [63]. The phase boundary between FM and A-AFM region for a doping level smaller than 0.2 is an assumption or rather an interpolation between the last calculated point in [116] for  $x=0.2$  and the known fact, that bulk LSMO with  $x=0.1$  exhibits the A-AFM structure [52]. Even though the doping level is kept at 0.33 for the samples under investigation, one can still "move" through the phase diagram by oxygen deficiencies (according to formula (7.2)) and strain and reach the A-AFM region. The  $\delta$  values give the necessary oxygen deficiency to reach the same  $\text{Mn}^{4+}/\text{Mn}^{3+}$  ratio as a fully oxygenated LSMO with a doping level at the corresponding position.

## 7.4 Possible explanation of EB effect in the LSMO/STO thin film system

After the data analysis, the question now remains, how an EB effect can be present in the LSMO/STO system. The combination of macroscopic magnetic characterization and the scattering experiments leads to the following interpretation: First of all the presence of an EB effect in the samples indicates that a somehow antiferromagnetically ordered region must be present in the sample coupled to the ferromagnetic part of the LSMO. Both, the PNR and XRMS measurements reveal a - if not vanishing - at least drastically reduced magnetization in the LSMO layer at the interface to the STO substrate in the samples exhibiting the EB effect. Since we can not resolve the magnetic structure on an atomic length scale with grazing incidence scattering, it is very likely that this macroscopically nonmagnetic region is in fact ordered antiferromagnetically. Similar to the magnetic inhomogeneities present in oxygen deficient LSMO layers in general, the small net magnetization could also be explained by small ferromagnetic grains in the interface region. The EB effect then can be caused by coupling between the (mostly) antiferromagnetically ordered interface region and the ferromagnetic part of the LSMO layer. The occurrence of the EB effect in our samples can be understood by looking at the strain-doping phase diagram of LSMO (figure 7.25). In principle, one could also expect that the ferromagnetic part of the LSMO itself is the origin for the EB effect: since the exact microscopic structure of the oxygen deficient LSMO is not fully clarified, but expected to be "magnetically inhomogeneous", even in this part of the LSMO layer antiferromagnetic regions (grains) could be present causing an EB by coupling to the ferromagnetically ordered regions. However, if this was the case, it would have been seen previously in oxygen deficient bulk LSMO. It therefore is very likely that the interface region causes the EB effect and that the necessary antiferromagnetic order is established in this part of the LSMO layer.

An explanation for a formation of an antiferromagnetic order of LSMO at the interface to STO can be given by the strain versus doping level phase diagram proposed theoretically by Fang et al. [116] and experimentally by Konishi et al. [63]. The structural characterization by x-ray-scattering and also the VSM measurements clearly indicate oxygen deficiencies in the LSMO layer. Furthermore we can adjust the oxygen content by varying the oxygen pressure. Effectively this leads to the same result like changing the La/Sr ratio to a lower Sr content in the LSMO layer: The  $\text{Mn}^{4+}$  content and thus the charge carrier density is decreased, which results in a shift in the phase diagram in figure 7.25 to the left according to formula (7.2) even though  $x$  might still be equal to 0.33. This alone seems not to be sufficient in our samples to reach the AFM region, as we still see a ferromagnetic order for the majority of the LSMO layer. But at the interface in addition to the change in charge carrier density we also have a compressive strain mediated by the STO substrate which is equivalent to a shift in the diagram downwards. To the best of my knowledge, there are no theoretical calculations nor experimental reports on a strain phase diagram for doping levels smaller than 0.2. The reason for this probably is, that the bulk phase diagram already becomes very complicated for these doping levels. However, it is well known for bulk LSMO that for doping levels smaller than 0.16 the antiferromagnetic A-type structure (A-AFM) is established [52]. By combining this information with the calculations (and experimental data) for larger doping levels, one can assume that the phase diagram between  $x = 0.1$  and 0.2 looks something like shown in figure 7.25. In this case, a combination of oxygen deficiency and compressive strain can result in an antiferromagnetic order at the STO interface. After relaxation a ferromagnetic order is established in the rest of the layer. This interpretation can only be valid, if the samples exhibiting an EB effect have a oxygen deficiency large enough to result in a  $\text{Mn}^{4+}/\text{Mn}^{3+}$  ratio smaller than 0.25 (which corresponds to a Sr doping of  $x=0.2$  for fully oxydized LSMO), as for larger  $\text{Mn}^{4+}/\text{Mn}^{3+}$  ratios a bigger strain than for the fully oxidized

LSMO with  $x=0.33$  is needed in order to reach the A-AFM phase (see phase diagram between  $x=0.2$  and  $x=0.33$ ). Therefore, according to formula (7.2) an oxygen deficiency larger than  $\delta = 0.07$  is needed. The fact that the antiferromagnetic layer gets thicker with increasing oxygen deficiencies also supports the assumption that the oxygen deficiencies are in the range between  $\delta = 0.07$  and  $0.1$ : in this region a sample with higher oxygen deficiencies need a smaller strain to reach the AFM phase. Therefore, a region at a certain strain that is ordered ferromagnetically in the sample grown at  $0.8$  mbar might be ordered antiferromagnetically at the same strain in the sample grown at  $0.6$  mbar due to the larger oxygen deficiency. Thereby, for the sample grown at  $0.6$  mbar a bigger relaxation is needed to end up in the FM region, resulting in a thicker AFM layer.

To finally proof this interpretation, a more detailed analysis of the relaxation process in the samples and on which length scale it occurs needs to be done. Some indication for the strain relaxation has been extracted from the x-ray diffraction data and at least for the single layer grown at  $0.6$  mbar the thickness of the strained region is very similar to the thickness of the AFM region (about  $30$  to  $40$  Å). Another way of proving our interpretation would be the investigation of multilayers by neutron diffraction: Magnetic reflections caused by an antiferromagnetic order could be detected by this method. Neutron diffraction is not possible for the samples discussed here, as the diffracted intensity would be too small. For the single and bilayers dicussed in this chapter, X-ray Magnetic Linear Dichroism (XMLD) is a promising experiment. Since the XMLD signal is proportional to the square of the magnetic moments, one is also sensitive to antiferromagnetic structures. By combining XMCD and XMLD data, it might be possible to deduce the ferromagnetic contribution to the XMLD signal and obtain the XMLD signal caused by antiferromagneti regions in the samples. By performing the experiments in reflectometry geometry one would again be able to analyze the magnetic profile - including antiferromagnetic regions - depth dependent.

## 8 Results and Discussion II: La<sub>0.5</sub>Sr<sub>0.5</sub>MnO<sub>3</sub>/BaTiO<sub>3</sub>

### 8.1 Preparation of stoichiometric and epitaxial LSMO/BTO bilayers by OMBE

La<sub>0.5</sub>Sr<sub>0.5</sub>MnO<sub>3</sub>/BaTiO<sub>3</sub> bilayers have been prepared by OMBE on monocrystalline (001) oriented conducting Nb doped SrTiO<sub>3</sub> substrates provided by Crystec (doping level 2 at%). The substrates have been cleaned first in acetone, then in iso-propanol and then in deionized water. After that the surface has been cleaned by putting the substrates in buffered hydrofluoric (HF) acid (10 NH<sub>4</sub>F:1 HF) for 25 sec. By this process not only the organic residues are removed, but also the surface gets TiO<sub>2</sub> terminated, since the etching process removes all SrO from the surface [117]. The clean substrate is first annealed in the preparation chamber of the OMBE device to 400 °C before transferring it to the main chamber. In the main chamber a base pressure in the low 10<sup>-9</sup> mbar region is reached for all samples. Ozone is distilled from a ozone-oxygen mixture created by an ozone generator. Prior to the rate calibration and the film deposition, the pure ozone is delivered to the main chamber from a water cooled nozzle pointing at the substrate. A constant ozone pressure of 2.0 · 10<sup>-6</sup> mbar is established at the position of the sample. Before the layer deposition, the rates for each effusion cell needed for one material, e.g. La, Sr and Mn for LSMO, is monitored for 20 minutes by the QCM one after another (figure 8.1). By subtracting the background level measured with all shutters closed, the true deposition rates are determined. Based on this calibration measurement, it is calculated for each of the elements, how long it takes to get enough material for one unit cell of the material, which should be deposited. Since the rates cannot be monitored during the growth - the QCM needs to be driven out of position to give room for the manipulator with the substrate -, the error on the stoichiometry of the deposited material is determined by the stability of the rates. In order to minimize this error, the rate for the element with the least stable effusion is taken last to minimize the time between the determination of the rate and the deposition. After taking the deposition rates, the manipulator is driven to the sample position and the substrate is heated to the deposition temperature of 650 °C. Typically, 30 minutes are needed after finishing the rate determination to start the growth. The substrate temperature is controlled by a pyrometer with emissivity correction. During the growth, the shutters for the effusion cells are opened accordingly to the sputter rates determined by the QCM to obtain one unit cell of the layer material. Typical shutter opening times are 40 to 60 sec. Between each unit cell an annealing step of 30 sec is inserted to allow the deposited material to settle and form a smooth surface. After the deposition the sample is cooled down in the ozone atmosphere to avoid oxygen deficiencies. Afterwards the rates of each element are taken again to check the stability of the effusion cells, this time in opposite order than before the deposition, i.e. the least stable effusion cell is measured first. Since the sample cooling takes longer than the heating, the rates can be taken again about 60 minutes after finishing the deposition. The difference between the rates before and after the deposition yields the drift of the evaporation rates, which gives an estimate of the possible deviation from the desired stoichiometry of the grown layer. The drift in the evaporation rates are usually significantly smaller than 1.0 % /hr for La and Ti and around 1.0 % /hr for Ba and Mn. The

Sr effusion cell is the least stable one with respect to evaporation rates having a average drift of about 2.0% /hr. Since the LSMO layers grown in this work have a thickness of 15 u.c., the deposition times are less than half an hour. By adding the 30 minutes needed for the substrate heating, one therefore can expect that the deviations of the evaporation rate during deposition is not significantly bigger than 1%. Since the other rates are much more stable, this is the dominant contribution to the error on the stoichiometry of the deposited layer.

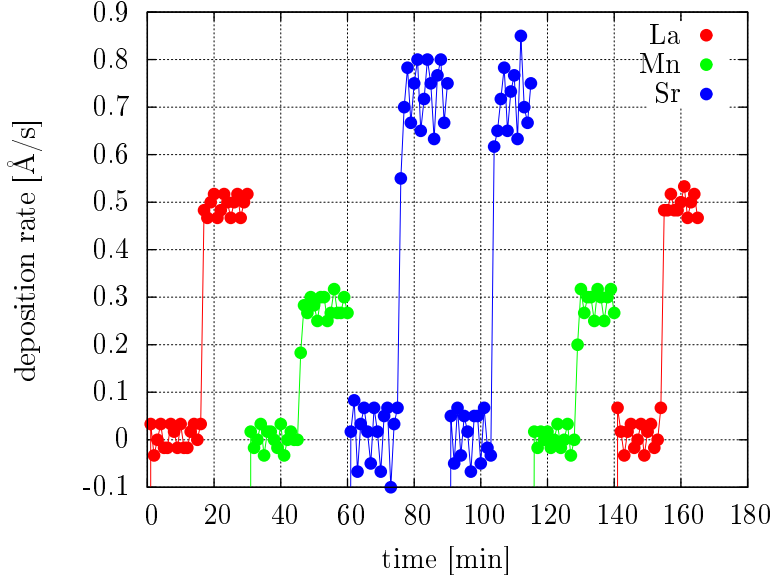


**Figure 8.1:** Deposition rate calibration measurement for the growth of an LSMO layer. For each of the required elements the background level is measured first for a couple of minutes followed by the deposition rate, if the shutter for the corresponding effusion cell is opened. The true deposition rate is obtained by the difference of the two rates. The first three measurements are taken before the layer growth with the least stable rate taken last (Sr). The three last measurements are taken after the growth (the time for the growth is left out in the plot) to check the drift of the evaporation rates.

The growth of each layer has been in-situ observed by RHEED. Figure 8.2 shows the RHEED pattern at different stages during a deposition of a BTO layer on a Nb:STO substrate. A very sharp RHEED pattern with point-like reflections is found before the deposition resulting from the atomically smooth and clean substrate surface (figure 8.2(a)). A change to more stripe like reflections is observed after deposition of the first few monolayers of BTO (figure 8.2(b)). With increasing layer thickness the reflections become broader due to a slight increase in the surface roughness (figure 8.2(c)). However, no additional peaks appear on the fluorescence screen until the end of the deposition indicating that the entire film grows in layer-by-layer growth mode.

This is confirmed by the analysis of the peak intensities of the specular (central spot/stripe in figure 8.2) and first order (spots/stripes to the left and right of the central spot) reflections (figure 8.3) during the layer growth: the integrated intensities of all three spots oscillate with a period matching the shutter times for the growth of one unit cell. These oscillations are often used to count the unit cells and hence to stop the deposition exactly at the desired layer thickness (chapter 6.1.2). In the growth procedure used for the samples in this work, the maxima of the oscillation of the specular reflection do not necessarily correspond to completed unit cells. During the annealing step after each deposition of one (calculated) unit cell, the surface gets smoother and therefore the specular intensity increases even if the unit cell might not be completed, yet (or the next one might already be started). In figure 8.3 the annealing periods can be identified with the time ranges where the intensity of the specular reflection slowly approaches a maximum value. When the shutters are opened for the deposition of the next unit cell, the intensity drops

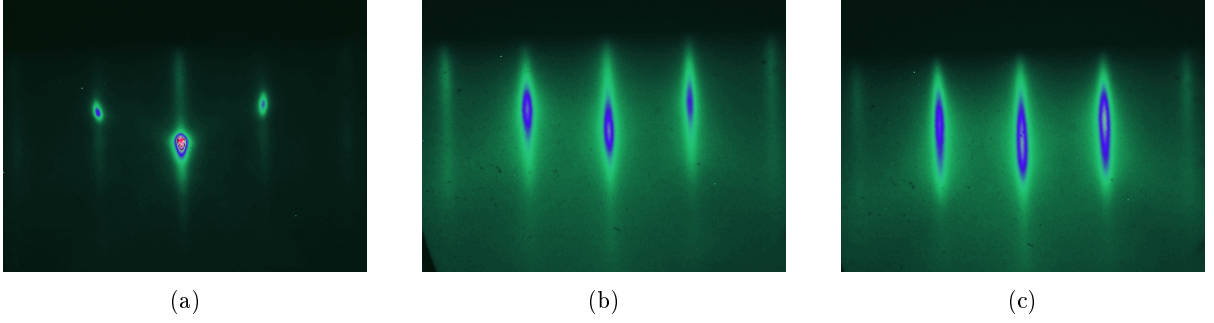


**Figure 8.2:** RHEED patterns during a deposition of a BTO thin film. a) picture of the clean Nb:STO substrate. b) RHEED pattern after deposition of 8 unit cells of BTO. c) RHEED pattern after deposition of 36 unit cells of BTO.

again and the next oscillation begins. Although it is not possible to exactly count the deposited unit cells, the fact that the oscillations are visible throughout the deposition of all layers grown in this work confirm the layer-by-layer growth and the high crystalline quality of the thin films.

As discussed in the introduction on this system (chapter 3.2), there are certain requirements and restrictions, which need to be taken into account, and which determine the structure chosen for the samples analyzed in this work. It is the aim of this work to investigate the theoretically predicted dependence of the interface near magnetic structure of LSMO on the direction of the electric polarization in BTO [2]. Therefore, the samples should be suitable to be analyzed by the interface sensitive scattering methods, which have also been used for the previous system discussed in chapter 7. Hence, especially for PNR, but also for XRMS, the area of the samples should be as big as possible. On the other hand, the BTO layer thickness should be very small: in case that the BTO layer is below the LSMO layer, the BTO thickness should be smaller than 15 u.c. to avoid relaxation, since the size of the predicted interface effect can be expected to scale with the size of the electric polarization of BTO at the interface. If the BTO layer is deposited on top of the LSMO layer, the thickness should be kept very small as well. Otherwise the sensitivity especially in a XRMS experiment to the magnetic structure at the LSMO/BTO interface is drastically reduced. Both requirements to the BTO layer - the large area and the thin thickness - conflict with the well known leakage problem in BTO: the larger the film area and the thinner the film thickness, the larger becomes the probability for leakage currents through the BTO layer, which inhibit that the electric polarization can be switched by an applied electric field. In fact it seems to be impossible to grow a 15 u.c. or thinner BTO layer with an area of at least  $1 \text{ mm}^2$  (which still would be too small for PNR), where the polarization can be controlled by an electric field, if it is placed in direct contact to a top and bottom electrode. Therefore, the following two sample structures are proposed here to cover all the discussed requirements (figure 8.4): for both samples a Nb:STO substrate is used as the bottom electrode. It also has a suitable lattice constant of  $3.905 \text{ \AA}$  to allow for epitaxial growth of both, LSMO and BTO. Furthermore it mediates a compressive in-plane strain to BTO, which therefore grows in a tetragonal structure with elongated out-of-plane lattice constant. This results in an out-of-plane electric polarization, which is needed in the theoretical model to influence the magnetic structure of LSMO. A 100 nm gold layer sputtered on top of the samples after the sample preparation in the OMBE serves as the top electrode. Between the two electrodes both samples contain of a LSMO<sub>15 u.c.</sub>/BTO<sub>15 u.c.</sub> bilayer, one of having LSMO on top of BTO and vice versa for the other sample. The reason for the preparation of both configurations is the much higher sensitivity of XRMS to the magnetic structure at the top interface of a layer compared to the bottom interface. Therefore, by having both configurations the magnetic profile in LSMO at the LSMO/BTO

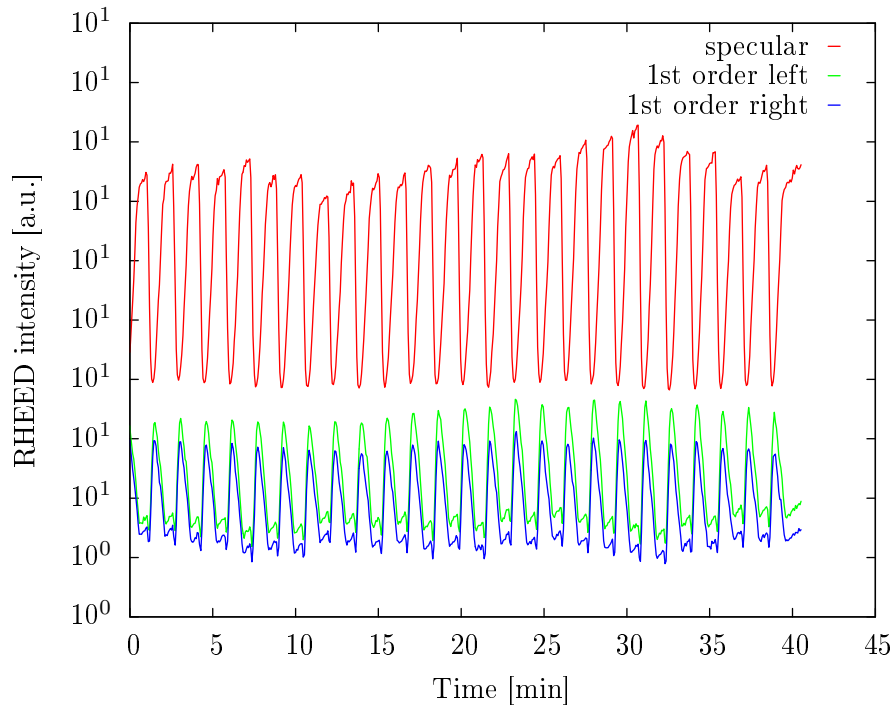


**Figure 8.3:** RHEED oscillations during a growth of a BTO thin film on Nb:STO. The plot shows the last 26 oscillation of a nominal 116 u.c. thick BTO layer. The RHEED measurement proves layer-by-layer growth for the entire layer. The specular intensity corresponds to the central peak in figure 8.2, the 1<sup>st</sup> order intensities to the peaks to the left and right of the central reflection in figure 8.2.

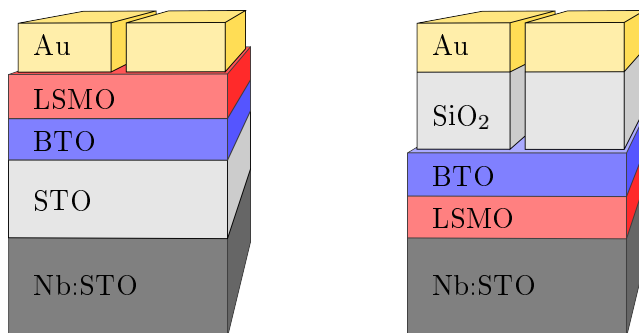


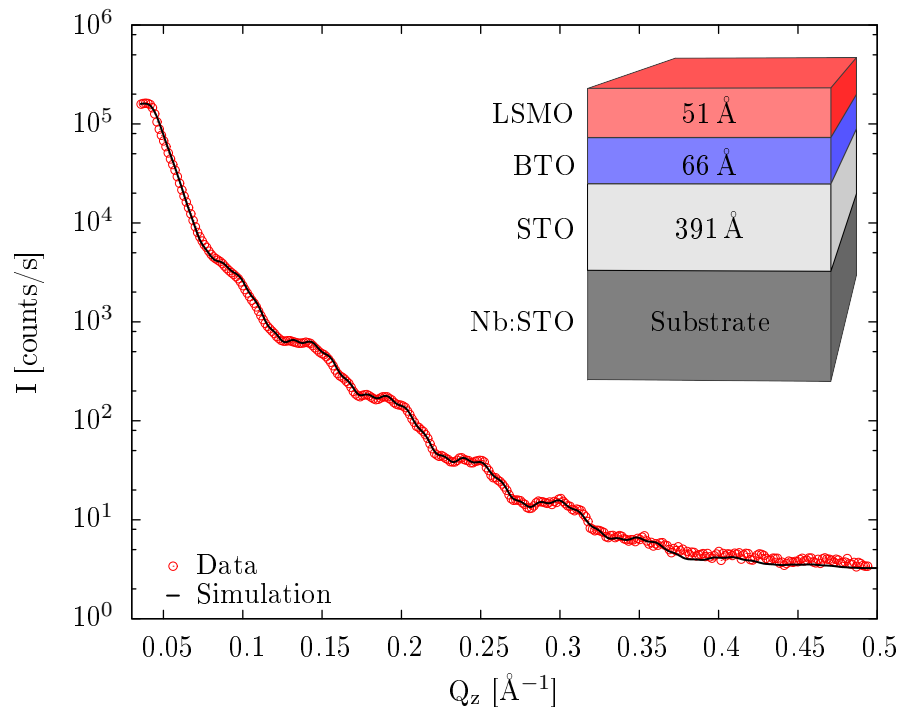
**Figure 8.4:** Sketch of the LSMO/BTO samples prepared for this work.

interface can be analysed best in the sample where BTO is deposited on top of LSMO by XRMS with energies around the Mn  $L_{II}$  and  $L_{III}$  edges. In the other sample, by XRMS with energies around the Ti  $L_{II}$  and  $L_{III}$  edges it can be checked, whether a magnetic moment is induced on Ti at the BTO/LSMO interface as has been predicted for example theoretically for  $\text{Fe}_3\text{O}_4/\text{BTO}$  interfaces [73]. Finally, to get a sufficient spacing between the top and bottom electrode an additional layer of an insulating material is destined in both samples. For the sample with the BTO layer on the bottom this layer needs to be between the substrate and BTO. Hence, for this sample a 100 u.c. thick non-doped STO layer is deposited first on top of the conducting substrate, which remains the lattice constants unchanged for the LSMO/BTO bilayer. For the sample with BTO on top of LSMO the insulating layer needs to be deposited on top of BTO. In order to allow for the XRMS measurement, this layer is not grown in the OMBE chamber. It rather is deposited afterwards in a sputter chamber with a mask to leave a gap of about 1 mm in the middle of the sample, where the x-ray beam can be reflected. For this sample a 80 nm thick  $\text{SiO}_2$  is used as the insulating layer. The gold electrodes for both samples are deposited in the same sputter chamber with the same mask.

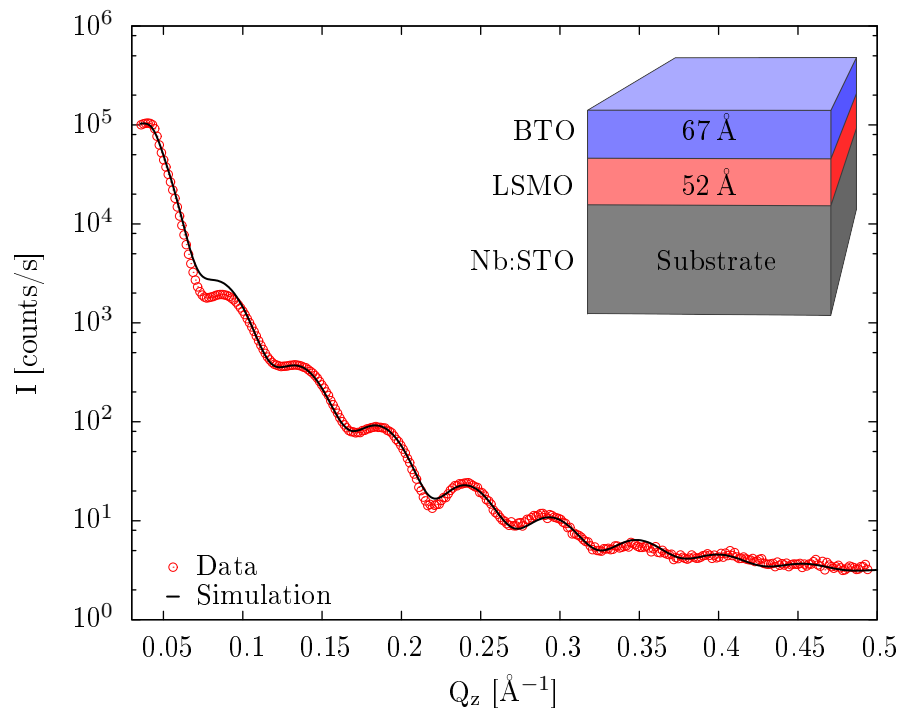
In the following, the structural characterization by XRR and XRD will be presented. Those measurements have been performed before the deposition of the sputtered top layers. The results are listed in table 8.1. Figure 8.5 shows the XRR measurements and simulations for both samples. The simulations have been done the same way as described in chapter 7 and also the results are in general very similar: good agreement with the data was found with the bulk values of the scattering length densities. The layer thicknesses are almost exactly matching with the nominal thicknesses for 15 u.c. LSMO and BTO layers and the 100 u.c. STO layer. Taking into account the out-of-plane lattice constants determined by XRD (see below and figure 8.6), the LSMO layer thicknesses correspond rather to 13 to 14 u.c. and the BTO layer thicknesses to about 16 u.c.. But since the oscillations visible in both data are due to the bilayer thickness, the single layer thicknesses can be determined less accurately. The bilayer thickness is very close to the nominal value. The rms-roughnesses for all interfaces are very small with values below 5 Å. For the sample with the BTO layer on top an additional 6 Å surface layer needs to be introduced as discussed in the previous chapter to model the surface structure more accurately. As expected for the OMBE growth, no layer inhomogeneities need to be taken into account to model the data.

In contrast to the LSMO/STO bilayers of the previously discussed system, the XRD data of the LSMO/BTO bilayers can be modeled quite well (figure 8.6). The reason for this is that the BTO has a sufficiently different out-of-plane lattice constant in comparison to the substrate. Therefore, the (002) reflection of the BTO layers is separated from the STO reflection and its position can be determined very accurately. For the LSMO reflection the same problem seems to be present as for the LSMO/STO bilayers. But in contrary to the LSMO/STO samples besides the LSMO (002) reflection, thickness oscillation are visible. First of all, this is an indication for a higher crystalline quality of the OMBE grown samples. Secondly, the thickness oscillation modulate the shape of the BTO reflection. From this modulation the position of the LSMO reflection can be extracted very accurately. In addition to the LSMO and BTO reflections, in the measurement of the sample with the LSMO layer on top the STO reflection of the 100 u.c. thick insulating layer deposited first on the Nb:STO substrate is visible at the position of the substrate reflection. Since it is very hard to model the contribution of this extra layer due to the strong merging with the substrate reflection, it has not been taken into account in the simulations. This does not affect the results for the LSMO and BTO lattice constants, since it has much shorter thickness oscillations, which would not affect the shape of the LSMO and BTO peaks. The layer thicknesses obtained from the XRD simulations are only reduced by 6 % with respect to the XRR results indicating that almost the entire layers scatter coherently. The resulting lattice constants are



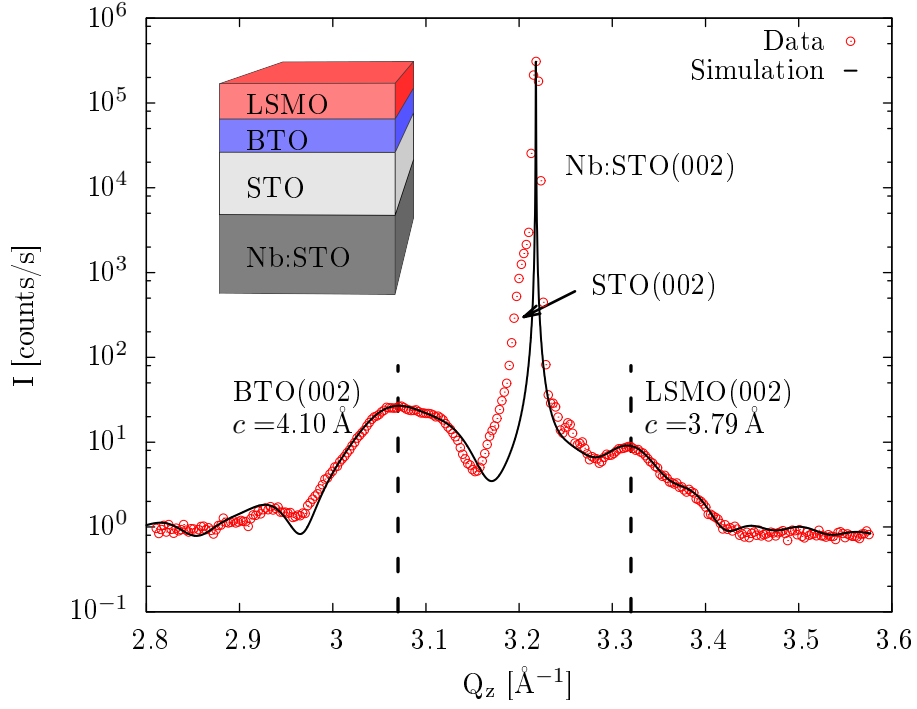


(a)

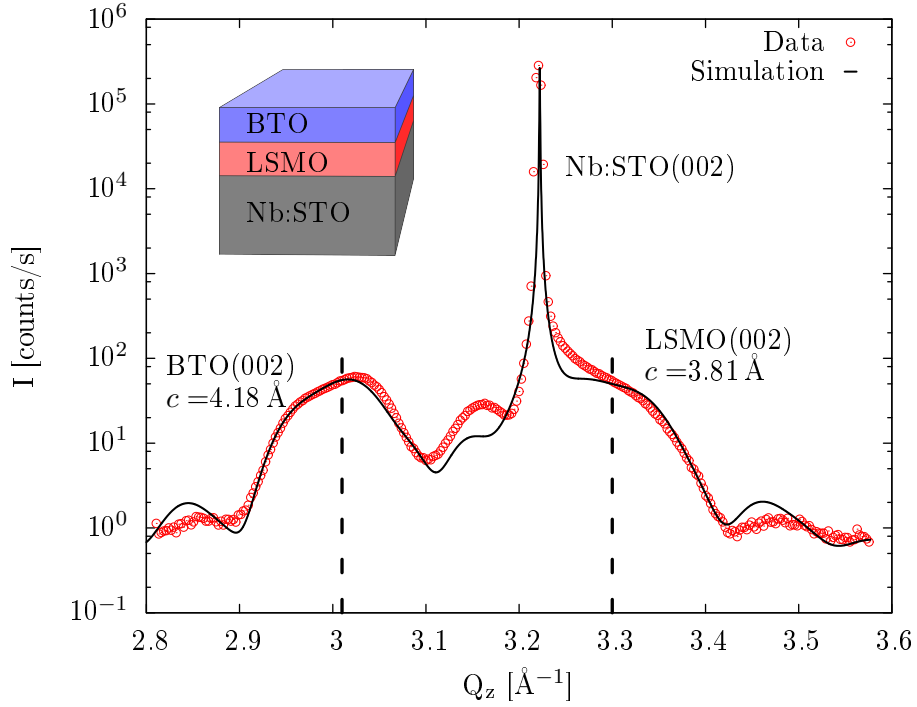


(b)

**Figure 8.5:** XRR measurements of both samples. The layer thicknesses resulting from the simulations are given in the sample sketches. Detailed results are listed in table 8.1



(a)



(b)

**Figure 8.6:** XRD measurements of both samples around the (002) reflections of the layers and the substrates. The given values for the out-of-plane parameters  $c$  are obtained by the peak positions resulting from the simulations. Simulations have been done by using the *plot.py* data evaluation software [108]. Detailed results are listed in table 8.1.

listed together with the XRR results in table 8.1. There is a significant difference in the BTO lattice constants of both samples: whereas the simulation yields 4.10 Å for the sample with the BTO layer below the LSMO layer, a value of 4.18 Å is obtained for the other sample. This can be due to a different strain mediated to both BTO layers due to the fact that it is deposited once directly on STO and once on LSMO. This explanation only can be true, if the LSMO layer is at least partly relaxed at the surface, since it otherwise would still have the same in-plane lattice constants as the Nb:STO substrate. If it relaxes, it has an even smaller lattice constant than the 3.905 Å of STO, resulting in a larger strain for the BTO and hence a larger out-of-plane lattice constant for the BTO layer deposited on LSMO. Another reason for the difference might be a slightly different stoichiometry in both BTO layers. In contrast, the lattice constants of the two LSMO layers are almost identical considering the error bars. A slightly smaller value for the LSMO layer deposited on BTO again can be explained by a slightly relaxed BTO layer underneath.

**Table 8.1:** Summary of the XRR and XRD characterization

Listed are the rms-roughnesses  $\sigma$ , layer thicknesses  $d$  and out-of-plane lattice constants  $c$  of the substrate (*sub*), the LSMO layer, the BTO layer and of the surface layer (*surf*). The FOM has been calculated from formula (7.1). For all additional parameters see Appendix, section A.

	BTO/LSMO	LSMO/BTO
$\sigma_{surf}$ [Å]	-	6.1 (6)
$\sigma_{LSMO}$ [Å]	4.0 (5)	3.8 (4)
$d_{LSMO}$ [Å]	51 (2)	52 (2)
$c_{LSMO}$ [Å]	3.79 (2)	3.81 (3)
$\sigma_{BTO}$ [Å]	2.5 (4)	2.0 (3)
$d_{BTO}$ [Å]	66 (2)	68 (2)
$c_{BTO}$ [Å]	4.10 (2)	4.18 (2)
$\sigma_{STO}$ [Å]	3.5 (5)	-
$d_{STO}$ [Å]	391 (2)	-
$\sigma_{sub}$ [Å]	2.7 (5)	3.2 (3)
$FOM$ [ $10^{-3}$ ]	1.16	2.56

In summary, LSMO/BTO bilayers of very high crystalline quality and smooth interfaces have been grown by OMBE. The in-situ RHEED characterization revealed layer-by-layer growth throughout the deposition of every single layer. The layer thicknesses are very close to the nominal values of 15 u.c. for both, LSMO and BTO layers. A significant difference in out-of-plane lattice constants of BTO deposited on STO and LSMO has been measured, which can be due to a different strain mediated by the different layers underneath or in a small variation of the stoichiometry.

## 8.2 Macroscopic magnetic and ferroelectric characterization

The characterization of the two samples has been done by performing temperature scans in a magnetic field of 0.5 mT from 5 to 340 K after cooling in a field of 1 T (figure 8.7). Both samples differ strongly in their magnetic behavior. The sample with the LSMO layer on top of the BTO layer clearly shows an antiferromagnetic temperature dependence. This is in agreement with the results found for 300 Å thick layers of LSMO having a nominal La/Sr ratio equal to one prepared

in the same OMBE device [61]. In contrast, the sample with the opposite stacking order exhibits rather a ferromagnetic shaped temperature scan. However, the measured saturated moment at low temperatures of  $4 \times 10^{-8} \text{ Am}^2$  corresponds to a magnetic moment per Mn atom of  $0.85 \mu_B$ . This is significantly smaller than expected for a perfect ferromagnetic order. In addition, a kink is visible in the temperature scan around 100 K, which also indicates a “non-perfect” ferromagnetic behavior. The most likely explanation for the deviation from the antiferromagnetic ordering is probably a deviation of the stoichiometry from the nominal values. A  $300 \text{ \AA}$  LSMO layer with a nominal doping level of  $x = 0.44$  has been found to be ferromagnetic with a moment per Mn atom of  $1.5 \mu_B$  [61]. Therefore, the doping level in the sample with the LSMO layer below the BTO layer might be somewhere between  $x = 0.44$  and  $x = 0.5$ . Since the Sr effusion cell shows drifts of the evaporation rate around 2% /hr, a reduction of the rate after the rate calibration until the start of the film growth might result in a ferromagnetic LSMO layer. There is another possible explanation for the different magnetic behavior of both samples: even if they have exactly the same stoichiometry, the different strain mediated by the underlying layer - which in one case is the Nb:STO substrate, but in the other case the BTO thin film - might result in a different magnetic ordering. For doping levels close to, but smaller than  $x = 0.5$ , bulk LSMO is ferromagnetic. But a small tensile in-plane strain is sufficient to change the order to an A-type antiferromagnet (see strain versus doping level phase diagram (figure 2.5(b), [63, 116])). Assuming that both samples have a stoichiometry in this doping level range, the LSMO layer deposited on BTO might slip in the antiferromagnetic phase due to the larger in-plane strain. However, we have seen in the previous section, that the out-of-plane lattice constants are only slightly different.

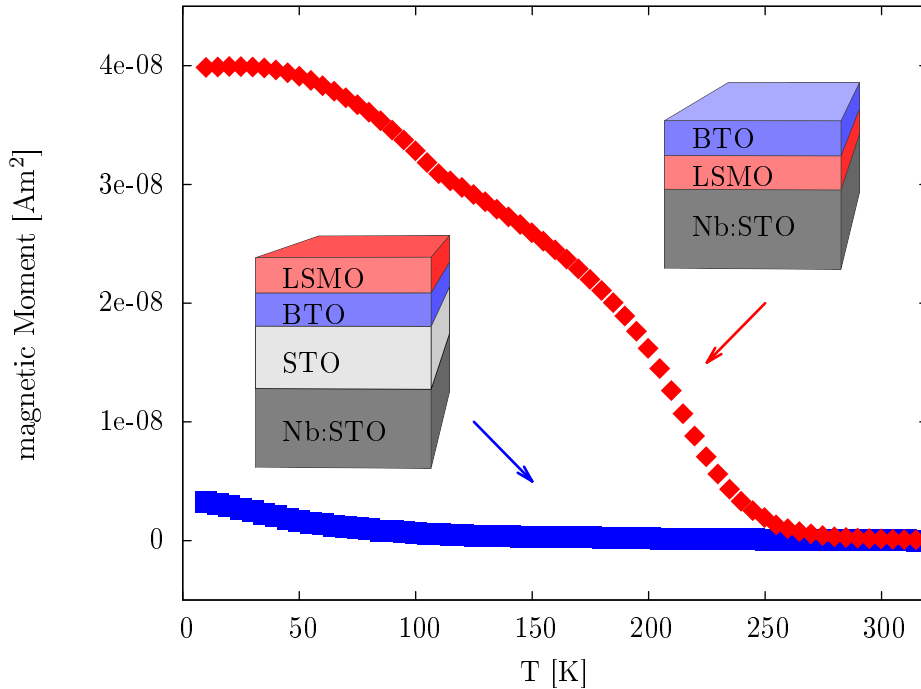


**Figure 8.7:** Temperature scans at 0.5 mT after cooling in a field of 1 T for both samples.

Even though the samples show clearly different magnetic properties, it needs to be emphasized that both LSMO layers have been grown one after another at the same day at the same growth conditions. Hence, there possibly is a small difference in the stoichiometry of both layers, but it is limited by the drifts of the evaporation rates. Therefore, the strong differences for LSMO

samples with equal or at least very similar stoichiometry show, that both LSMO layers have exactly the intended properties: they have a stoichiometry close to the phase boundary between the antiferromagnetic and ferromagnetic phases of LSMO.

The only missing requirement to the LSMO/BTO bilayers in order to investigate the theoretical predictions is for the BTO layers to be ferroelectric and the possibility of switching the polarization by an electric field. Not surprisingly, this has been proven to be a difficult task for the samples under investigation in this work with the very thin BTO layers. Indeed, the ferroelectric characterization is far from being completed and further work needs to be done in this part of the work (see also chapter 9 (outlook)). So far, it has been tried to analyze the ferroelectric properties with a commercial Radiant Precision LC apparatus (section 6.2.2). As mentioned before, a 80 nm SiO<sub>2</sub> film was deposited on the sample with the BTO layer on top of the LSMO layer. Afterwards, 100 nm thick gold electrodes have been sputtered on top of both samples to serve as a top electrode. Both electrodes have been contacted by bonding a wire on top of the gold pads and to the Nb:STO substrates. The wires have then be connected to the Radiant tester. In order to estimate the voltage needed to switch the polarization in a 15 u.c. ferroelectric BTO layer, the dielectric constants  $\epsilon$  of the materials between the electrodes need to be compared: as the voltage  $U$  applied to a capacitor is inversely proportional to the capacitance  $C$ , for the ratio  $U_1/U_2$  of the voltages dropping at the two layers in the samples follows:

$$\frac{U_1}{U_2} = \frac{C_2}{C_1} = \frac{\epsilon_2 A/d_2}{\epsilon_1 A/d_1} = \frac{\epsilon_2 d_1}{\epsilon_1 d_2} \quad (8.1)$$

where  $A$  is the area of the sample and  $d$  are the layer thicknesses. Since the two layers between the electrodes can be treated like a serial connection of two capacitors, the total voltage applied to the sample, i.e. between the gold pad and the substrate, adds up to  $U = U_1 + U_2$ . The required voltage to switch a BTO layer placed in a capacitor without additional material has been found to be about 3 V independent of the layer thickness and the dielectric constant of a BTO layer as thin as in our samples can be expected to be well below 20 [118]. Since SiO<sub>2</sub> has a very small dielectric constant of 4, this results with the thicknesses in the sample with the BTO layer on top of the LSMO in rather high voltages somewhere in the range between 10 and 100 V in order to get a sufficient voltage drop over the BTO layer. Since such high voltages can not be applied with the available Radiant tester, the measurements have been performed only for the sample with the LSMO layer on top. Due to the much higher dielectric constant of STO ( $\epsilon = 200$ ), it can be expected that more than half of the voltage applied between the top and bottom electrode of the sample drops at the BTO layer. Therefore, voltage well below 10 V should be sufficient to switch the ferroelectric polarization in BTO, if it behaves ferroelectric. In order to reduce the leakage currents, the sample has been cooled down to 70 K in the PPMS by placing it on a resistivity puck, which can be contacted from outside the cooling chamber.

Hysteresis curves have been measured with different voltage ranges up to 5 V and varying measurement times (1 to 100 ms). All  $Q$  versus  $V$  curves show the similar shape shown in figure 8.8. The measurements reveal the typical hysteretic artefacts known for lossy dielectric materials. The opening of the curve and the remanent  $Q$  value at zero voltage do not correspond to ferroelectric behavior, but are due to the second term in formula 6.7, which describes the leakage currents. Therefore, no ferroelectric behavior could be detected by using the Radiant tester up to now. In principle there are two possible reasons for this. The ferroelectric signal might be too weak to be clearly visible compared to the stronger dielectric loss signal caused by both, the STO and BTO layer. Secondly, the leakage currents could be too strong and avoid the switching of the electric dipole moments. In order to get a more accurate picture of the ferroelectric properties, a more detailed analysis of the reasons for the dielectric loss currents needs to be done. The most likely one to cause the leakage currents probably is the too extreme sample dimensions, especially

the BTO layer thickness. A study of smaller area capacitors of the same layer structure might reveal a the maximum possible values for the sample dimensions. It is also planned to analyze the samples by Piezo-Force-Microscopy in order to check the ferroelectric properties on smaller length scales and to obtain information on the domain sizes.

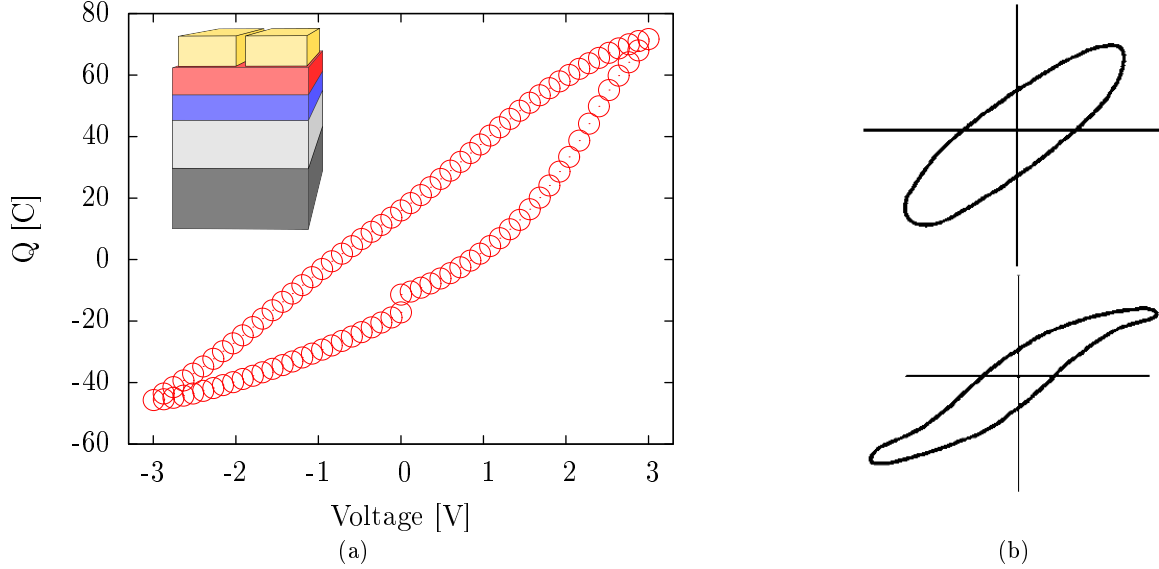


**Figure 8.8:** (a) Exemplary electrical characterization measurement of the sample with the LSMO layer on top of the BTO layer measured in 1 ms. No clear ferroelectric behavior is visible. The shape of the  $Q(E)$  curve looks very similar to a mixture of the well known hysteresis artefacts caused by linear ((b) top sketch) or nonlinear ((b) bottom sketch) lossy dielectric. The sketches in (b) are taken from [119].

### 8.3 Analysis of the magnetic depth profile

Even though the analysis of the ferroelectric properties of the BTO thin films still remains a challenging task to be done, the magnetic depth profile of the samples has been analyzed by XRMS measurements. The experimental setup has been used as described for the experiments in chapter 7. The samples have been mounted and adjusted in a way that the incoming and reflected x-ray beams pass through the gap left in the gold electrodes. By this, the strong absorption, which would result from the gold layer, is avoided, and the top two layers seen by the x-ray beam are the BTO and LSMO layers of the samples. In order to apply electric fields to the sample, small amounts of indium have been attached on the gold pads of the samples. To the indium thin copper wires have been compressed, which are lead out of the cryostat to a Keithley voltmeter. Data has been taken for both samples at 50, 100 and 150 K. At each temperature energy scans have been performed around the Mn  $L_{II}$  and  $L_{III}$  edges from 630 to 660 eV for three different incident angles  $\theta = 5, 10$  and  $20^\circ$ . Like for the LSMO/STO system discussed in the previous chapter, each measurement was done twice at opposite magnetic fields. The two resulting XMCD data sets are subtracted to eliminate a possible error signal caused by a difference between the initial intensities of the incoming LCP and RCP beam.

An exemplary set of temperature dependent XMCD measurements for the sample with the BTO on top of the LSMO layer is shown in figure 8.9. Similar to the LSMO/STO system in the previous chapter, no significant temperature dependence of the shape of the XRMS signal is

visible. Only the magnitude of the signal decreases with increasing temperature corresponding to the drop of the total magnetic moment of the samples.

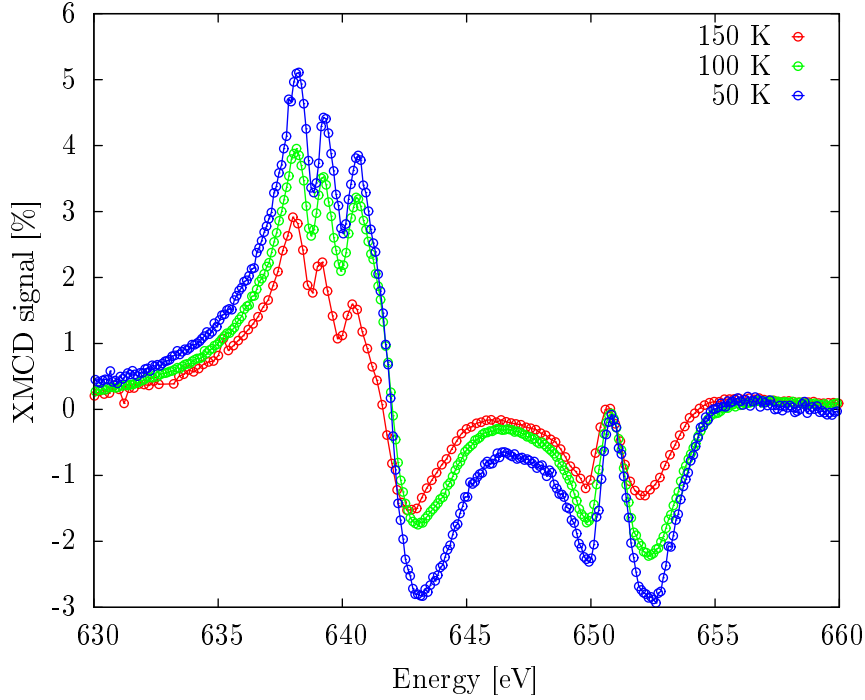


**Figure 8.9:** Temperature dependence of the XRMS signal at  $\theta = 10^\circ$  of the sample with the BTO layer on top of the LSMO layer.

A possible influence of an electric field on the magnetic profile has been investigated for a variety of different conditions for the sample with the BTO layer on top of the LSMO sample. An interface effect on the magnetic profile is expected to have a much stronger influence on the experimental data for this sample than for the one with the LSMO layer on top, since the LSMO/BTO interface is the top interface of the LSMO layer. As discussed before, the XRMS data is much more sensitive to changes at the top interface of the magnetic layer. Data has been taken again at 50, 100 and 150 K. The XMCD signal was measured at a lot of different applied electric fields up to 5 V, also at 0 V after applying +5 or -5 V. In addition the field dependent measurements have been taken in the maximum magnetic field of 0.05 T and at zero field, since it is not obvious under which condition the magnetic profile would be easier to manipulate. Data was also taken after field cooling and zero field cooling the sample to 50 and 100 K. No change in the magnetic profile has been detected for any of the described experimental conditions. In figure 8.10 three scans are shown for zero, maximum and negative maximum applied electric voltage at 50 K. The only difference visible is a change of the magnitude of the signal. However, this can not be due to an interface effect, since the shape and thus the magnetic profile remains the same. It seems to be unlikely, that an applied voltage changes the magnitude of the magnetic moment of the entire LSMO layer. It needs to be clarified, whether the difference in the scaling is an experimental artefact caused by the voltage. One possible reason could be a slightly different sample temperature, but, since the high voltage data shows the strongest signal, the temperature needs to be smaller at applied fields. A heating of the sample by the electric current would rather be expected.

Even though a reduced sensitivity to a change in the magnetic profile at the LSMO/BTO interface is expected, the electric field dependence was also checked for the sample with the LSMO layer

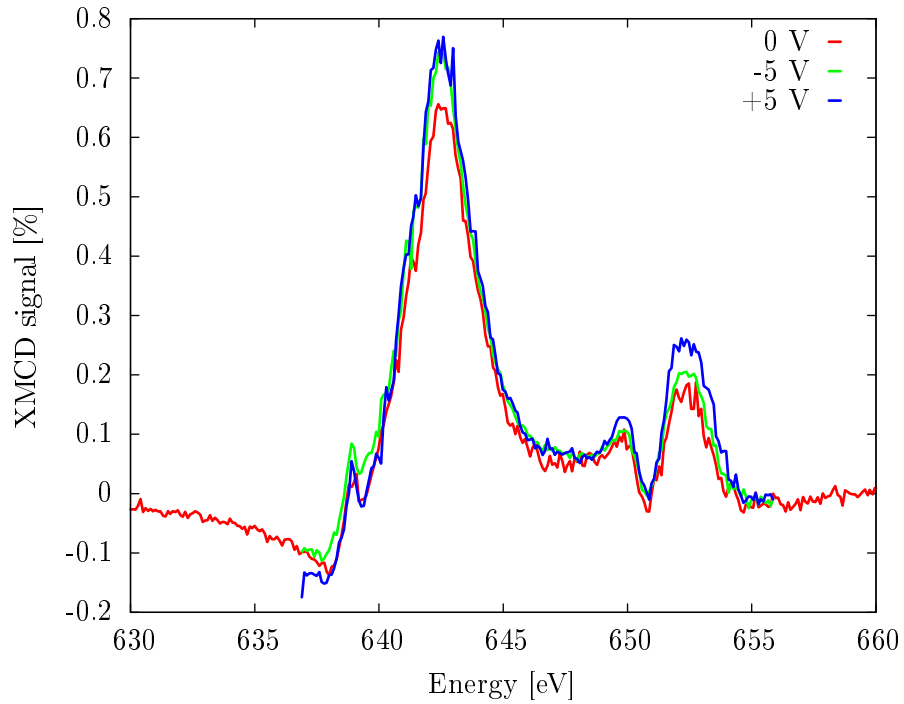


**Figure 8.10:** Electric field dependence of the XRMS signal of the sample with the BTO layer on top of the LSMO layer at 50 K for an incident angle of  $\theta = 10^\circ$ .

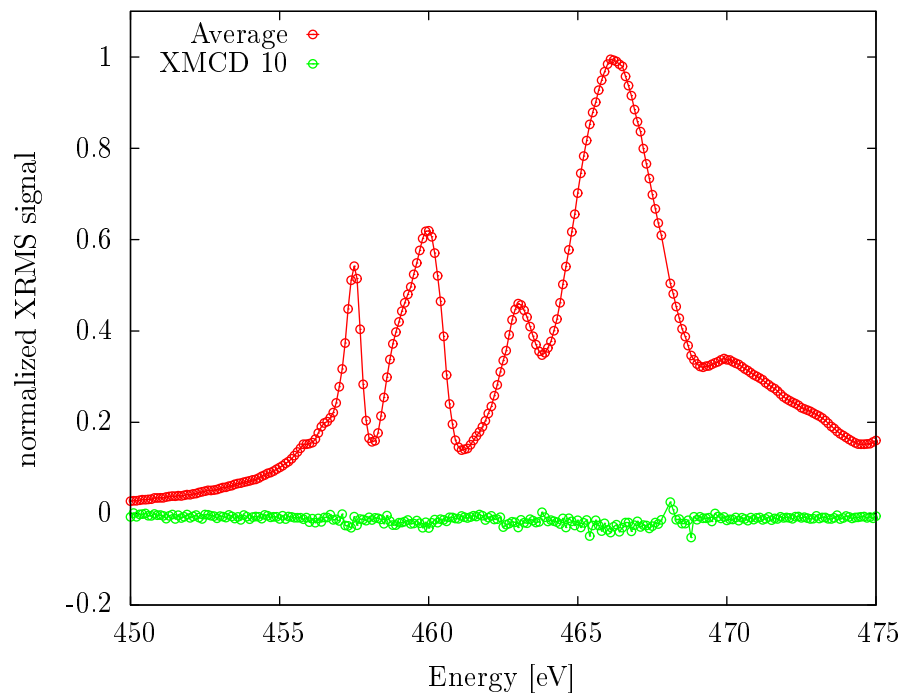


**Figure 8.11:** Average (LCP plus RCP) and XMCD signal measured around the Ti  $L_{II}$  and  $L_{III}$  edges on the sample with the LSMO on top of the BTO layer at 50 K and an incident angle of  $5^\circ$ .



on top of the BTO layer. As mentioned in the previous section, higher electric fields are expected to be needed for this sample, due to the small dielectric constant of SiO<sub>2</sub>. Similar to the previous sample, up to voltages of 8 V no influence on the XMCD data was detected. Unfortunately, a dielectric breakdown occurred after applying 10 V resulting in a short circuit through the sample, even though this voltage was expected to be well below the breakdown voltage. Therefore, further investigation was not possible. However, this sample was used to analyze a possible induced magnetization on Ti at the LSMO/BTO interface. In contrast to the magnetic profile in LSMO, this sample is better suited for the analysis of the BTO at the interface to LSMO. For this purpose energy scans at maximum field have been performed around the Ti L<sub>II</sub> and L<sub>III</sub> edges from 450 to 475 eV. The measurement at 50 K and an incident angle  $\theta = 5$  deg is shown in figure 8.11. Within the resolution of the experiment, no induced moment has been detected on Ti (the XMCD signal in the plot has already been multiplied by 10).

Since there is no dependence of the data visible on neither temperature nor electric field, in the following only the data taken at 50 K will be discussed in order to analyze the magnetic profile of the LSMO layer for both samples quantitatively. The biggest obstacle for the simulations is the fact that no indices of refraction and magneto-optical constants are available for the LSMO with doping level  $x = 0.5$ . It has been tried to determine the data by measuring the XMCD fluorescence signal of a thick LSMO standard sample of the same composition. However, the data was too noisy to extract reliable parameters for the  $N(E)$  and  $Q(E)$  values. Therefore, the indices of refraction and magneto-optical constants for LSMO with doping level  $x = 0.33$  have been used for the simulations. It has been seen in the previous chapter that the error made by using the “wrong” parameters is not too big, since good agreement to the PNR data was obtained even for samples with supposedly different Mn<sup>3+</sup>/Mn<sup>4+</sup> ratios.

The results for the sample with the BTO layer on top, which showed a ferromagnetic like behavior in the PPMS characterization, is shown in figure 8.12. Even though, there are some differences between the data and the best found simulation especially in the data for  $\theta = 15^\circ$ , the shape of the XMCD signal is reproduced very well by the simulations. It can be assumed, that the majority of the discrepancies is caused by using the  $N(Q)$  and  $Q(E)$  values for a doping level of  $x = 0.33$ . In spite of this, the results obtained from the best fit are in agreement with the general tendencies found on the LSMO/STO system and the macroscopic sample characterization: similarly to the results on the LSMO/STO samples in chapter 7, the best simulations yield slightly thinner layer thicknesses than obtained by XRR (about 5 %). Since no or only small thickness inhomogeneities are expected for the samples grown by OMBE (which was also proven by XRR), there must be an additional reason for the tendency of thinner layer thicknesses determined by XRMS. Apart from that, the parameters obtained from the fit are in agreement with the previous sample characterization. A homogeneous magnetization is found for the majority of the LSMO layer. The value for the size of the magnetization is about 30 % of the bulk value for LSMO having a doping level of  $x = 0.33$ . This conforms to a magnetic moment per Mn atom of roughly  $1 \mu_B$ . In addition, there is indication for slightly reduced magnetic moment at the interface to the Nb:STO substrate. Due to the strongly reduced magnetic moment compared to the maximum value for a purely ferromagnetic ordering, we already assumed from the PPMS measurements that the sample has a strong tendency to an antiferromagnetic order. The reduced magnetic moment at the interface could again be caused by the tensile in-plane strain caused by the substrate which favors the antiferromagnetic a-type order. From the magnetic profile given in figure 8.12 one can calculate an average magnetic moment of  $0.94 \mu_B$  per Mn atom. This value is slightly higher than the one obtained from PPMS. There are (at least) two possible reasons for the difference: If by XRMS only a smaller than the real chemical thickness is measured, but the total magnetic moment is determined correctly, one obtains a higher moment per Mn atom. Secondly, the size of the sample of  $7.5 \times 7.5 \text{ mm}^2$  can cause a systematic error in the PPMS measurement: the more

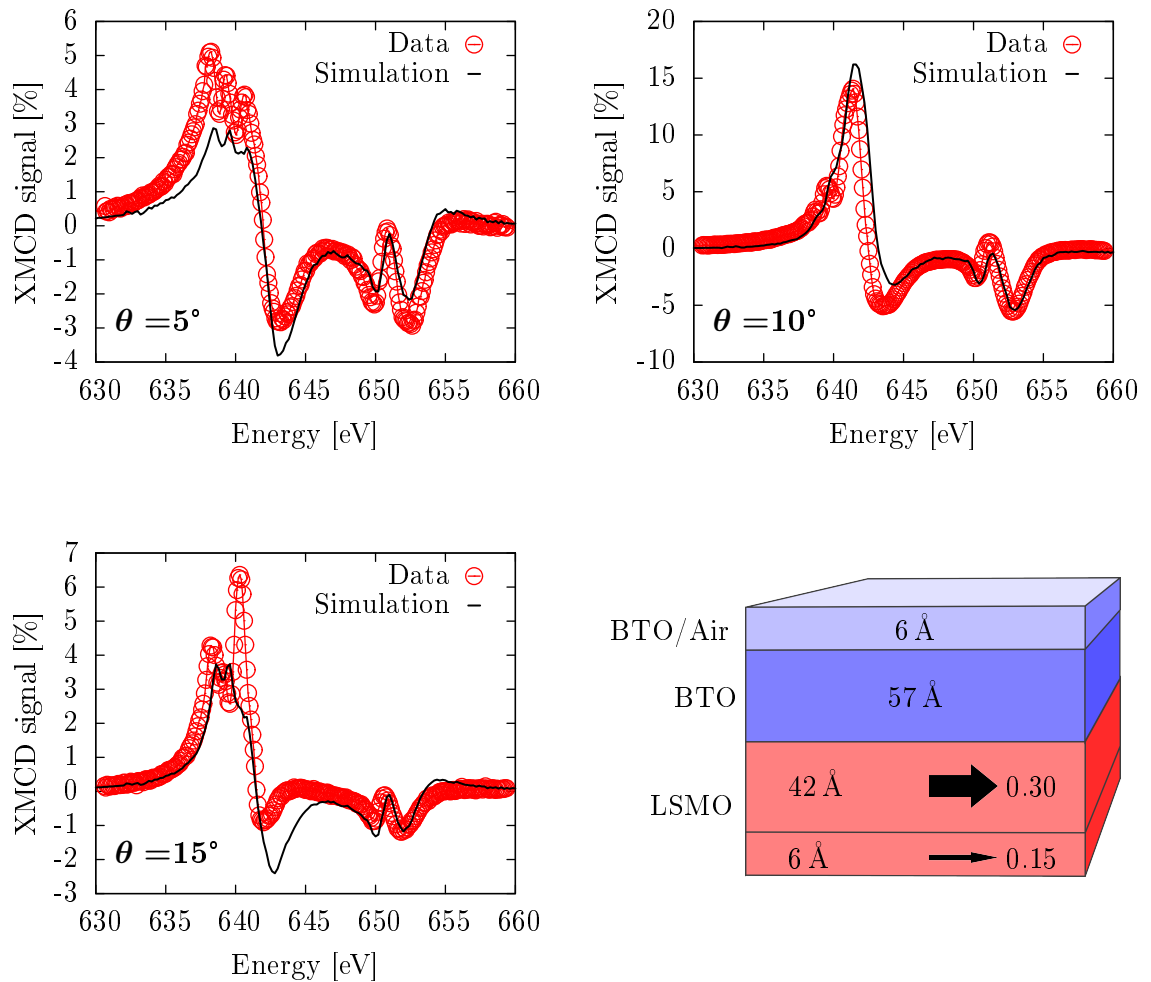


**Figure 8.12:** XMCD signal of the sample with the BTO layer on top of the LSMO layer for all three incident angles. The slab structure of the sample for the simulations is shown in the bottom right. Only the BTO and LSMO layer of the sample are shown. The thicknesses indicated are determined by the simulation of the reflectivity data. The arrow indicates a layer with non zero magnetic scattering length density, where the number to the right gives the fraction of the maximum theoretical value of LSMO having a doping level of  $x = 0.33$ .

a sample deviates from a point-like shape in the direction of the sample vibration, the more does the resulting moment deviate to smaller values.

The best fit for the sample with the LSMO top layer are shown in figure 8.13. First of all, it can be seen, that the XMCD signal is about 20 times smaller than for the previous sample. From the PPMS measurement the strong reduction was expected due to the antiferromagnetic like behavior of the sample. There is still a clear XMCD signal visible. For an antiferromagnetic material this can be explained by canted moments due to the applied magnetic field during the measurement. There is an additional factor that hampers the data evaluation: It was discussed before that there is a small difference between the incident intensities for the LCP and RCP x-ray beam. This results in an erroneous contribution in the XMCD data after subtracting the LCP from the RCP measurement. This error signal can be eliminated by measuring opposite fields and subtracting both XMCD signal from each other. This works very well in general, but it might cause additional uncertainties to the data of the antiferromagnetic sample: Since the error signal has a relative strength compared to the average signal, i.e. LCP plus RCP, of 0.5 to 0.7%, it is almost negligible for ferromagnetic samples, but it is stronger than the true XMCD signal of the antiferromagnetic sample discussed here (figure 8.14). Even though the elimination of the signal seems to work, it might add some variation to the resulting data. Despite all this, it was possible to reproduce most features of the data fairly good. Again the thicknesses are slightly smaller as compared to the XRR data, but reduced by the same amount as for the previous sample. The magnetic profile shows a very small magnetic moment in general having a value of 1.2% for the first 32 Å of the LSMO layer and 0.2% for the top 16 Å. The size of the magnetization seems to be reasonable for a canted antiferromagnet. The reduction of the moment at the surface might be due to a hindered canting by the reduced dimensionality compared to the rest of the layer. It needs to be clarified, that the absolute values obtained for thicknesses and magnetic moments have much bigger uncertainties than for the other sample or for the data evaluation of the LSMO/STO system. However, the magnetic profile is fairly fixed by the shape of the XMCD data. Therefore, at least the significant reduction of the average magnetic moment at the interface is a robust qualitative result even though the absolute values might not be as accurate as for the previous samples. This is a very important fact, since similar subtleties are probably not, but definitely not in the same amount of time detectable by PNR. It therefore shows the possible application of XRMS for determining even detailed magnetic profiles of samples with small average magnetic moments.

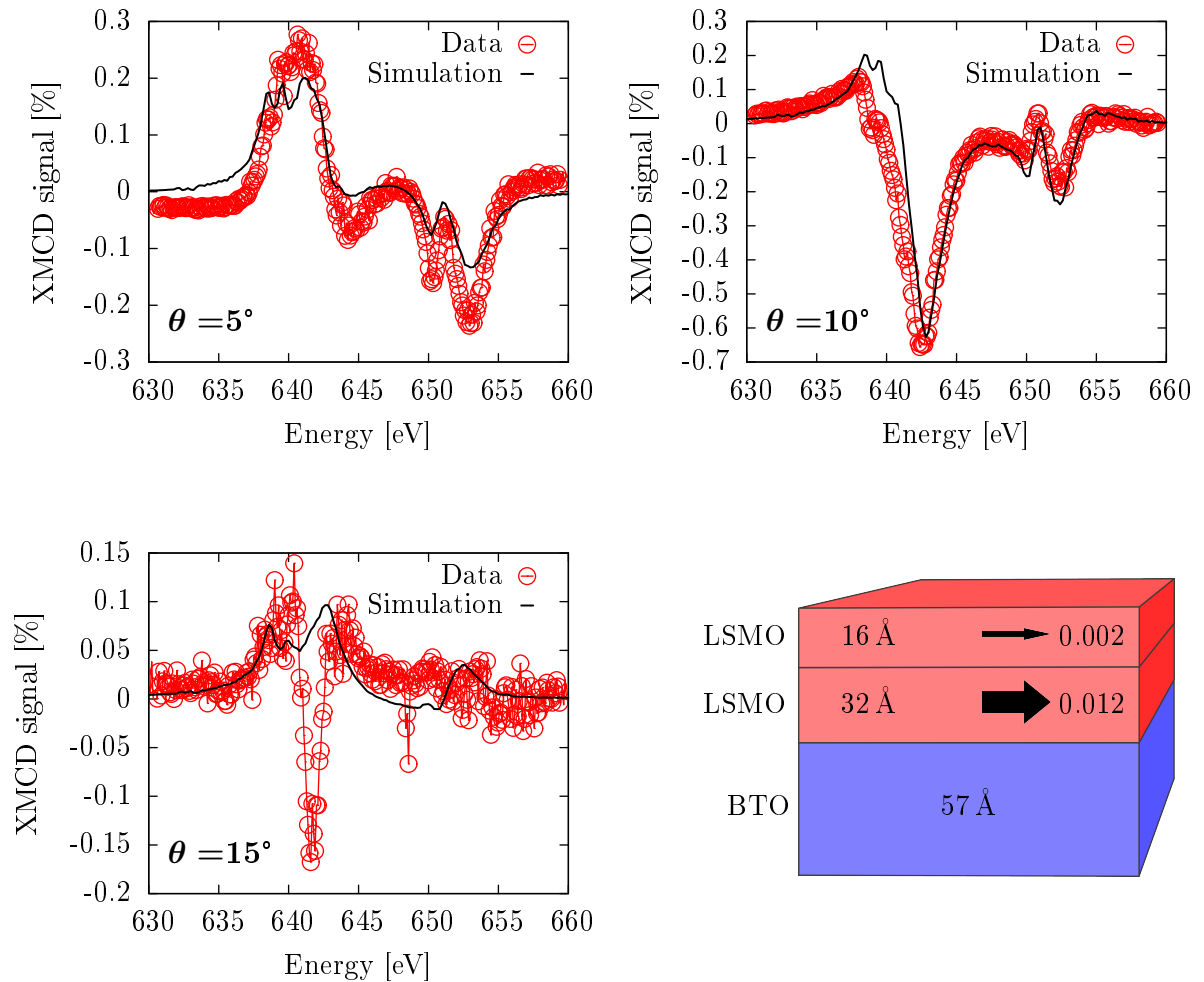
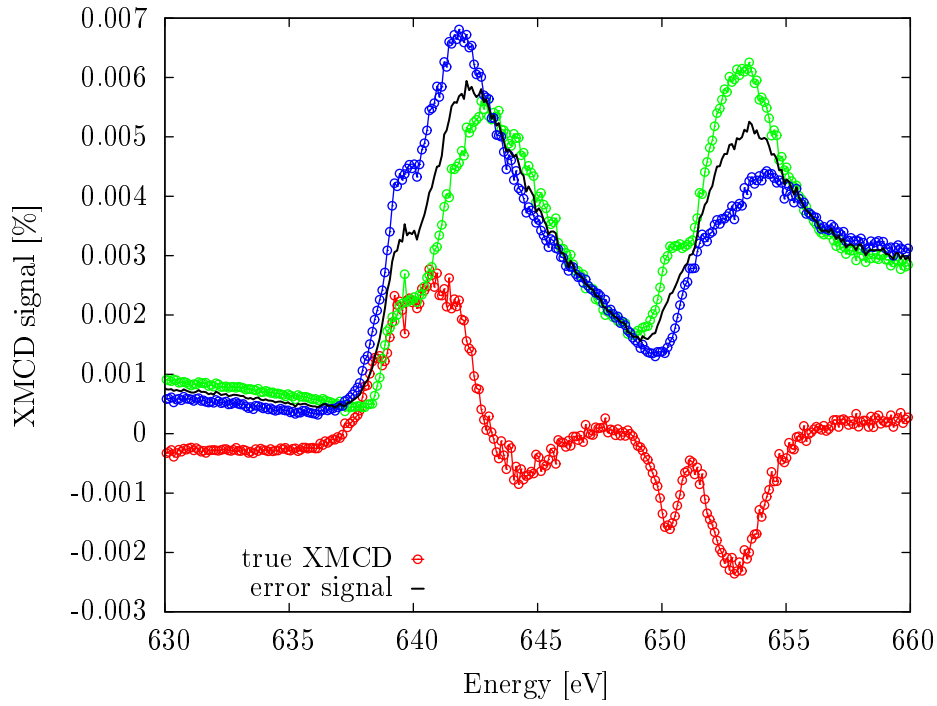
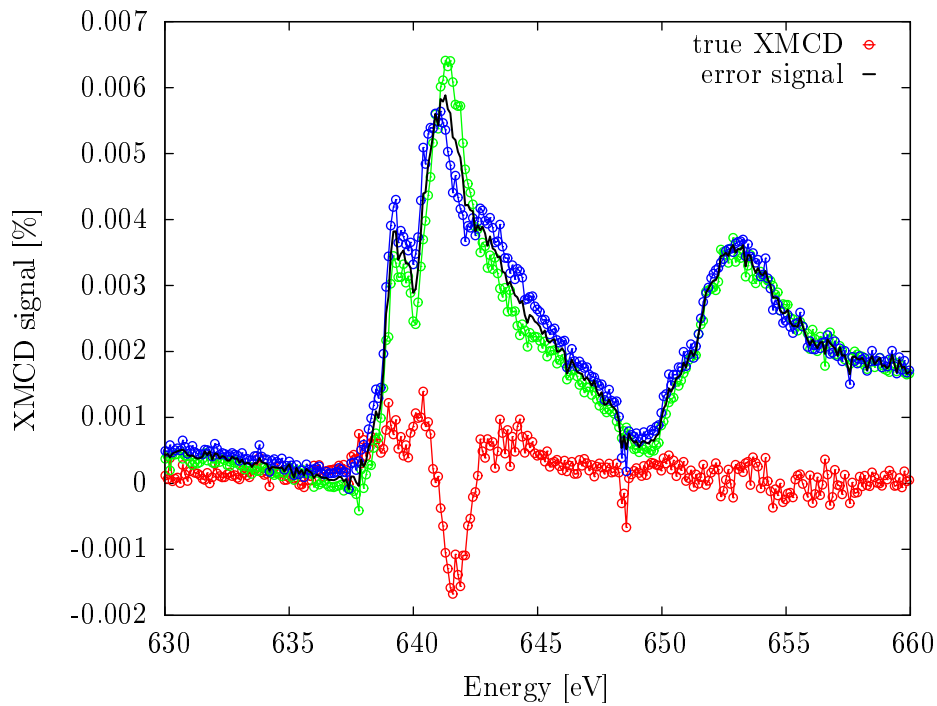


**Figure 8.13:** XMCD signal of the sample with the LSMO layer on top of the BTO layer for all three incident angles. The slab structure of the sample for the simulations is shown in the bottom right. Only the BTO and LSMO layer of the sample are shown. The thicknesses indicated are determined by the simulation of the reflectivity data. The arrow indicates a layer with non zero magnetic scattering length density, where the number to the right gives the fraction of the maximum theoretical value of LSMO having a doping level of  $x = 0.33$ .



(a)



(b)

**Figure 8.14:** Error signal for the sample with the top LSMO layer at incident angles  $\theta = 5^\circ$  (a) and  $\theta = 15^\circ$  (b). Plotted are the XMCD signal determined at  $+500$  Oe and  $-500$  Oe in green and blue, respectively. The average of both measurements (black solid line) gives the error signal. The difference (red) is the true XMCD signal shown in figure 8.13.

## 9 Summary, Conclusion and Outlook

In this work single crystalline thin films of oxide materials have been prepared and analysed. The results for both systems will be summarized and an outlook for possible future experiments will be given in the following.

### **La<sub>0.66</sub>Sr<sub>0.33</sub>MnO<sub>3-δ</sub>/SrTiO<sub>3</sub>**

The aim for the analysis of this system was a deeper understanding of the unusual occurrence of an Exchange Bias effect (EB) in this system reported by Zhu et al. [1] even though there is no nominal antiferromagnetic material present. Single crystalline La<sub>0.66</sub>Sr<sub>0.33</sub>MnO<sub>3-δ</sub> (LSMO) single and La<sub>0.66</sub>Sr<sub>0.33</sub>MnO<sub>3-δ</sub>/SrTiO<sub>3</sub> (LSMO/STO) bilayers have been prepared by High Oxygen Pressure Sputter Deposition and Pulsed Laser Deposition on (001) oriented SrTiO<sub>3</sub> substrates. The stoichiometry of the layers was confirmed by RBS except for the oxygen content, since the sensitivity of the RBS measurement is not sufficient to check the amount of oxygen contained in the layers.

It was possible, to reproduce the EB effect in samples grown by sputter deposition by varying the oxygen pressure during the growth. Whereas samples grown at oxygen pressures higher than 1.0 mbar showed symmetric ferromagnetic hysteresis curves, samples grown at lower oxygen pressures revealed an exchange bias effect. With decreasing oxygen pressure, the exchange bias field was increasing. Additionally, very strong indications have been found that the samples grown at lower oxygen pressures are oxygen deficient: enhanced out-of-plane lattice constants and reduced Curie temperatures have been detected. Both effects are well known consequences of oxygen deficiencies in LSMO or other manganite thin films. Furthermore, increasing coercive fields and reduced magnetic moments per Mn atom are also in accordance with previous findings, where they have been explained by inhomogeneities in the magnetic structure of the LSMO films [109, 110].

In order to understand, whether and how the oxygen deficiencies are linked to the exchange bias effect, the magnetic depth profiles in the samples have been determined by combining X-ray Reflectometry (XRR), Polarized Neutron Reflectometry (PNR) and X-ray Resonant Magnetic Scattering (XRMS). The analysis of the experimental data taken by the two complementary methods yield a completely ferromagnetically ordered LSMO layer in the sample without exchange bias effect. In contrary, in the samples grown at lower oxygen pressures, a region with strongly reduced magnetization was detected at the interface to the STO substrate. The thickness of this interface region is increasing with increasing exchange bias effect.

The results of the various experimental techniques lead to the following interpretation of the origin of the exchange bias in this system on the bases of the strain versus doping phase diagram established by Fang et al. [116] and Konishi et al. [63]: By a combination of oxygen deficiency and strain, the interface-near LSMO can shift to the antiferromagnetic region of the phase diagram. The major part of the LSMO layer, where the strain is released completely - or at least partly -, then orders ferromagnetically. In this way, the antiferromagnetic region in the sample can define the preferred orientation for the magnetization in the ferromagnetic part of the LSMO

layer, which is needed in order to create an exchange bias effect. It is important to note that since the EB effect is purely due to the LSMO layer and the STO substrate is only needed to mediate the strain, one is not limited to having to choose an antiferromagnet on the one side and a ferromagnet on the other side of the chemical interface to create an EB effect. This opens up the opportunity of choosing the second material independently as long as it sets the right strain to the magnetic layer. As in our case, one layer need not to be magnetic at all, but could have other properties, which possibly create completely new and more versatile functionalities.

Even though the single results can be put together to a comprehensive picture of the origin of the exchange bias effect in the LSMO single and LSMO/STO bilayers, there are open questions, which are of big interest for future investigations: In order to proof that the reduction of the magnetization at the interface is caused by strain, a detailed analysis of the lattice parameters in the LSMO needs to be done depth resolved. Since the intensity at laboratory x-ray instruments is not sufficient for this purpose, these experiments need to be performed at a synchrotron source. Instead of analyzing the existing samples, preparing a set of very thin LSMO layers of varying layer thicknesses under the same growth conditions might be an alternate way to approach this question. In these samples it might be easier to investigate the evolution of the out-of-plane lattice constant as a function of the distance to the STO interface. Secondly, it might be interesting to analyze, how the properties of the samples alter after annealing them in vacuum and oxygen atmosphere, respectively. It has been reported by other groups [120] that the oxygen stoichiometry can be influenced by annealing even after the preparation of the samples. Therefore, one should investigate, whether the size of the exchange bias can be shifted to larger or smaller values by such annealing treatments. Finally, the exact magnetic structure on a microscopic length scale - especially in the near interface region - needs to be resolved. Information on the proposed inhomogeneous magnetic structure of the LSMO layers could be analysed by off-specular PNR. In addition, Polarized Neutron Diffraction could be applied in order to detect additional magnetic reflections, which are caused by a possible antiferromagnetic structure in the samples. E.g. an layered antiferromagnetic order would give rise to half-integer reflections due to the doubling of the unit cell. Both neutron experiments require the preparation of LSMO/STO superlattices, since the expected intensities are too small for single or bilayer samples. Another promising experiment to reveal antiferromagnetic regions in the samples might be the application of X-ray Magnetic Linear Dichroism (XMLD): since the XMLD signal is proportional to the square of the magnetic moments, it is also sensitive to antiferromagnetic structures. By subtracting the contributions of the ferromagnetic part of the sample to the XMLD signal, one may be able to provide evidence for antiferromagnetic ordered regions in the sample. By performing the experiment in reflectometry geometry - similar to the XMCD experiments in this work -, it might even be possible to gain depth resolved information on the antiferromagnetic structure of the sample and thus get a more detailed picture of the overall magnetic structure in the LSMO/STO system. By this, it might not only be possible to proof, to what extend the interface region is ordered antiferromagnetically. One might also gain information, whether the ferromagnetic part of the layers is ordered homogeneously or whether there are also antiferromagnetic regions present in this part of the layer. This might lead to a deeper understanding of the proposed inhomogeneities in the oxygen deficient LSMO layers, which are believed to cause the experimental results discussed in chapter 7.2 (enhanced coercive fields, lower Curie temperatures, lower saturation moments).

## **La<sub>0.5</sub>Sr<sub>0.5</sub>MnO<sub>3</sub>/BaTiO<sub>3</sub>**

Burton et al. proposed the possibility of creating an artificial multiferroic material by arranging La<sub>0.5</sub>Sr<sub>0.5</sub>MnO<sub>3</sub> and BaTiO<sub>3</sub> in a thin film system [2]. Their theoretical calculations resulted in the possibility of changing the magnetic structure of LSMO at the interface by switching

---

the electric polarization in the BTO layer. Therefore,  $\text{La}_{0.5}\text{Sr}_{0.5}\text{MnO}_3/\text{BaTiO}_3$  bilayers have been prepared by Oxide Molecular Beam Epitaxy (OMBE). The stoichiometry of the samples has been controlled by evaporation rate calibration prior and after the deposition. Epitaxial layer-by-layer growth was confirmed by in-situ RHEED analysis. The Nb doped STO substrate and a gold layer sputtered on top of the sample have been used as a bottom and top electrode, respectively, for the electrical contacting. The intention to analyze the magnetic depth profile by XRMS and PNR limited the thicknesses of the LSMO and BTO layer to values smaller than 15 u.c.. Therefore, in order to minimize the leakage currents of the samples, when an electric field is applied, an additional insulating layer was placed between the top and bottom electrode.

Atomically smooth interfaces and high crystalline quality have been detected by XRR and XRD. The macroscopic magnetic properties of the samples have been shown to be strongly dependent on the stacking order of the BTO and LSMO layers: whereas the sample with the BTO layer on top of the LSMO layer showed ferromagnetic behavior, the sample with the opposite arrangement revealed antiferromagnetic signature in the temperature dependent magnetization measurements. Since both sample have been grown under the same conditions, this proves that the stoichiometry of the LSMO films is very close to the desired value, namely at the border in the phase diagram between the ferromagnetic and antiferromagnetic region. The characterization and controlling of the electric polarization of the thin BTO layers remains the major problem in this system. So far no clear proof of ferroelectricity was obtained in the thin film samples.

The XRMS measurements did not reveal any influence of the application of an electric voltage between the top and bottom electrodes of the samples on the magnetic profile of the LSMO layer, which can be due to two reasons: in contrary to the theoretical predictions, the switching of the polarization in BTO in the samples does not cause a change in the magnetic profile at the interface. Or, secondly, the thin BTO layer is not ferroelectric at least not on the large length scales, which have been used in this work. However, it was possible to analyze the magnetic profiles of the samples quantitatively by simulating the experimental data. The results are in agreement with the macroscopic magnetic characterization: a much larger ferromagnetic moment was detected for the ferromagnetic sample than for the antiferromagnetic one. The small non-zero net magnetization in the antiferromagnetic sample probably is caused by tilted magnetic moments due to the applied magnetic field during the measurement. The tilting seems to be suppressed at the interface to air. Especially the analysis of the antiferromagnetic sample proofs the strength of the XRMS experimental technique: Even in samples with very weak magnetic signal - like antiferromagnetic ordered thin films - it is possible to analyze the magnetization depth dependent, which is much harder e.g. by PNR.

Future investigations of this system definitely need to prioritize the characterization of the ferroelectric properties of the BTO in order to be able to switch the polarization reliably. This can be done on the one hand by applying additional experimental techniques like Piezo-Force-Microscopy. On the other hand, since the leakage currents in BTO are a well known problem, one might think about alternate ferroelectric materials even though the theoretical calculations have been done for BTO. Alternatively, the use of different substrates might reduce the leakage currents as has been seen in previous works [118].





# A. Fit results of the XRR and PNR data evaluation

In this section all parameters and results will be listed for the best obtained fits to the experimental XRR and the PNR data taken at 5 K. The statistical errors are determined as discussed in the result sections. Parameters indicated as “fixed” have been kept constant during the fitting procedure. Layer thicknesses and rms roughness are given in Å, scattering length densities (SLD) in  $10^{-6} \text{Å}^{-2}$ . In chapter 7 and 8 the thicknesses of the surface layers have been added to the thicknesses of the top material as described in the discussion.

## A.1 $\text{La}_{0.66}\text{Sr}_{0.33}\text{MnO}_{3-\delta}/\text{SrTiO}_3$

### A.1.1 XRR

LSMO/STO bilayer grown by PLD:

Surface layer thickness	8.0 (fixed)
Surface layer SLD real part	3.6 (6)
Surface layer SLD imaginary part	0.16 (3)
Surface layer rms roughness	4.2 (5)
STO layer thickness	70 (2)
STO layer SLD real part	15.0 (fixed)
STO layer SLD imaginary part	0.68 (fixed)
STO layer rms roughness	2.5 (5)
LSMO layer thickness	85 (2)
LSMO layer SLD real part	18.0 (fixed)
LSMO layer SLD imaginary part	1.88 (fixed)
LSMO layer rms roughness	2 (5)
STO substrate SLD real part	15.0 (fixed)
STO layer SLD imaginary part	0.68 (fixed)
STO substrate rms roughness	2.4 (5)
Layer inhomogeneity parameter [%]	6.8 (4)
Figure of merit (x1000)	0.66

**LSMO/STO bilayer grown by HSD at 1.0 mbar:**

Surface layer thickness	8.0 (fixed)
Surface layer SLD real part	5.2 (6)
Surface layer SLD imaginary part	0.23 (3)
Surface layer rms roughness	12 (1)
STO layer thickness	60 (2)
STO layer SLD real part	15.0 (fixed)
STO layer SLD imaginary part	0.68 (fixed)
STO layer rms roughness	4.4 (5)
LSMO layer thickness	87 (2)
LSMO layer SLD real part	18.0 (fixed)
LSMO layer SLD imaginary part	1.88 (fixed)
LSMO layer rms roughness	4.5 (5)
STO substrate SLD real part	15.0 (fixed)
STO layer SLD imaginary part	0.68 (fixed)
STO substrate rms roughness	3.0 (5)
Layer inhomogeneity parameter [%]	5.0 (3)
Figure of merit (x1000)	1.95

**LSMO single layer grown by HSD at 0.8 mbar:**

Surface layer thickness	8.0 (fixed)
Surface layer SLD real part	9.0 (8)
Surface layer SLD imaginary part	0.9 (1)
Surface layer rms roughness	3.3 (5)
LSMO layer thickness	105 (1)
LSMO layer SLD real part	18.0 (fixed)
LSMO layer SLD imaginary part	1.88 (fixed)
LSMO layer rms roughness	16 (2)
STO substrate SLD real part	15.0 (fixed)
STO layer SLD imaginary part	0.68 (fixed)
STO substrate rms roughness	4.4 (5)
Layer inhomogeneity parameter [%]	5.6 (4)
Figure of merit (x1000)	2.69

---

### LSMO single layer grown by HSD at 0.6 mbar:

Surface layer thickness	10 (2)
Surface layer SLD real part	9.4 (8)
Surface layer SLD imaginary part	1.0 (1)
Surface layer rms roughness	2.0 (5)
LSMO layer thickness	177 (2)
LSMO layer SLD real part	18.0 (fixed)
LSMO layer SLD imaginary part	1.88 (fixed)
LSMO layer rms roughness	21 (3)
STO substrate SLD real part	15.0 (fixed)
STO layer SLD imaginary part	0.68 (fixed)
STO substrate rms roughness	2.0 (5)
Layer inhomogeneity parameter [%]	3.9 (3)
Figure of merit (x1000)	2.93

### A.1.2 PNR at 5 K

Since the chemical interfaces can not be resolved by PNR due to the very similar nuclear SLD of STO and LSMO, the layer with a non-zero magnetic SLD is denoted as “FM layer” in the following lists. One has to keep in mind that the layers in the following lists do not necessarily correspond to the true chemical layers, but to regions of different magnetic SLDs. For details see discussion in chapter 7.

### LSMO/STO bilayer grown by PLD:

STO layer thickness	66 (3)
STO layer SLD real part	3.5 (3)
STO layer SLD imaginary part	0 (fixed)
STO layer rms roughness	10 (7)
FM layer thickness	86 (3)
FM layer SLD real part	3.5 (3)
FM layer SLD imaginary part	0 (fixed)
FM layer magnetic SLD	1.35 (8)
FM layer rms roughness	6 (6)
STO substrate SLD real part	3.3 (3)
STO layer SLD imaginary part	0 (fixed)
STO substrate rms roughness	5 (5)
Figure of merit (x1000)	11.3

**LSMO single layer grown by HSD at 0.8 mbar:**

FM layer thickness	95 (4)
FM layer SLD real part	3.5 (3)
FM layer SLD imaginary part	0 (fixed)
FM layer magnetic SLD	1.06 (8)
FM layer rms roughness	15 (7)
STO substrate SLD real part	3.4 (3)
STO layer SLD imaginary part	0 (fixed)
STO substrate rms roughness	5 (5)
Figure of merit (x1000)	6.64

**LSMO single layer grown by HSD at 0.6 mbar:**

LSMO layer thickness	140 (10)
LSMO layer SLD real part	3.1 (3)
LSMO layer SLD imaginary part	0 (fixed)
LSMO layer magnetic SLD	0.34 (4)
LSMO layer rms roughness	24 (10)
STO substrate SLD real part	3.3 (3)
STO layer SLD imaginary part	0 (fixed)
STO substrate rms roughness	5 (5)
Figure of merit (x1000)	82.1

**A.2  $\text{La}_{0.5}\text{Sr}_{0.5}\text{MnO}_3/\text{BaTiO}_3$** **A.2.1 XRR****LSMO/BTO bilayer with LSMO on top of BTO:**

LSMO layer thickness	51 (2)
LSMO layer SLD real part	17.6 (fixed)
LSMO layer SLD imaginary part	1.62 (fixed)
LSMO layer rms roughness	4.0 (5)
BTO layer thickness	66 (2)
BTO layer SLD real part	16.8 (fixed)
BTO layer SLD imaginary part	1.82 (fixed)
BTO layer rms roughness	2.5 (4)
STO layer thickness	391 (2)
STO layer SLD real part	15.0 (fixed)
STO layer SLD imaginary part	0.68 (fixed)

---

STO layer rms roughness	3.5 (5)
Nb:STO substrate SLD real part	15.8 (4)
Nb:STO layer SLD imaginary part	0.72 (2)
Nb:STO substrate rms roughness	2.7 (5)
Layer inhomogeneity parameter [%]	6.8 (4)
Figure of merit (x1000)	1.16

**LSMO/BTO bilayer with BTO on top of LSMO:**

Surface layer thickness	6 (2)
Surface layer SLD real part	6.2 (2)
Surface layer SLD imaginary part	0.23 (3)
Surface layer rms roughness	6.1 (6)
BTO layer thickness	66 (2)
BTO layer SLD real part	16.8 (fixed)
BTO layer SLD imaginary part	1.82 (fixed)
BTO layer rms roughness	2.0 (3)
LSMO layer thickness	52 (2)
LSMO layer SLD real part	17.6 (fixed)
LSMO layer SLD imaginary part	1.62 (fixed)
LSMO layer rms roughness	3.8 (4)
Nb:STO substrate SLD real part	15.4 (4)
Nb:STO layer SLD imaginary part	0.70 (2)
Nb:STO substrate rms roughness	3.2 (3)
Layer inhomogeneity parameter [%]	5.0 (3)
Figure of merit (x1000)	2.56



## B. List of Figures

2.1	Different unit cells for the perovskite structure. a) cubic, b) tetragonal: the unit cell is elongated along $\vec{c}$ . In addition the central atom is shifted along the same direction, c) rhombohedral unit cell due to tilting of the oxygen octahedra . . . .	4
2.2	Influence of the octahedral coordination of the transition metal ion on the electronic energy levels in a local picture . . . . .	5
2.3	Figurative explanation of exchange interactions in LSMO. A superexchange interaction between the $t_{2g}$ orbitals and the double exchange between Mn ions of different valencies is shown. The illustrated $t_{2g}$ SE between Mn ions of the same valence state results in a preferred antiferromagnetic orientation (strictly speaking, this only holds for a $180^\circ$ Mn-O-Mn bonding angle). The DE between Mn ions of different valence state results in a preferred ferromagnetic ordering of the magnetic moments. In addition, further SE interactions can occur also between Mn ions of the same valency via the $e_g$ orbitals. Depending on the occupation of the $d$ orbitals, the semi-empirical Goodenough-Kanamori rules can be applied to predict the magnetic SE mechanisms in LSMO [55–57]. . . . .	9
2.4	Orbital order in LMO due to Jahn-Teller distortions. By applying the Goodenough-Kanamori rules one obtains ferromagnetic order in the x-y-plane and antiferromagnetic order along z, resulting in total in an a-type antiferromagnetic order. The empty $d_{x^2-y^2}$ orbitals are not depicted. . . . .	10
2.5	Magnetic phase diagrams of $\text{La}_{1-x}\text{Sr}_x\text{MnO}_3$ . a) Temperature versus doping level phase diagram taken from [52]. b) Strain versus doping level phase diagram taken from [62] (Original data by [63]). The magnetic structures of the different phases are shown in the right diagram. The notation follows the definitions by [64]. . . .	11
3.1	Schematic explanation of the Exchange Bias effect: When cooled in field, the ferromagnet orders at the Curie temperature $T_C$ (1). Further cooling results in ordering of the antiferromagnetic material at $T_N$ (2). In this simple example of a layered antiferromagnetic material, the direction of spins at the interface is determined by the exchange energy between the ferromagnet and antiferromagnet. Due to this pinning by the uncompensated spins of the antiferromagnet, the magnetization of the ferromagnet resists to being turned to the opposite direction by switching the magnetic field (3). Hence the coercive field becomes bigger compared to the case, when the ferromagnet is not coupled to the antiferromagnet (4). On the other hand, when the field is switched back to the original cooling field direction, the magnetization of the ferromagnet already reverses at a lower field in order to return to the energetically favored orientation (5). As a result the hysteresis curve is shifted along the magnetic field axis. . . . .	14
4.1	Scattering geometry for a general scattering event of a particle with incoming wavevector $k_i$ and outgoing wavevector $k_f$ . . . . .	18
4.2	Plot of the Laue function for $N=5$ and $N=10$ . . . . .	20
4.3	Definitions of symbols for the general case of a reflectometry experiment . . . . .	21



4.4	Graphical explanation for the non-sensitivity to microscopic length scales in a reflectometry experiment (taken from [76]). . . . .	22
4.5	Reflectometry from a single layer: The path difference between the beam reflected at the surface and at the interface leads to the Bragg condition for constructive interference . . . . .	23
4.6	Scattering geometry of the PNR experiment: The Up-Up channel is shown, i.e. the spins of both the incoming and reflected neutrons are oriented parallel to the applied magnetic field $\vec{H}$ . $\vec{H}$ causes a magnetization $\vec{M}$ , leading to a magnetic induction $\vec{B} = \mu_0(\vec{H} + \vec{M})$ in the sample with two in plane components $B_{\parallel}$ and $B_{\perp}$ . . . . .	25
4.7	Figurative explanation of the first order and second order processes described by formula (4.28). . . . .	26
4.8	Illustration of the origin of XMCD. Depicted is the band structure and atomic electronic configuration for a $3d$ metal with half filled d-orbital. The calculated absorption probabilities depending on the angular momentum $q$ fo the photon (+1 corresponds to RCP, -1 to LCP) for the $L_3$ and $L_3$ edges. On the left hand side, the resulting sum and difference signal of the two possible circular polarizations is shown. A,B and C indicated intensities needed to apply the sum rules (formula (4.30) and (4.31)). . . . .	28
4.9	Scattering geometry of the XRMS experiment: the incoming circular polarized beam is reflected from the surface of the sample. In contrast to the PNR scattering geometry, the magnetic field is applied in the scatterin plane. This also results in a magnetic induction in the sample in the scattering plane, i.e. $B_{\parallel} = 0$ . In this case the dielectric tensor $\epsilon$ is given by (4.33). . . . .	29
5.1	The different possible growth modes for homoepitaxial (left) and heteroepitaxial growth (right). . . . .	32
5.2	Sketch of the HSD chamber used in this work. The picture shows the oxygen plasma burning at the target during deposition. In the lower part the shielding of the substrate heater is visible. The substrate is deposited on top of it facing the target. . . . .	33
5.3	Sketch of the PLD chamber used in this work. The picture shows the oxygen plasma burning at the target during deposition. In the lower part the shielding of the substrate heater is visible. The substrate is deposited on top of it facing the target. Figure is taken from [97]. . . . .	35
5.4	Picture of the OMBE system used in this work. . . . .	36
6.1	Schematic explanation of the RHEED intensity oscillations of the specular intensity during layer by layer growth. Depending on the coverage rate $\theta$ , the roughness of the surface and hence off-specular scattering increases resulting in a reduction of the specular intensity. After arriving at a minium for $\theta = 0.5$ , the specular intensity increases again until it returns to a maximum, when the layer is completed. . . . .	38
6.2	Schematic drawing of the AFM instrument used in this work taken from [97]. . . . .	39
6.3	Sketch of a VSM like it is used in this work inside the Quantum Design PPMS. . . . .	40
6.4	Drawing of the reflectometer geometry taken from [97]. . . . .	41
6.5	Drawing of the 4-circle geometry taken from [97]. . . . .	42
6.6	Beamline layout of the polarized neutron reflectometer MAGICS at the SNS taken from [100] . . . . .	43
6.7	Schematic drawing of the TOF principle for the parameters used at MAGICS . . . . .	43
6.8	Scattering geometry of beamline 4-ID-C at Sector 4 of the APS taken from [101] . . . . .	44
6.9	Experimental configuration at the XRMS station of beamline 4-ID-C (taken from [102]). . . . .	44

7.1	AFM picture of a substrate after the annealing procedure. Atomically flat surfaces can be seen in the topography picture. In the phase picture different colored areas correspond to different terminated surface regions (SrO or TiO <sub>2</sub> ) . . . . .	45
7.2	RBS measurement of a LSMO/STO bilayer grown by PLD. The colored areas correspond approximately to the contributions of the different elements to the RBS spectrum for incidence along a random direction (but almost perpendicular to the sample surface). The simulation is the expected spectrum for a La <sub>0.66</sub> Sr <sub>0.33</sub> MnO <sub>3</sub> /SrTiO <sub>3</sub> bilayer grown on a SrTiO <sub>3</sub> substrate with layer thicknesses of 95 and 580 Å, respectively, confirming the desired stoichiometry. The channeling spectrum is shown as well (blue data points). . . . .	46
7.3	Motivation for the two additional aspects introduced to fit the XRR data . . . .	47
7.4	Three different profiles for the surface of a LSMO layer of a total thickness of 100 Å. Red: 100 Å LSMO with rms-roughness 5 Å and no additional surface layer. For the simulations of the XRR measurement this simple model of the surface is not sufficient to represent the data. Green: 96 Å LSMO layer with rms-roughness 3 Å and a 8 Å surface layer with rms-roughness 7 Å. The density of the surface layer is 50 % resulting in a total LSMO layer thickness of 100 Å. Blue: 96 Å LSMO layer with rms-roughness 8 Å and a 8 Å surface layer with rms-roughness 3 Å. . .	48
7.5	XRR data of the four samples under detailed investigation in this work. The thicknesses indicated are determined by the simulation of the reflectivity data. Detailed results can be found in table 7.1 . . . . .	49
7.6	AFM measurements of the surfaces of (a) the bilayer grown by PLD and (b) the LSMO single layer grown by HSD at 0.8 mbar. The histograms of the height distribution for both samples is shown in (c) and (d), respectively. Higher roughnesses and asymmetric height distribution is visible for the HSD sample, which probably is the reason for the necessity of introducing a surface layer in the XRR experiments: the surface roughness cannot be simulated by a single rms roughness parameter. . . . .	50
7.7	$\theta/2\theta$ -scan around the (004) reflections of STO and LSMO. Red: data taken on Bruker reflectometer without monochromator. Blue: data taken on Bruker diffractometer with monochromator . . . . .	52
7.8	$\theta/2\theta$ -scans around the (004) reflections of STO and LSMO. Fits are obtained by using the <i>plot.py</i> data evaluation software [108]. Left: LSMO single layer grown at 0.8 mbar. The fit yields an out-of-plane lattice constant of 3.840 Å. Right: LSMO single layer grown at 0.6 mbar. The fit yields an out-of-plane lattice constant of 3.876 Å (solid line). The corresponding positions of the LSMO (004) reflections are indicated, which seem to be shifted to higher $Q_z$ values due to the merging with the substrate reflection. A possible explanation for the additional intensity at higher $Q_z$ is a strained LSMO region at the STO interface (dashed line). . . .	53
7.9	(0KL)-maps of a (a) LSMO/STO multilayer with 5 periods grown by PLD under the same conditions like the PLD bilayer discussed in this work and (b) a thick ( $\sim 1500$ Å) LSMO single layer grown by HSD. The K and L indices refer to the lattice parameter. In (a) the substrate reflection is splitted in a Cu- $K_{\alpha 1}$ and Cu- $K_{\alpha 2}$ reflection. The strong background in $K = L$ direction is due to Bremsstrahlung. In (b) the splitting between Cu- $K_{\alpha 1}$ and Cu- $K_{\alpha 2}$ is not resolved, but the Bremsstrahlung background is visible as well. For both samples, the thin film reflection reveals the same K value - and hence the same in-plane lattice parameter - like the STO substrate indicating epitaxial growth. The L values are about 2.04 and 3.04 in (a) and (b), respectively. Data was taken on the Huber diffractometer without monochromator. . . . .	54

7.10	Rocking curves ( $\theta$ -scans) around the (004) reflections of the LSMO single layers grown at 0.8 and 0.6 mbar. Small FWHM indicate high crystalline quality for both samples. The broad Lorentzian-shaped background is probably caused by the nearby substrate reflection. . . . .	55
7.11	Temperature scans at 0.5 mT. The magnetic moment has been normalized to the moment at 5 K. $T_C$ drops significantly with decreasing oxygen pressure during growth. . . . .	56
7.12	Hysteresis curve measurements. (a) Comparison of the hysteresis curves taken at 5 K of the samples grown at different oxygen pressure measured after field cooling in 1 T. (b) The same data shown with a smaller field range to highlight the shift of the hysteresis curves. $H_C$ and $H_E$ values can be seen in table 7.2. (c) Temperature dependence of the coercive and EB field of the sample grown by HSD at 0.8 mbar. Before each hysteresis curve the sample has been cooled down in from room temperature in a field of 1 T. $H_C$ and $H_E$ values are listed in table 7.3. $H_E$ vanishes around 50 K comparable to the results of Zhu et al [1]. (d) Hysteresis curve measured several times at 5 K for the sample grown by HSD at 0.8 mbar after field cooling in 1 T. A subsequent decay of the $H_E$ is visible (training effect). . . . .	57
7.13	Overview of the SNS data reduction procedure. Top left: raw data picture on the 2-dimensional position sensitive detector. The angle of reflection can be calculated from the x-pixel position (the farther to the left, the larger the angle of reflection). The red rectangle indicates the reflected signal, the green one the direct (the part of the primary beam which passes the sample) and diffracted beam. The direct beam is mostly shaded by the beamstop (white rectangle). Top right: the same raw data set, but shown in x-pixel versus TOF (first angle, $\theta = 0.2^\circ$ ). Also shown are the measurements at the two other angles $\theta = 0.4^\circ$ and $\theta = 0.8^\circ$ . In the first angle picture the diffracted beam can clearly be seen. In the third angle measurement thickness oscillations already are visible in the reflected signal. An error signal is caused by the instruments electronics and is related to the chopper rotation speed (therefore, it always is at the same TOF pixel). This error signal is eliminated by subtraction of the data to the background. The region of interest (ROI) is shown for all three angles. Bottom: the raw data within the ROI for every angle is reduced and transferred to the corresponding $Q_z$ values. The measurements at different angles can be combined by matching them in the overlap regions to obtain a single reflectivity curve. . . . .	59
7.14	PNR data of the PLD sample. Top: 340 K data measured with an unpolarized beam at 1 T. Bottom: 6 K data taken at 1 T. The thicknesses indicated are determined by the simulation of the low temperature reflectivity data. The arrow indicates a layer with non zero magnetic scattering length density, where the number to the right gives the fraction of the maximum theoretical value. Detailed results can be found in table 7.4. . . . .	61
7.15	PNR data of the HSD sample grown at 0.8 mbar. The $R^{--}$ data are divided by 10 for better visibility. Top: 6 K data taken at 1 T. The thicknesses indicated are determined by the simulation of the PNR data. The arrow indicates a layer with non zero magnetic scattering length density, where the number to the right gives the fraction of the maximum theoretical value. Detailed results can be found in table 7.4. Bottom: Two alternative simulations are shown to emphasize the significant difference to the best fit profile: one for a completely ferromagnetic LSMO layer (solid line) and one for a nonmagnetic LSMO layer on the top of the LSMO layer at the interface to air (dashed line). . . . .	63

7.16	PNR data of the HSD sample grown at 1.0 mbar taken at 6 K and 1 T. The $R^{--}$ data are divided by 10 for better visibility. The simulation of a completely ferromagnetic LSMO layer (solid line) and a non-magnetic LSMO layer at the interface to STO (dashed line) are shown. Due to the smaller signal-to-noise-ratio both cases can not be distinguished. . . . .	64
7.17	PNR data of the HSD sample grown at 0.6 mbar and 1 T. Top: best fit to the 6 K data. The $R^{--}$ data are divided by 10 for better visibility. The thicknesses indicated are determined by the simulation of the reflectivity data. The arrow indicates a layer with non zero magnetic scattering length density, where the number to the right gives the fraction of the maximum theoretical value. Detailed results can be found in table 7.4. Bottom: Alternative simulation for the case of a completely FM layer. Especially the thickness oscillation visible in the $R^{--}$ channel is shifted to too small $Q_z$ values. . . . .	66
7.18	Temperature dependence of the XRMS signal at $\theta = 10^\circ$ of the LSMO single layer grown by HSD at 0.8 mbar and 0.05 T. Like for all other XMCD plots, the reflected XMCD signal (difference of reflected intensities for an incident LCP and RCP x-ray beam) is given in percent of the average signal (sum of reflected intensities for an incident LCP and RCP x-ray beam) . . . . .	67
7.19	Average signal - i.e. sum of reflected RCP and LCP incident x-rays - of the LSMO single layer grown by HSD at 0.8 mbar for all three incident angles. The maxima at around 641 and 652 eV correspond to the $L_{III}$ and $L_{III}$ absorption edges, respectively. The slab structure of the sample for the simulations is shown in the bottom right. . . . .	68
7.20	XMCD signal of the LSMO/STO bilayer grown by PLD for all three incident angles taken at 30 K in a field of 0.05 T. The slab structure of the sample for the simulations is shown in the bottom right. The thicknesses indicated are determined by the simulation of the reflectivity data. The arrow indicates a layer with non zero magnetic scattering length density, where the number to the right gives the fraction of the maximum theoretical value. Detailed results can be found in table 7.4. . . . .	70
7.21	XMCD signal of the LSMO single layer grown by HSD at 0.8 mbar for all three incident angles taken at 30 K in a field of 0.05 T. The slab structure of the sample for the simulations is shown in the bottom right. The thicknesses indicated are determined by the simulation of the reflectivity data. The arrow indicates a layer with non zero magnetic scattering length density, where the number to the right gives the fraction of the maximum theoretical value. Detailed results can be found in table 7.4. . . . .	71
7.22	Alternate simulation for the PNR data at 6 K of the LSMO single layer grown by HSD at 0.8 mbar. A similar good agreement compared to the fit presented in figure 7.15(a) can be found with a small net magnetization at the LSMO/STO interface. This alternate magnetic profile is identical to the one found by XRMS. . . . .	72

7.23	Alternate simulations to the XMCD data taken at $\theta = 15^\circ$ of the LSMO single layer grown by HSD at 0.8 mbar in order to emphasize the sensitivity of the XMCD signal to small changes in the magnetic and/or chemical profile of the sample. All parameters are kept identical to the parameters obtained by the best fit shown in figure 7.21 except for the following changes. a) Simulation for a 5 Å thick interface layer and 80 Å rest layer (instead of 10 Å and 75 Å, respectively). b) Simulation for a 15 Å thick interface layer and 70 Å rest layer (instead of 10 Å and 75 Å, respectively). c) Simulation for an LSMO layer having a homogeneous magnetization of 60 % of the theoretical bulk value. d) Simulation for a 10 Å interface layer with no net magnetic moment. . . . .	73
7.24	XMCD signal of the LSMO single layer grown by HSD at 0.6 mbar for all three incident angles taken at 30 K in a field of 0.05 T. The slab structure of the sample for the simulations is shown in the bottom right. The thicknesses indicated are determined by the simulation of the reflectivity data. The arrow indicates a layer with non zero magnetic scattering length density, where the number to the right gives the fraction of the maximum theoretical value. Detailed results can be found in table 7.4. . . . .	75
7.25	Strain vs. doping phase diagram of LSMO. The information for the doping range between $x = 0.2$ and $x = 0.6$ is taken from [116] and [63]. The phase boundary between FM and A-AFM region for a doping level smaller than 0.2 is an assumption or rather an interpolation between the last calculated point in [116] for $x=0.2$ and the known fact, that bulk LSMO with $x=0.1$ exhibits the A-AFM structure [52]. Even though the doping level is kept at 0.33 for the samples under investigation, one can still "move" through the phase diagram by oxygen deficiencies (according to formula (7.2)) and strain and reach the A-AFM region. The $\delta$ values give the necessary oxygen deficiency to reach the same $Mn^{4+}/Mn^{3+}$ ratio as a fully oxygenated LSMO with a doping level at the corresponding position. . . . .	76
8.1	Deposition rate calibration measurement for the growth of an LSMO layer. For each of the required elements the background level is measured first for a couple of minutes followed by the deposition rate, if the shutter for the corresponding effusion cell is opened. The true deposition rate is obtained by the difference of the two rates. The first three measurements are taken before the layer growth with the least stable rate taken last (Sr). The three last measurements are taken after the growth (the time for the growth is left out in the plot) to check the drift of the evaporation rates. . . . .	80
8.2	RHEED patterns during a deposition of a BTO thin film. a) picture of the clean Nb:STO substrate. b) RHEED pattern after deposition of 8 unit cells of BTO. c) RHEED pattern after deposition of 36 unit cells of BTO. . . . .	81
8.3	RHEED oscillations during a growth of a BTO thin film on Nb:STO. The plot shows the last 26 oscillation of a nominal 116 u.c. thick BTO layer. The RHEED measurement proves layer-by-layer growth for the entire layer. The specular intensity corresponds to the central peak in figure 8.2, the 1 <sup>st</sup> order intensities to the peaks to the left and right of the central reflection in figure 8.2. . . . .	82
8.4	Sketch of the LSMO/BTO samples prepared for this work. . . . .	82
8.5	XRR measurements of both samples. The layer thicknesses resulting from the simulations are given in the sample sketches. Detailed results are listed in table 8.1	84

8.6	XRD measurements of both samples around the (002) reflections of the layers and the substrates. The given values for the out-of-plane parameters $c$ are obtained by the peak positions resulting from the simulations. Simulations have been done by using the <i>plot.py</i> data evaluation software [108]. Detailed results are listed in table 8.1. . . . .	85
8.7	Temperature scans at 0.5 mT after cooling in a field of 1 T for both samples. . . .	87
8.8	(a) Exemplary electrical characterization measurement of the sample with the LSMO layer on top of the BTO layer measured in 1 ms. No clear ferroelectric behavior is visible. The shape of the $Q(E)$ curve looks very similar to a mixture of the well known hysteresis artefacts caused by linear ((b) top sketch) or nonlinear ((b) bottom sketch) lossy dielectric. The sketches in (b) are taken from [119]. . . .	89
8.9	Temperature dependence of the XRMS signal at $\theta = 10^\circ$ of the sample with the BTO layer on top of the LSMO layer. . . . .	90
8.10	Electric field dependence of the XRMS signal of the sample with the BTO layer on top of the LSMO layer at 50 K for an incident angle of $\theta = 10^\circ$ . . . . .	91
8.11	Average (LCP plus RCP) and XMCD signal measured around the $Ti L_{II}$ and $L_{III}$ edges on the sample with the LSMO on top of the BTO layer at 50 K and an incident angle of $5^\circ$ . . . . .	91
8.12	XMCD signal of the sample with the BTO layer on top of the LSMO layer for all three incident angles. The slab structure of the sample for the simulations is shown in the bottom right. Only the BTO and LSMO layer of the sample are shown. The thicknesses indicated are determined by the simulation of the reflectivity data. The arrow indicates a layer with non zero magnetic scattering length density, where the number to the right gives the fraction of the maximum theoretical value of LSMO having a doping level of $x = 0.33$ . . . . .	93
8.13	XMCD signal of the sample with the LSMO layer on top of the BTO layer for all three incident angles. The slab structure of the sample for the simulations is shown in the bottom right. Only the BTO and LSMO layer of the sample are shown. The thicknesses indicated are determined by the simulation of the reflectivity data. The arrow indicates a layer with non zero magnetic scattering length density, where the number to the right gives the fraction of the maximum theoretical value of LSMO having a doping level of $x = 0.33$ . . . . .	95
8.14	Error signal for the sample with the top LSMO layer at incident angles $\theta = 5^\circ$ (a) and $\theta = 15^\circ$ (b). Plotted are the XMCD signal determined at +500 Oe and -500 Oe in green and blue, respectively. The average of both measurements (black solid line) gives the error signal. The difference (red) is the true XMCD signal shown in figure 8.13. . . . .	96



## C. Abbreviations

AFD	anti-ferro-distortive
AFM	Atomic Force Microscopy
ANL	Argonne National Laboratory
APS	Advanced Photon Source at ANL
BTO	BaTiO <sub>3</sub>
CFS	Crystal Field Splitting
CFT	Crystal Field Theory
CNM	Center for Nanoscale Materials at ANL
CMR	Colossal Magneto Resistance
DE	Double Exchange
EB	Exchange Bias
FOM	Figure of Merit
HSD	High-oxygen-pressure Sputter Deposition
FM	ferromagnetic
LCP	left circular polarized
LMO	LaMnO <sub>3</sub>
LSMO	La <sub>1-x</sub> Sr <sub>x</sub> MnO <sub>3</sub>
OMBE	Oxide Molecular Beam Epitaxy
ORNL	Oak Ridge National Laboratory
PLD	Pulsed Laser Deposition
PNR	Polarized Neutron Reflectometry
PPMS	Physical Properties Measurement System
QCM	Quartz Crystal Monitor
RBS	Rutherford Backscattering
RCP	right circular polarized
RHEED	Reflection High Energy Electron Diffraction
SE	Superexchange
SLD	Scattering length density
SNS	Spallation Neutron Source at ORNL
SMO	SrMnO <sub>3</sub>
STO	SrTiO <sub>3</sub>
TMO	Transition Metal Oxides
UHV	Ultra High Vacuum
VSM	Vibrating Sample Magnetometry
XMCD	X-ray Magnetic Circular Dichroism
XRD	X-ray Diffraction
XRMS	X-ray Resonant Magnetic Scattering
XRR	X-ray Reflectometry





## D. Physical Constants

$c = 2.998 \cdot 10^8 m/s$	Speed of light in vacuum
$e = 1.602 \cdot 10^{-19} C$	Elementary charge
$\mu_B = 9.274 \cdot 10^{-24} J/T$	Bohr magneton
$\hbar = 1.055 \cdot 10^{-34} Js$	Planck constant
$\epsilon_0 = 8,854 \cdot 10^{-12} F/m$	Vacuum permittivity
$m_e = 9.109 \cdot 10^{-31} kg$	Mass of electron
$m_n = 1.675 \cdot 10^{-27} kg$	Mass of neutron
$N_A = 6.022 \cdot 10^{23} mol^{-1}$	Avogadro constant



# Bibliography

- [1] Zhu, S., Yuan, J., Zhu, B., Zhang, F., Xu, B., Cao, L., Qiu, X., Zhao, B., and Zhang, P. (2007) Exchange bias effect and enhanced magnetoresistance in  $\text{La}_{0.67}\text{Sr}_{0.33}\text{MnO}_3/\text{SrTiO}_3$  superlattices. *Appl. Phys. Lett.*, **90**, 112502.
- [2] Burton, J. D. and Tsymbal, E. Y. (2009) Prediction of electrically induced magnetic reconstruction at the manganite/ferroelectric interface. *Phys. Rev. B*, **80**, 174406.
- [3] Heber, J. (2009) Materials science: Enter the oxides. *NATURE*, **459**, 28–30.
- [4] Bednorz, J. G. and Müller, K. A. (1986) Possible high  $t_c$  superconductivity in the  $\text{Ba}_{1-x}\text{K}_x\text{BiO}_3$  system. *Z. Phys. B Cob. Mat.*, **64**, 189–193, 10.1007/BF01303701.
- [5] Haghiri-Gosnet, A.-M. and Renard, J.-P. (2003) CMR manganites: physics, thin films and devices. *J. Phys. D: Appl. Phys.*, **36**, R127–R150.
- [6] Fiebig, M. (2005) Revival of the magnetoelectric effect. *J. Phys. D: Appl. Phys.*, **38**, R123.
- [7] Poppe, U., Schubert, J., Arons, R., Evers, W., Freiburg, C., Reichert, W., Schmidt, K., Sybertz, W., and Urban, K. (1988) Direct production of crystalline superconducting thin films of  $\text{YBa}_2\text{Cu}_3\text{O}_7$  by high-pressure oxygen sputtering. *Solid State Commun.*, **66**, 661 – 665.
- [8] Petraru, A., Kohlstedt, H., Poppe, U., Waser, R., Solbach, A., Klemradt, U., Schubert, J., Zander, W., and Pertsev, N. A. (2008) Wedgelike ultrathin epitaxial  $\text{BaTiO}_3$  films for studies of scaling effects in ferroelectrics. *Appl. Phys. Lett.*, **93**.
- [9] Brandt, M., Frenzel, H., Hochmuth, H., Lorenz, M., Grundmann, M., and Schubert, J. (2009) Ferroelectric thin film field-effect transistors based on  $\text{ZnO}/\text{BaTiO}_3$  heterostructures. *J. Vac. Sci. Technol.*, **27**, 1789–1793.
- [10] Schlom, D. G., Chen, L.-Q., Pan, X., Schmehl, A., and Zurbuchen, M. A. (2008) A thin film approach to engineering functionality into oxides. *J. Am. Ceram. Soc.*, **91**, 2429–2454.
- [11] Reyren, N., et al. (2007) Superconducting interfaces between insulating oxides. *Science*, **317**, 1196–1199.
- [12] Brinkman, A., Huijben, M., van Zalk, M., Huijben, J., Zeitler, U., Maan, J. C., van der Wiel, W. G., Rijnders, G., Blank, D. H. A., and Hilgenkamp, H. (2007) Magnetic effects at the interface between non-magnetic oxides. *Nat Mater*, **6**, 493–496.
- [13] Dagotto, E., Hotta, T., and Moreo, A. (2001) Colossal magnetoresistant materials: the key role of phase separation. *Physics Reports*, **344**, 1 – 153.
- [14] Meiklejohn, W. H. and Bean, C. P. (1956) New magnetic anisotropy. *Phys. Rev.*, **102**, 1413–1414.
- [15] Berkowitz, A. E. and Takano, K. (1999) Exchange anisotropy – a review. *Journal of Magnetism and Magnetic Materials*, **200**, 552 – 570.

- [16] Nogues, J. and Schuller, K. (1999) Exchange bias. *Journal of Magnetism and Magnetic Materials*, **192**, 203–232.
- [17] Zhu, S. J., Zhao, B. R., Zhu, B. Y., Xu, B., Cao, L. X., and Qiu, X. G. (2007) Oscillatory exchange coupling in  $\text{La}_{0.67}\text{Sr}_{0.33}\text{MnO}_3/\text{SrTiO}_3$  superlattices. *Appl. Phys. Lett.*, **91**, 012505.
- [18] Zhu, S. J., Zhao, B. R., Xu, B., Zhu, B. Y., Cao, L. X., and Qiu, X. G. (2008) Training effect of exchange bias in  $\text{La}_{0.67}\text{Sr}_{0.33}\text{MnO}_3/\text{SrTiO}_3$  superlattice. *J. Phys. D: Appl. Phys.*, **41**.
- [19] Wu, S. M., Cybart, S. A., Yu, P., Rossell, M. D., Zhang, J. X., Ramesh, R., and Dynes, R. C. (2010) Reversible electric control of exchange bias in a multiferroic field-effect device. *Nat. Mater.*, **9**, 756–761.
- [20] Hill, N. A. (2000) Why are there so few magnetic ferroelectrics? *J. Phys. Chem. B*, **104**, 6694–6709.
- [21] Izyumska, N., Alivov, Y., and Morkoc, H. (2009) Oxides, oxides, and more oxides: High-oxides, ferroelectrics, ferromagnetics, and multiferroics. *Crc. Cr. Rev. Sol. State*, **34**, 89–179.
- [22] Rose, G. (1839) Beschreibung einiger neuen Mineralien des Urals. *Ann. Phys. Chem.*, **48**, 551–573.
- [23] Goldschmidt, V. M., Barth, T., Lunde, G., and Zachariassen, W. H. (1926) Geochemische Verteilungsgesetze der Elemente, VII. Die Gesetze der Krystallochemie. *Skr. Norske Vidensk. Akad.*, **1**, Mat.–Nat. Kl. No.2.
- [24] Howard, C. and Stokes, H. T. (1998) Group-theoretical analysis of octahedral tilting in perovskites. *Acta Cryst. B*, **54**, 782–789.
- [25] Bersuker, I. B. (1996) *Electronic structure and properties of transition metal compounds*. Wiley, New York.
- [26] Jahn, H. A. and Teller, E. (1937) Stability of polyatomic molecules in degenerate electronic states. i. orbital degeneracy. *Proc. R. Soc.*, **161**, 220–235.
- [27] Dresselhaus, M. S., Dresselhaus, G., and Jorio, A. (2008) *Group theory: Application to the physics of condensed matter*. Springer-Verlag, Berlin Heidelberg.
- [28] Khomskii, D. I. (2006) Multiferroics: Different ways to combine magnetism and ferroelectricity. *J. Magn. Magn. Mater.*, **306**, 1–14.
- [29] Cohen, R. (1992) Origin of ferroelectricity in perovskite oxides. *Nature*, **358**, 136–138.
- [30] Filippetti, A. and Hill, N. A. (2002) Coexistence of magnetism and ferroelectricity in perovskites. *Phys. Rev. B*, **65**, 195120.
- [31] Neville, R. C., Hoeneisen, B., and Mead, C. A. (1972) Permittivity of strontium titanate. *J. Appl. Phys.*, **43**, 2124–2131.
- [32] Müller, K. A. and Burkard, H. (1979)  $\text{SrTiO}_3$ : An intrinsic quantum paraelectric below 4 K. *Phys. Rev. B*, **19**, 3593–3602.
- [33] Unoki, H. and Sakudo, T. (1967) Electron spin resonance of  $\text{Fe}^{3+}$  in  $\text{SrTiO}_3$  with special reference to the 110°K phase transition. *J. Phys. Soc. Jpn.*, **23**, 546–552.

- 
- [34] Fleury, P. A., Scott, J. F., and Worlock, J. M. (1968) Soft phonon modes and the 110°K phase transition in SrTiO<sub>3</sub>. *Phys. Rev. Lett.*, **21**, 16–19.
- [35] Vogt, H. (1995) Refined treatment of the model of linearly coupled anharmonic oscillators and its application to the temperature dependence of the zone-center soft-mode frequencies of KTaO<sub>3</sub> and SrTiO<sub>3</sub>. *Phys. Rev. B*, **51**, 8046–8059.
- [36] Yamanaka, A., Kataoka, Y., Inaba, Y., Inoue, K., Hehlen, B., and Courtens, E. (2000) Evidence for competing orderings in strontium titanate from hyper-Raman scattering spectroscopy. *Europhys. Lett.*, **50**, 688–694.
- [37] Li, Y. L., et al. (2006) Phase transitions and domain structures in strained pseudocubic (100) SrTiO<sub>3</sub> thin films. *Phys. Rev. B*, **73**, 184112.
- [38] Zhong, W. and Vanderbilt, D. (1996) Effect of quantum fluctuations on structural phase transitions in SrTiO<sub>3</sub> and BaTiO<sub>3</sub>. *Phys. Rev. B*, **53**, 5047–5050.
- [39] Martoňák, R. and Tosatti, E. (1994) Path-integral Monte Carlo study of a model two-dimensional quantum paraelectric. *Phys. Rev. B*, **49**, 12596–12613.
- [40] Haeni, J. H., et al. (2004) Room-temperature ferroelectricity in strained SrTiO<sub>3</sub>. *Nature*, **430**, 758–761.
- [41] Itoh, M., Wang, R., Inaguma, Y., Yamaguchi, T., Shan, Y.-J., and Nakamura, T. (1999) Ferroelectricity induced by oxygen isotope exchange in strontium titanate perovskite. *Phys. Rev. Lett.*, **82**, 3540–3543.
- [42] Cochran, W. (1960) Crystal stability and the theory of ferroelectricity. *Adv. Phys.*, **9**, 387–423.
- [43] Zhang, Q., Cagin, T., and Goddard III, W. A. (2006) The ferroelectric and cubic phases in BaTiO<sub>3</sub> ferroelectrics are also antiferroelectric. *Proc. Nat. Acad. Sci. USA*, **103**, 14695–14700.
- [44] Ponomareva, I., Bellaiche, L., Ostapchuk, T., Hlinka, J., and Petzelt, J. (2008) Terahertz dielectric response of cubic BaTiO<sub>3</sub>. *Phys. Rev. B*, **77**, 012102.
- [45] Hlinka, J., Ostapchuk, T., Nuzhnyy, D., Petzelt, J., Kuzel, P., Kadlec, C., Vanek, P., Ponomareva, I., and Bellaiche, L. (2008) Coexistence of the phonon and relaxation soft modes in the terahertz dielectric response of tetragonal BaTiO<sub>3</sub>. *Phys. Rev. Lett.*, **101**, 167402.
- [46] Choi, K. J., et al. (2004) Enhancement of ferroelectricity in strained BaTiO<sub>3</sub> thin films. *Science*, **306**, 1005–1009.
- [47] Yoneda, Y., Okabe, T., Sakaue, K., Terauchi, H., Kasatani, H., and Deguchi, K. (1998) Structural characterization of BaTiO<sub>3</sub> thin films grown by molecular beam epitaxy. *J. Appl. Phys.*, **83**, 2458.
- [48] Li, Y. L. and Chen, L. Q. (2006) Temperature-strain phase diagram for BaTiO<sub>3</sub> thin films. *Appl. Phys. Lett.*, **88**, 072905.
- [49] Schlom, D. G., Chen, L.-Q., Eom, C.-B., Rabe, K. M., Streiffer, S. K., and Triscone, J.-M. (2007) Strain tuning of ferroelectric thin films. *Ann. Rev. Mater. Res.*, **37**, 589–626.
- [50] Volger, J. (1954) Further experimental investigations on some ferromagnetic oxidic compounds of manganese with perovskite structure. *Physica (Amsterdam)*, **20**, 49–66.

- [51] Urushibara, A., Moritomo, Y., Arima, T., Asamitsu, A., Kido, G., and Tokura, Y. (1995) Insulator-metal transition and giant magnetoresistance in  $\text{La}_{1-x}\text{Sr}_x\text{MnO}_3$ . *Phys. Rev. B*, **51**, 14103–14109.
- [52] Hemberger, J., Krimmel, A., Kurz, T., Krug von Nidda, H.-A., Ivanov, V. Y., Mukhin, A. A., Balbashov, A. M., and Loidl, A. (2002) Structural, magnetic. and electrical properties of single-crystalline  $\text{La}_{1-x}\text{Sr}_x\text{MnO}_3$  ( $0.4 < x < 0.85$ ). *Phys. Rev. B*, **66**, 094410.
- [53] Szewczyk, A., Gutowska, M., and Dabrowski, B. (2005) Specific heat and phase diagram of heavily doped  $\text{La}_{1-x}\text{Sr}_x\text{MnO}_3$  ( $0.45 \leq x \leq 1.0$ ). *Phys. Rev. B*, **72**, 224429.
- [54] Heisenberg, W. (1928) Zur theorie des ferromagnetismus. *Zeitschrift für Physik A Hadrons and Nuclei*, **49**, 619–636, 10.1007/BF01328601.
- [55] Goodenough, J. B. (1955) Theory of the role of covalence in the perovskite-type manganites  $[\text{La},\text{M}(\text{II})]\text{MnO}_3$ . *Phys. Rev.*, **100**, 564–573.
- [56] Goodenough, J. B. (1958) An interpretation of the magnetic properties of the perovskite-type mixed crystals  $\text{La}_{1-x}\text{Sr}_x\text{CoO}_{3-\lambda}$ . *J. Phys. Chem. Solids*, **6**, 287–297.
- [57] Kanamori, J. (1959) Superexchange interaction and symmetry properties of electron orbitals. *J. Phys. Chem. Solids*, **10**, 87 – 98.
- [58] Zener, C. (1951) Interaction between the  $d$ -shells in the transition metals, II. Ferromagnetic compounds of manganese with perovskite structure. *Phys. Rev.*, **82**, 403–405.
- [59] Li, H. F., Su, Y., Persson, J., Meuffels, P., Walter, J. M., Skowronek, R., and Brückel, T. (2007) Correlation between structural and magnetic properties of  $\text{La}_{7/8}\text{Sr}_{1/8}\text{Mn}_{3-\gamma}\text{O}_{3+\delta}$  with controlled nonstoichiometry. *J. Phys: Condens. Mat.*, **19**, 016003.
- [60] de Gennes, P. G. (1960) Effects of double exchange in magnetic crystals. *Phys. Rev.*, **118**, 141–154.
- [61] Santos, T. S., May, S. J., Robertson, J. L., and Bhattacharya, A. (2009) Tuning between the metallic antiferromagnetic and ferromagnetic phases of  $\text{La}_{1-x}\text{Sr}_x\text{MnO}_3$  near  $x=0.5$  by digital synthesis. *Phys. Rev. B*, **80**, 155114.
- [62] Horiba, K., et al. (2009) Pressure-induced change in the electronic structure of epitaxially strained  $\text{La}_{1-x}\text{Sr}_x\text{MnO}_3$  thin films. *Phys. Rev. B*, **80**, 132406.
- [63] Konishi, Y., Fang, Z., Izumi, M., Manako, T., Kasai, M., Kuwahara, H., Kawasaki, M., Terakura, K., and Tokura, Y. (1999) Orbital-state-mediated phase-control of manganites. *Journal of the Physical Society of Japan*, **68**, 3790–3793.
- [64] Wollan, E. and Koehler, W. (1955) Neutron diffraction study of the magnetic properties of the series of perovskite-type compounds  $[(1-x)\text{La}, x\text{Ca}]\text{MnO}_3$ . *Phys. Rev.*, **100**, 545–563.
- [65] Salvador, P. A., Haghiri-Gosnet, A.-M., Mercey, B., Hervieu, M., and Raveau, B. (1999) Growth and magnetoresistive properties of  $(\text{LaMnO}_3)_m(\text{SrMnO}_3)_n$  superlattices. *Appl. Phys. Lett.*, **75**, 2638–2640.
- [66] Bhattacharya, A., Zhai, X., Warusawithana, M., Eckstein, J. N., and Bader, S. D. (2007) Signatures of enhanced ordering temperatures in digital superlattices of  $(\text{LaMnO}_3)_m/(\text{SrMnO}_3)_{2m}$ . *Appl. Phys. Lett.*, **90**, 222503.
- [67] Radu, F. and Zabel, H. (2008) Exchange bias effect of ferro-/antiferromagnetic heterostructures. Zabel, H. and Bader, S. (eds.), *Magnetic Heterostructures*, vol. 227 of *Springer Tracts in Modern Physics*, pp. 97–184, Springer Berlin / Heidelberg.

- [68] Spaldin, N. A. and Fiebig, M. (2005) The renaissance of magnetoelectric multiferroics. *Science*, **309**, 391–392.
- [69] Lee, J. H., et al. (2010) A strong ferroelectric ferromagnet created by means of spin-lattice coupling. *Nature*, **466**, 954–958.
- [70] Gepraegs, S., Opel, M., Goennenwein, S. T. B., and Gross, R. (2007) Multiferroic materials based on artificial thin film heterostructures. *Phil. Mag. Lett.*, **87**, 141–154.
- [71] Ramesh, R., Zavaliche, F., Chu, Y. H., Martin, L. W., Yang, S. Y., Cruz, M. P., Barry, M., Lee, K., Yang, P., and Zhan, Q. (2007) Magnetoelectric complex-oxide heterostructures. *Phil. Mag. Lett.*, **87**, 155–164.
- [72] Singh, M. P. and Prellier, W. (2007) Oxide superlattices for multiferroics: opportunities, issues, and challenges. *Phil. Mag. Lett.*, **87**, 211–222.
- [73] Niranjana, M. K., Velev, J. P., Duan, C.-G., Jaswal, S. S., and Tsymbal, E. Y. (2008) Magnetoelectric effect at the  $\text{Fe}_3\text{O}_4/\text{BaTiO}_3$  (001) interface: a first-principles study. *Phys. Rev. B*, **78**, 104405.
- [74] Suzuki, T., Nishi, Y., and Fujimoto, M. (1999) Analysis of misfit relaxation in heteroepitaxial  $\text{BaTiO}_3$  thin films. *Philos Mag A*, **79**, 2461–2483.
- [75] Pratt, I. H. (1971) Characteristics of rf sputtered barium titanate thin films. *Pr. Inst. Electr. Elect.*, **59**, 1440–1447.
- [76] Brückel, T., Heger, G., Richter, D., and Zorn, R. (eds.) (2008) *Neutron Scattering*. Forschungszentrum Jülich GmbH.
- [77] Lekner, J. (1987) *Theory of Reflection*. Dordrecht, Boston.
- [78] Als-Nielsen, J. (1986) *Topics in Current Physics. Structure and Dynamics of Surfaces*. Springer, Berlin.
- [79] Parratt, L. G. (1954) Surface studies of solids by total reflection of x-rays. *Phys. Rev.*, **95**, 359–369.
- [80] Henke, B., Gullikson, E., and Davis, J. (1993) X-ray interactions: Photoabsorption, scattering, transmission, and reflection at  $E = 50\text{--}30,000$  eV,  $z = 1\text{--}92$ . *Atom. Data Nucl. Data*, **54**, 181 – 342.
- [81] Kramers, H. A. (1927) La diffusion de la lumiere par les atomes. *Atti. Cong. Intern. Fisica, (Transactions of Volta Centenary Congress) Como*, **2**, 545–557.
- [82] Kronig, R. d. L. (1926) On the theory of the dispersion of x-rays. *J. Opt. Soc. Am.*, **12**, 547–556.
- [83] Stöhr, J. and Siegmann, H. (2006) *Magnetism*. Springer Berlin / Heidelberg.
- [84] Kramers, H. A. and Heisenberg, W. (1925) Über die Streuung von Strahlung durch Atome. *Z. Phys.*, **31**, 681–708.
- [85] Dirac, P. A. M. (1927) The quantum theory of the emission and absorption of radiation. *Proc. R. Soc. A*, **114**, 243–265.
- [86] Als-Nielsen, J. and McMorrow, D. (2011) *Elements of modern x-ray physics*. Wiley, New York.
- [87] Argyres, P. N. (1955) Theory of the Faraday and Kerr Effects in Ferromagnetics. *Phys. Rev.*, **97**, 334–345.



- [88] Kao, C., Hastings, J. B., Johnson, E. D., Siddons, D. P., Smith, G. C., and Prinz, G. A. (1990) Magnetic-resonance exchange scattering at the iron L<sub>III</sub> and L<sub>II</sub> edges. *Phys. Rev. Lett.*, **65**, 373–376.
- [89] Kortright, J. B. and Kim, S.-K. (2000) Resonant magneto-optical properties of Fe near its 2p levels: Measurement and applications. *Phys. Rev. B*, **62**, 12216–12228.
- [90] Jones, R. C. (1941) A new calculus for the treatment of optical systems. *J. Opt. Soc. Am.*, **31**, 488–493.
- [91] Jones, R. C. (1942) A new calculus for the treatment of optical systems, IV. *J. Opt. Soc. Am.*, **32**, 486–493.
- [92] Yang, Z. J. and Scheinfein, M. R. (1993) Combined three-axis surface magneto-optical kerr effects in the study of surface and ultrathin-film magnetism. *J. Appl. Phys. Lett.*, **74**, 6810–6823.
- [93] You, C.-Y. and Shin, S.-C. (1996) Derivation of simplified analytic formulae for magneto-optical Kerr effects. *Appl. Phys. Lett.*, **69**, 1315–1317.
- [94] Zak, J., Moog, E., Liu, C., and Bader, S. (1990) Universal approach to magneto-optics. *J. Magn. Magn. Mater.*, **89**, 107 – 123.
- [95] Zak, J., Moog, E. R., Liu, C., and Bader, S. D. (1991) Magneto-optics of multilayers with arbitrary magnetization directions. *Phys. Rev. B*, **43**, 6423–6429.
- [96] Waser, R. (2003) *Nanoelectronics and Information Technology*. Wiley-VCH.
- [97] Glavic, A. (2011) *Multiferroicity in oxide thin films and heterostructures*. Ph.D. thesis, RWTH Aachen.
- [98] Oura, K., Lifshitz, V. G., Saranin, A. A., V., Z. A., and Katayama, M. (2003) *Surface science: an introduction*. Springer, Berlin.
- [99] Ichimiya, A. and Cohen, P. I. (2004) *Reflection High-Energy Electron Diffraction*. Cambridge University Press.
- [100] <http://http://neutrons.ornl.gov/mr/>.
- [101] <http://www.aps.anl.gov/Sector4/4idc/>.
- [102] Freeland, J. W., et al. (2007) Suppressed magnetization at the surfaces and interfaces of ferromagnetic metallic manganites. *J. Phys.: Condens. Mat.*, **19**, 315210.
- [103] Stettner, J. (1995) *Charakterisierung von rauhen MBE-CoSi<sub>2</sub>/Si-Schichtsystemen mittels Röntgenbeugung*. Ph.D. thesis, Christian-Albrechts-Universität zu Kiel.
- [104] Li, J., Liu, J. M., Li, H. P., Fang, H. C., and Ong, C. K. (1999) Magnetoresistance in oxygen deficient La<sub>0.75</sub>Sr<sub>0.25</sub>MnO<sub>3-δ</sub> thin films prepared by pulsed laser deposition. *J. Magn. Magn. Mater.*, **202**, 285 – 291.
- [105] Ju, H. L., Gopalakrishnan, J., Peng, J. L., Li, Q., Xiong, G. C., Venkatesan, T., and Greene, R. L. (1995) Dependence of giant magnetoresistance on oxygen stoichiometry and magnetization in polycrystalline La<sub>0.67</sub>Ba<sub>0.33</sub>MnO<sub>z</sub>. *Phys. Rev. B*, **51**, 6143–6146.
- [106] Goyal, A., Rajeswari, M., Shreekala, R., Lofland, S. E., Bhagat, S. M., Boettcher, T., Kwon, C., Ramesh, R., and Venkatesan, T. (1997) Material characteristics of perovskite manganese oxide thin films for bolometric applications. *Appl. Phys. Lett.*, **71**, 2535–2537.

- 
- [107] Sun, J. R., Yeung, C. F., Zhao, K., Zhou, L. Z., Leung, C. H., Wong, H. K., and Shen, B. G. (2000) Strain-dependent vacuum annealing effects in  $\text{La}_{0.67}\text{Ca}_{0.33}\text{MnO}_{3-\delta}$  films. *Appl. Phys. Lett.*, **76**, 1164–1166.
- [108] Glavic, A. (2011), Documentation: Plot.py - data plotting and evaluation software - version 0.7.9. [Http://iffwww.iff.kfa-juelich.de/~glavic/plotwiki/](http://iffwww.iff.kfa-juelich.de/~glavic/plotwiki/).
- [109] Ju, H. L. and Sohn, H. (1997) Magnetic inhomogeneity and colossal magnetoresistance in manganese oxides. *J. Magn. Magn. Mater.*, **167**, 200 – 208.
- [110] Fu-Chang, Z., Wei-Ran, C., Wei-Zhi, G., Bo, X., Xiang-Gang, Q., and Bai-Ru, Z. (2004) Spin-glass-like behaviour and positive magnetoresistance in oxygen deficient  $\text{La}_{2/3}\text{Ca}_{1/3}\text{MnO}_{3-\delta}$  thin films. *Chinese Phys.*, **13**, 783–788.
- [111] Chien, C. L., Xiao, J. Q., and Jiang, J. S. (1993) Giant negative magnetoresistance in granular ferromagnetic systems (invited). *Journal of Applied Physics*, **73**, 5309–5314.
- [112] Xiao, G., Liou, S. H., Levy, A., Taylor, J. N., and Chien, C. L. (1986) Magnetic relaxation in Fe-( $\text{SiO}_2$ ) granular films. *Phys. Rev. B*, **34**, 7573–7577.
- [113] Madhukar, S., Aggarwal, S., Dhote, A. M., Ramesh, R., Krishnan, A., Keeble, D., and Poindexter, E. (1997) Effect of oxygen stoichiometry on the electrical properties of  $\text{La}_{0.5}\text{Sr}_{0.5}\text{CoO}_3$  electrodes. *J. Appl. Phys.*, **81**, 3543–3547.
- [114] Petrov, A., Cherepanov, V., Kononchuk, O., and Gavrilova, L. (1990) Oxygen nonstoichiometry of  $\text{La}_{1-x}\text{Sr}_x\text{CoO}_{3-\delta}$  ( $0 < x < 0.6$ ). *J. Solid State Chem.*, **87**, 69 – 76.
- [115] Abbate, M., et al. (1992) Controlled-valence properties of  $\text{La}_{1-x}\text{Sr}_x\text{FeO}_3$  and  $\text{La}_{1-x}\text{Sr}_x\text{MnO}_3$  studied by soft-x-ray absorption spectroscopy. *Phys. Rev. B*, **46**, 4511–4519.
- [116] Fang, Z., Solovyev, I. V., and Terakura, K. (2000) Phase diagram of tetragonal manganites. *Phys. Rev. Lett.*, **84**, 3169–3172.
- [117] Koster, G., Kropman, B. L., Rijnders, G. J. H. M., Blank, D. H. A., and Rogalla, H. (1998) Quasi-ideal strontium titanate crystal surfaces through formation of strontium hydroxide. *Appl. Phys. Lett.*, **73**, 2920–2922.
- [118] Trithaveesak, O., Schubert, J., and Buchal, C. (2005) Ferroelectric properties of epitaxial  $\text{BaTiO}_3$  thin films and heterostructures on different substrates. *J. Appl. Phys.*, **98**, 114101.
- [119] Dawber, M., Rabe, K. M., and Scott, J. F. (2005) Physics of thin-film ferroelectric oxides. *Rev. Mod. Phys.*, **77**, 1083–1130.
- [120] Petrisor, T. J., Gabor, M., Boule, A., Bellouard, C., Tiusan, C., Pana, O., and Petrisor, T. (2011) Oxygen incorporation effects in annealed epitaxial  $\text{La}_{1-x}\text{Sr}_x\text{MnO}_3$  thin films. *Journal of Applied Physics*, **109**, 123913.



# Acknowledgments

This work would not have been possible without the help and support of numerous people. I want to thank everyone, who has contributed to this work:

**Prof. Dr. Thomas Brückel** for offering me the opportunity to work in this very interesting field and for supporting me throughout the time. I want to thank him in particular for enabling me to work at the APS for one year. By this, I had the opportunity to get to know a broad spectrum of experimental techniques during this work.

**Prof. Dr. Uwe Klemradt** for agreeing to take the second revision of this work.

**Jörg Voigt** for the great support in every part of this thesis. Your continuous mentoring, the numerous discussions with you, and your new ideas really brought this work forward.

**Jonathan Lang** for the opportunity to work in his group at the APS for one year.

**John Freeland** first of all for making the stay at APS possible. But I want to thank you in particular for all the scientific support and advice and for enabling me to get to know a huge variety of different experimental methods not only in your group.

**Tiffany Santos** for all the time and patience, that you invested in our work at CNM, and for opening the doors and introducing me to all the experimental techniques in your group.

**Jürgen Schubert** for all the effort in the sample preparation by PLD and the RBS measurements and for all the fruitful discussions and suggestions during this work.

**Alexandra Steffen** for continuing and bringing forward the sample preparation of the LSMO/STO system by HSD and also for your help at the APS beamtime.

**Artur Glavic** for the scientific and technical support especially by the huge effort, which you put in providing and continuously upgrading the plotting software. I also want to thank you for the numerous scientific discussions about our projects.

**Valeria Lauter and Hailemariam Ambaye** for the scientific support during and after the neutron reflectometry beamtimes at the SNS.

I want to thank all my fellow students, who shared the office with me over the years, and all members of the Institute for Scattering Methods in Jülich and the Magnetic Materials Group in Argonne not only for the scientific discussions, but especially for creating such a friendly and positive working atmosphere.

Zum Schluss möchte ich mich bei meiner gesamten Familie für die stetige Unterstützung in jeder Hinsicht - nicht nur während dieser Arbeit - bedanken. Mein größter Dank geht natürlich an Jenny: Ich weiß, ich habe Deine Geduld mehr als einmal auf eine harte Probe gestellt. Danke, dass du mich trotzdem in den stressigen Zeiten ertragen und vor allem zu jeder Zeit unterstützt hast.



# Selbstständigkeitsversicherung

Ich versichere eidesstattlich, dass ich die vorliegende Dissertation selbstständig verfasst und keine anderen als die angegebenen Quellen und Hilfsmittel benutzt habe.

Daniel Schumacher